UNIVERSITY OF SOUTHAMPTON

School of Civil Engineering and the Environment

Particle Form and its Impact on Packing and Shear Behaviour of Particulate Materials

by

Chandra Obula Reddy ABBIREDDY

A Thesis Submitted in Fulfilment of the Degree of Doctor of
Philosophy in the School of Civil Engineering and the Environment
of the University of Southampton

June 2008

This work is dedicated to my parents, sister Lakshmi and brothers Seshu and Narasimha.

ABSTRACT

A small but important body of geomechanics literature now exists to show qualitatively that whether a specimen is composed of particles that are bulky or platy can have a significant effect on its behaviour during compression and shear. This particle shape characteristic has been termed 'form', which has sometimes been estimated on the basis of 'sphericity', a measure of how close a given particle form comes to that of a sphere. Before the effects of form can be established in an objective manner it will be necessary to develop and evaluate simple, practical, and robust three-dimensional measures of this aspect of particle shape, and to assess the importance of these in controlling the behaviour of particulate materials.

As a contribution to this fundamental study this thesis reviews experimental evidence on the importance of particle shape, the nature of clastic and crushed rock particles, and examines previous definitions of sphericity. It then considers potential methods of obtaining data to define the three-dimensional form of particles, and proposes two practical methods (one based on a volumetric equivalent scalene ellipsoid for coarse particulates and the other based on laser diffraction and turbidity measurement for fine particulates) by which this can be done. The proposed methods are applied to specimens with a number of particle shapes, and the results are assessed by comparison with other possible measures of form, and against the visual estimates obtained from either the static imaging in 3-orthogonal directions or the SEM images. Subsequently, the effects of form on packing arrangement of particles during deposition and on drained shear behaviour (in triaxial compression) of particulate materials are examined by carrying out laboratory tests on a variety of particle shapes and DEM simulations on wide range of particle forms. Novel techniques of determining the limiting void ratios and preparing the samples over a range of densities (with more or less the same fabric) are developed for DEM simulations. The results indicate that the limiting void ratios, inherent anisotropy, stiffness, peak strength and the strain to reach peak state, ultimate strength and the strain to reach ultimate state, the strain and the moblised stress ratio at the onset of dilation, the maximum dilatancy rate and the amount of dilation, particle breakage, and the existence of critical state, are all highly dependent on the form of constituent particles.

CONTENTS

LIST OF FIGURES

LIST OF TABLES

LIST OF SYMBOLS

δ	implied angle of rise of surface asperity
σ'_1	major principal stress
σ'_3	minor principal stress or effective confining stress
ε_a	axial strain
α_i	distortion angle at ith sampling point along the particle boundary
ε_v	volumetric strain (compression +ve and dilation –ve)
A	projected area of particle
A_0	initial cross-sectional area of the specimen
A_{actual}	actual area of clump
A_{CO}	Anisotropy index of particle orientations (equation 6.2)
A_{max}	maximum projected area of an oblate particle
A_{mean}	mean projected area of an oblate particle
A_{PFC}	area of clump calculated by PFC
A_{PO}	Anisotropy index of particle orientations (equation 6.1)
b	path length of the measuring cell
B_r	Hardin's relative breakage
C_{act}	actual volume concentration of particles
C_f	correction factor for theoretical concentration to account for the random orientation of particles
C_s	solids concentration in gm/cm^3
CSL	Critical State Line
C_{th}	theoretical volume concentration of particles
CVR	Critical Void Ratio
D_a	Diameter of a circle with the same projection area as the particle
D_{cc}	Diameter of the circumscribing circle in plan view
D_{cs}	Diameter of the circumscribing sphere ($\equiv D_{cc}$)
D_{ESZ}	volume equivalent spherical diameter obtained from electro sensing zone method

Dia(max)	Length of the longest line joining two points of object's outline and passing through centroid
Dia(min)	Length of the shortest line joining two points of object's outline and passing through centroid
D_{ic}	Diameter of the largest inscribed circle in plan view
D_{is}	Diameter of the largest inscribed circle (≡ smallest D_{ic} among the 2-orthogonal views perpendicular to plan view)
D_{LD}	laser diffraction equivalent spherical diameter of particles
D_{max}	maximum dilatancy factor
D_p	Diameter of a circle with the same perimeter as the particle
Dr	relative density
D_{RD}	equivalent spherical diameter obtained by electric-birefringence method
$D_{Stokes'}$	Stokes' equivalent spherical diameter of a particle
D_{vs}	Diameter of a sphere with the same volume as the particle
E'_{sec}	secant stiffness
e_{max}	maximum void ratio
e_{min}	minimum void ratio
F	form
F_n	normal force at the contact
$F_{s(max)}$	maximum elastic shear force at the contact
G_s	specific gravity of the particles
I	intermediate dimension of the particle
I_o	intensity of incident light
I_t	intensity of light transmitted through the cell
L	major dimension of the particle
M_i	number of particles in size band i per unit volume
N	Number of sampling points
NCL	Normal Consolidation Line
Obscuration	fraction of incident light that is attenuated due to extinction (scattering and/or absorption) by the particles
P	projected perimeter of particle
p'	mean effective stress

q	deviatoric stress (principal stress difference)
Q	ram load
r	ratio of major to minor dimension equivalent i.e., the inverse of *Form*
S	minor dimension of the particle
S, I and L	the smallest, intermediate and largest dimensions of the particles, measured in three orthogonal directions.
SEES	Scalene Ellipsoid Equivalent Sphericity
$\mathrm{S_p}$	Actual surface area of the particle
$\mathrm{S_s}$	Surface area of a sphere of the same volume as the particle
T	extinction factor accounting for scattering and absorption
V_i, Q_i, d_i	volume (%), extinction coefficient and the mean diameter of particles in size band *i*
V_l	volume of liquid used to disperse and circulate the sample through the Malvern cell
W	dry mass of the sample material
μ	inter-particle friction
δ	implied angle of rise
ρ	mass density of particles
ρ_w	mass density of water

ACKNOWLEDGEMENTS

I like to gratefully acknowledge the help and support of many colleagues, organisations, staff in other schools and/or universities and commercial test houses who carried out the tests on my behalf, and the individuals who made this thesis possible:

- My supervisor, Prof. C. R. I. Clayton, for introducing me to this topic, and for his constant motivation, invaluable supervision and support.
- ORSAS, and School of Civil Engineering and the Environment, University of Southampton for the financial support.
- Dr. Antonis Zervos for his comments and suggestions on 9-month and 18-month reports.
- Prof. Malcom Bolton for his helpful discussions/comments on this subject in GM3-2006, ISY-06 and GM3-2007.
- Dr. Michael Frenz (NOCS, Southampton) for carrying out Sedigraph tests on my behalf.
- Prof. Elsabe Kearsley (University of Pretoria, South Africa), and Dr. Veerle Huvenne and Dr. Michael Frenz (NOCS, Southampton) for their help with the laser diffraction testing.
- Dr. Stephen Ward-Smith (Malvern Instruments Ltd., UK) for his helpful discussions on optical properties selection for the range of materials analysed using Mastersizer 2000.
- Dr. Ralf Schiebel (NOCS, Southampton) for allowing me to use the Automated Particle Analysis System and his assistance.
- Dr. Barbara Cressey and Mr. Sumeet Mahajan (School of Chemistry, University of Southampton) for their assistance with the Scanning Electron Microscopy.
- Prof. Ian Sinclair (School of Engineering Sciences, University of Southampton) for his help with the CT scanning and post-processing of the data.
- Mr. Robert Bunker (Beckman Coulter, UK) for carrying out Electro sensing zone tests under a commercial testing contract.

- Dr. Steve Hunt (School of Chemistry, University of Southampton) and Elizabeth Davenport for carrying out nitrogen gas adsorption tests and mercury porosimetry tests, respectively, on my behalf.
- Harvey Skinner for all his help in the lab with electrical and electronic components. The members of technical workshop Ken, Dave and Earl, and Baldev (PSB Engineering Ltd) for their help with the mechanical components.
- All the fellow researchers of geomechanics research group for all the technical and social conversations.
- My housemates, Arun, Sakthivel and Tesmi, for the lively atmosphere in the house, regular get-togethers and of course the lovely food.

My highest regard of thanks goes to my parents, Sister Lakshmi, and Brothers Seshu and Narasimha who made it possible for me to achieve this position through their financial, priceless emotional support and encouragement all through my life. I would like to acknowledge the love and support of all my cousins, brother-in-laws, sister-in-laws, nephews, nieces and all the family friends who have been there for me all the time.

I also wish to use to use this opportunity to thank all my friends and everyone else who helped me either directly or indirectly and made it possible for my stay to be enjoyable in Southampton.

CHAPTER 1 INTRODUCTION

1.1 Background

It has long been understood that particle size and shape have an important influence on the mechanical behaviour of particulate materials. As early as 1925 Terzaghi, in reviewing differences in soil behaviour, noted that "on superficial examination sand and clay seem to be essentially different materials" but concluded that "throughout the author's studies no essential difference was found to exist between sands and clays other than the difference in grain size and shape" and that "these two differences [were] fully adequate to explain the more obvious distinguishing features of the two materials." In 1928 Gilboy noted that "the shape of the grains ... [had] an almost unbelievable influence on the compression characteristics of a granular material". Later, Olson and Mesri (1970) examined the relative importance of physico-chemical and mechanical factors to clay mineral compressibility and found that "in clayey soils, the physico-chemical effects dominate[d] only the initial packing and … the subsequent behaviour of most clays [was] largely controlled by mechanical effects".

Early attempts to characterise soil particles were necessarily simple. For example, Grengg and Kammel's (1924) approach was to estimate the percentage of flat grains by counting them under the microscope. Terzaghi recognised the futility of such a method, and whilst criticising it, advocated an experimental approach with a "view to accumulating sufficient empirical data ... to permit eventually the formulation of a complete and rational system of soil mechanics". At that time it was clear that a fundamental grain-up approach to understanding and modelling the behaviour of soil was impractical, but during the past decade the use of discrete element modelling (DEM) software has demonstrated that such an approach might be the way forward. An important issue is what elements of soil particles, including shape, sliding, bending, and crushing, need to be modelled to obtain realistic geomechanics simulations. This thesis considers the first element (particle shape) and makes a contribution to that debate.

1.2 Objectives of this research

- Development of practical methods of estimating the form of coarse as well as the fine particulates.
- Improving the understanding of the effects of particle form on depositional packing and on drained shear behaviour.

1.3 Organisation of this thesis

This thesis is structured into eight chapters, as follows:

- **Chapter 1** provides a brief background and states the objectives of the work.
- **Chapter 2** presents a detailed literature review on various topics that are necessary to accomplish the objectives of this research.
- **Chapter 3** proposes a practical method of estimating the form of 'coarse' particulates, evaluates the proposed measure by applying it to a range of particle shapes, and compares its results with other possible measures of form.
- **Chapter 4** proposes a practical method of estimating the form of 'fine' particulates, evaluates the proposed measure by applying it to a range of fine grained materials, and compares it with other possible measures of form.
- **Chapter 5** presents the results of an experimental study that was carried out on a range of particle shapes in order to investigate the effects of form on depositional packing, and on drained shear behaviour in triaxial compression.
- **Chapter 6** presents the results of a numerical study (using PFC2D) that have been obtained for particles of various forms, looking at the effects of form on depositional packing, and on drained shear behaviour in biaxial compression.
- **Chapter 7** brings together the information presented in Chapters 3 to 6, compares it with the literature wherever appropriate and draws further conclusions.

- **Chapter 8** presents the conclusions derived from this research, practical implications of this research, and recommendations for future research.

CHAPTER 2 LITERATURE REVIEW

This chapter provides a detailed literature review on the background topics such as (i) the importance of particle form on mechanical behaviour of soils, (ii) the evolution of sizes and shapes of clastic and crushed rock particles as they form, (iii) principles of operation of the available PSD tests, (iv) previous definitions of form of coarse particles, (v) the existing methods of determining the form of fine particles, (vi) the methods of determining the limiting densities, (vii) reconstituted sample preparation techniques, (viii) lubricated end platens. It then summarises the main points (that are relevant to this research) from the literature and list out the specific issues addressed in this thesis.

2.1 The importance of form

It is widely agreed that there are three elements of particle shape

- roughness,
- roundness (or angularity) and
- form (sometimes termed 'sphericity')

that can be distinguished, and may be of importance in affecting the mechanical behaviour of an assembly of particles. Figure 2.1 shows these elements schematically.

Roughness is a measure of the smallest scale of surface irregularities. Roundness (or angularity) is a measure of major surface irregularities (i.e. the corners and edges) of a particle. Form is a measure of overall shape of a particle. Because the shapes of natural soil particles are highly irregular, researchers have over time proposed different parameters for estimating sphericity, roundness and roughness. This thesis considers only form. The term 'form' is preferred in this thesis because there is no implied connection with a spherical shape. For a smooth solid particle, form can be thought of as the ratio of the volume of a particle to its surface area. Bulky particles have a high volume, whilst platy particles have a low volume / unit surface area.

Much of the experimental evidence for the importance of form has been derived using mixtures of bulky and platy particles. In some studies (for example Gilboy, 1928, Mundegar, 1997, Leroueil and Hight, 2003, pp. 114-115, Hight and Leroueil, 2003, p.283-287) bulky particles have had platy particles of the same size mixed with them. The effect has been a very significant increase in void ratio, coupled with increased compressibility and reduced shear strength.

In other studies tests have been carried out on materials composed of fine platy material mixed within coarse bulky material. Gold mine tailings were studied by Vermeulen (2001), who observed that a 'clay-like' high volumetric compression occurred under isotropic and oedometric loading as the proportion of fines increased, and that this was associated with initially contractive behaviour, and excess pore pressure development in 'slimes' (gold tailing fines) during the initial stages of triaxial shear. Similar results have been obtained using mixtures of bulky sand and mica (Clayton et al., 2004, Theron et al., 2005), see Figures 2.2(a) and (b). The commonly observed subsequent phase transfer from contractive to dilative behaviour may well be a feature of the triaxial loading path that is commonly used in the laboratory (Shibuya and Hight, 1991, Ishihara, 1993, Yoshimine et al., 1999, Olson and Stark, 2002, Leroueil and Hight, 2003, pp. 82-87), suggesting that for a given initial effective stress level, platy particles fail at lower shear strength.

Nouguier-Lehon et al. (2003) have reported the influence of grain shape and angularity on the behaviour of granular materials from two-dimensional numerical modelling by means of DEM using the Contact Dynamics method. They claim that the critical state concept is "meaningless" for elongated grains because the behaviour of samples generated with such particles is highly dependent on the direction of loading with respect to the initial fabric. Clayton and Obula Reddy (2006) carried out a two-dimensional study using the Itasca DEM code PFC in which the effects of particle shape on both depositional void ratio and dilation during compressive shear were found to be important. They observed that particle shape had a controlling effect on initial void ratio. They also found that platy particles did not dilate, again challenging the concept of a critical state for such grain shapes. A similar study, based on direct shear simulation, has recently been reported by Kock and Huhn (2007), who concluded that 'the deformation behaviour of clay is mainly controlled by their particle shape which directly influences the specimens' ability to dilate or contract' and that "different particle sphericity and roughness lead to fundamentally different deformation mechanisms". Modelling using two-dimensional photo-elastic disc, elliptic and pear-shaped particles (Zuriguel and Mullin, 2007) has shown the importance of particle shape in developing force chains and therefore the distribution of vertical stress within a sandpile.

The research findings reviewed above clearly suggest that form can have a significant impact on undrained strength (through dilatancy), volumetric compressibility, and stress distribution. Whilst it is reasonable to argue that experimental data may not reflect the effects of form alone, but be influenced by particle bending and crushing (Hardin, 1985, Lade et al., 1996, Cheng et al., 2003, Cheng et al., 2004 and Coop et al., 2004), the results of numerical modelling (where crushing and bending are not generally modelled) would suggest that form is a key parameter. However, in the absence of viable definitions of roughness, roundness and form it is impossible to test for the effects of the different components of particle shape. For example, Clayton et al. (2006) have recently reported the important effect of apparently minor differences in particle shape (between Leighton Buzzard sand and glass ballotini) on load build-up during cyclic loading, and Wesseloo (2004) has observed the reduced dilatancy occurring in coarse gold tailings when compared with that in sedimentary sands, see Figure 2.3. Without further definition of shape parameters it cannot be known if these differences result from differences in form or angularity.

2.2 Nature of clastic and crushed rock particles

Clastic material is directly derived from pre-existing rocks. Most clastic sediment is formed from weathering and erosion of the parent igneous, sedimentary, and metamorphic rocks. It consists of the resistant components of primary rock-forming minerals (mainly quartz and muscovite mica) and the clay minerals produced by weathering of non-resistant components of primary rock-forming minerals (e.g. feldspars).

The sizes of the resistant components of mineral grains are controlled by their original formation, Moss defects (Moss, 1966), and the rock cycle. Moss defects are the fracture planes within the crystals that are formed during the high-to-low transformation of quartz (Moss and Green, 1975). These defects promote grain breakage during weathering.

The overall shape (i.e. form) of the original quartz crystals that are present in igneous rocks is largely controlled by their internal atomic structure, apart from small distortions that take place during the high-to-low transformation of quartz (Bokman, 1952) whereas in metamorphic rocks it is affected by an additional factor, i.e. the distortion caused by metamorphic action (Smalley, 1966). As a result, the overall shape of quartz crystals is bulky in granitic rocks, but may be bulky to platy in metamorphic rocks depending on the origin of the rock (igneous or sedimentary) and the style of metamorphism (thermal, regional or dynamic). The shape of mica particles is always sheet-like, but particle size (both the length and thickness) varies depending on the type of weathering mechanism and transporting agent that have operated. On the other hand, the atomic structure of clay mineral particles dictates their shape to be sheet-like. However, thickness varies with the type of clay mineral due to variations in the bond strengths between their basic elemental sheets.

A number of mechanical and chemical processes take place between the time of release of clasts from the parent rock, and deposition. These processes alter the sizes and shapes of grains. The dominant processes seem to vary with the size of particles. Krinsley and Smalley (1973) and Margolis and Krinsley (1974) have noted that majority of coarse quartz particles (typically >50μm) break by concoidal fracture whereas fine particles (typically <50μm) fracture along their cleavage planes. A significant amount of research has been carried out by Smalley and his co-workers (Smalley and Glendinning, 1991, Rogers and Smalley, 1993, Smalley, 1995, Wright, 1995, Jefferson et al., 1997, Wright et al., 1998, Assallay et al., 1998, Wright, 2001, Wright, 2004, Smalley et al., 2004, Smalley et al. 2005 and Smalley et al, 2006) in order to explore the possible mechanisms behind the formation of huge amounts of silt and clay-sized quartz particles, which include significant quantities of loess deposits all over the world. It has been concluded that glacial grinding, aeolian abrasion, fluvial comminution, salt weathering and frost weathering are the probable mechanisms responsible for this material.

The shape of most natural fine clastic particles appears to be platy (Smalley et al., 1978, Blatt, 1987, Rogers and Smalley, 1993, Jefferson and Smalley, 1995, and Jefferson and Smalley, 2002). Similar observations have been reported by Vermeulen (2001) and Wesselloo (2004) in the case of fine fraction of mine tailings material i.e. crushed rock particles. Similarly, Guimaraes et al. (2007) have noted that the particle sphericity and roundness decrease as the size of fines produced by one-dimensional and shear loading decreases, and that eventually the fine particles (retained on sieves #60, #100, #200) tend to become flat and/or blade-like.

The surface features of coarse clastic particles vary from smooth and well-rounded to rough and angular depending on the nature of formation (i.e. the type of weathering mechanism and transporting agent) and the depositional environment (Margolis and Krinsley, 1974). On the other hand, fine particles do not seem to have many surface irregularities since they tend to fracture along their cleavage planes. The nature of clastic and crushed rock particles described above (e.g. Figures 2.4(a) to (h)) clearly suggest that particle size, either alone or in combination with 2D particle shape descriptors, is insufficient to describe or characterise their shape, and that fine particles may tend to be platy.

2.3 Principles of operation of PSD tests

There is a lack of definition of the exact meaning of 'particle size'. Soil and rock particles are three dimensional, and of irregular shape. The size of a particle cannot be uniquely expressed by a single parameter unless the particle is as a sphere or cube. Because particle size plays an important role in quality control in many industries (e.g. adhesives, chemicals, biotechnology, ceramics, food, pharmaceuticals etc.) very many different ways of expressing and measuring particle size have developed depending on need. Some definitions are illustrated in Figure 2.5.

Automated PSD measurement techniques that have been developed include:

- Sieving
- Sedimentation
- Electrical sensing zone (ESZ)
- Laser diffraction (LD)
- Single particle optical sizing (SPOS)

- Traditional microscopy techniques
- Automated image analysis methods

Each of these is based on a different principle of measurement (and/or definition of size), and is applicable only to a specific range of particle sizes, as summarised in Table 2.1. The principles underlying each of the above-mentioned techniques are briefly discussed in the subsequent paragraphs. In general, the available techniques will yield the same results only for spherical particles.

'Wet' sieving (BS 1377-2:1990, ASTM D422-63:2002) is the most common method of PSD analysis used by geotechnical laboratories. Wet sieving involves preliminary removal of fines by washing over a fine sieve, followed by dry sieving of the residual coarse fraction. In sieving, the particle size is effectively defined as the length of the side of a square aperture through which a particle can just pass (for example see Lambe 1951). Sieving is applicable for coarser (sand and some gravel) particles only. Finer material (between approximately 1μm and 100μm) is sized using a sedimentation test. BS1377 Part 2 uses sieves with apertures of up to 75mm, although sieves as large as 125mm are readily available.

Sedimentation methods define the particle size as that of the diameter of an equivalent a sphere settling with the same velocity and in the same liquid. In soil testing the pipette method is preferred in BS1377-2:1990, but much of the world uses the hydrometer test, as in ASTM D422-63:2002. Automated sedimentation can be carried out in x-ray gravitational sedimentation equipment such as the Micromeritics SediGraph, developed in the 1960's.

As noted above, particle diameter is estimated based on Stokes' law, which assumes the particle shape to be spherical and flow to be laminar. However, in general the fine particles for which the sedimentation methods are used are not spherical, but are platy. If the particles are platy, the settling velocity decreases drastically due to the increased drag resistance, and in addition particles do not fall vertically, but drift from side to side during their fall. Therefore, the sedimentation method underestimates the size of platy particles (e.g. Konert and Vandenberghe 1997, Lu et al. 2000), if length is considered as the particle size. This effect increases with the increased platiness of the particles.

In general, sedimentation methods are applicable for particles sizes of the order of 0.1 – 100μm. Since Stokes' Law assumes laminar flow, results cannot be correctly interpreted if Reynold's number is less than about 0.2. For quartz spheres ($G_s = 2.65$) falling in water at 20°C the critical upper diameter is about 60μm. The lower size limit can be determined by considering the relative importance of Brownian motion and gravitational sedimentation (Lambe 1951). This limit occurs theoretically at about 1μm, although convection currents further increase the limit, perhaps to 2μm or more.

PSD analysis by sedimentation requires (ASTM D422-63:2002, BS1377-2:1990) pre-treatment with hydrogen peroxide to remove any organic matter (which would tend to float if present), and washing to remove any soluble salts, followed by dispersion. BS1377 recommends dispersion using sodium hexametaphosphate (calgon) to separate individual particles. The suggested methods of agitation differ between standards, with ASTM D422-63 recommending either a high-speed mechanical stirrer or air dispersion and noting that 'the results from the two types of devices differ in magnitude, depending upon soil type, leading to marked differences in particle size distribution, especially for sizes finer than 20 micron'. It is evident that dispersion processes can have a significant impact on the PSD measured by sedimentation.

The ESZ (BS ISO 13319:2000) method, as used by the Beckman Coulter Multisizer 3, defines particle size as the volume equivalent diameter of an electrically non-conducting spherical particle. In this method, the particles are made to flow in an electrolyte solution through an orifice, which separates the two electrodes between which an electric current is applied. As particles pass through the orifice they displace their own volume of electrolyte solution, and the reduced electrical resistance produces voltage pulses. The height of that voltage pulse is directly proportional to the volume of the particle that produces it. This method is applicable for a size range of 0.4 – 1200μm.

The LD method (BS ISO 13320-1:1999), as used in the Malvern Mastersizer system, is based upon Mie scattering by particles in a dilute suspension. It provides an equivalent diameter of a sphere based on the measured diffraction pattern. It works on the principle that particles of a given size diffract light at an angle that increases with decreasing particle size. It assumes the particle shape to be spherical. Due to the increased number of particles per unit volume (Hayton et al. 2001), this leads to an overestimation of the volume concentration of particles if the particles are in reality platy; However, size calculations are not much affected, since the diffraction pattern is not much influenced by the third dimension of a particle. Particle size results are biased by the random orientation of particles in 3-D space (since the flow is more likely to be turbulent during the measurement process, see Figure 2.6(d)), and the assumed optical properties (refractive index and absorption coefficient) of the material. This method is applicable for particles of size between 0.1 and 2000μm.

The Single Particle Optical Sizing (SPOS) method (White 2003) provides the projected area equivalent diameter of a circular particle as size, but uses a different principle to that of laser diffraction (LD). As in LD, the particles are made to flow across the path of a laser beam, however under laminar flow conditions. The passage of particle across the laser beam causes changes in output voltage of a light sensor which is proportional to its projected area at that instant. Since the flow is laminar during the measurements, the particles align their larger dimension perpendicular to the direction of the laser beam. In this method the results are affected by the random orientation of particles (along the major axis of their revolution i.e. in 2 rather than 3 dimensions, see Figure 2.6(c)), but the effect is not significant when compared to laser diffraction. Another advantage of SPOS is that it is applicable to a wider range of particle-sizes (i.e. 1 – 5000μm) than LD.

Traditional microscopy techniques provide an opportunity to examine the size and shape of individual particles directly. But at present they can only be used to supplement the results obtained from other particle sizing methods (e.g. sieving, sedimentation, laser diffraction) since only small amounts of sample can be examined. This occurs because of the limitation in number of coarse particles that can be seen in a single field of view, and because of an inability to prepare the sample without overlaps in the case of fine particles.

Automated image analysis methods are of two types, namely, static and dynamic (ISO 13322-1:2004 and ISO 13322-2:2006). In static image analysis, still particle images are captured by dispersing them on to a xy-movable stage and minimising the overlaps. When (as is normal) particles are dispersed onto a horizontal stage, they settle into their most mechanically stable state (see Figure 2.6(b)), and present their largest projection area to the camera. This method cannot be successfully applied for fine cohesive particles as sample preparation becomes an extremely difficult task. However this problem can be overcome by using dynamic image analysis methods, by dispersing the particles into a liquid or gas medium and forcing them to flow with their greatest area facing the camera (as in the patented 'sheath flow' mechanism – US Patent 6576194). In dynamic imaging systems images must be captured at high frequency whilst the particles are in motion. PSD can be determined by analysing the images of statistically representative number of particles for the required size parameter. With the advances in image analysis and computational power, many such automated systems are now commercially available e.g. Morphologi G2, FPIA-3000, Camsizer etc.. The available techniques and applicable size ranges are summarised in Table 2.1.

For the particle sizing methods described above, particle size distribution is biased by random orientation of particles during measurements in all the methods except image-based ones (i.e. microscopy and automated image analysis methods). This means, for example, that if the PSD of uniform anisotropic (scalene ellipsoid-like) particles was to be determined using any of these techniques, sizes would be obtained ranging from the minor dimension (S) to its major dimension (L), since particle orientation is random (or uncontrolled) during the measurements, as illustrated in Figure 2.6(a) to 2.6(d). Therefore, it can be concluded that only the automated image analysis methods produce physically meaningful particle size distribution in the case of anisotropic particles provided that the particles are dispersed well.

2.4 Previous definitions of form of coarse particles

Some selected definitions of form are given in Table 2.2.

Although form is essentially a three-dimensional concept, a number of researchers (Wadell, 1933 and 1935, Riley, 1941, Pye and Pye, 1943, Krumbein and Sloss, 1963, Koerner, 1970a, Powers, 1982, Podczeck, 1997, Sukumaran and Ashmawy, 2001, Hentschel and Page 2003, Alshibli and Alsaleh, 2004, Cho et al., 2006) have proposed two-dimensional estimates, based on measurements of projected areas or Feret's diameters[1] and/or visual comparison charts (e.g. Figure 2.7), because of their relative simplicity.

Alternatively, lower-order harmonics (or descriptors) of Fourier series (Ehrlich and Weinberg, 1970, Ehrlich et al., 1980, Clark, 1981, Santamarina et al., 2001, Wettimuny and Penumadu, 2004) or Fourier descriptor methods (Clark, 1981, Thomas et al., 1995, Bowman et al., 2001), can be used to obtain the 2D estimates of shape parameters based on outlines of particles captured using imaging systems. The attraction of Fourier methods is that a particle's outline, at all scales, can be traced and reproduced with the required accuracy simply by varying the order of the harmonics (or descriptors). The practical difficulty in using a two-dimensional silhouette of a three-dimensional object is, however, that finer surface detail (such as that associated with roughness and angularity) may become obscured. In future, computerised tomographic (CT) imaging may overcome this difficulty, at least for coarse particulates.

The main drawback of all two-dimensional estimates of form is, however, that they do not differentiate between bulky and platy particles having similar outlines, i.e. between discs and spheres of same diameter, assemblies of which might intuitively be supposed to behave quite differently from each other during compression and shear. A number of strategies have therefore been suggested in order to develop three-dimensional measures of form.

Zingg (1935), Krumbein (1941), Corey (1949), Aschenbrenner (1956), Sneed and Folk (1958), Al-Rousan et al., (2007) and Blott and Pye (2007), have proposed 3D estimates of form, based on the three-orthogonal dimensions of a particle. However, these methods cannot easily be applied to small particles (e.g. fine sediments) or large

---

[1] The Feret's diameter of an irregular particle is defined as the measured distance between parallel lines that are tangent to an object's profile on a plane perpendicular to the direction of viewing. Maximum and minimum values are typically determined.

numbers of variable particles, such as are typically found in soil specimens, since it is difficult and extremely time-consuming to obtain their three-orthogonal dimensions.

Other, potentially more practical definitions of form have been suggested by Wadell (1932) and Hawkins (1993). Wadell (1932) suggested a 3D estimate based on comparing the measured surface area of a given mass of particles with the surface area of an equivalent mass of spheres with the same grain density. Neither Wadell's nor Hawkins' definitions of form can adequately distinguish between rod-like and plate-like forms. A definition based on a plate-like form is more likely to be relevant in attempting to predict soil behaviour, given the general scarcity in nature of rod-like soil particles.

2.5 Existing methods of determining the form of fine particles

The past two decades have seen the development and use of a growing number of automated particle sizing techniques, each based on a different principle as discussed in Section 2.3. A number of researchers (e.g. Novak and Thompson, 1986, Clift, 1988, Parslow and Jennings, 1986, Jennings and Parslow, 1988, Allen, 1990, Jennings, 1993, Slepetys and Cleland, 1993, Ferreira et al., 1993, Inoue, 1995, Barreiros et al., 1996, Endoh et al., 1998, Pabst et al., 2000) have compared particle size distribution (PSD) data obtained by different techniques. For a given particle size, the various techniques will produce identical (or similar) results only for spherical particles, and results will differ in the case of anisometric particles.

A number of researchers (e.g. Novak and Thompson, 1986, Clift, 1988, Allen, 1990, Ferreira et al., 1993, Barreiros et al., 1996, Endoh et al., 1998) have attempted to extract shape information by comparing the mean particle sizes obtained from pairs of sizing techniques, see Table 2.3 for the corresponding expressions. However, the shape factors determined by any of these methods have been found to be very different from the actual values determined, for example, from imaging. This could be due to the random orientation of particles during PSD testing using sedimentation and/or laser diffraction methods, which has not been accounted for.

On the other hand, Parslow and Jennings (1986), Jennings and Parslow (1988) and Jennings (1993) have proposed techniques for determining the aspect ratio (ratio of major to minor dimension) of different shapes (oblate, prolate, discoidal, rod-like) of particles based on the PSD data derived from sedimentation with those of electric birefringence (based on rotary diffusion coefficients) or laser diffraction methods, accounting for the random orientation of particles during measurements. The expressions derived by Parslow and Jennings (1986) and Jennings and Parslow (1988) for oblate particles based on the ratio of D_{50} obtained from sedimentation and electric birefringence (rotary diffusion), and sedimentation and laser diffraction, respectively, are presented in Table 2.3. The techniques were applied by these authors to kaolin samples. It is worth noting here that electric birefringence method is applicable for sub-micron sized particles (Oakley et al. 1982), and cannot be applied for particles larger than few microns.

Subsequently Slepetys and Cleland (1993) applied a size comparison technique using sedimentation and laser diffraction methods, to determine the form of kaolin pigment samples. The aspect ratio values they determined were not, however, compared with the actual aspect ratios of individual particles. Inoue (1995) has also applied this technique to a range of clay-sized (plate-, and rod-like) particles and compared the results with the actual aspect ratio values determined by imaging. There were major inconsistencies between the results obtained using particle sizing and imaging methods.

2.6 Methods of determining the limiting densities

The limiting maximum and minimum densities of clean sands are usually determined by the recommended procedures set out by the national standards (e.g. BS 1377-4:1990, ASTM D 4253 – 00).

Both these standards recommend the vibratory compaction technique for determining the limiting maximum density, which is applicable for soils consisting of non-crushable particles. However, in reality majority of soil particles are crushable, so crushing is inevitable. Therefore, the maximum density determined by compaction based methods does not correspond to the original material, but to an altered material, because of particle crushing.

Alternatively, Cresswell et al. (1999) have demonstrated that maximum density can be achieved by pluviation technique; the values obtained by this method are similar to those obtained by the BS method, but with minimal or no degradation. Later, Lagioia et al (2006) confirmed that densities higher than those from the ASTM vibration table test can be achieved by vacuum pluviation technique.

Minimum densities can be determined reasonably well either by the inverted cylinder method (BS 1377-4:1990 or ASTM D 4254 – 00) or by the water-pluviation method (Lagioia et al., 2006).

2.7 Reconstituted sample preparation techniques

In cohesionless soils, it is almost impossible to obtain good quality undisturbed samples. Therefore, the laboratory element tests are usually carried out on reconstituted samples. As a result, it is necessary to reproduce the fabric that exists in the field while preparing the samples in the laboratory, since fabric plays a significant role in shear behaviour (e.g. Vaid et al., 1999 – see Figure 2.8). Consequently, researchers have developed many different sample preparation techniques over time. These techniques can be classified based on the moisture condition of the soil (e.g. dry, moist, or wet), the method of soil placement (e.g. pluviation, or spooning) and the medium through which the soil is placed (e.g. air or water). Samples of the desired density can be achieved by a combination of the above factors and mechanical densification (i.e. tamping, tapping, rodding, and vibrating). Moist tamping and pluviation techniques are most popular and commonly used. Moist tamping is said to mimic the fabric of the hydraulically filled materials whereas pluviation is said to mimic the fabric of the naturally deposited materials.

The moist tamping technique has the advantage that sample density can be controlled relatively easily. However, samples prepared by this method are non-uniform compared to those prepared using the pluviation technique (Vaid et al., 1999; Frost & Park, 2003). Though the moist tamping technique has the ability to mimic the fabric of hydraulically filled materials, the extent of non-uniformities for a laboratory sized sample is large (Frost & Park, 2003).

The density of pluviated sample is controlled by the kinetic energy of the particles, which is a function of depositional velocity (fall height) and intensity (flow rate). Sample homogeneity is a function of the uniformity of sand rain with respect to its cross section and height. Horizontal and vertical uniformities of the sample can be achieved by maintaining the uniform sand rain over its cross section (using a series of six or more closely spaced diffuser meshes – Cresswell et al., 1999) and a constant fall height relative to the rising surface of the specimen during pluviation (Jang, 1997), respectively.

Until recently, moist tamping was the only method that could be used to produce a wide range of densities, but the recent work of Lagioia et al (2006) suggests that a wide range of relative densities (between 5 and 140% - it is to be noted here that the minimum and maximum densities were determined as per ASTM D 4253 Method A and ASTM D 4254 Method 1A), can be achieved by a combination of water, air and vacuum pluviation, by varying the depositional intensities and fall heights. Water pluviation produces loose samples whilst vacuum pluviation (at low depositional intensities and high fall heights) produces dense samples (Lagioia et al., 2006).

2.8 Free-ends (or lubricated-end platens)

In triaxial experiments, if conventional end platens are used, the sample deforms non-uniformly at all (except very small) strains. This is mainly due to the frictional resistance mobilised between the end platens and the sample leading to the formation of dead zones and localised failure zones, and sample barrelling as shown in Figure 2.9. This non-uniformity results in strain localisation in the sample, making it difficult obtain accurate (or representative) estimates of strains, stresses and volume changes. To overcome the effect of this lateral restraint, Taylor (1941) suggested using 2:1 samples (height-to-diameter ratio of two) with an implied assumption that the sample would deform uniformly at its mid-height. However, strain localisation and barrelling are inevitable.

An alternative way is to eliminate (or minimise) the end friction so that the sample can deform uniformly over its full height. Rowe and his co-workers at Manchester University developed the concept of free-ends (Rowe & Barden, 1964). Free-ends consist of the following components:

- enlarged end platens of size slightly more than the sample's diameter (e.g. 5 in. for 4 in. sample) to accommodate the lateral movement of the sample;
- a disc of latex rubber membrane of size equal to that of the platen attached to the loading face by a thin layer of high vacuum silicone grease. Together this is usually referred to as a 'lubricated membrane'; and
- a small porous stone at the centre of each platen for saturation and/or pore pressure measurement.

Subsequently, Bishop & Green (1965) investigated the effect of sample slenderness ratio and number of lubricated membranes on end friction, and concluded that efficient lubrication can be achieved by using two layers of lubricated membranes in conjunction with 1:1 samples. Furthermore, uniform strain conditions within the samples were also confirmed by Kirkapatrick & Belshaw (1968) using the X-ray technique and Frost (2003) by performing image analysis on thin sections of resin impregnated samples.

Therefore, it can be concluded from the literature that free ends allow a specimen to retain its cylindrical shape even at large strains by imposing uniform stress and strain conditions in the sample, thereby making the right cylinder area correction to be applicable, and strain localisation to be avoided.

Bedding errors associated with lubricated end platens

When free ends are used in the triaxial apparatus, external deformation measurements cannot be relied upon, due to associated bedding errors. Bedding errors are mainly due to the lack of fit between the sample surface and the lubricated platens, compression and distortion of the latex discs, and distortion of the grease layer (Sarsby et al., 1982). The bedding error can be as much as 80% of the externally recorded deformation at low strains. Sarsby et al. (1982) have attempted to quantify the bedding error, but it seems quite complicated as it varies with the particle size, shape etc. Therefore, local strain instrumentation is necessary if reliable deformation measurements are to be obtained, especially at low strains.

Challenges with local strain instrumentation

When free-ends are used in conjunction with lubricated ends on 1:1 samples:

- not all types of local strain instrumentation can fit in, due to the reduced height of the sample and enlarged ends
- special care has to be taken if tests are to be continued until critical state strains with local strain instrumentation in place, since they may either stiffen the sample or become damaged

However, the above difficulties can be overcome by using Hall-effect gauges (Clayton and Khatrush, 1986; Clayton et al., 1989) due to their compactness, large linear range (~7mm), light weight, flexibility to adjust the gauge length as per the requirement, and the ability of the gauges to undergo large movements without disturbing the sample (i.e. tests can be continued to very large strains with local strain instrumentation in place).

Finally, a special sliding type split mould is required if good quality samples are to be prepared with enlarged ends (e.g. Rowe & Barden, 1964).

2.9 Conclusions drawn from literature

- The sizes and shapes of clastic and crushed rock particles normally encountered by geotechnical engineers may vary very widely. Size varies from a few tens of millimetres to fractions of a micron. There appear to be several geological mechanisms that could produce large amounts of silt and clay-sized quartz particles. The overall shape of particles ranges from bulky to platy. Surface features on coarse particles vary from smooth and well-rounded to rough and angular depending on the nature of formation and depositional environment, whilst the finer fraction does not seem to have significant surface irregularities, since they tend to fracture along their cleavage planes.

- Traditionally, the measurement of the particle size distribution of the coarse fraction is carried out by sieving and of the fine fraction by sedimentation. Many automated particle sizing techniques are now commercially available. Among these, only the image based techniques provide physically meaningful

PSD in case of well-dispersed anisotropic particles. In others PSD is biased by the random orientation of particles during measurements.

- Most existing measures of form of coarse particles are two-dimensional. They cannot differentiate between bulky and platy particles with similar outline. Of the remaining, three-dimensional parameters, most require the measures of the largest, intermediate and smallest particle dimensions (L, I and S). It is very difficult and time consuming to obtain reliable measurement of these dimensions for irregular particles, such as those normally encountered by geotechnical engineers. In future high-resolution computerised tomographic (CT) scanning (nanotomography) may help to overcome this difficulty, but for the present, simple and reliable measurement techniques are required.

- In the case of fine particles, many researchers (in other scientific fields) have proposed methods of determining the aspect ratios based on the ratio of particle sizes obtained by pairs of particle sizing techniques. However, in most cases these methods have been applied to a limited range of particle shapes. The aspect ratios determined using these methods were very different from those measured by microscopy techniques.

- Limiting maximum density can be better determined by pluviation methods rather than by compaction based (BS or ASTM) methods, whilst the limiting minimum density can be determined by inverted cylinder method.

- Fabric reproduction and specimen uniformity are essential when preparing reconstituted samples for laboratory element tests. Samples prepared by pluviation mimic the fabric of naturally deposited materials and can be very uniform. Whereas those prepared by moist tamping method mimic the fabric of hydraulic fill materials and are less uniform. The extents of non-uniformities for an element test can be large and questionable.

- Free (or frictionless or lubricated) ends should be adopted in triaxial testing when large strain behaviour needs to be investigated. When free ends are used, strains should be measured locally on the specimen if small-strain behaviour needs to be captured, in order to eliminate the bedding errors.

- The literature reveals that particle form can have enormous influence on the mechanical behaviour of soils, however systematic study is lacking. The immediate obstacle to carrying out systematic study is the lack of a proper form characterisation method.

- Experimental evidence available on mixtures of bulky and platy particles reveals that the presence of even small quantities of platy particles in rotund sands converts 'sand-like' behaviour (high stiffness, low compressibility, and dilation during shear) into 'clay-like' behaviour (low stiffness, high compressibility and contractive behaviour during shear).

- Even in clays, physico-chemical effects appear to dominate only the initial structure, and the subsequent behaviour is largely controlled by the mechanical interaction between particles. Limited DEM studies also suggest that particle form is a key parameter that controls the mechanical behaviour the most.

2.10 Specific issues addressed in this thesis

- Development of practical methods for estimating the form of coarse and fine particles, which would effectively distinguish the bulky and platy particles.
- A systematic laboratory study investigating the effects of particle form on depositional packing, and on shear behaviour in triaxial compression.
- A systematic numerical study using DEM to explore the possible particle level mechanisms.

Table 2.1: Size ranges for various particle sizing techniques

Measurement technique	Particle size definition	Applicable size range (microns)
Sieving	Side of a square sieve aperture	63 – 75,000
Sedimentation	Stoke's diameter	0.1 – 100
Electric sensing zone (ESZ)[1]	Spherical diameter of same displaced volume	0.4 – 1200
Laser diffraction (LD)	Spherical diameter equivalent to observed Mie scattering	0.1 – 2000
Single Particle Optical Sizing (SPOS)	Circular diameter equivalent to projected area	1 – 5000
Imaging	Minimum length of projected image of particles	0.5 – 100,000

[1] Coulter Counter

Table 2.2: Some existing definitions of particle form

Parameter	Formula	Range	Measures	Reference
Two-dimensional parameters				
Projection sphericity	$\frac{D_a}{D_{cc}}$	0 - 1	D_a, D_{cc}	Wadell, 1933 and Wadell, 1935
Inscribed circle sphericity	$\sqrt{\frac{D_{ic}}{D_{cc}}}$	0 - 1	D_{ic}, D_{cc}	Riley, 1941
Projection sphericity	$\sqrt{\frac{I}{L}}$	0 - 1	I, L	Pye and Pye, 1943
Shape Factor	$\left[\sum_{i=1}^{N} \alpha_{i\ particle}\right] / (\pi N / 4)$	0 - 1	$\alpha_{i\ particle}$	Sukumaran and Ashmawy, 2001
Aspect ratio	$\frac{I}{L}$	0 - 1	I, L	Hentschel and Page, 2003
Sphericity Index	$\frac{D_p}{I} - \frac{D_p}{L}$	> 0	D_p, I, L	Alshibli and Alsaleh, 2004
Inscribed Circle Sphericity	$\frac{D_{ic}}{D_{cc}}$	0 - 1	D_{ic}, D_{cc}	Cho et al., 2006
Three-dimensional parameters				
Degree of true Sphericity	$\frac{S_s}{S_p}$	0 - 1	S_s. S_p	Wadell, 1932
True sphericity	$\frac{D_{vs}}{D_{cs}}$	0 - 1	D_{vs}, D_{cs}	Hawkins, 1993
Elongation ratio and Flatness ratio	$\frac{S}{I}$ and $\frac{I}{L}$	0 - 1	S, I, L	Zingg, 1935
Intercept sphericity	$\sqrt[3]{\frac{I.S}{L^2}}$	0 - 1	S, I, L	Krumbein, 1941; and Pye and Pye, 1943
Corey shape factor	$\frac{S}{\sqrt{LI}}$	0 - 1	S, I, L	Corey, 1949
Working sphericity	$\frac{12.8\sqrt[3]{p^2 q}}{1+p(1+q)+6\sqrt{1+p^2(1+q^2)}}$ where $p = S/I; q = I/L$	0 - 1	S, I, L	Aschenbrenner, 1956
Maximum projection sphericity	$\sqrt[3]{\frac{S^2}{L.I}}$	0 - 1	S, I, L	Sneed and Folk, 1958
Flat and Elongation Ratio; or Degree of Equancy	$\frac{S}{L}$	0 - 1	S, L	Al-Rousan et al., 2007; Blott and Pye, 2007

Table 2.3: Form parameters proposed by various researchers for fine materials

Parameter	Formula	Reference
Aspect ratio (r)	$\frac{D_{Stokes'}}{D_{RD}}=\left(\frac{3}{2}\right)^{1/3}\frac{r}{\sqrt[3]{1-r^4}}\left(\frac{\arctan\sqrt{r^2-1}}{\sqrt{r^2-1}}\right)^{1/2}\left(\frac{\left(2-r^2\right)\arctan\sqrt{r^2-1}}{\sqrt{r^2-1}}-1\right)^{1/3}$	Parslow and Jennings (1986)
Aspect ratio (r)	$\frac{D_{Stokes'}}{D_{LD}}=\left\{\frac{2r\arctan\sqrt{r^2-1}}{\left(r\sqrt{r^2-1}\right)+\ln\left[r+\sqrt{r^2-1}\right]}\right\}^{\frac{1}{2}}$	Jennings and Parslow (1988)
Aspect ratio (r)	$\left[\frac{D_{ESZ}}{D_{LD}}\right]^3$	Clift (1988)
Wadell sphericity	$\left[\frac{D_{Stokes'}}{D_{ESZ}}\right]^4$	Allen, (1990)
Wadell sphericity	$\left[\frac{D_{ESZ}}{D_{LD}}\right]^2$	Barreiros et al. (1996)
Flatness (r)	$\frac{D_{LD}}{D_{Stokes'}}$	Endoh et al. (1998)

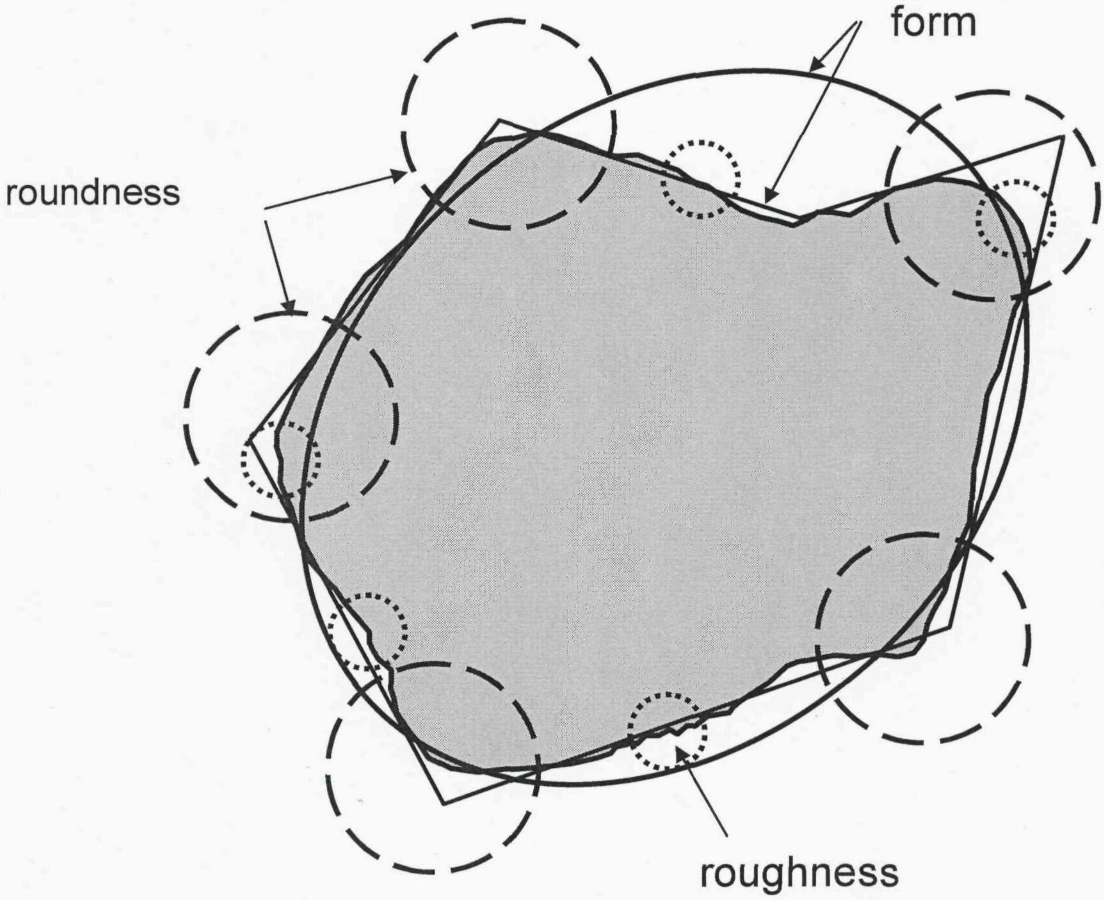

Figure 2.1: Elements of particle shape (after Barrett, 1980)

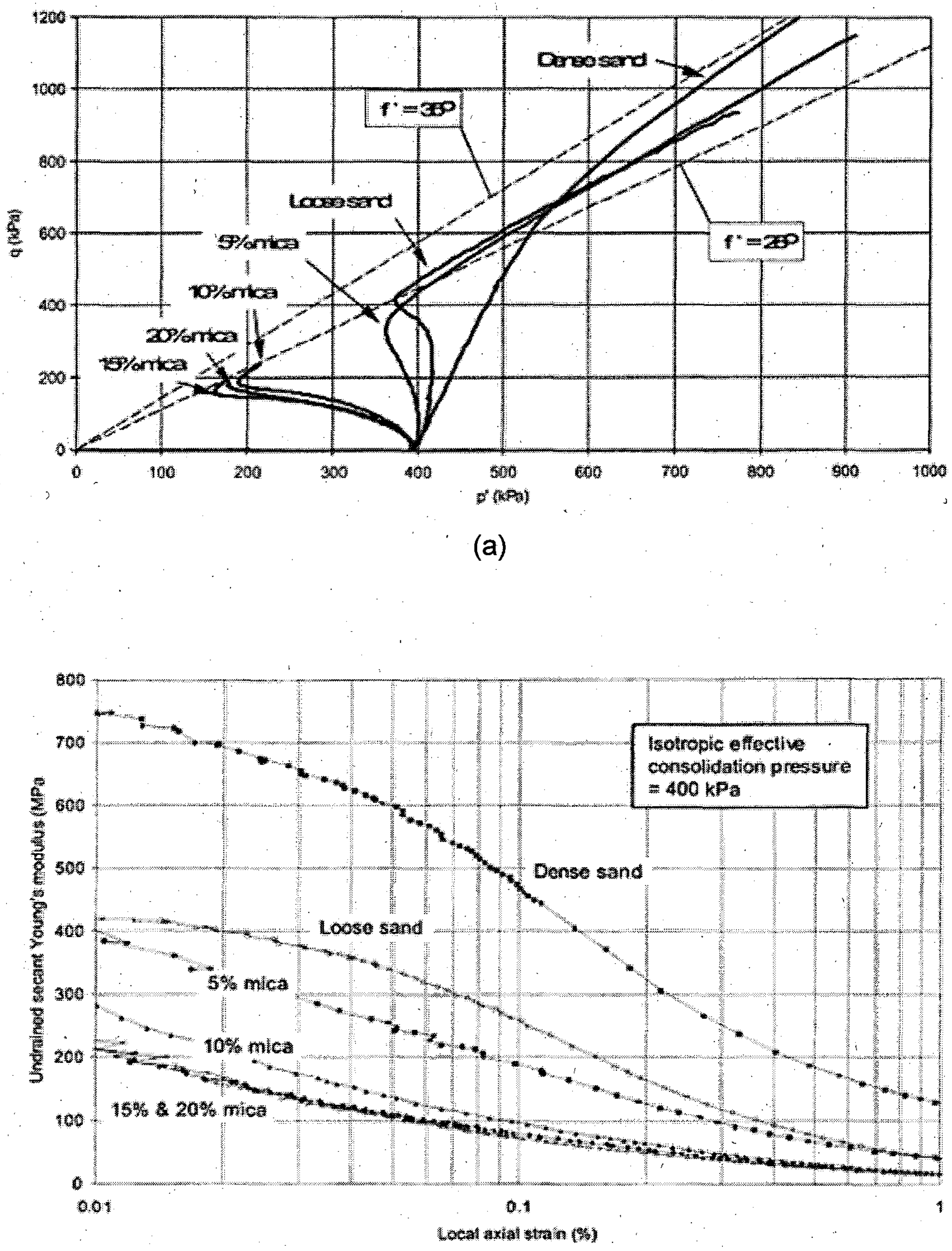

Figure 2.2: Effect of mica content on (a) stress paths, and (b) undrained Young's modulus (Clayton et al., 2004).

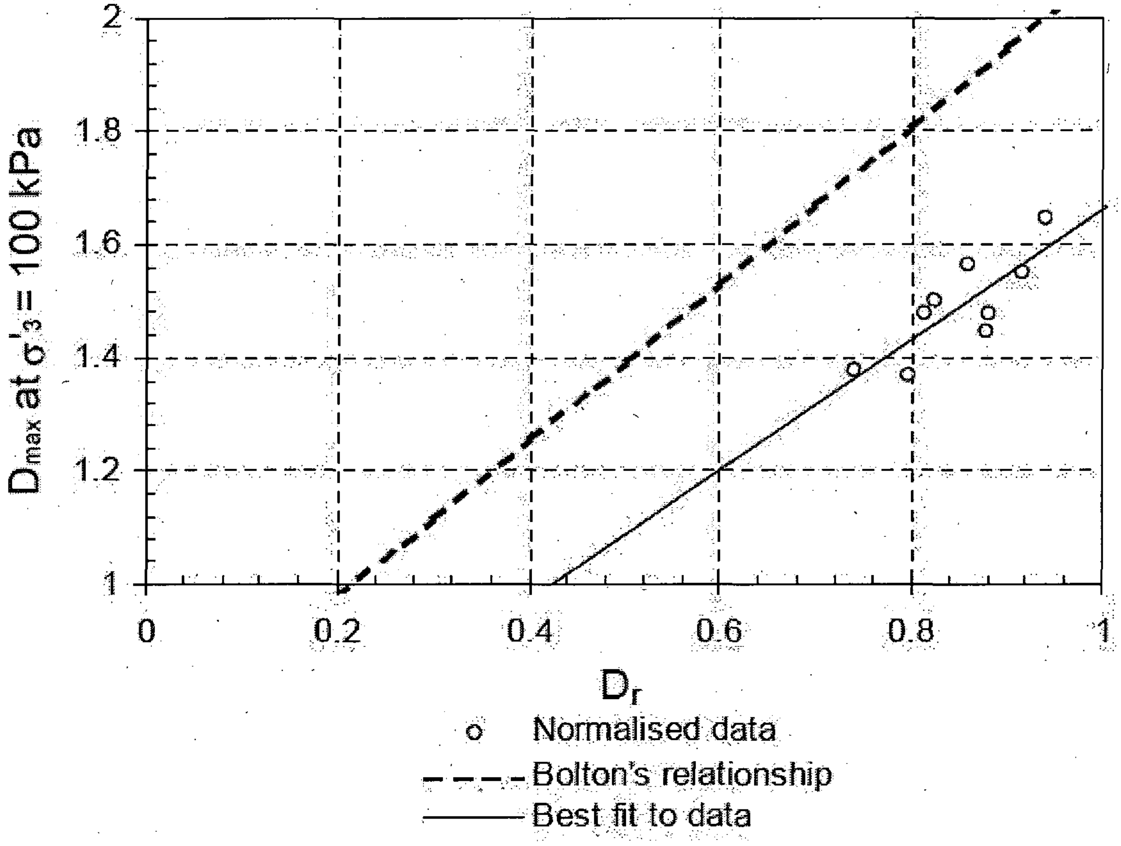

Figure 2.3: Comparison between the Dmax obtained experimentally and with Bolton's (1986) expressions (Wesseloo, 2004)

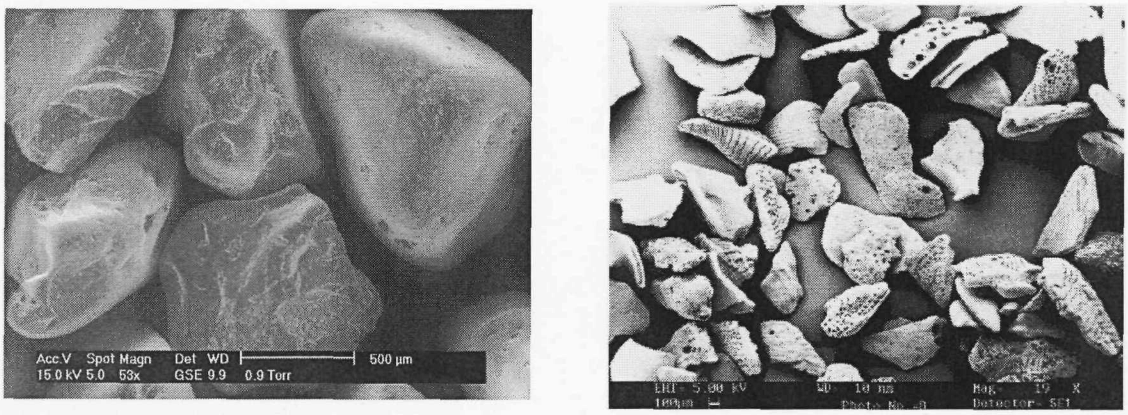

(a) Leighton Buzzard sand fraction B (Xu, 2005)

(b) Dog's bay sand (Bowman et al., 2001)

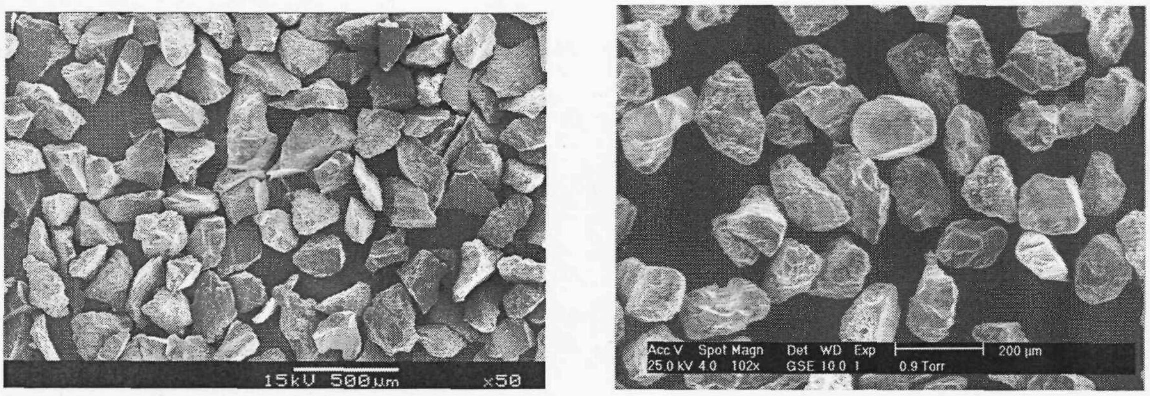

(c) Coarse fraction of Mizpah tailings (Clayton et al., 2004)

(d) Leighton Buzzard sand fraction E (Clayton et al., 2004)

Figure 2.4: SEM images of materials commonly encountered by engineers (contd.).

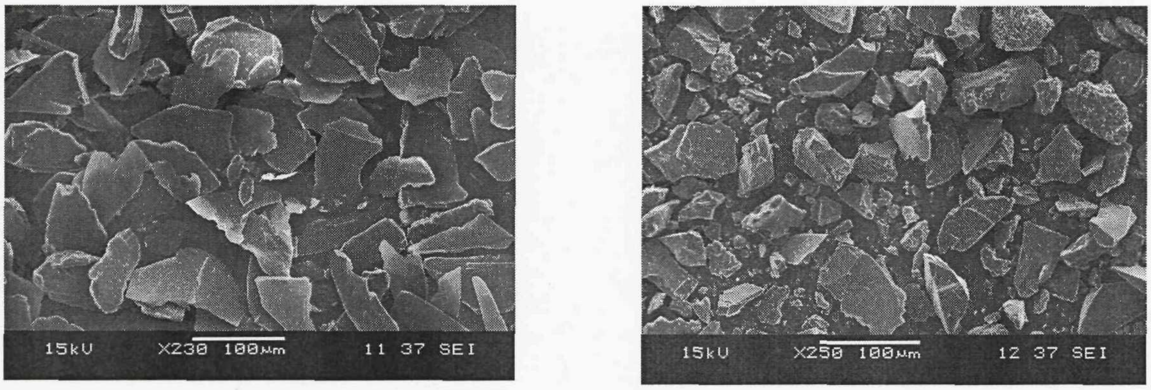

(e) Mica

(f) Classified tailings (Wesseloo, 2004)

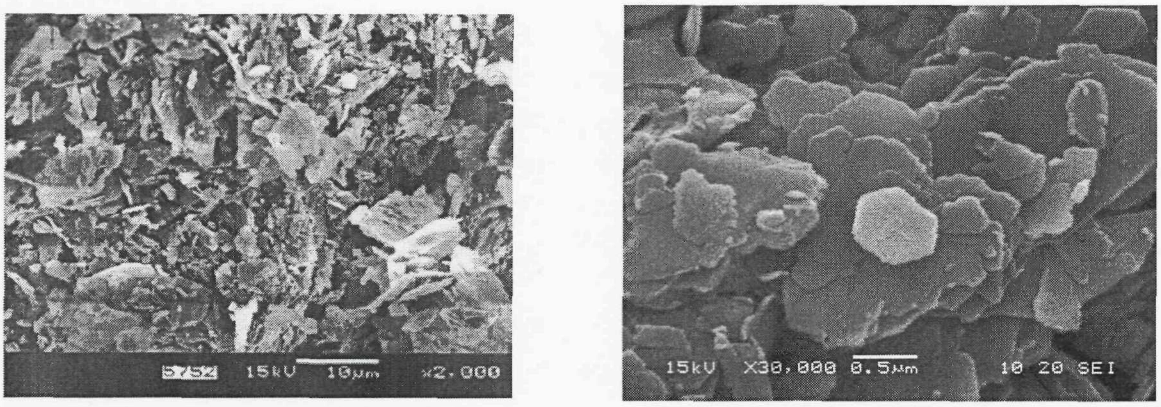

(g) Fine fraction of Mizpah tailings (Clayton et al., 2004)

(h) Kaolin

Figure 2.4: SEM images of materials commonly encountered by engineers.

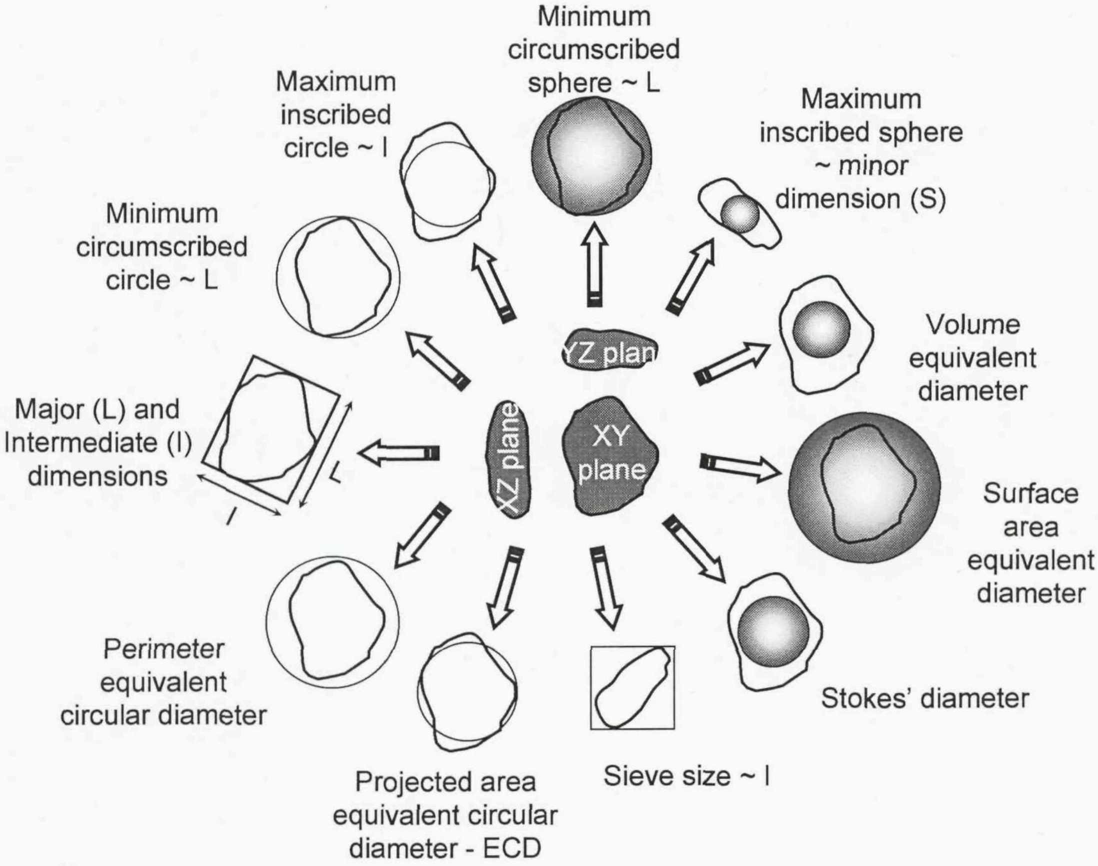

Figure 2.5: Various definitions of particle size

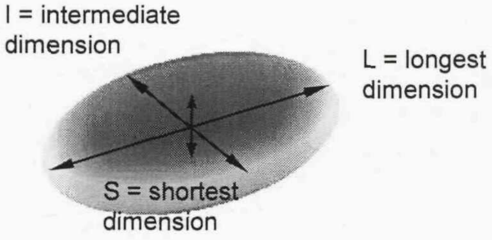

(a) Scalene Ellipsoid – 3D view

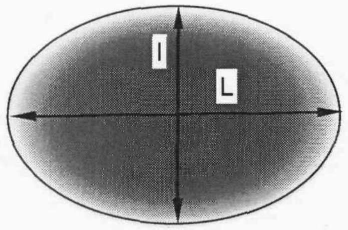

(b) Static imaging – mechanically stable orientation

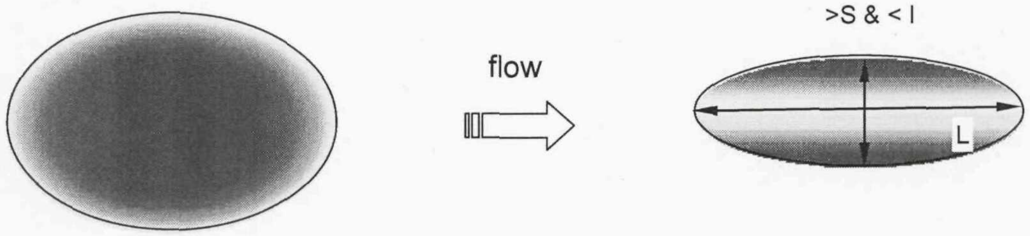

(c) SPOS - laminar flow conditions

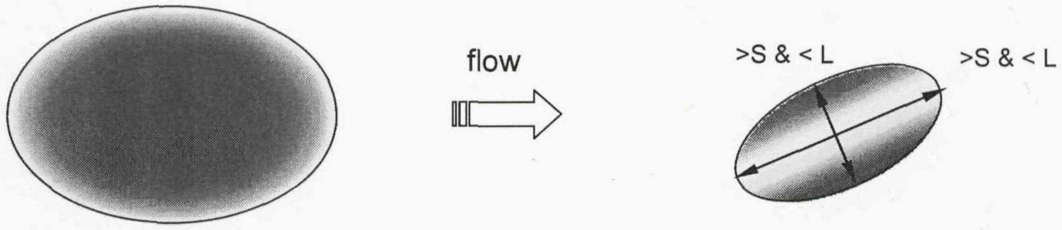

(d) Laser diffraction - turbulent flow conditions

Figure 2.6: Effects of particle orientation on measured dimension (a) scalene ellipsoid-like particle in 3D view; and possible orientations of particles in static imaging (b), SPOS (c) and laser diffraction (d) measurements.

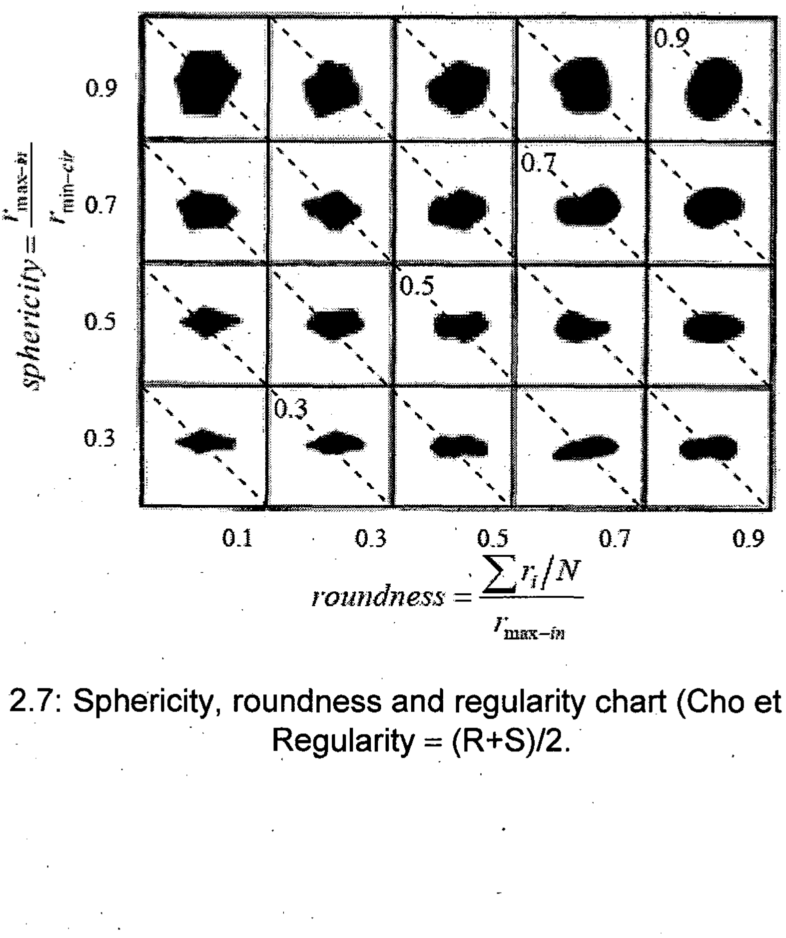

Figure 2.7: Sphericity, roundness and regularity chart (Cho et al., 2006). Regularity = (R+S)/2.

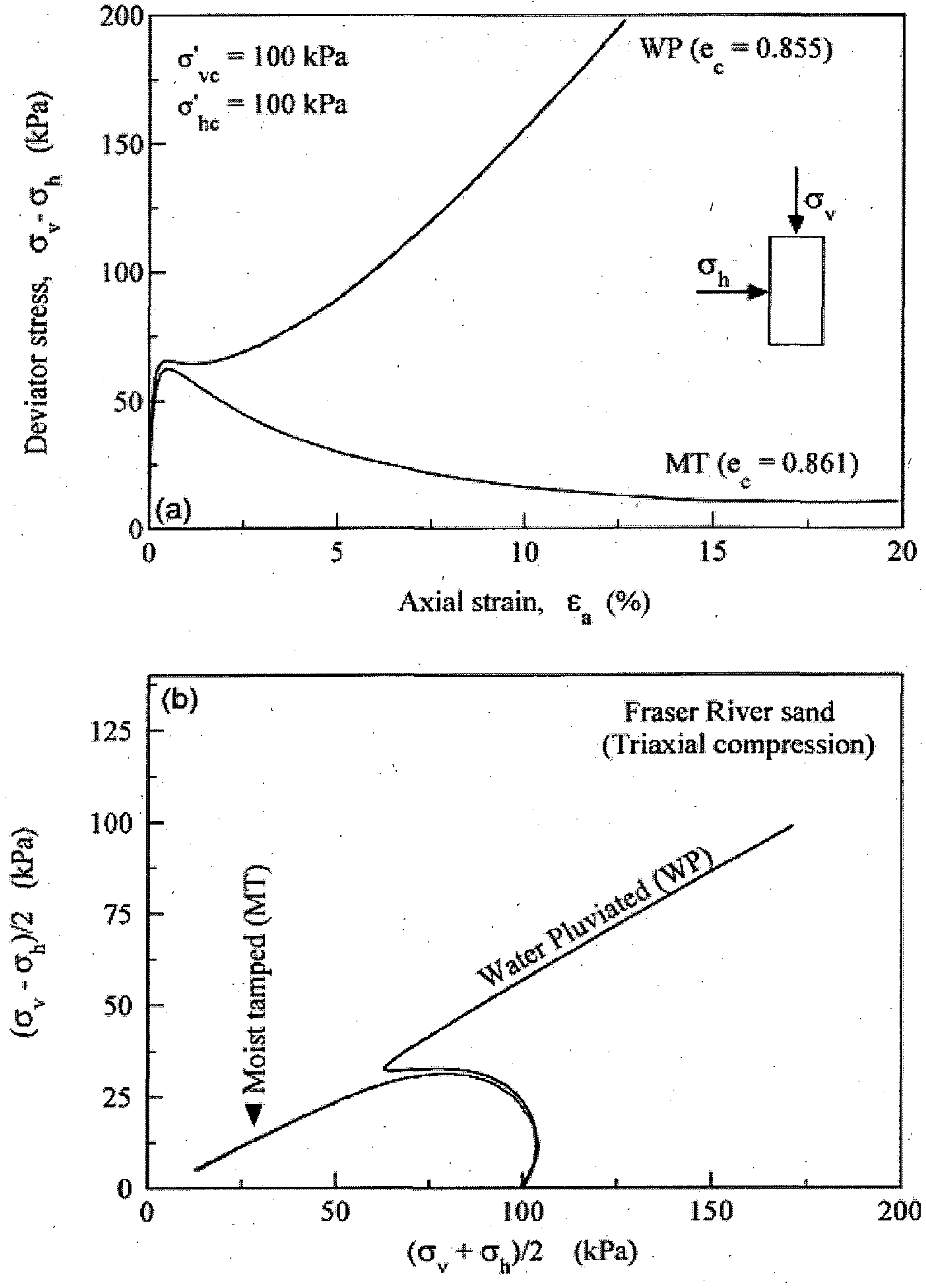

Figure 2.8: Undrained triaxial compression response of loose Fraser river sand specimens reconstituted by water pluviation and moist tamping (Vaid et al., 1999).

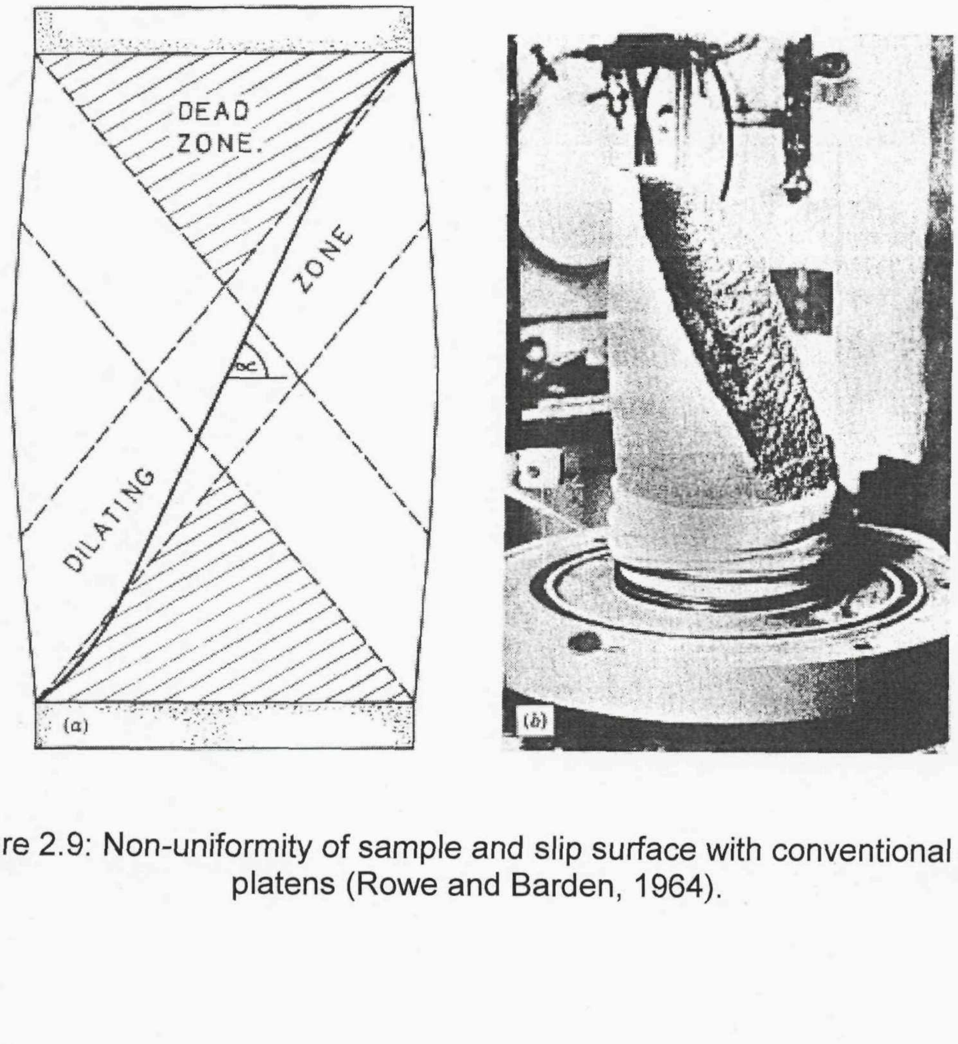

Figure 2.9: Non-uniformity of sample and slip surface with conventional end platens (Rowe and Barden, 1964).

CHAPTER 3 FORM OF COARSE PARTICULATES

Firstly, this chapter proposes a practical definition of form based on a scalene ellipsoid. Secondly, it evaluates the proposed measure of form, by applying it to various geometrical shapes, regular and irregular particles ranging from spherical to platy, and comparing with the existing measures. Thirdly, it proposes an automated method of estimating the proposed measure of form. A summary is provided at the end of the chapter.

3.1 A practical definition of form

The literature reviewed in section 2.4 suggests that many of the existing measures of form are two-dimensional, and therefore not well suited to the characterisation of particulate materials. Of the remaining, (three-dimensional) parameters, most require measures of the three-orthogonal dimensions, namely, the largest, intermediate and smallest particle dimensions (L, I and S). It is difficult and extremely time consuming to obtain the three-orthogonal dimensions (especially S), therefore the existing three-dimensional measures are impractical.

From the review of the currently available particle sizing methods (section 2.3), it can be concluded that:

- In general each particle sizing technique will only work over a limited range of particle size, thus requiring at least two methods to size between 2μm (the clay/silt size boundary) and 75mm (the upper size used in British Standard BS1377);
- Different techniques can lead to quite different measured particle size distributions, since each of them is based on a different principle of operation. Sedimentation methods are particularly problematical in this respect;
- Automated image analysis appeared promising, particularly for more demanding applications where more than one dimension is required.

Automated image analysis methods are of two types, namely, static and dynamic (ISO 13322:1-2004 and ISO 13322:2-2006). In static image analysis, still particle images are captured by dispersing them on to a xy-movable stage and minimising the overlaps. When (as is normal) particles are dispersed onto a horizontal stage, they settle into their most mechanically stable state, and present their largest projection area to the camera. This method cannot easily be applied for fine particles as sample separation becomes an extremely difficult task. For this reason the estimation of the form of fine particulates is covered in the next chapter (i.e. Chapter 4) using a different technique.

The writer's working hypothesis has been that the platy or bulky nature of soils can be suitably expressed through the ratio of the minimum to maximum particle dimensions (S / L), and that these can be approximated to the three-dimensional inscribed and circumscribed spherical diameters, D_{is} and D_{cs}. We further assume that within each limited particle size range the form of the particles is approximately uniform. When non-spherical particles are placed on a horizontal surface and separated they fall with their major and intermediate dimensions (L, I) parallel to the surface that they lie on, and normal to the imaging system. Direct measurement (e.g. using static imaging) of the minor dimensions of a specimen comprised of a large number of non-spherical particles is therefore impractical, and other methods must be sought.

For the purposes of this work, and as a starting position, the author has arbitrarily adopted a reference particle shape that is neither two dimensional nor spherical, but is a scalene ellipsoid. The smallest dimension (S) of an equivalent ellipsoid can potentially be obtained indirectly in two ways:

1. By measuring the major and intermediate dimensions using imaging, and then determining the average surface area of the particles, or
2. By measuring the major and intermediate dimensions using imaging, and then determining the average volume of the particles.

Whilst the volume of a scalene ellipsoid particle is easily calculated from

$$V = \frac{\pi}{6}.L.I.S \qquad (3.1)$$

where *L*, *I* and *S* are the largest, intermediate and smallest dimensions of the ellipsoid, measured along three orthogonal axes, the surface area is not. An approximate solution (Thomsen, 2004) can be obtained from

$$A = \frac{\pi}{2}\left[(LI)^p + (IS)^p + (SL)^p\right]^{1/p} \tag{3.2}$$

where $p \approx \ln(3)/\ln(2)$.

Surface area measurements can be carried out using a number of techniques, for example nitrogen or krypton or argon gas adsorption, methylene blue dye absorption, mercury porosimetry, air-permeability etc. However, such estimates are sensitive to surface irregularities and roughness, as well as pores, and particularly to test procedures and measurement techniques used to measure surface area. In trials carried out on the particulates described later in this chapter it was found that there were unexpected discrepancies between the expected surface areas of uniformly-graded materials and those measured using either the nitrogen gas adsorption technique (Micromeritics Gemini 2375 BET surface area analyser) or the mercury porosimetry technique (Pascal 440) (for example, more than one order of magnitude difference between the surface area measurements for (visually) smooth glass ballotini and the measured value). The effects of surface irregularities, pores and test technique have also been reported by others (Hofmann, 1959, Koerner, 1970b, Holubec and D' Appolonia, 1973, Santamarina et al., 2002, Blott et al., 2004), and the surface area measurement method was therefore abandoned.

Determination of the average volume of particles proved relatively easy. For a given material, the specimen is weighed, the specific gravity determined, and imaging software used to calculate the number of particles. On this basis the scalene ellipsoid equivalent sphericity can be calculated from

$$SEES = \frac{S}{L} = \frac{\left[\dfrac{W}{nG_s}\cdot\dfrac{6}{\pi.L.I}\right]}{L} \tag{3.3}$$

where W is the mass of the specimen, n is the number of particles, G_s is specific gravity and L and I are the average major and intermediate particle dimensions determined from image analysis.

3.2 Evaluation of the proposed measure of form

The proposed measure of form was evaluated in three ways:

1. By applying it to standard geometric shapes (spheres, cylinders, cubes, plates, etc.) and qualitatively evaluating its effectiveness alongside other available measures of form;
2. By making individual measurements on regular (spherical) and irregular particles from samples with different forms, and then comparing SEES and other measures of form for the samples.
3. Using static images obtained using the Automated Particle Analysis System (Figure 3.1) at the National Oceanographic Centre Southampton (NOCS).

Image-Pro Plus version 6.0 was used to analyse the images, and the results are discussed below.

Figure 3.2 shows normalised particle volume as a function of form, where form is determined using a number of available measures (see Table 2.2 for the definitions), for different standard geometric shapes. The volume of the given particle is normalised by dividing it by the volume of a cube with dimension equal to the largest dimension of the given particle, L. Normalised volumes for all shapes therefore fall between zero and unity. A number of points arise from these data:

- Two-dimensional parameters such as Inscribed Circle Sphericity (Riley, 1941 and Cho et al., 2006) can be determined easily from the projected particle images, but cannot differentiate bulky and platy particles (e.g. cubes and square plates, cylinders and discs, and spheres and oblates, differentiated by the two boxed areas), since they do not consider the particle's smallest dimension.
- 3D form parameters based on the 3-orthogonal (major, intermediate and minor) dimensions of a particle (Krumbein, 1941; Corey, 1949; Aschenbrenner, 1956; Sneed and Folk, 1958, Al-Rousan et al., 2007 and Blott and Pye, 2007) cannot differentiate between particles having the same major, intermediate and minor dimensions but very different volumes (e.g. cubes, cylinders, and spheres).
- Hawkins (1993) true sphericity does not sufficiently differentiate bulky and platy particles having same major and intermediate dimensions (e.g. cubes and

plates, cylinders and discs, and spheres and oblates), since it assumes the particle to be a sphere.

In contrast, SEES can differentiate bulky particles having the same major, intermediate and minor dimensions but (because of their shape) different volumes, and can effectively distinguish the bulky and platy particles having same major and intermediate dimensions. However, the limitation of this parameter is that it cannot differentiate between rod-like and plate-like particles having the same major and minor dimensions, since it does not give much weightage to the intermediate dimension. However, the population of rod-like particles is insignificant in almost all clastic sediments, so can probably be ignored.

To further explore SEES, six samples (5 glass, and one Leighton Buzzard sand, selected for their widely differing shapes (Figure 3.3), but all with an approximate particle size of 1mm, determined by sieving) were characterised in detail. Originally these tests were carried out with the expectation of being able to determine the individual grain dimensions with some accuracy, but experience showed that for irregular grains such as these (and soil particles) there were significant difficulties and uncertainties. Six particles of each material were individually weighed and measured. The mass of each individual particle was measured using a high resolution (0.01mg) electronic weighing balance (Mettler Toledo XP 205). Their volumes were then calculated from the known values of particle's mass and specific gravity. Each individual particle was dropped on to a flat surface, captured the image in their plan view and then fixed to a small metallic block using double-sided adhesive tape (by gently pressing the block against the particle's surface), to facilitate viewing and image capture in two orthogonal directions perpendicular to the maximum projection plane, using an optical microscope and a digital camera.

The first difficulty encountered was that of the limited depth of focus offered by the optical microscope. Depth of focus reduces with increasing magnification, requiring continual compromise between resolution and visual clarity, and necessitating a careful search for the dimensions required. Secondly, because most of the particles were irregular, the concept of major, intermediate and minor dimensions (L, I, and S) occurring in three orthogonal directions was not useful. The diameters D_{cc} (diameter of the circumscribed circle), and D_{ic} (diameter of the largest inscribed circle) were determined (Figure 3.4) from each of the projected images of particles in 3-orthogonal directions. For the purpose of calculating 3D form parameters, the orthogonal dimensions L and I were assumed to be equal to D_{cc} and D_{ic} in the plan view, and S was taken as the smallest value of D_{ic} measured on the two elevations (i.e. in the x-z and y-z planes). The volume equivalent spherical diameter (D_{vs}) and the volume equivalent minor dimension of a scalene ellipsoid (S_{vse}) of each particle were then calculated from the known values of masses, the diameter of the circumscribed circle, D_{cc}, and the diameter of the largest inscribed circle, D_{ic} (assumed to be L and I) in the plan view (x-y plane).

Figure 3.5 shows a comparison of the calculated minor dimension for a volumetrically equivalent scalene ellipsoid (S_{vse}) with the measured minor dimension ($S \equiv D_{is}$). It can be seen that:

- Despite more or less similar particle sizes determined by sieving, the measured minor dimension S varied by about one order of magnitude, confirming the visual observation of a wide range of form.
- For glass glitter (essentially broken glass plate, and therefore cuboid) S_{vse} overestimated S, as might be expected.
- For many particles S_{vse} significantly underestimated the measured minor dimension obtained from an optical search for the smallest inscribed sphere. However, for irregular particles the identification of the inscribed sphere was extremely difficult, and it was recognised that the values measured might not be accurate.

Figure 3.6 shows the same data, but in terms of Flat and Elongated Ratio (Al-Rousan et al., 2007) as a function of Scalene Ellipsoid Equivalent Sphericity. The trends expected from the above are clearly shown. It is interesting to note that Leighton Buzzard sand (fraction B), a material often used in geotechnical experiments, has a minor dimension of only one half of its major dimension.

Table 3.1 gives the average values of S/L obtained from measurement of individual particles of each type, and compares them with existing measures of form, and with the proposed measure. Krumbein's, Corey's, Aschenbrenner's and Sneed and Folk's parameters require 3-orthogonal dimensions to be measured, so are impracticable for routine use. In the case of Corey's shape factor this is unfortunate, as it differentiates between bulky and platy material quite well, giving results that are comparable with measured S/L values.

The remaining three parameters can be applied with relative ease. However the data show that because it does not consider the minor particle dimension (S), Cho et al's method cannot differentiate between bulky and platy materials. Hawkins true sphericity has a restricted range compared with SEES. The SEES values are quite comparable with the 'directly measured' S/L values.

The results of these initial trials, although imperfect, were felt to be sufficiently encouraging to seek a viable, and if possible automated method of determining SEES. Static images of assemblies of particles were obtained using the Automated Particle Analysis System (APAS) at the National Oceanographic Centre Southampton (NOCS) (Bollmann et al., 2004), and these were again processed using Image-Pro Plus version 6.0.

In order to improve the uniformity of the sample, and to allow the number of particles to be assessed on the basis of their projected areas, the chosen materials were sieved (using BS sieves) and separated into narrow size fractions as follows:

- Glass ballotini – 0.6 to 1.18mm
- LB sand B – 0.6 to 1.18mm
- fine glass nuggets – 0.6 to 1.18mm and coarse glass nuggets – 1.18 to 2.0mm
- fine glass glitter – 0.6 to 1.18mm and coarse glass glitter – 1.18 to 2.0mm

Each sample was carefully spread out and was imaged using a Leica© Z16APO monocular microscope fitted with a CC12 colour camera (SIS©) on a motorized xy-stage (see Figure 3.1), taking a patchwork of 152 images, each covering an area of about 9mm by 7mm. In this work, no attempt was made to stitch the images together. The average largest and intermediate particle dimensions and the average projected particle area were obtained from full particles (i.e. excluding particles cutting across the image boundaries). Dia(max) and Dia(min) were considered as appropriate for the largest and intermediate particle dimensions among the several options available in Image-Pro Plus software. The total number of particles in each sample was obtained by dividing the total projected area (summed across all images) by the average particle area. These values were checked by comparing them with the number of particles obtained by hand counting. The errors (Table 3.2) were generally less than 2%, with a maximum error of 4%.

The average Scalene Ellipsoid Equivalent Sphericity (SEES) of each sample was obtained from Equation (3.3), and are compared with calculated values of True Sphericity and Inscribed Circle Sphericity in Table 3.3. It can be seen that SEES differentiates well between particles of different shape, and that similar samples (fine and coarse nuggets, and fine and coarse glitter) give similar values. True sphericity appears less able to distinguish the platy particles, which are thought to be important in geomechanics. Because it is a two-dimensional parameter, inscribed circle sphericity does not differentiate between materials with a similar outline in plan view.

3.3 Summary

- A practical definition of form (namely the Scalene Ellipsoid Equivalent Sphericity (SEES)) has been proposed and evaluated its effectiveness by applying it to standard geometrical shapes and regular and irregular particles of wide range of shapes, and by comparing with the existing measures of form.

- The proposed measure of form (SEES) can differentiate bulky particles having same major, intermediate and minor dimensions but different volumes, and can effectively distinguish the bulky and platy particles having same major and intermediate dimensions. The only limitation of this parameter is that it cannot differentiate the rod-like and plate-like particles having the same major and minor dimensions, since it does not give much weightage to the intermediate dimension. However, the population of rod-like particles is insignificant in almost all clastic sediments, so can probably be ignored.

- An automated method of determining the SEES of particles has been proposed, described, applied to various groups of regular and irregular particles of wide range of shapes and demonstrated its effectiveness over the other methods.

Table 3.1: Average values of S/L, existing measures of form and SEES obtained from individual particle measurements

Material	S/L	Krumbein's Sphericity	Corey's Shape factor	Aschenbrenner's Working Sphericity	Sneed and Folk (1958) - Max. Projection Sphericity	Hawkins True Sphericity	Cho et al's Inscribed Circle Sphericity	New parameter SEES
Glass ballotini	1.000	1.000	1.000	0.956	1.000	1.008	1.000	1.023
Leighton Buzzard sand fraction B	0.532	0.742	0.605	0.896	0.715	0.750	0.776	0.549
Fine glass nuggets	0.279	0.506	0.403	0.765	0.544	0.475	0.479	0.229
Coarse glass nuggets	0.259	0.515	0.557	0.711	0.487	0.471	0.557	0.198
Fine glass glitter	0.071	0.330	0.099	0.374	0.213	0.384	0.515	0.113
Coarse glass glitter	0.048	0.284	0.068	0.298	0.167	0.320	0.488	0.068

Table 3.2: Comparison of number of particles obtained by manual counting and from image analysis

Material	Number of particles		Error (%)
	Manual counting	Image analysis	
Glass ballotini	465	460	-1.17
Leighton buzzard sand fraction B	1482	1491	0.57
Fine glass nuggets	937	974	3.95
Coarse glass nuggets	623	636	2.03
Fine glass glitter	1389	1386	-0.22
Coarse glass glitter	724	740	2.23

Table 3.3: Average values of Scalene Ellipsoid Equivalent Sphericity (SEES), True Sphericity and Inscribed Circle Sphericity obtained from automated imaging

Material	Number of full particles	L_{ave} (≡Dia(max)) (mm)	I_{ave} (≡Dia(min)) (mm)	Total number of particles	Average S_{vse} (mm)	Average SEES	Average D_{vs} (mm)	Average True Sphericity	Average Inscribed Circle Sphericity
Glass ballotini	311	0.918	0.852	460	0.986	1.000	0.914	0.999	0.928
Leighton Buzzard sand fraction B	1060	1.137	0.789	1491	0.606	0.533	0.818	0.718	0.694
Fine glass nuggets	550	2.010	1.122	974	0.395	0.197	0.975	0.479	0.558
Coarse glass nuggets	333	2.440	1.495	636	0.582	0.239	1.294	0.527	0.613
Fine glass glitter	906	1.640	0.901	1386	0.220	0.134	0.687	0.419	0.549
Coarse glass glitter	400	2.384	1.341	740	0.268	0.112	0.956	0.398	0.562

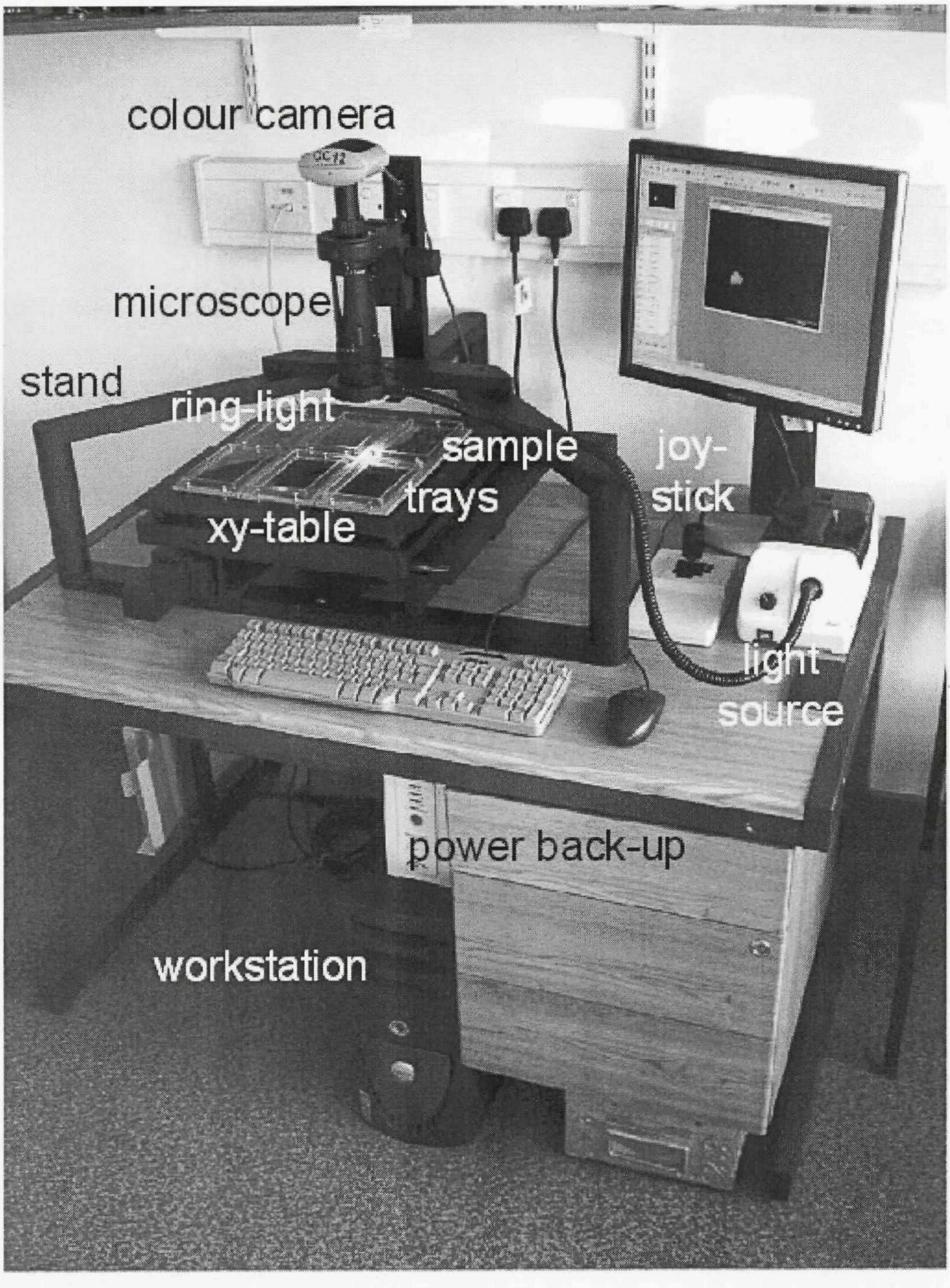

Figure 3.1: Automated Particle Analysis System (NOCS)

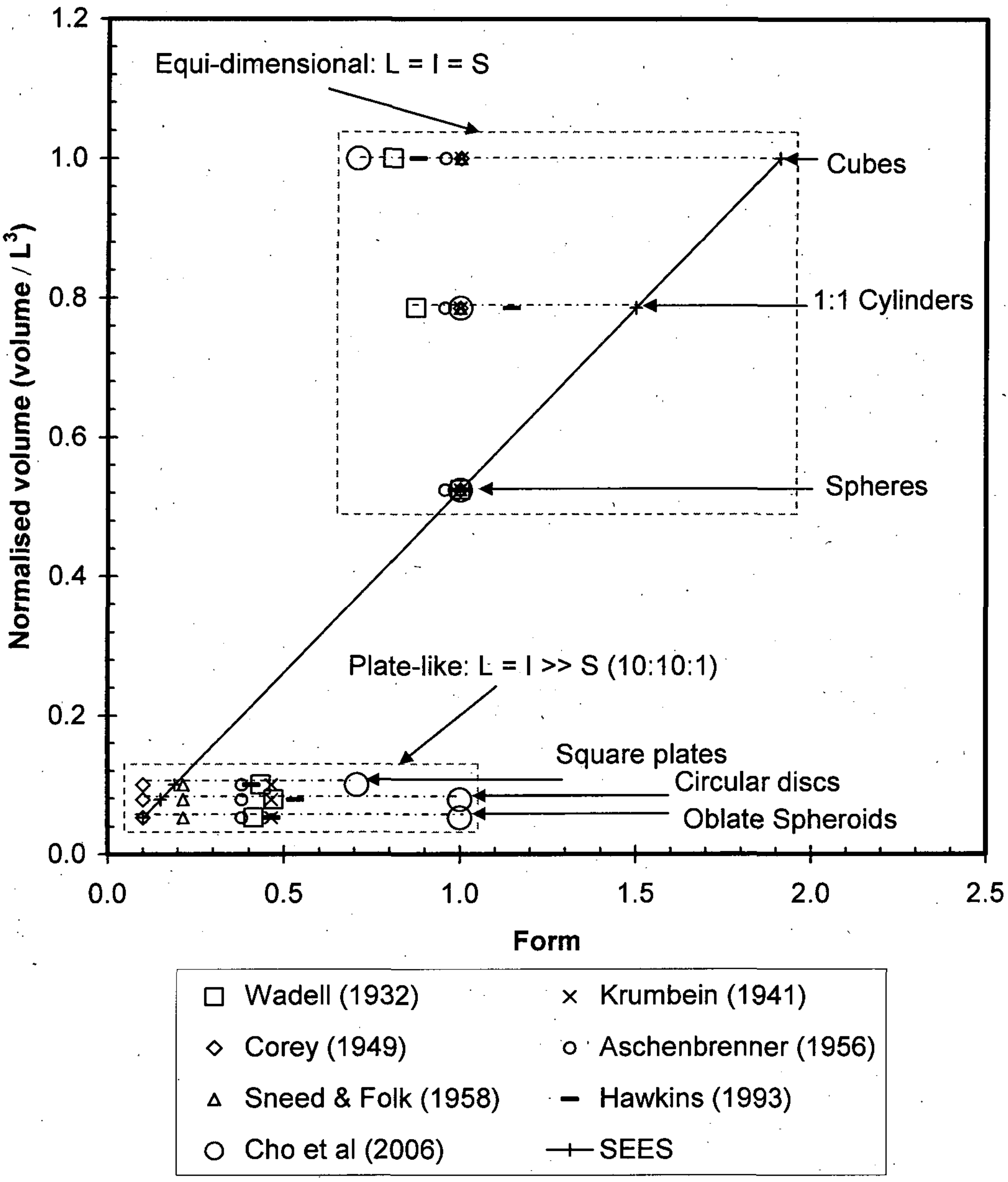

Figure 3.2: Comparison of different measures of form for standard geometric shapes

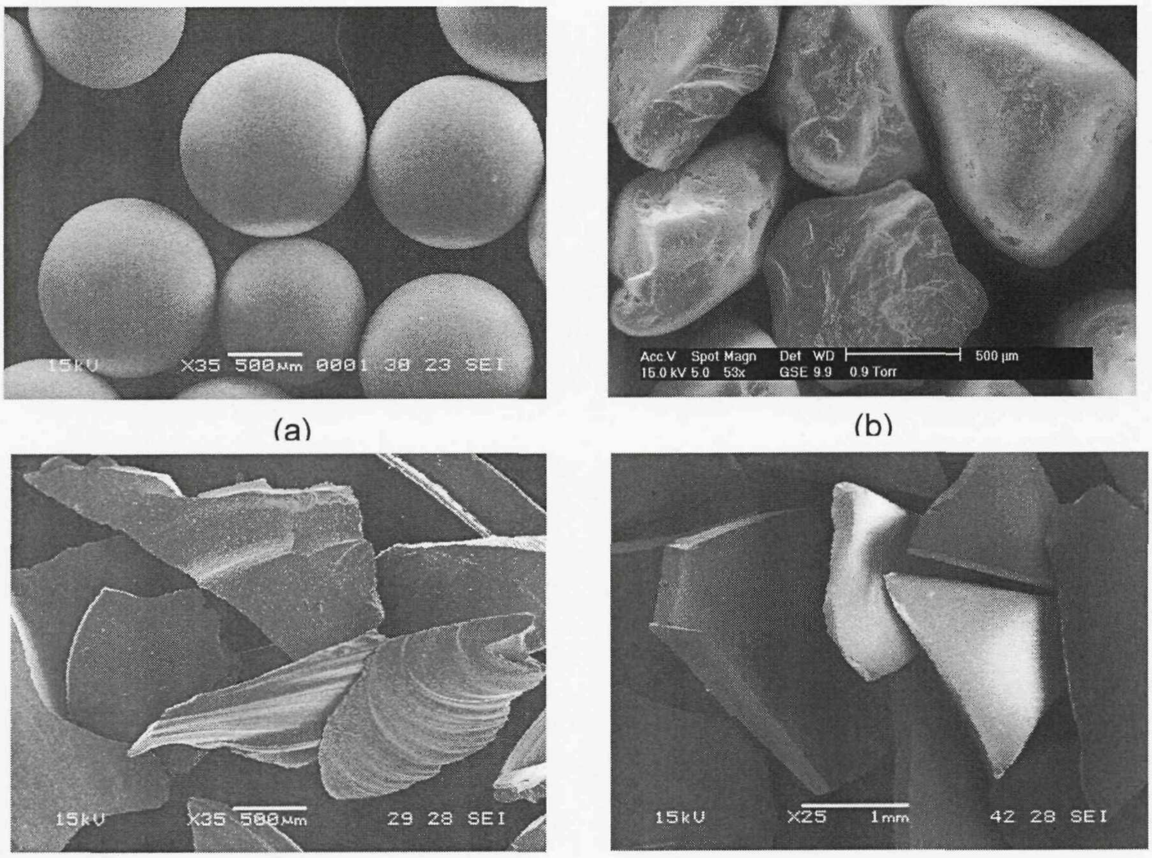

(a) (b)

(c) (d)

Figure 3.3: Scanning electron microscope images of coarse materials. (a) Glass ballotini, (b) Leighton Buzzard fraction B, (c) nuggets and (d) glitter (Glass ballotini and Leighton Buzzard B images from Xu (2005)).

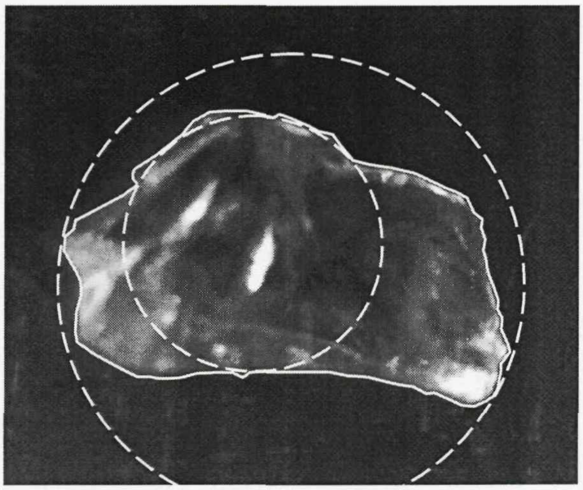

Plan view - x-y plane

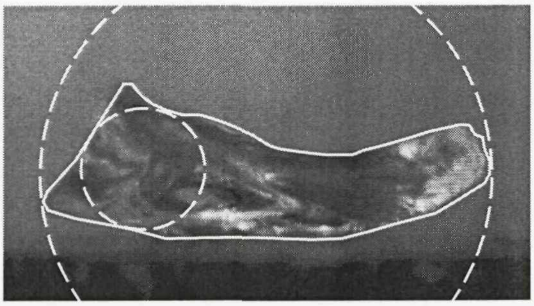

Elevation – y-z plane

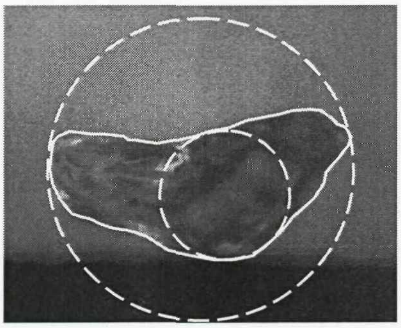

Elevation – x-z plane

Note: Dashed lines show circumscribed circles and largest inscribed circles for each view

Figure 3.4: Example of measurement of individual grain dimensions

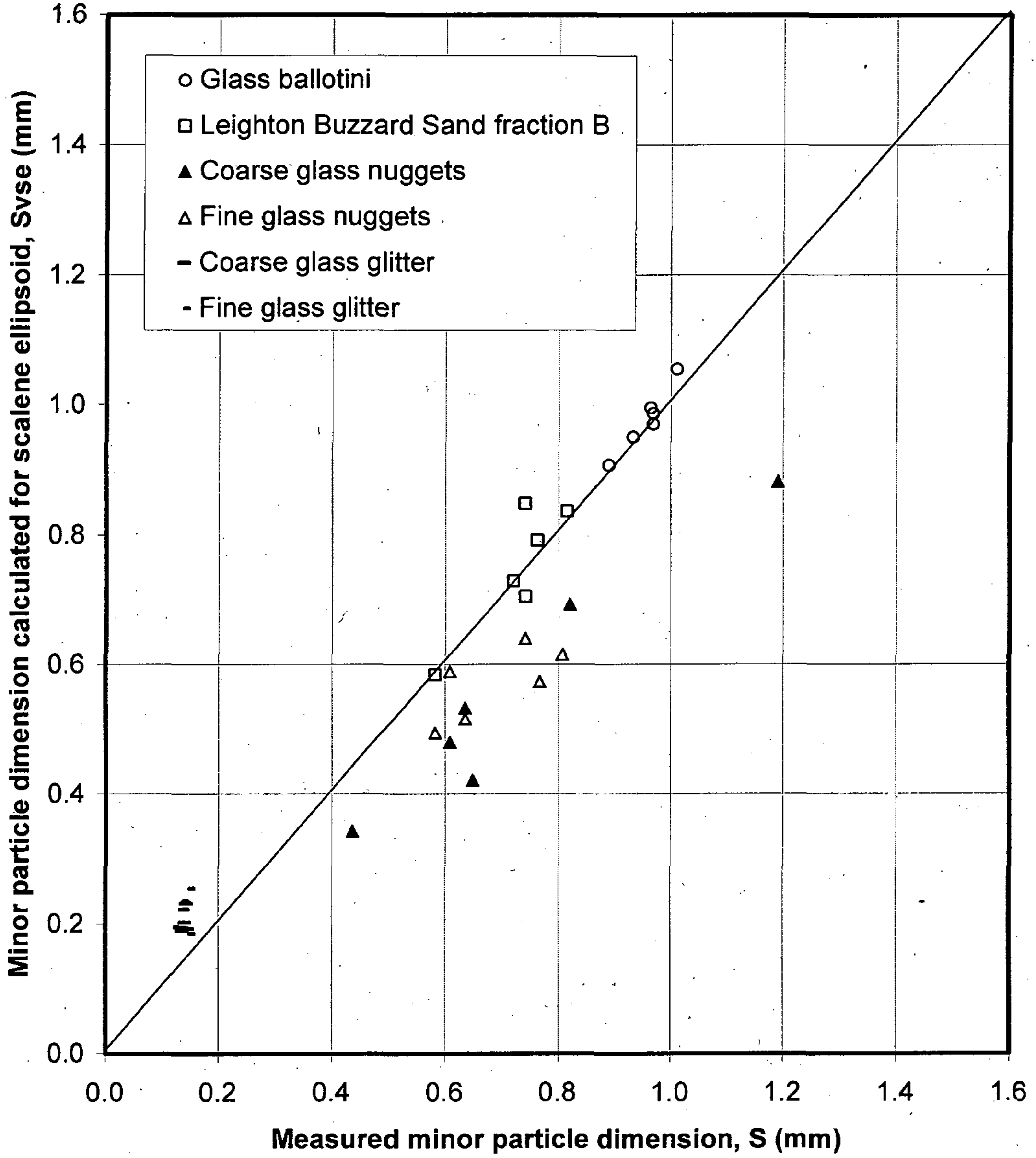

Figure 3.5: Comparison of calculated minor dimension for an equivalent scalene ellipsoid with measured minor dimension

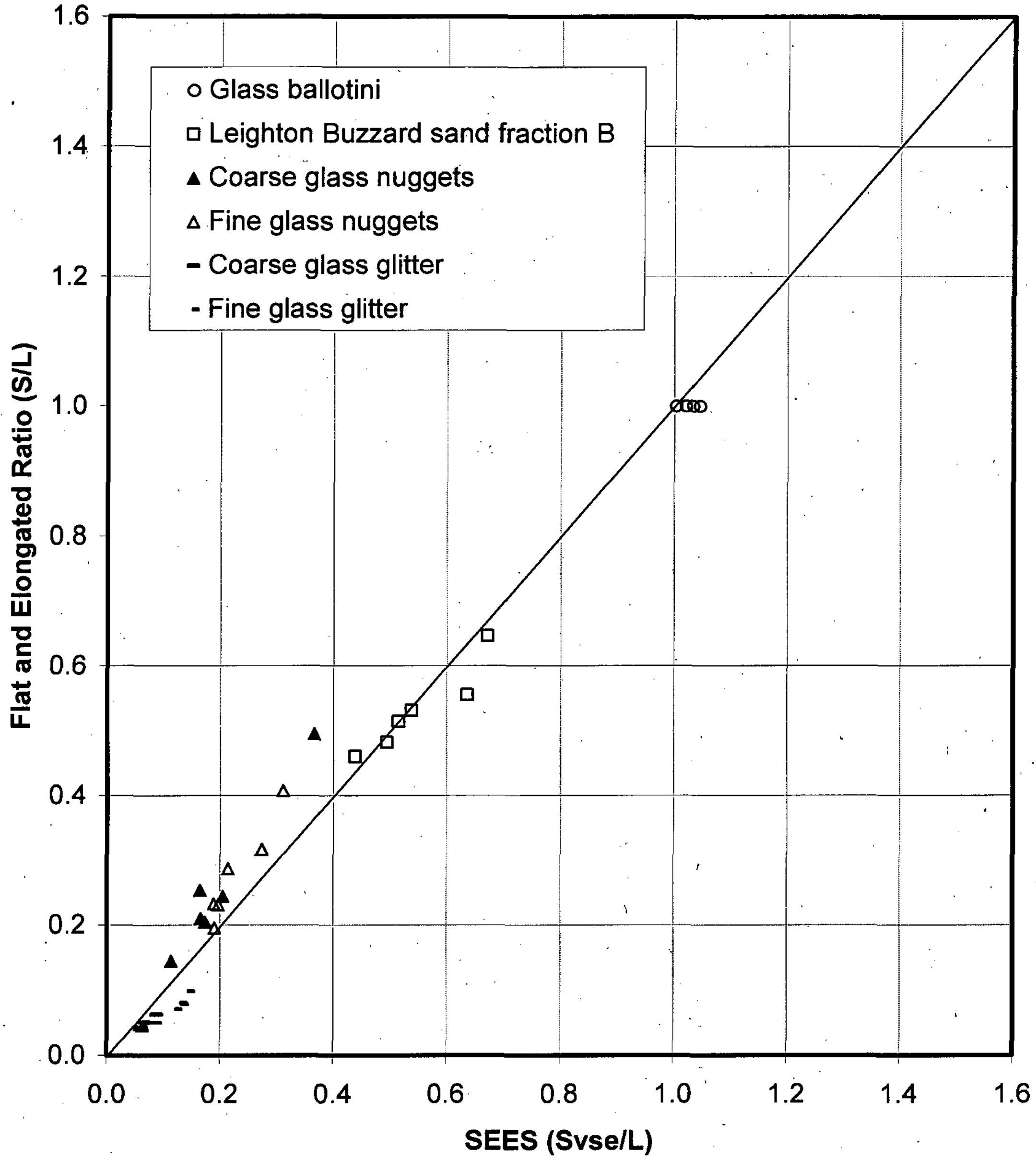

Figure 3.6: Comparison of Al-Rousan et al. (2007) Flat and Elongated Ratio with Scalene Ellipsoid Equivalent Sphericity (SEES)

CHAPTER 4 FORM OF FINE PARTICULATES

This chapter first tests the applicability of the existing methods of determining the form of fine particles for a range of particle shapes. It then proposes a new method based on laser diffraction and turbidity measurement using Malvern Mastersizer 2000, and evaluates the proposed method by applying it to a wide range of synthetic, natural and crushed rock particles of various shapes and compares with the existing methods. A summary is provided at the end of this chapter.

4.1 Evaluation of existing methods

It is evident from the literature reviewed in section 2.5 that existing methods of determining form have been tested for a limited range of shapes (essentially platy clay mineral particles). To evaluate the applicability of the existing methods over a wider range of form, three materials of widely differing shapes (glass ballotini, 'classified' tailings and mica) were chosen. The PSD of each of these materials was obtained by three different sizing techniques, namely laser diffraction (LD, using the Malvern Mastersizer 2000), electrical sensing zone (ESZ, using the Beckman Coulter Multisizer 3) and sedimentation (using the SediGraph 5100). Form (the inverse of aspect ratio) was evaluated as suggested by various researchers using the equations presented in Table 2.3.

Scanning electron microscope (SEM) images of the three materials are shown in Figure 4.1 (a) to (c). Also shown (Figure 4.1(d)) is an image of fine Mizpah gold tailings, which were used in subsequent experiments (see section 4.3). The images give a qualitative impression; glass ballotini is approximately spherical whereas the mica is platy (or sheet-like), and the 'classified' tailings fall in between the other two in terms of their form. Figure 4.2 shows the PSD obtained for the three materials by Sedimentation, LD and ESZ techniques. It is apparent from the figure that all the techniques produced approximately the same PSD for the glass ballotini (which were nearly spherical) and 'Classified tailings', but deviated strongly in the case of mica. However, there appeared to be no specific trend in deviation with respect to their form (compare the PSD data for glass ballotini and 'classified' tailings in Figure 4.2).

The average form (1/r or sphericity) of each of the materials were determined using the equations presented in Table 2.3, based on D_{50} obtained by different sizing techniques. It should be noted that while determining the aspect ratio using Jennings and Parslow's (1988) method, particles were assumed to be oblate spheroids for all materials. Table 4.1 shows the average form values determined by the parameters suggested by various researchers. Only Clift's (1988) and Barrieros et al.'s (1996) methods show a reasonable trend with respect to particle shape. Even these measures are suspect, however, as the values of form predicted by them appears to be very low for 'classified' tailings and mica when compared with visual estimates based on SEM images.

4.2 Laser diffraction and turbidity-based measurement of form

The laser diffraction particle sizing technique is based on the principle that particles passing through laser beam will scatter the light at an angle and with an intensity that are directly related to particle size (BS ISO 13320-1:1999). The scattering angle is inversely proportional to, and the intensity is directly proportional to, the particle size (i.e. large particles scatter light at narrow angles with higher intensity whereas small particles scatter at wider angles but with lower intensity). The instrument (in this case a Malvern Mastersizer 2000) records the scattered light using a series of logarithmically spaced photo-detectors placed at various angles with respect to the direction of the laser beam. The recorded scattering pattern is transformed into a volume-weighted particle size distribution using Mie theory, and assuming the particles to be smooth spheres.

In addition, the instrument measures the intensity of un-scattered light, which is recorded by an obscuration detector placed at the far end of the laser beam. The un-scattered light can be related to the volume concentration (or turbidity) of particles present inside the Malvern cell using the Beer-Lambert law, using the following equation (Lips et al., 1992 and Baudet et al., 1993, Application note - Malvern Instruments Ltd):

$$C_{th} = \frac{100\log_e(1 - Obscuration)}{-\frac{3}{2}b\sum\frac{V_i Q_i}{d_i}} \tag{4.1}$$

where

- C_{th} is the theoretical volume concentration (%) of particles calculated by the Mastersizer assuming the particles to be spheres;
- "Obscuration" is the fraction of incident light that is attenuated due to extinction (scattering and/or absorption) within the particles;
- b is the path length of the measuring cell, and
- V_i, Q_i and d_i, respectively, are the volume (%), extinction coefficient and the mean diameter of size band i.

Since the Mastersizer treats the particles as spheres, the volume concentration calculated using equation (4.1) will be equal to the actual volume concentration presented to the Mastersizer only if the sample particles are perfect spheres, as illustrated in Figure 4.3(a), and always provided that the optical properties chosen for particles are correct (Lips et al., 1992).

The actual concentration (C_{act}) of particles can be determined fairly easily if the specific gravity of the particles (G_s), dry mass of the sample material (W) and volume of the liquid used to disperse and circulate the sample (V_l) are known, using the following expression:

$$C_{act} = \frac{\left(W / G_s \rho_w \right)}{V_l} \times 100 \qquad (4.2)$$

However, if (as is normally the case) the material has high absorbance of laser light and its particle shape deviates from spherical then the theoretical concentration calculated using equation (4.1) will be different from the actual concentration calculated using equation (4.2). For example, if the particles were discs the same mass of sample would be composed of a much larger number of particles, as illustrated in Figure 4.3(b). Thus, the ratio of the actual to the calculated concentration potentially provides a measure of average particle form, which can be expressed as follows:

$$Form = \frac{S}{L} = fn\left[\frac{C_{act}}{C_{th}} \right] \qquad (4.3)$$

If the particles were to pass across the laser beam with their major and intermediate dimensions perpendicular to the laser beam, as illustrated in Figure 4.3(b), then the volume concentration of disc-shaped particles would be overestimated by a factor equal to two-third times their major to minor dimension, L/S. If the particles were oblate spheroids then the volume concentration would be overestimated by a factor equal to L/S.

In reality, particle orientation is likely to be random during measurement, since flow is turbulent inside the Mastersizer cell onto which the laser beam is focussed. Under conditions of turbulent flow, the projected area of a given number of particles seen by the Mastersizer will be less than the possible maximum projected area for any given anisometric particle shape (Figure 4.3(c)), leading to an underestimation of the concentration of particles with known dimensions S and L. However, this effect may be removed by applying a correction factor *(C_f)*, which can be expressed as a function of initial estimate of form (determined using equation (4.3)) (see Appendix for the derivation of correction factor). Equation (4.3) can then be re-written as follows:

$$Form = \frac{C_{act}}{C_{th}.C_f} \tag{4.4}$$

where $C_f = \dfrac{2}{\left[1+\left(\dfrac{S}{L}\right)^p+\left(\dfrac{S/L}{I/L}\right)^p\right]^{1/p}}$

The correction factor, C_f, (Figure 4.4) varies from 2 to 1 for oblate spheroids (I/L = 1) forming an upper bound curve and from 1.29 to 1 for prolate spheroids (I/L = S/L) forming a lower bound curve, as form (S/L) goes between its limits of 0 to 1. For intermediate values of I/L, the rate of variation of C_f with respect to S/L is steeper at lower values than at higher values, all reaching a maximum value of 2 as S/L approaches zero.

4.3 Evaluation of turbidity-based measurement of form

The proposed method of estimating form, described in the previous section, was evaluated using the Malvern Mastersizer 2000 at National Oceanography Centre Southampton (NOCS) in two ways:

1. By applying it to a range of particles of varying shapes (i.e. spherical to platy), all passing 63μm sieve. The materials used were glass ballotini, 'classified' tailings, fine Mizpah gold tailings and mica, in order of decreasing form, see Figures 4.1(a) to (d).
2. By applying it to a platy material of various narrow size fractions, namely, mica <63μm, mica 63 to 150μm, mica 150 to 300μm, and mica 300 to 600μm, again in order of decreasing form, the minor dimension (S) of the material being more or less constant.

There are two measurement modes of operation in Mastersizer 2000, namely, manual and automatic. In the manual mode, the user is able to explore the full range of available options and carry out tests in order to establish SOP's (standard operating procedures) relevant to the specific application. In automatic mode the user is provided with a consistent measurement framework in order to obtain comparable results with the minimum of training, but does not have control over the volume of liquid and the weight of material used for the measurements, due to the deployment of an auto-sampler.

After several trials, a practical test procedure was established in manual measurement mode, which gave consistent measurements of the actual volume concentration with reasonable accuracy. The materials described at the beginning of this section were analysed in manual mode with a fixed volume of liquid (i.e. 903ml including the dispersant) and at pump and stirrer speeds of 2400rpm and 940rpm respectively, to keep the particles in suspension during the measurements.

BS ISO 13320-1:1999 states that particle concentration in the dispersion should be above a minimum threshold (corresponding to about 5% obscuration) in order to produce an acceptable signal-to-noise ratio in the detector, and should be below a maximum threshold (corresponding to about 35% obscuration) in order to avoid multiple scattering. Pilot trials were made to arrive at the approximate quantity of sample required for the laser diffraction measurement of each of the materials bearing in mind the threshold obscuration limits specified by BS ISO 13320-1:1999.

Figure 4.5 shows the particle size distribution curves of the materials produced using the standard Mastersizer 2000 procedure. It can be clearly seen from the figure that the mean particle size of glass ballotini, classified tailings and mica < 63μm are almost same, Mizpah tailings are finer and other fractions of mica are coarser. These observations are, qualitatively, in agreement with the sieve size fractions described at the beginning of this section.

The tests were repeated at different concentrations (between the minimum and maximum threshold limits of obscuration) to investigate the effect of concentration on PSD. PSD was found to be very consistent for all the materials and concentrations analysed. Figure 4.6 compares the actual and theoretical volume concentrations for the four materials. Actual concentration was calculated using equation (4.2) whereas the theoretical concentration was automatically calculated by the Mastersizer. The following points should be noted:

- The slope of the actual vs. theoretical concentrations curves were approximately linear for all the materials, which suggested that estimates of form would not be affected by concentration.
- The slope was nearly unity for (approximately spherical) glass ballotini and decreased with increasing platiness for other materials, indicating that the proposed method was able to differentiate qualitatively between particles of differing shapes.

Figure 4.7(a) and (b), respectively, show the variation of initial estimates of form (calculated using equation (4.3), i.e. without correcting for random orientation) for four different particle shapes, and for platy material of different size fractions over a wide range of obscuration values. A number of observations can be made from this data:

- For a given material, form was found to be more or less constant over a range of obscuration values, indicating that form is independent of obscuration

- The proposed method was able to differentiate well between particles of different shapes and form, as well as between particles of same shape but with different form.
- Form estimates were in line with values obtained from qualitative interpretations of the SEM images.

Though the initial estimates of form are qualitatively in agreement with the SEM images the absolute values will have been underestimated because of the random orientation of particles in the Mastersizer cell. Therefore, the initial estimates of form were corrected to account for the effect of particles random orientation on obscuration (and eventually on form) using equation (4.4). The correction was applied assuming the shape of particles to be oblate, since prolate soil particles are rare (especially at lower S/L where the C_f variation is significant with respect to *I/L*, see Figure 4.4), and were not seen in the SEM images of the materials that were tested. Initial estimates of form, correction factors (assuming particles to be oblate spheroids) and corrected form values of all the materials are summarised in Table 4.2.

4.4 Summary

- The existing methods of determining the form of fine particles, which have been based on comparisons of particle sizes obtained from two different instruments, were evaluated for their applicability for three different particle shapes. The results show that only the methods of Clift (1988) and Barreiros et al. (1996) gave plausible results, and that (based upon visual estimates from SEM images) these appeared unreliable.

- A method of measuring the form of fine-grained materials, based on turbidity and laser diffraction measurement using a single instrument (the Malvern Mastersizer 2000), has been developed, used, and described. It has been applied to a range of synthetic, natural and crushed rock particles with widely varying shapes. The method appears practical, and for the materials tested yields in qualitative agreement with those that could be estimated from SEM images.

Table 4.1: Form values predicted by the existing methods

Material (passing 63µm)	Jennings and Parslow (1988)	Clift (1988)	Allen (1990)	Barrieros et al. (1996)	Endoh et al. (1998)
Glass ballotini	0.286	0.910	0.48	0.939	0.807
'Classified' tailings	0.333	0.800	0.69	0.862	0.847
Mica	0.040	0.160	0.18	0.295	0.352

Table 4.2: Form values predicted by the proposed method

Material	Initial estimate of form	Correction Factor, C_f	Corrected form
Glass ballotini	0.770	1.175	0.655
'Classified' tailings	0.610	1.328	0.459
Fine Mizpah gold tailings	0.338	1.649	0.205
Mica < 63µm	0.087	1.949	0.045
Mica 63 to 150µm	0.057	1.974	0.029
Mica 150 to 300µm	0.049	1.979	0.025
Mica 300 to 600µm	0.041	1.984	0.021

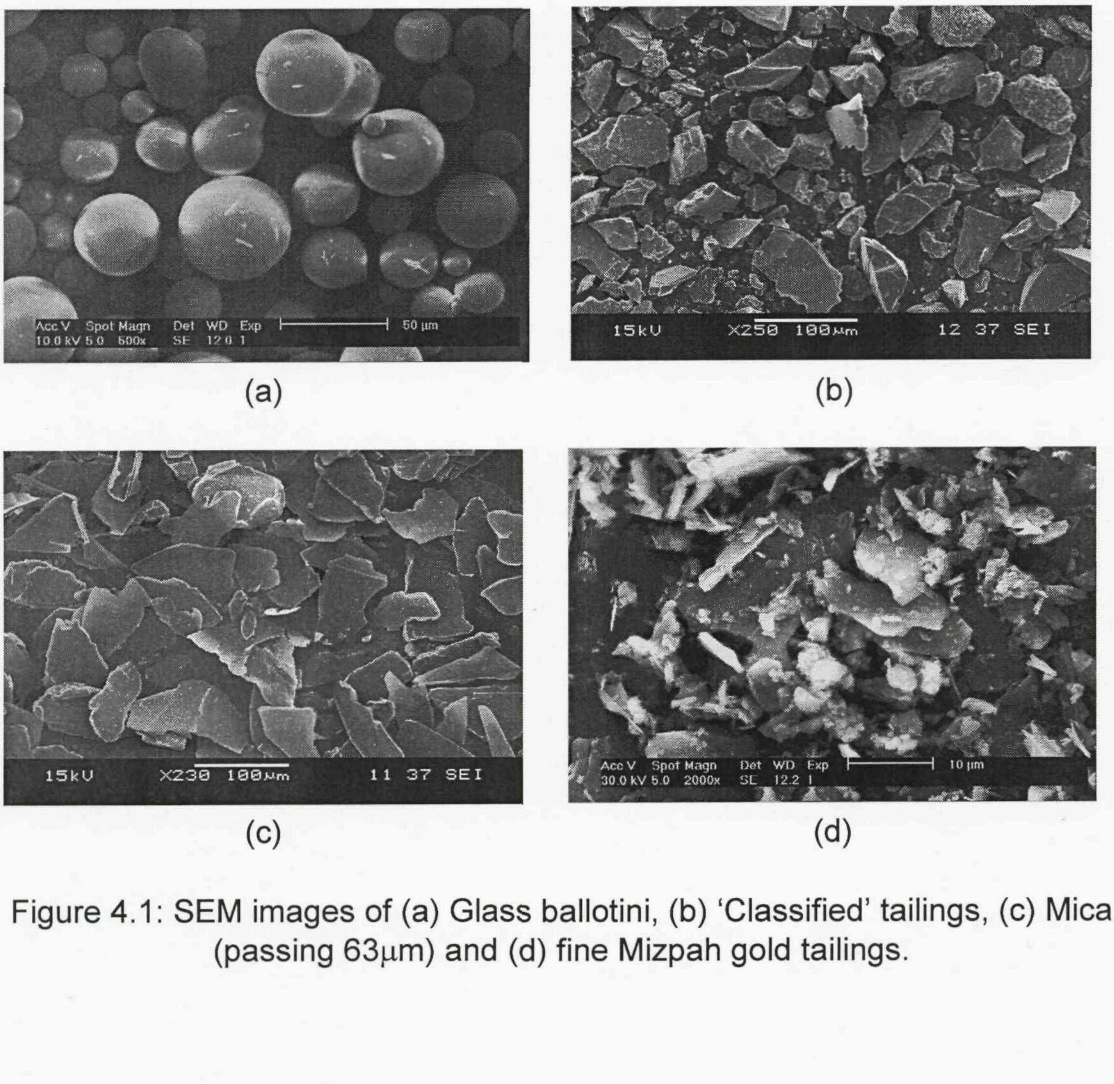

(a) (b)

(c) (d)

Figure 4.1: SEM images of (a) Glass ballotini, (b) 'Classified' tailings, (c) Mica (passing 63μm) and (d) fine Mizpah gold tailings.

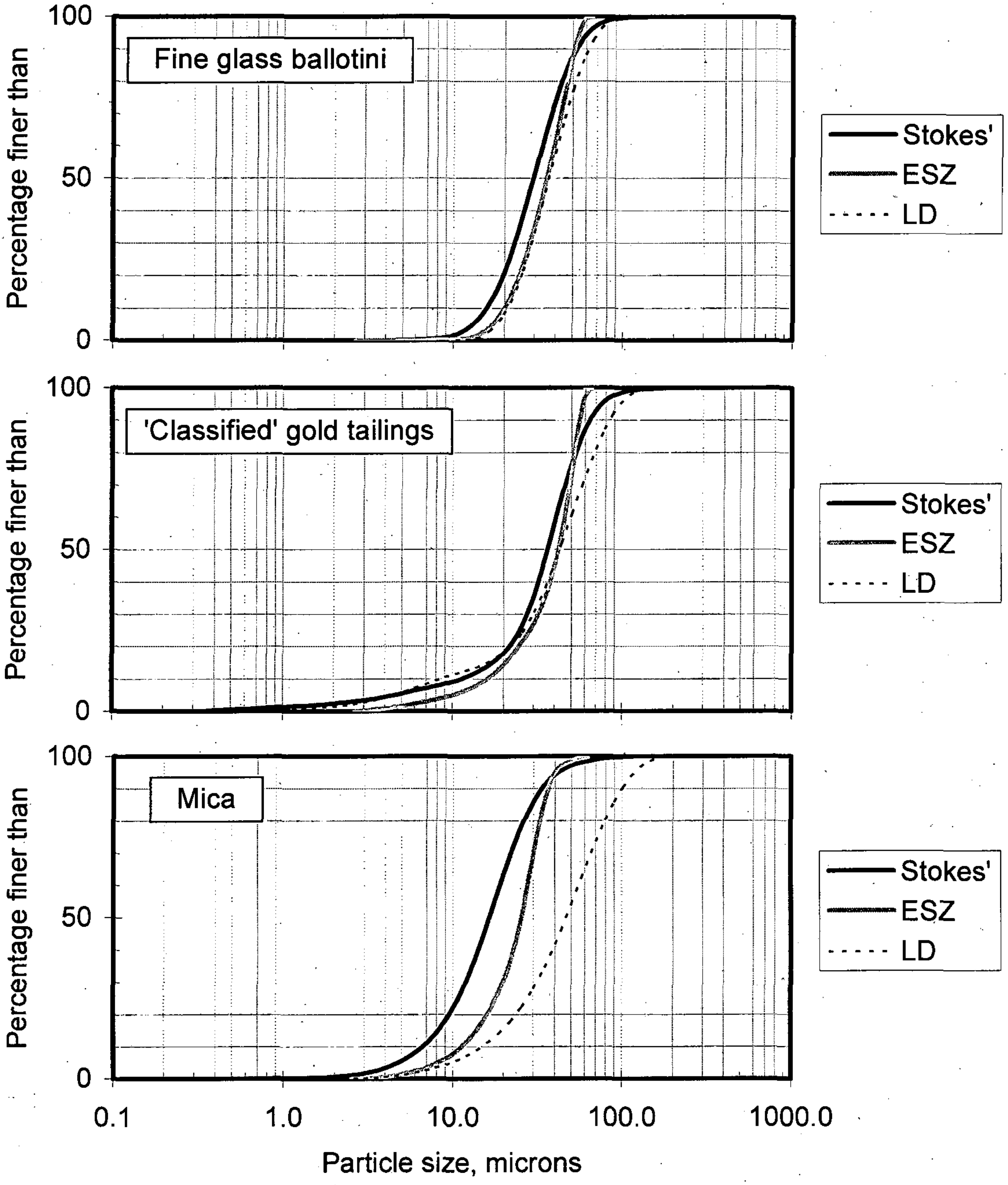

Figure 4.2: Comparison of PSD obtained by sedimentation, electro sensing zone and laser diffraction techniques

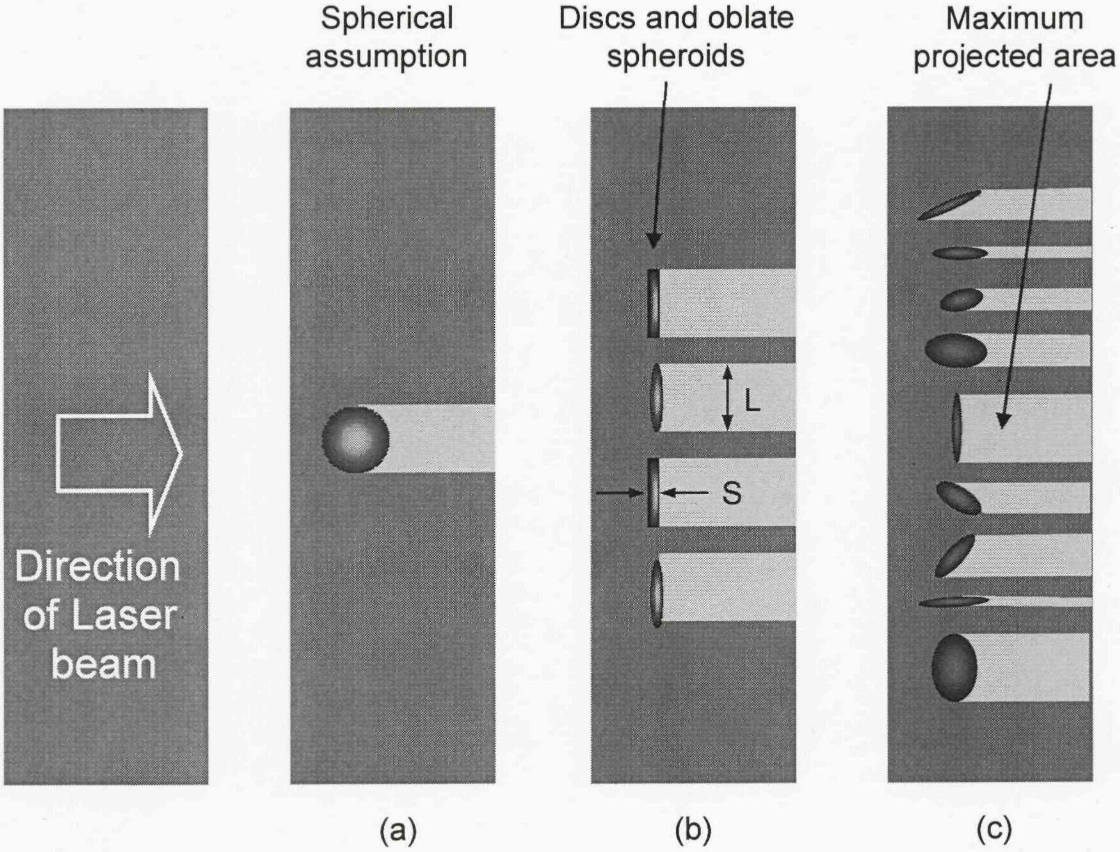

Figure 4.3: Illustration of volume concentration of spheres (a), discs and oblate spheroids (b), effect of particle orientation on projected areas during measurement by the Mastersizer 2000.

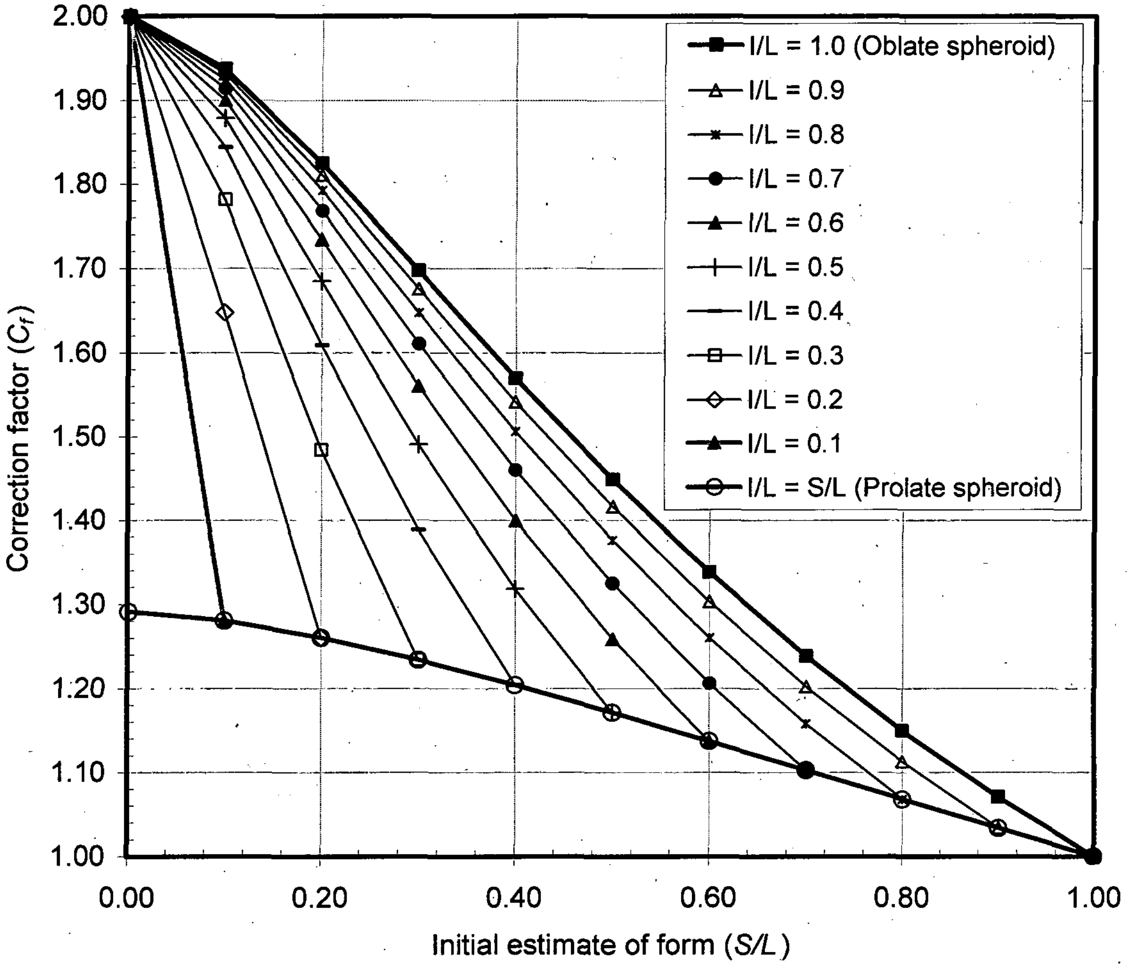

Figure 4.4: Correction factor for random orientation of particles for different *I/L*

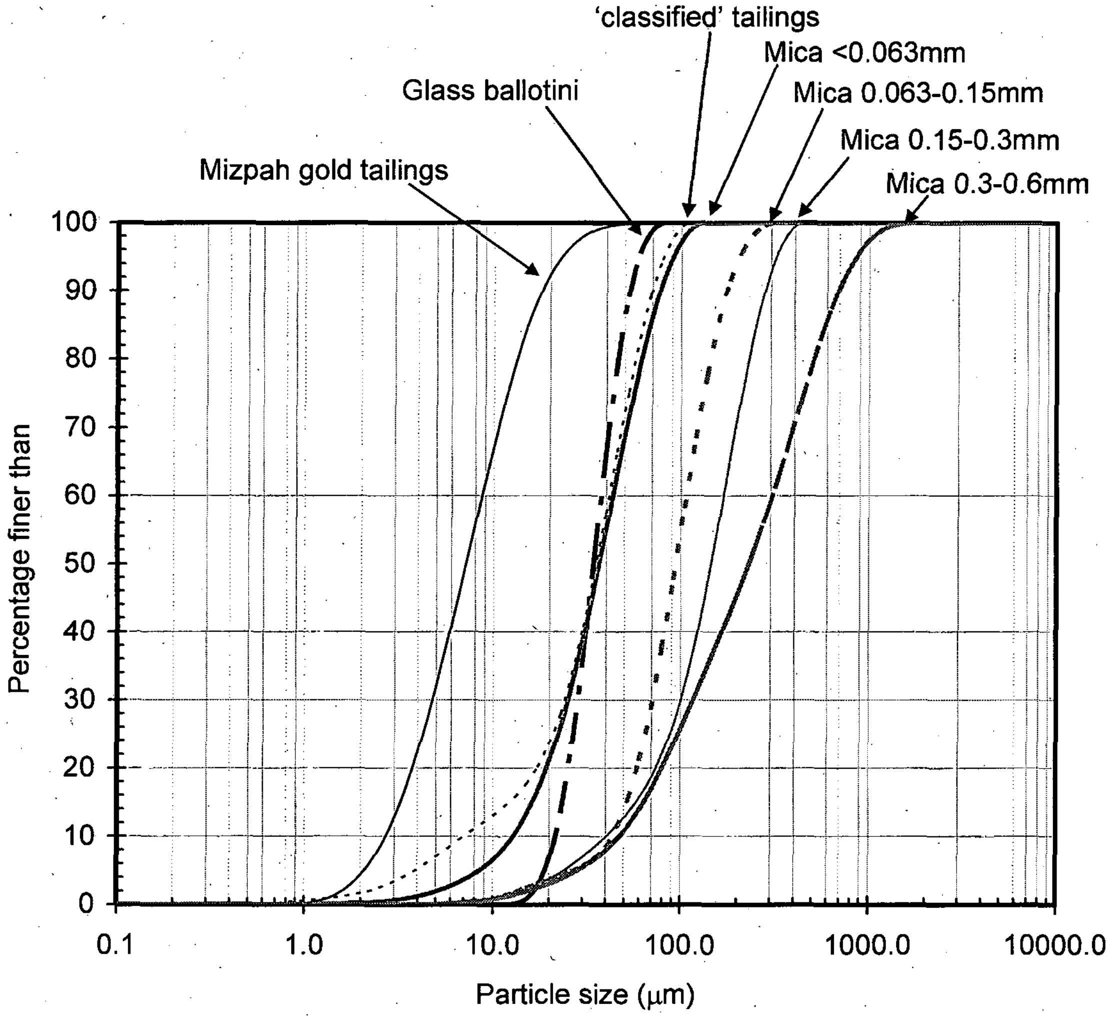

Figure 4.5: PSD of materials of different shapes by laser diffraction method

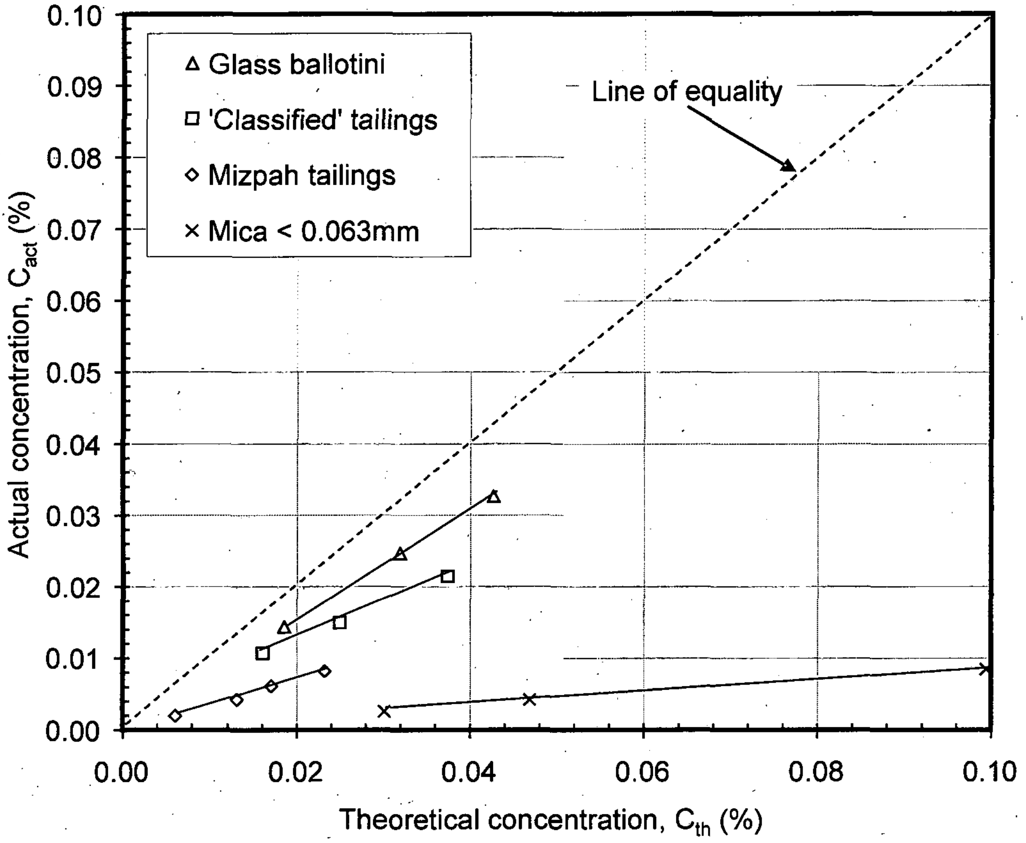

Figure 4.6: Actual versus theoretical volume concentrations of fine materials of different shapes

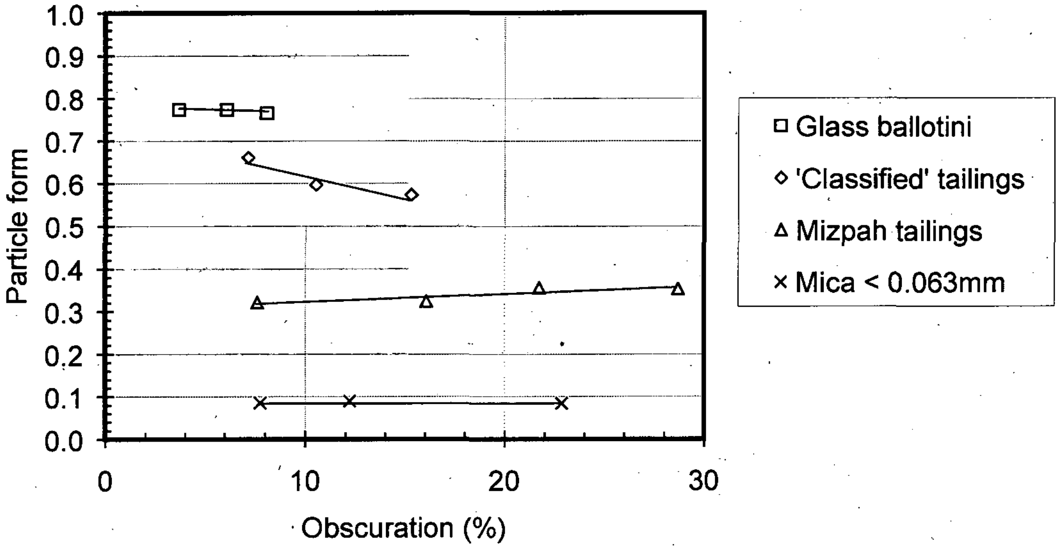

(a)

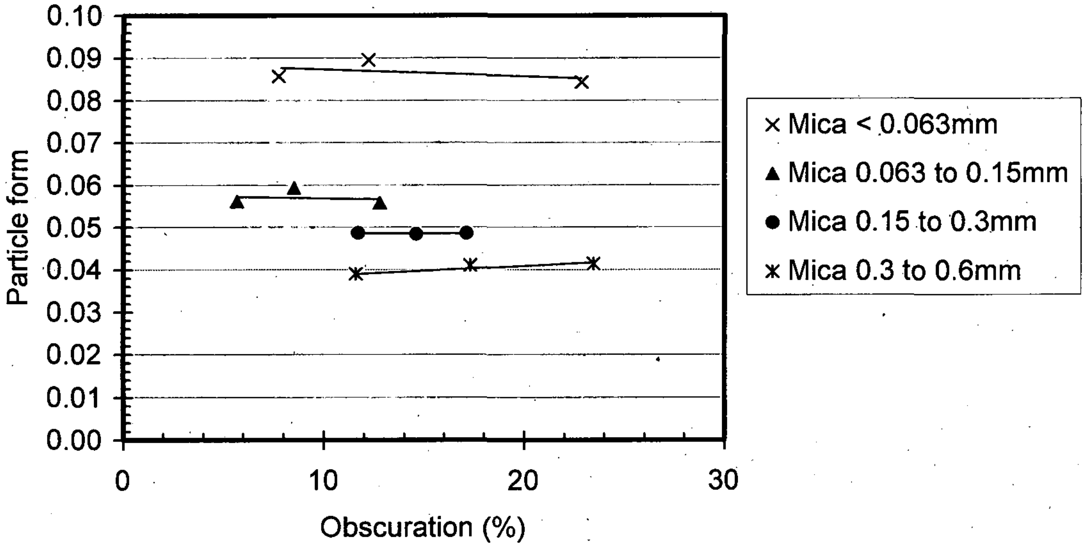

(b)

Figure 4.7: Initial estimates of form over a wide range of obscuration values for a variety of particle shapes (a), and platy material of different size fractions (b)

CHAPTER 5 LABORATORY EXPERIMENTS

This chapter provides the description of experimental setup and materials used in this research, and then presents the experimental results examining the effects of particle form on packing (loose and dense) by carrying out limiting void ratio tests and on drained shear behaviour by triaxial compression tests, on a wide range of particle shapes. The main findings are summarised at the end of the chapter.

5.1 Experimental setup

The experimental setup used in this research consisted of the following components:

- the Bishop and Wesley triaxial apparatus,
- free-ends,
- a special sliding type 6-part split mould,
- a pluviation device,
- the pressure control system,
- the data acquisition system, and
- measuring devices

Figure 5.1 shows a photograph of the triaxial testing system when in operation. The whole system was operated in an air-conditioned room, at a constant temperature of 20°C. The whole system was controlled and logged the data using a computer via Visual Basic programming.

5.1.1 The Bishop and Wesley triaxial apparatus

In this research, a Wykeham Farrance Bishop and Wesley cell (Bishop and Wesley, 1975) was modified to incorporate the free-ends and used for triaxial tests.

The base pedestal and the top cap were modified to incorporate the enlarged end platens (Figure 5.2 (a) and (b)). The cell chamber had an inside diameter of 166mm, which was slightly larger for 100mm diameter specimen with enlarged end platen system and local strain instrumentation. Therefore, great care and patience was required while closing the cell to avoid disturbing the specimen and local strain instrumentation.

Three pressure transducers were fitted to the cell-ring for measuring the pressures inside the cell, the base chamber and the sample. Each of the transducers was fitted with a de-airing block, and two values (one on each side). The sensing membranes (of transducers) and the air-bleed plugs were fitted inline, and oriented vertical in order to expel the air while flushing. The valves fitted on either side of the transducers were particularly useful to calibrate the transducers without removing them from the de-airing blocks as well as to flush the pipe lines during testing.

5.1.2 Free-ends

The free-end system used in this research consisted of an enlarged top platen, an enlarged bottom platen with a small porous stone at its centre, and two sets of lubricated membranes.

Figures 5.2(a) & (b) show the schematic diagrams of the enlarged top and bottom end platens. The top platen was made of Perspex while the bottom platen was made of aluminum. The loading faces of both the platens were polished to minimise friction, and the edges were smoothed to avoid puncturing the membranes while preparing the samples. A small porous stone (~10mm dia low air entry) was fitted at the centre of the bottom platen for saturating the sample as well as for drainage purposes.

Two sets of lubricated membranes were used, one for the top platen and the other for the bottom platen. The lubricated membranes consisted of three alternate layers of latex rubber membrane discs (cut from a 100mm diameter sample membrane) separated by thin layers of high vacuum silicone grease, as shown in Figure 5.3(a). They were attached to the loading faces of the platens as schematically shown in Figure 5.3(b). A small circular cut was made at the centre of the latex discs to uncover the porous stone (in order to allow free drainage) in the case of bottom platen.

5.1.3 Sliding type 6-part split mould

A special sliding type 6-part split mould was designed to facilitate the preparation of samples with the enlarged end platens. Figure 5.4 shows the schematic diagram of this special mould. The outer diameter of the mould was kept equal to the diameter of the enlarged end platen and the internal diameter was kept equal to the diameter of the sample.

The main advantages of this mould were as follows:

- Easy to stretch and wrap the membrane around the enlarged platens without disrupting/dislocating the lubricated membranes as well as the sample.
- Easy to align and level the top cap while closing the sample.
- Easy to place O-rings onto enlarged end platens as they can just be pushed up/down onto the platens from around the mould.
- Easy to remove the mould without disturbing the specimen (after preparing and making the sample self standing by applying suction) since the top three pieces of the mould can be slid down without disrupting the top platen.
- Making the sample perfectly vertical.

5.1.4 Pluviation device

A simple pluviation device was designed to prepare 100mm diameter specimens directly into the triaxial cell. It consisted of a hopper, a series of closely spaced diffuser meshes, a plastic guide tube and a metallic ring connected to the guide tube at its bottom to provide stability without any additional support as shown in a schematic diagram (Figure 5.5). The hopper was made of a small plastic tube and had a funnel connected at its bottom. Diffuser meshes were made from a perforated metallic sheet, which had 68% opening area with 8mm diameter circular perforations. A series of 12 diffuser meshes were connected in a staggered manner to disperse the initial flow (originating from the hopper) effectively and spread over a larger area. The guide tube controlled the dispersion of initial flow and ensured uniform rain over the whole cross section of sample. It has been widely accepted by researchers that the density increases with increasing fall height and is very sensitive at lower fall heights (for example, see Cresswell et al., 1999; and Lagioia et al., 2006) when pluviated at low depositional intensities. Therefore, a fall height of approximately 800mm was adopted to ensure that density variation would be insignificant with the rising surface of the specimen while pluviating the material.

5.1.5 Pressure control system

Three GDS controllers (filled with de-aired water) were used for pressure control. The cell and base chamber pressure were controlled by two advanced controllers whilst the back pressure was controlled by a standard controller, through the computer via IEEE-488 and RS-232 interfaces, respectively.

5.1.6 Data acquisition system

The data acquisition unit used in this research was supplied by ELE International Ltd, and had a 12-bit resolution i.e. the digital readings ranged between 0 and 4096.

In total, eight channels were used to monitor the signals coming from the load cell, the pore pressure transducer, the cell pressure transducer, the base chamber pressure transducer, two DC-to-DC LVDT transducers for external strain measurement, and two Hall-effect gauges for local strain measurement. The monitored signals were logged via an RS232 interface and converted into engineering units using the calibration constants, as will be discussed in the next section.

5.1.7 Measuring devices

The measuring devices consisted of following:

- an internal submersible type load cell for measuring the axial load
- three pressure transducers for measuring the pressures inside the cell, the base chamber and the sample
- two DC-to-DC LDC transducers for measuring the external strains
- two Hall-effect gauges for measuring the local strains
- a standard pressure controller for measuring the volume changes inside the sample

All the measuring devices were calibrated along with the data acquisition system to evaluate their accuracy and precision, adopting the calibration methodology suggested by Heymann (1998). The load cell and the pressure transducers were calibrated against the Budenberg dead weight calibration system. The load cell was calibrated for three measurement ranges to get good resolution and accuracy at lower ranges by choosing the appropriate gain and offset values, and the same was incorporated in the control program to change the gain, offset and corresponding calibration constants according to the output reading. That is, a higher gain was allocated at the start of shearing and when the output reached towards the end of the current measurement range, a lower gain was allocated automatically without interrupting the test.

The pressure transducers were calibrated for up to 900kPa. The LDC type transducers were calibrated against a micrometer (Mitutoyo series 152-348) up to their full linear range (i.e. 50mm) in two-fold. The micrometer had a range of 25mm and a least count of 2µm. Hall-effect gauges were calibrated using a special calibration jig which had a provision to fix the gauges and move the sensor relative to the magnet by a micrometer (Starrett No. 436M). This particular micrometer had a range of 10mm and a least count of 10µm.

Typical calibration results of each of the measuring devices are presented in Appendix B (see Figure B.1 to B.4), and a summary of all the calibration results is presented in Table 5.1.

5.2 Description of the materials

A wide variety of uniform materials, ranging from spherical to platy, was chosen for testing which included:

- glass ballotini (0.6 to 1.18mm sieve),
- Leighton Buzzard sand fraction B (0.6 to 1.18mm sieve),
- glass nuggets (0.6 to 2.0mm sieve),
- fine glass glitter (0.6 to 1.18mm sieve), and
- coarse glass glitter (1.18 to 2.0mm sieve).

All the glass particles (ballotini, nuggets and glitter) were produced from soda-lime glass and procured from Sigmund Linder GmbH, Germany. Whereas the Leighton Buzzard sand is a natural silica sand free from silt, clay or organic matter, and procured from David Ball Group plc. However, the major composition of all these materials is silica.

Figures 3.3(a) to (d), respectively, shows the SEM images of the materials listed above. It can be clearly seen from the images that glass ballotini are nearly spherical; LB sand B is sub-rounded, slightly elongated and flattened; nuggets are angular, elongated and flattened; and glitter is angular, elongated and platy. However, the surface roughness of the particles of all these materials was similar. The form (using SEES) and roundness (defined as $\sqrt{P^2/4\pi A}$, using Image-Pro Plus 6.0) of each of these materials were quantified and the values are tabulated in Table 5.2. It can be seen from the Table that both SEES and roundness vary in the case of glass ballotini and LB sand B whereas in the other three materials (namely glass nuggets, fine glitter and coarse glitter) only the form varies but the roundness remains constant.

5.3 Effect of particle form on packing

The maximum and minimum void ratios of the materials were determined by inverted cylinder and air-pluviation methods due to their advantages over the other methods as discussed in Section 2.6.

Figures 5.6(a) and (b), respectively, shows the variation of limiting void ratios and the void ratio range with respect to form. It can be clearly seen from Figure 5.6(a) that both e_{max} and e_{min} increases with decreasing SEES, although e_{max} is more sensitive than e_{min}. Therefore, the void ratio range increases with decreasing SEES (Figure 5.6(b)). The exact values of maximum and minimum void ratios, and void ratio range are tabulated in Table 5.3.

In minimum void ratio tests, low SEES particles tend to fall with their major axis parallel to the rising surface of the deposited material since they were pluviated at low depositional intensities in order to achieve the highest density. Therefore, one can expect anisotropic packing in the case of plate-like materials i.e. face-to-face arrangement of particles. If we extend the same analogy in terms of SEES, it is logical to expect increased packing anisotropy with decreasing SEES.

CT Scans

To verify the above-mentioned hypothesis, the CT (Computed Tomography) scanning technique was adopted to visually examine the orientations of particles (as opposed to traditional and time-consuming thin sections) in pluviated specimens. For this purpose, a cylindrical specimen, 100mm diameter and 40mm high (enclosed by a metallic ring, altogether placed in a tray), was prepared by air-pluviation process. Its fabric was then preserved by a three step process as follows:

- Firstly, the pluviated specimen was slowly flooded with a 5% solution of PVA (Polyvinyl Acetate – an adhesive and bonding agent, in particular 'B&Q Multi purpose PVA') and water and left inundated with the solution for about an hour.
- Secondly, the solution was drained out of the specimen, and the specimen was dried in the oven.
- Thirdly, the sample was extracted from the ring and trimmed down to a cylinder of 20mm diameter (approx.) to allow better resolution while performing CT scanning.

The trimmed specimen was then scanned using a Micro-focus Computed Tomography facility (X-Tek CT 160Xi μCT, supplied by X-Tek Systems Ltd., UK). The specimen was scanned at a voltage of 95kV and a current of 90μA. The pixel resolution was typically 1/1000th of the width of object imaged. The sample size used in this study is 20mm diameter; therefore, it had a resolution of 0.02mm. CT-Pro and VGStudio Max v 2.0, respectively, were used for 3D reconstruction, voxel visualisation, analysis and segmentation.

The same procedure was followed for all the specimens. Figure 5.7 (a) to (d) show the horizontal and vertical sections of the pluviated specimens made of glass ballotini, LB sand B, glass nuggets and coarse glitter.

As expected, the comparison of corresponding horizontal and vertical CT slices of the pluviated samples reveal the increased packing anisotropy with decreasing SEES (Figures 5.7 (a) to (d)). An increase in e_{min} with decreasing SEES would be mainly due to small bridge-like openings in face-to-face arrangements of particles (e.g. see vertical slice of Figure 5.7(d)). Whereas in maximum void ratio tests, low SEES particles tend to pack themselves in random orientations and form large openings (like open card-house structures) which in turn increases the maximum void ratio greatly with decreasing SEES.

5.4 Triaxial compression tests using free-ends

Triaxial compression tests were carried out on cylindrical specimens (of 100mm diameter) incorporating free-ends in order to impose uniform stress and strain conditions. The details of the free-ends adopted in this research were discussed in Section 5.1.2. It is usual to carry out tests on 1:1 (height-to-diameter ratio) specimens when free-ends are used. However, a height-to-diameter ratio of 1.3:1 was adopted in this research to provide enough room for the local strain instrumentation.

5.4.1 Specimen preparation and setup

De-aeration of back pressure line

At first, the back pressure line was thoroughly flushed with de-aired water at high pressure to ensure that no air was trapped inside the tubing system as well as the porous stone. Then the back pressure line was closed and the water surrounding the porous stone was wiped off using paper towels.

Problems with the accidental fall of particles into the Bishop and Wesley cell

While preparing (or dismantling) the test specimens in Bishop and Wesley triaxial cell, Xu (2005) identified the problems with the accidental fall of particles into the annular space around the base pedestal and jamming the ram. He found it very difficult and time-consuming to remove those particles since the gap is very narrow and deep. To overcome this problem, the annular space around the base pedestal of the cell chamber was fully covered using a sample membrane cut along its length and with a small circular hole at its centre (to wrap around base pedestal and seal it completely), as shown in Figure 5.8. The particles that fell on the membrane cover (while preparing/dismantling the specimen) were blown-off using compressed air.

Preparation of frictionless ends

Six latex discs (~120mm diameter) were cut out of 100mm diameter sample membrane, to make two sets of lubricated membranes. Three discs were used for each end platen, as discussed in Section 5.1.2. Small circular holes were made at the centers of three of the discs, to uncover the porous stone portion (for free drainage) in the bottom platen (see Figure 5.8).

A thin smear of silicone grease was applied to the loading face of the bottom platen with the help of a smooth edged ruler, avoiding the porous stone portion. One of the latex discs with a circular hole at its centre was then placed on top of the grease layer, and the entrapped-air removed by gently pressing and stretching the latex disc against the platen towards its outer periphery using a smooth edged ruler. Two more layers of grease and latex discs were then added to the bottom platen in a similar fashion. These three layers of grease and latex discs are referred as a 'lubricated membrane'. Similarly, another set of lubricated membranes (without circular holes at their centers) were prepared for the top platen on its loading face.

Markings on the membrane

The specimen membrane was then marked for the positions of the top and bottom platens circumferences, the top and bottom of the specimen's circumferences, the gauge length (~50mm in this case) and the Hall-effect gauges clips.

Assembling the special sliding type 6-part split mould

Then, the six-part sliding type split mould was assembled, sealed all the joints using a plastic tape (to minimise leakages while applying suction later on) and clamped. The sample membrane was then stretched and wrapped around the top and bottom ends of the mould as per the marked circumferences on the membrane. The ends were then sealed using O-rings (100mm dia, two on each side) to facilitate the application of suction. The same sets of O-rings were later used to seal the top and bottom ends of the specimen after preparation. A small amount of suction (~15kPa) was then applied to the mould through the tube located at its mid-height, to firmly hold the membrane against mould and avoid formation of wrinkles. The split mould with the membrane wrapped around at its ends was then placed on top of the lubricated membranes of bottom platen aligning the mould's outer diameter inline with the platen's.

Pluviation of material into the mould

The pluviation device was then placed on top of the split mould aligning their internal diameters. A pre-determined amount of the material was poured into the hopper of the pluviation device which was then delivered into a series of diffuser meshes through a funnel and then rained into the mould uniformly over its area through the guide tube (see Figure 5.5). When whole material was rained, the pluviation device was gently lifted and removed from the mould. The excess material was then removed and the specimen's surface levelled using the smooth-edged ruler (Figure 5.9).

Loss of material while levelling the specimen's surface and associated problems

While levelling the specimen's surface, it was found that much of the material was lost in the case of coarse rotund particles (e.g. LB sand fraction B) resulting in much less number of particles being in contact with the top platen (when compared with the bottom platen), which ultimately lead to non-uniform densities at the specimen ends. When these kinds of specimens were sheared, they started to bulge at the bottom. This could be because, at the start of shearing, the bottom portion of the sample was denser than the top portion (especially at the ends), therefore bottom portion started to dilate whilst the top portion contracted until the establishment of strong force networks at the initial stages of shearing. Consequently, the bottom portion continued to dilate (since it became weak after initial dilation) until the end of test whereas the top portion acted as a dead zone, which ultimately resulted in non-uniform stress and strain conditions even with the frictionless ends. Therefore, to overcome this problem, an extra amount of material was spread uniformly over the top surface of the specimen to account for the lost material while leveling the surface. Specimens prepared in this way deformed uniformly either throughout the height or at the sample ends. Therefore, this procedure was followed for all the specimens.

Flushing the sample with de-aired water and closing the sample

The bottom end of the membrane was then unwrapped from the mould onto the bottom platen and sealed using two O-rings by directly slipping them down from the mould (Figure 5.9). The specimen was then flushed with the de-aired water from the reservoir through the backpressure line under constant low head (approx. 1.5m). A small collar ring (of diameter slightly larger than the internal diameter of the mould) was placed on top of the mould to avoid overflowing of particles along with the water.

The over-flowing water was routed into the cell and then subsequently drained-off. Flushing was continued until the over-flowing water amounted to approximately four times the specimen's volume. The back pressure line from the reservoir was then closed, and the top surface of the mould wiped off. The top platen (together with the lubricated membranes) was then placed on the top of the mould. The top end of the membrane was then unwrapped onto the top platen by firmly pressing the platen against the mould minimizing the gap between mould and the platen. The top end of the specimen was then sealed using two O-rings, which were simply slipped onto the platen from around the mould while the platen was being pressed down.

Removal of the special sliding type 6-part split mould

A suction pressure of -15kPa was applied to the specimen through the back pressure line using the GDS controller in order to make the sample self-supporting. After achieving the targeted suction pressure, the mould was removed without disturbing the specimen by first sliding the top three parts and then lifting the bottom three parts, slowly one-by-one. The Hall-effect gauges were then glued on to the specimen at the pre-marked positions. Figure 5.10 shows a photograph of the prepared specimen together with the Hall-effect gauges for local strain measurements.

Isotropic compression and shearing

The ram was lowered to its extreme downward position by slowly draining the water out of the base chamber. The cell chamber was then closed and the load cell was lowered until it reached close to the top platen. The purpose of lowering the ram to its extreme downward position and load cell close to the sample top platen, was to utilize the whole ram movement while shearing the sample after isotropic compression stage. The cell chamber was then completely filled with the de-aired water. After filling, the pressure inside the cell chamber was approximately equal to 15kPa and the back pressure was -15kPa, therefore the effective stress was around 30kPa. Both the cell and the back pressures were then simultaneously increased to the target values (i.e. σ_{cell} = 280kPa and σ_{back} = 250kPa in this case) in small increments (i.e. 5kPa) in order to keep the effective stress as constant as possible, by the corresponding GDS controllers via a computer program written in Visual Basic 6.0. The specimen was then left at these pressures for a day, to help dissolve the air bubbles into water. Then the cell pressure was increased to 350kPa to impose an effective stress of 100kPa. At these pressures, the B-value was found to be a minimum of 0.96 in all the tests. The specimen was then compressed at a constant strain rate of approximately 2% per hour under constant cell and back pressures of 350kPa and 250kPa respectively.

A computer program (using Visual Basic 6.0) was developed and used to perform the drained shear test and log the data from various measuring devices at every 10sec automatically. Tests were continued up to an axial strain of around 22%. Same procedure was followed for all the tests.

5.4.2 Definitions of various parameters

Vertical effective stress (σ'_1)

$$\sigma'_1 = \frac{Q(1-\varepsilon_a)}{A_0(1-\varepsilon_v)} + \sigma'_3 \tag{5.1}$$

Principal stress ratio (R)

$$R = \frac{\sigma'_1}{\sigma'_3} \tag{5.2}$$

Peak angle of friction (ϕ_{peak})

$$\phi_{peak} = \frac{(\sigma'_1/\sigma'_3)_{peak} - 1}{(\sigma'_1/\sigma'_3)_{peak} + 1} \tag{5.3}$$

Maximum dilatancy factor (D_{max})

$$D_{\max} = 1 - \left(\frac{d\varepsilon_v}{d\varepsilon_1}\right)_{\max} \tag{5.4}$$

D_{max} *using Bolton's empirical equation (Bolton, 1986)*

$$D_{\max} = 1 + 0.3\left[D_r\left(10 - \ln p'\right) - 1\right] \tag{5.5}$$

Secant stiffness

$$E'_{\text{sec}} = \frac{\sigma'_1 - \sigma'_3}{\varepsilon_a} \tag{5.6}$$

5.4.3 Effect of form on shear behaviour

All the specimens were prepared by the air pluviation technique. The height of fall was kept sufficiently high to ensure uniform density with the rising surface of the specimen. The relative densities of the tested specimens ranged between 82 % and 93% (Table 5.4), and were considered to be dense and effectively identical. The one and only variable parameter in all these tests was particle shape; and therefore any differences that were observed in the behaviour could be attributed to the particle shape alone. The samples were sheared by increasing the vertical stress (i.e. the stress in the direction of deposition) under a constant effective confining pressure of 100kPa.

The following observations can be made from the results of the triaxial compression tests which were carried out on a range of materials (comprising spherical to platy particles) in their dense states:

- Figures 5.11(a) & (b) indicate that the stiffness, peak strength and the strain to reach peak state or failure, ultimate strength and the strain to reach ultimate state, and the rate of dilation are all highly dependent on the form of the constituent particles.

- All the tests (except coarse glitter) were stopped at an axial strain (external) of around 22% (approx.) because of the limited movement of the ram in Bishop and Wesley triaxial apparatus. However, in the case of test on coarse glitter the membrane got punctured at around 19% axial strain, therefore the test data after that point was discarded. It can be seen from Figure 5.11(a) that except coarse glitter all the other materials (namely, glass ballotini, LB sand B, nuggets and fine glitter) had reached peak state within this limited axial strain whereas the coarse glitter needed further axial straining to reach the peak or failure state. Therefore, the data points of the coarse glitter shown later in Figures 5.19, 5.20 and 5.23 do not correspond to the peak but the termination stage of the test. However, the end points of the corresponding 'small arrow heads' represent the expected positions of those data points, if the test on coarse glitter was continued until the peak state or further more.

- Figures 5.12 (a) to (c), respectively, shows the deformed shape of the specimens (glass ballotini, glass nuggets and fine glitter) at the end of shearing (i.e. ≈22% axial strain). Comparison of the three figures gives an impression that sample barrelling/bulging is a function of shape of constituting particles. The fine glitter sample deformed uniformly throughout its height (Figure 5.12(c)) whereas the glass ballotini specimen barrelled quite significantly (Figure 5.12(a)). Sample barrelling seems to be inevitable in the case of rotund particles even if free ends are used. Close observation of these figures reveal that sample barrelling decreases with decreasing form (SEES).

- Figure 5.13 shows the comparison of external and local strain measurements corresponding to different materials tested. It can be clearly seen from the figure that external strain was always higher than the local strain, in all the samples. When the external strain was 10% the local strain was 8.5% in the case of coarse glitter and 5.5% in the case of glass ballotini. This meant that the local strain was 15% lower in the case of coarse glitter and 45% lower in the case of glass ballotini. Other results fell in between these two extremes in accordance with their form. This huge difference may have resulted from the combination of error sources such as the compliance of the loading system (Jardine et al., 1984, Clayton and Khatrush, 1986), and bedding errors associated with free ends as discussed in Section 2.8. There were also errors associated with local strain measurement (especially when the sample barrelled) because of tilting of the Hall-effect gauges. This leads to an underestimation of local strains but only at large strains. The large difference between local and external strains in the case of glass ballotini (especially at the higher levels of strain, see Figure 5.13) could be attributed to barrelling, see Figure 5.12(a).

- *Secant stiffness*

Figure 5.14 shows the variation of secant stiffness with local axial strain for four of the materials tested. The Figure indicates that secant stiffness is highly dependent on particle shape, and its effect seems to be more pronounced at small strains than at large strains. Among the materials shown in figure, the small strain stiffness was highest in glass ballotini (rotund) and least in glitter (platy). The Figures also suggests that the stiffness degradation may well be a function of particle shape. Stiffness degradation was highest in glass ballotini (rotund) and least in glitter (platy) whereas others fell in between these two in accordance with their form.

Figure 5.15 shows the variation of secant stiffness at 0.1% strain with form (SEES). Secant stiffness was found to decrease with decreasing SEES. The secant stiffness of glass ballotini was five times higher than that of coarse glitter. It should be noted that in the current study all the samples were tested in their dense states. The effect of SEES on stiffness would be much more significant if tested in their loose states because of excessive sliding of particles.

- *Onset of dilation*

The axial strain, volumetric strain and the mobilised friction at the onset of dilation (at which the volumetric behaviour changes from contractive to dilative), increased with decreasing SEES (see Figures 5.16 to 5.18).

- *Peak state*

The peak angle of friction (determined using Mohr-Coulomb failure criterion i.e. equation 5.3) and the strain to reach peak (or failure) state were found to increase with decreasing SEES (see Figures 5.19 and 5.20).

- *Ultimate state*

Comparison of stress ratio versus axial strain curves of Glass ballotini, LB sand B, glass nuggets and fine glitter in Figure 5.11(a) give the impression that the ultimate strength and strain to reach the ultimate state might increase enormously as the materials tend to become platy.

- *Dilatancy*

Figure 5.21(a) indicates that the initial relative density was high (~90%) in all the samples and that decreased as shear progressed (since the samples dilated) and was consistent in all the samples except coarse glitter, but at different rates. The maximum rate of decrease of relative density with respect to axial strain was highest in glass ballotini and least (in fact the trend was reversed leading to contraction instead of dilation) in coarse glitter. Other materials fell in between in accordance with their form.

Figure 5.21(b) shows the difference in relative density between the start and the end of shearing in relation to SEES. A clear trend of decreasing dilation with decreasing SEES is evident from this figure. Although initial relative densities were quite high and almost identical, towards the end of shearing the glass ballotini dilated and became 30% (approx.) looser than the initial state whilst the coarse glitter contracted and became 5% denser than the initial state.

The maximum dilatancy factor (determined using equation 5.4) was found to decrease with decreasing SEES (see Figure 5.22(a)) and to approach unity in the case of extremely platy material.

The maximum rate of volumetric strain with respect to shear strain (Figure 5.22(b)) decreased with decreasing SEES and approached zero in the case of extremely platy material.

Bolton's empirical equation for predicting the rate of dilatancy (based on initial relative density and mean effective stress at failure, equation 5.5) seemed to be applicable only for rotund (or high SEES) particles and overestimated dilatancy in the case of low SEES particles (Figure 5.23).

- *Particle breakage*

The comparison of PSD curves before and after testing shown in Figures 5.24 (a) to (c) revealed that significant particle breakage and/or crushing was observed in the case of glass nuggets, fine glitter and coarse glitter. Therefore, particle breakage was quantified using the widely accepted Hardin's relative breakage parameter, the definition of which is illustrated in Figure 5.25. The relative breakage has a lower limit of zero and theoretical upper limit of unity. Relative breakage was found to increase with decreasing SEES (Figure 5.26).

5.5 Summary

- A special sliding type six-part split mould was developed in this research to ease the sample preparation with enlarged lubricated end platens.

- A simple air-pluviation device was developed to prepare 100mm diameter samples directly on the triaxial apparatus.

- The base pedestal and top cap of the Bishop and Wesley triaxial apparatus were modified to incorporate enlarged end platens.

- The CT scanning technique has been successfully used, for the first time, to visually examine the orientations of particles in the pluviated samples.

- The maximum and minimum void ratios, void ratio range, and packing anisotropy (in dense state) were found to increase with decreasing SEES of particles.

- In initially dense materials:
    - Sample barrelling is inevitable in the case of rotund particles even if free ends are used. It decreases with decreasing SEES. Local strain measurements underestimate the strain if the sample barrels.
    - The external strain measurements overestimate the strain significantly although this decreases with decreasing SEES.
    - The secant stiffness at small strains and its degradation is highly dependent on particle shape. Both small strain stiffness and the rate of degradation decreases with decreasing SEES.
    - The axial strain, volumetric strain and mobilised friction at the onset of dilation increases with decreasing SEES.

- The peak strength and strain to reach peak state increases with decreasing SEES.
- The ultimate strength and strain to reach the ultimate state increases with decreasing SEES.
- The maximum rate of decrease of relative density with respect to axial strain (i.e. a measure of maximum rate of dilation) decreases with decreasing SEES.
- The difference in relative density (between the start and end of shearing) decreases with decreasing SEES, and becomes negative (i.e. contractive) in extremely platy material.
- The maximum dilatancy factor decreases with decreasing SEES and may approach unity in case of extremely platy material.
- The maximum rate of volumetric strain with respect to shear strain decreases with decreasing SEES and may approach zero in the case of extremely platy material.
- Bolton's empirical equation overestimates the rate of dilatancy in case of materials comprising low SEES particles.
- Particle breakage increases with decreasing SEES.

Table 5.1: Calibration results of the measuring devices used

Measuring device	Measurement	Supplier	Serial No.	Design range	Calibration range	Resolution	Accuracy	Accuracy Calibration range (%)
Load cell	Axial load (internal)	GDS	805030	16kN	3.6kN	0.948N	±0.983N	±0.03
					7.2kN	1.845N	±3.383N	±0.05
					14.4kN	3.634N	±9.474N	±0.07
Pressure transducer	Cell pressure	Druck	1239787	1000kPa	900kPa	0.431kPa	±0.606kPa	±0.07
Pressure transducer	Pore pressure	Druck	1239783	1000kPa	900kPa	0.430kPa	±1.226kPa	±0.14
Pressure transducer	Lower chamber pressure	Druck	1239782	1000kPa	900kPa	0.429kPa	±1.462kPa	±0.16
LDC	Axial displacement (external)	RDP	98490	50mm	50mm	13.689μm	±152.128μm	±0.30
LDC	Axial displacement (external)	RDP	98491	50mm	50mm	13.539μm	±68.945μm	±0.14
Hall-effect gauge	Axial displacement (local)	University of Surrey, UK	CSR61 & 396-2	7mm	7mm	2.798μm	±56.691μm	±0.81
Hall-effect gauge	Axial displacement (local)	University of Surrey, UK	CSR66 & 397-1	7mm	7mm	2.619μm	±81.347μm	±1.16

Table 5.2: Average form and roundness of the materials

Material	Form (SEES)	Roundness $\left(\sqrt{\frac{P^2}{4\pi A}}\right)$
Glass ballotini	1.000	1.043
LB sand B	0.533	1.224
Glass nuggets	0.214	1.419
Fine glitter	0.134	1.480
Coarse glitter	0.112	1.435

Table 5.3: Maximum and minimum void ratios, and void ratio range

Material	e_{max}	e_{min}	e_{max}-e_{min}
Glass ballotini	0.6750	0.5290	0.1460
LB sand B	0.7881	0.4635	0.3246
Glass nuggets	1.2363	0.7427	0.4936
Fine glitter	1.2091	0.6799	0.5292
Coarse glitter	1.3573	0.7260	0.6313

Table 5.4: Initial states of the specimens

Material	e	D_r (%)
Glass ballotini	0.55	83
LB sand B	0.50	88
Glass nuggets	0.78	93
Fine glitter	0.77	82
Coarse glitter	0.80	87

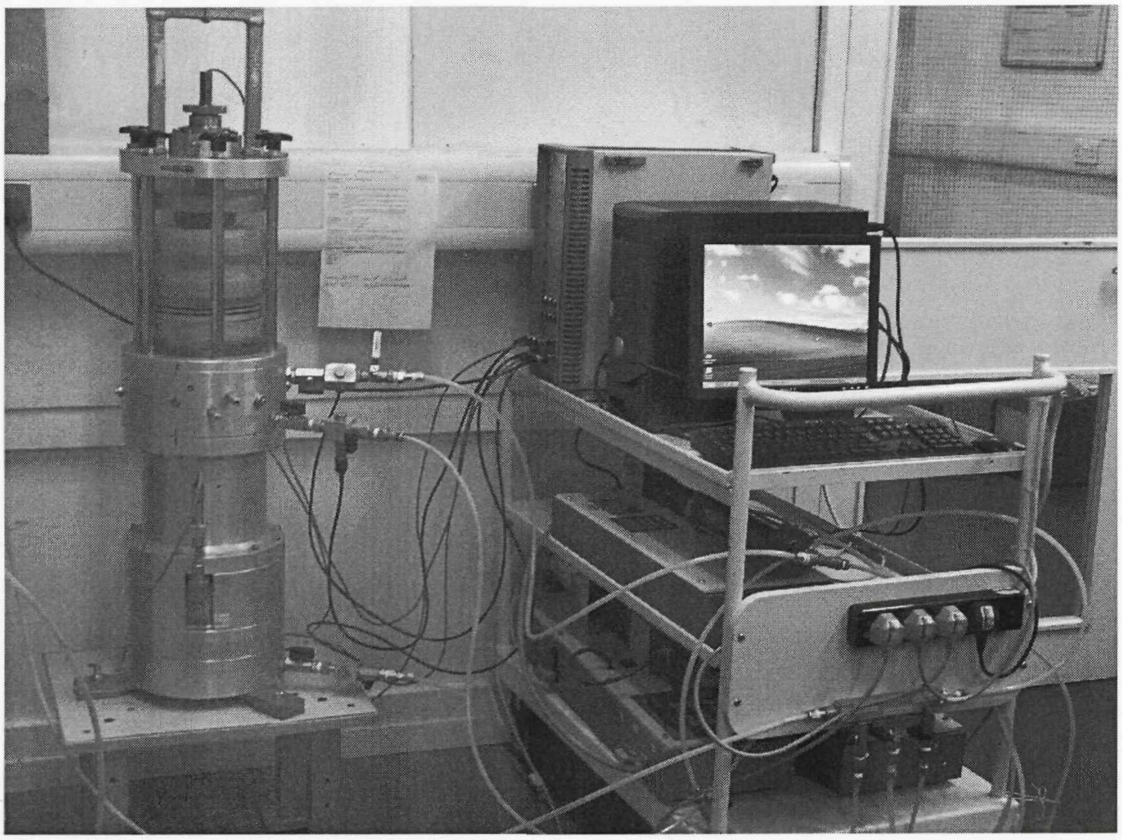

Figure 5.1: Photograph of the triaxial testing system used in this research

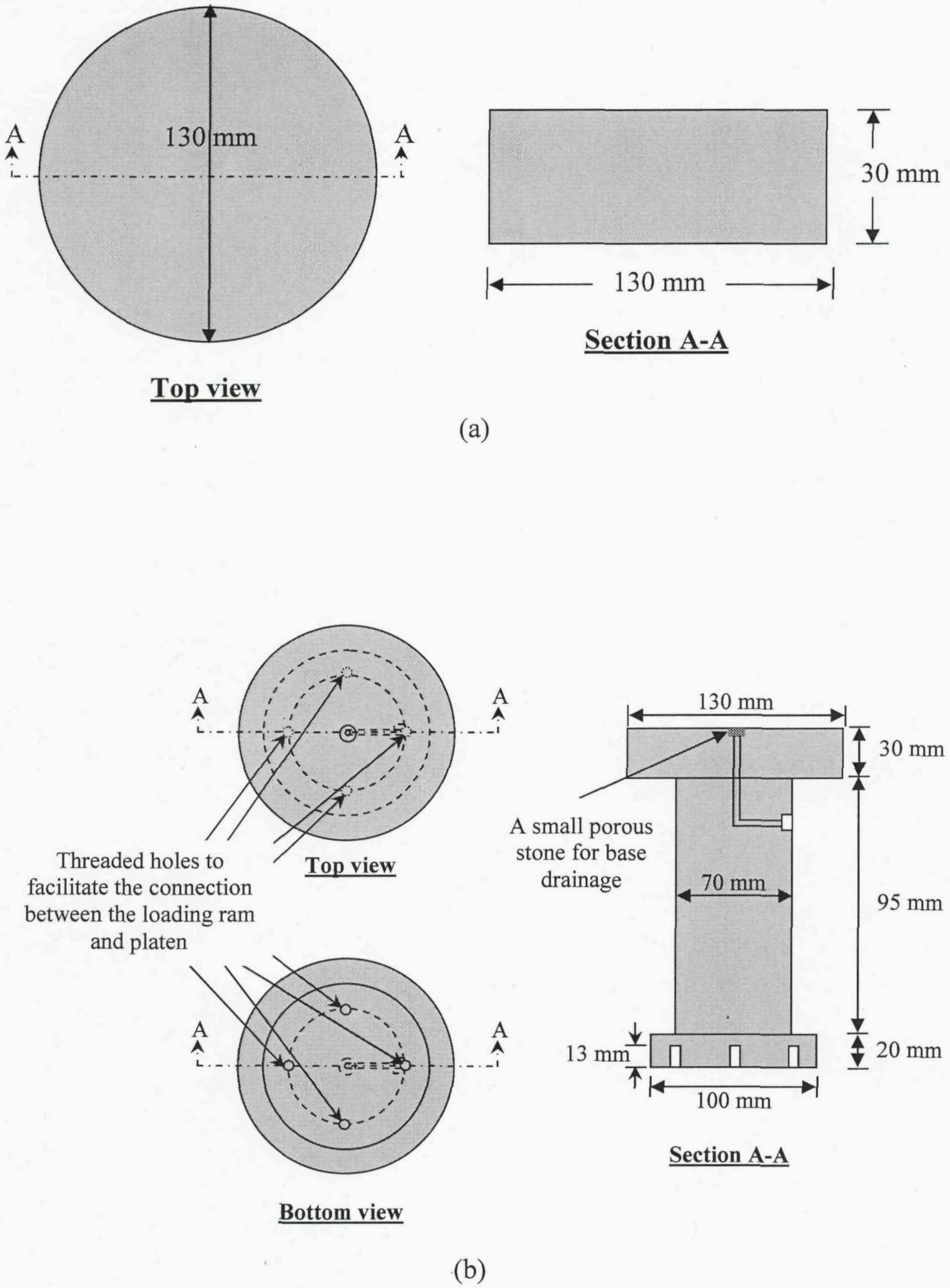

Figure 5.2: Schematic diagram of the enlarged top (a) and bottom (b) end platens for 100mm diameter specimens

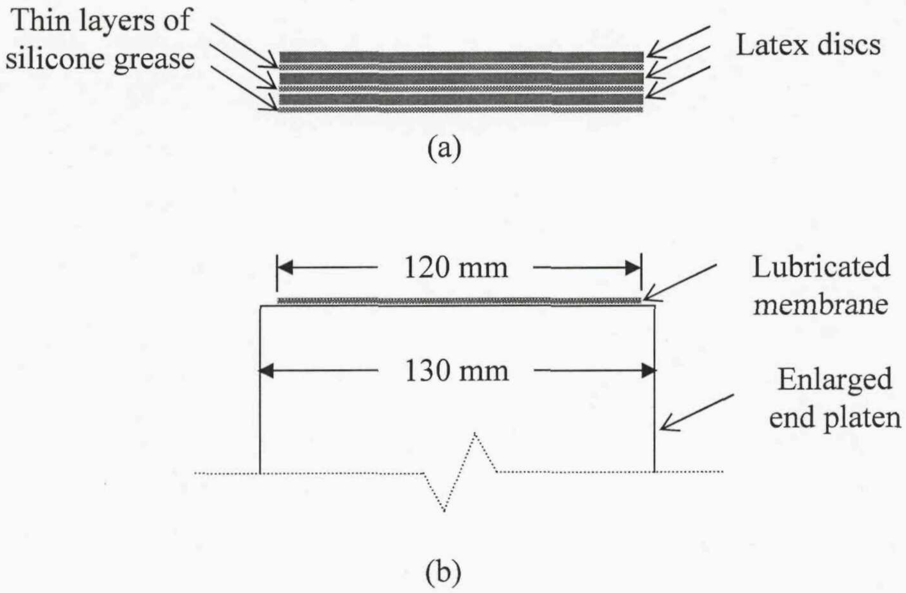

Figure 5.3: Schematic diagram of the layering details of the lubricated membranes (a) and its arrangement on the platen's loading face (b).

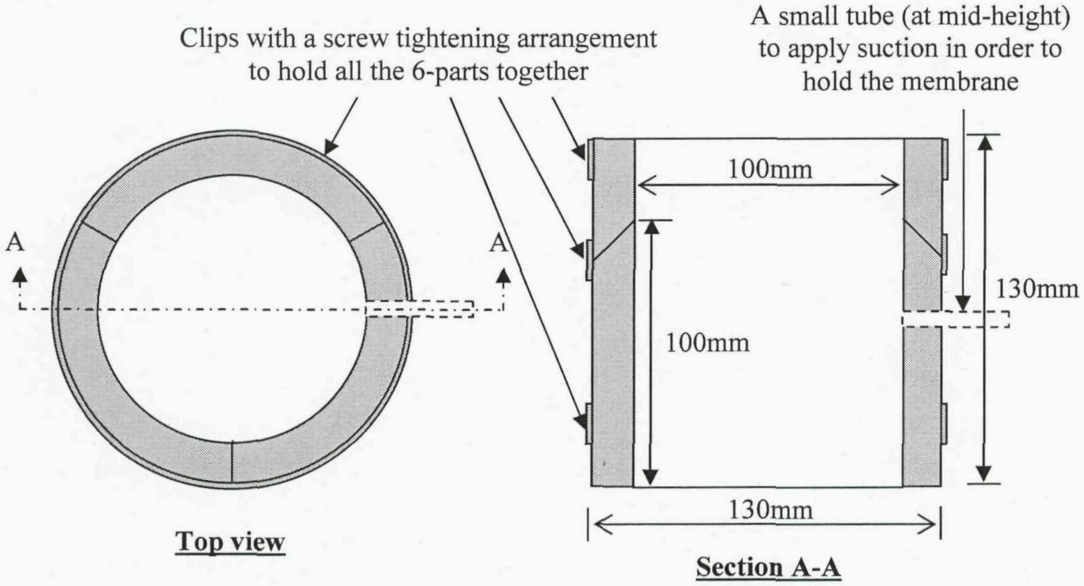

Figure 5.4: Schematic diagram of the 6-part split mould specially designed for enlarged end platens

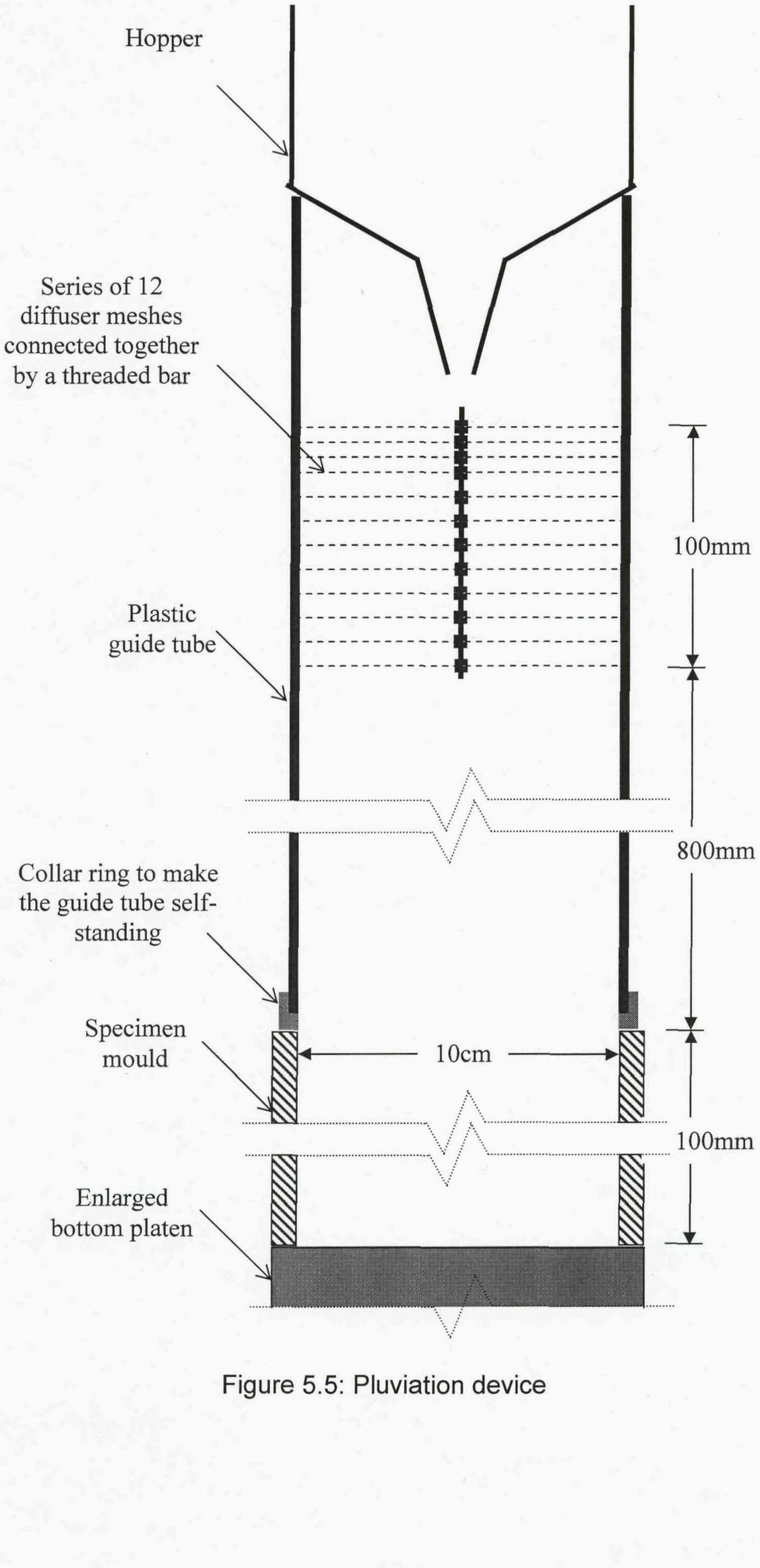

Figure 5.5: Pluviation device

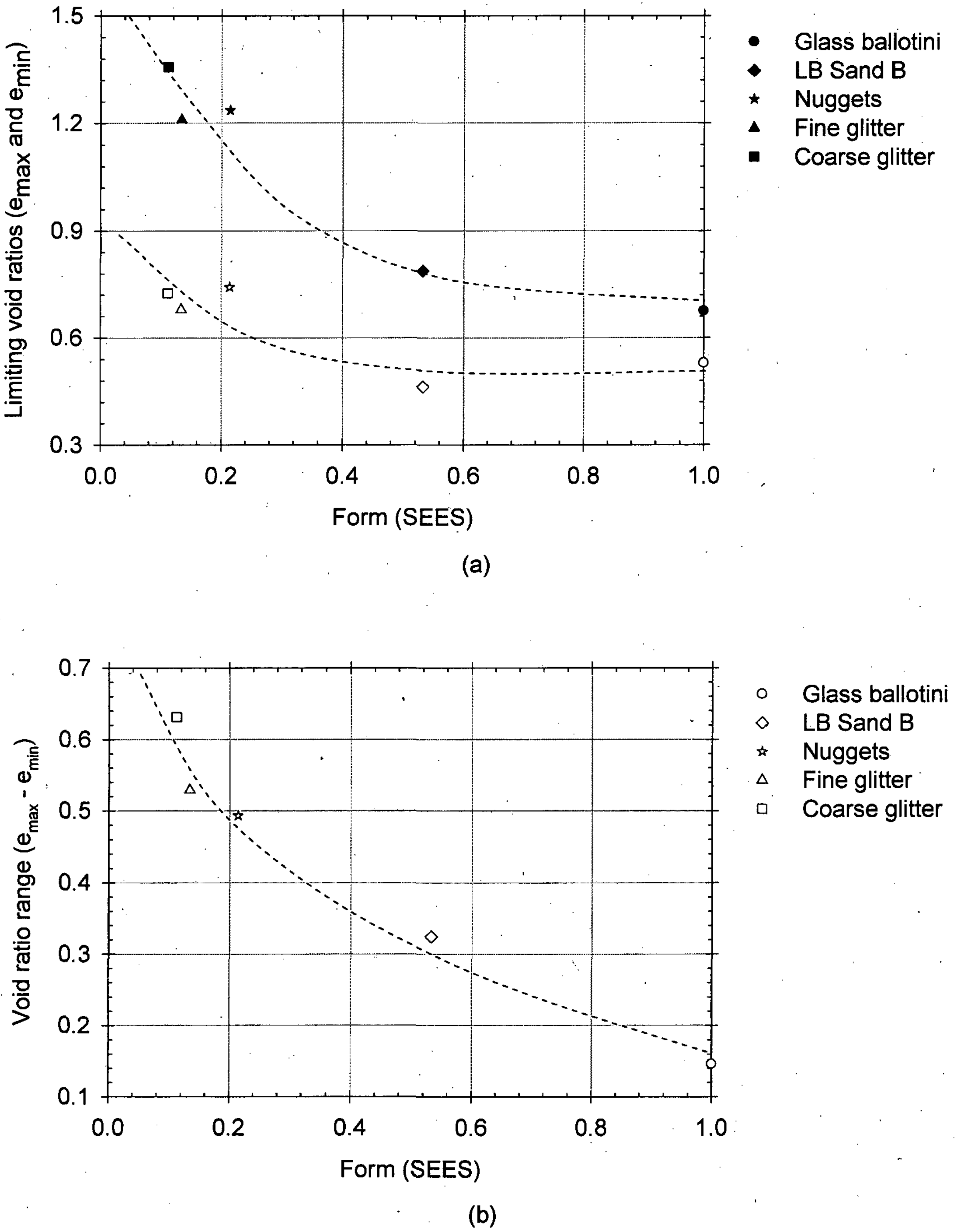

Figure 5.6: Limiting void ratios (a) and void ratio range (b) as a function of SEES

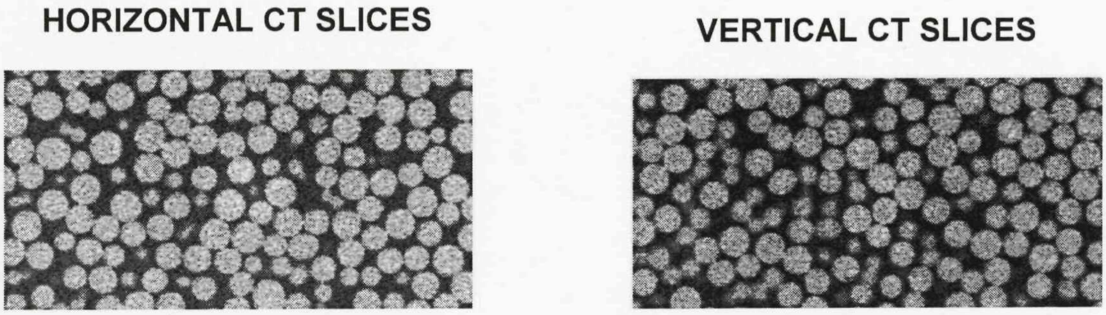

(a) Glass Ballotini: SEES = 1.000

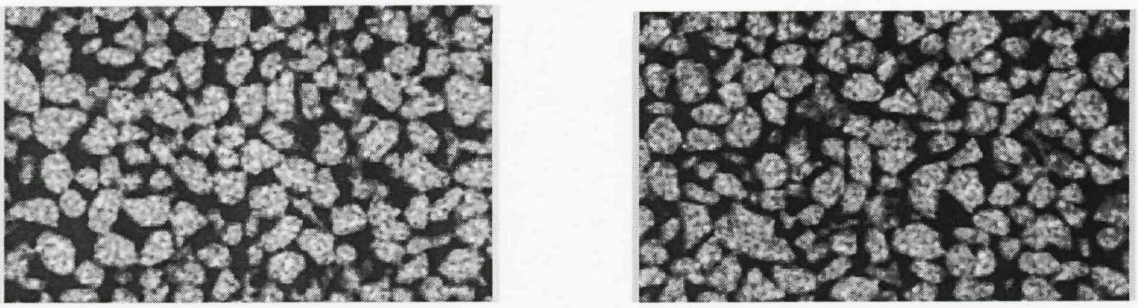

(b) L B Sand B: SEES = 0.533

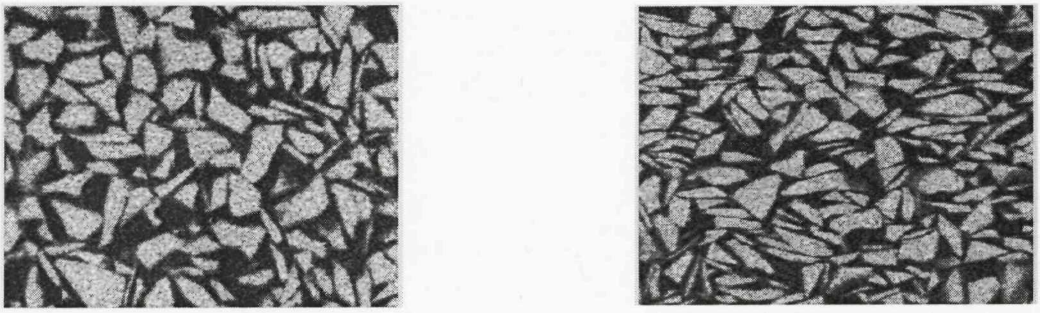

(c) Nuggets: SEES = 0.214

(d) Glitter: SEES = 0.112

Note: Mean grain size ~ 1.0mm (sieve)

Figure 5.7: Evolution of inherent anisotropy with respect to form (SEES) in air-pluviated samples.

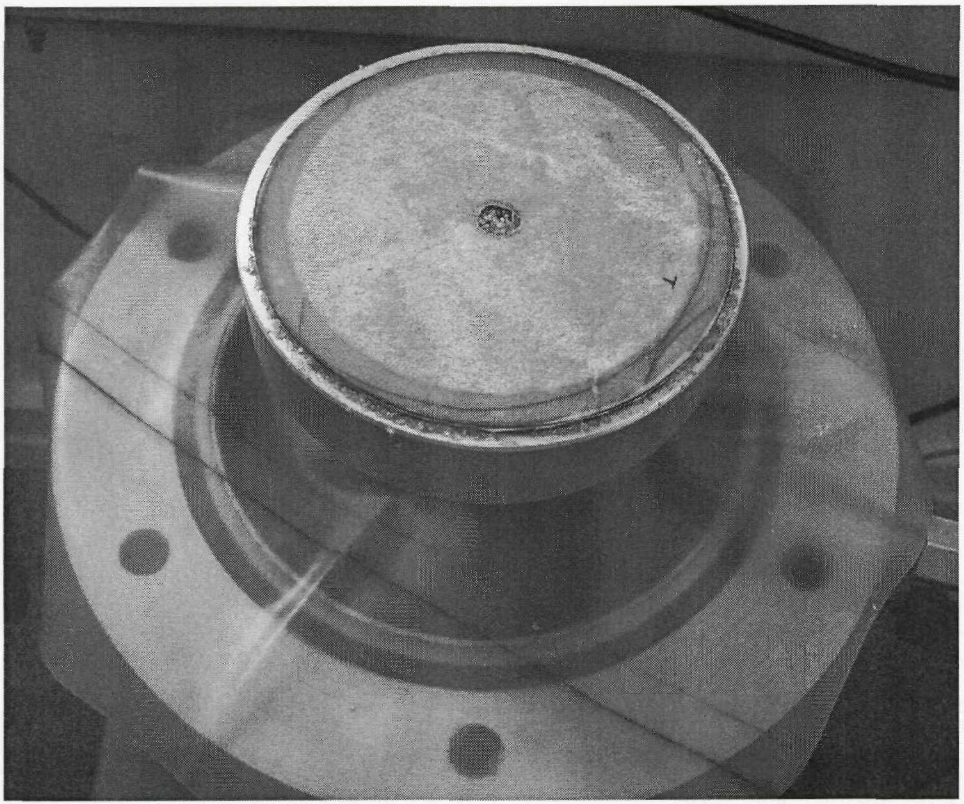
Figure 5.8: A photograph showing an arrangement to avoid accidental fall of particles into the annular space while preparing/dismantling the specimen

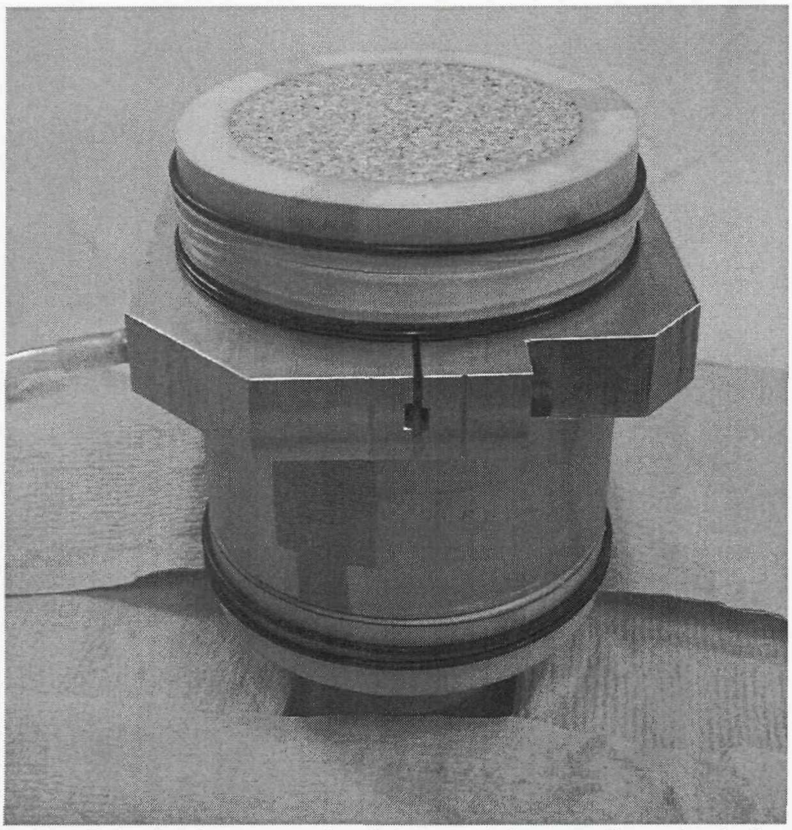
Figure 5.9: A photograph of the specimen after pluviation.

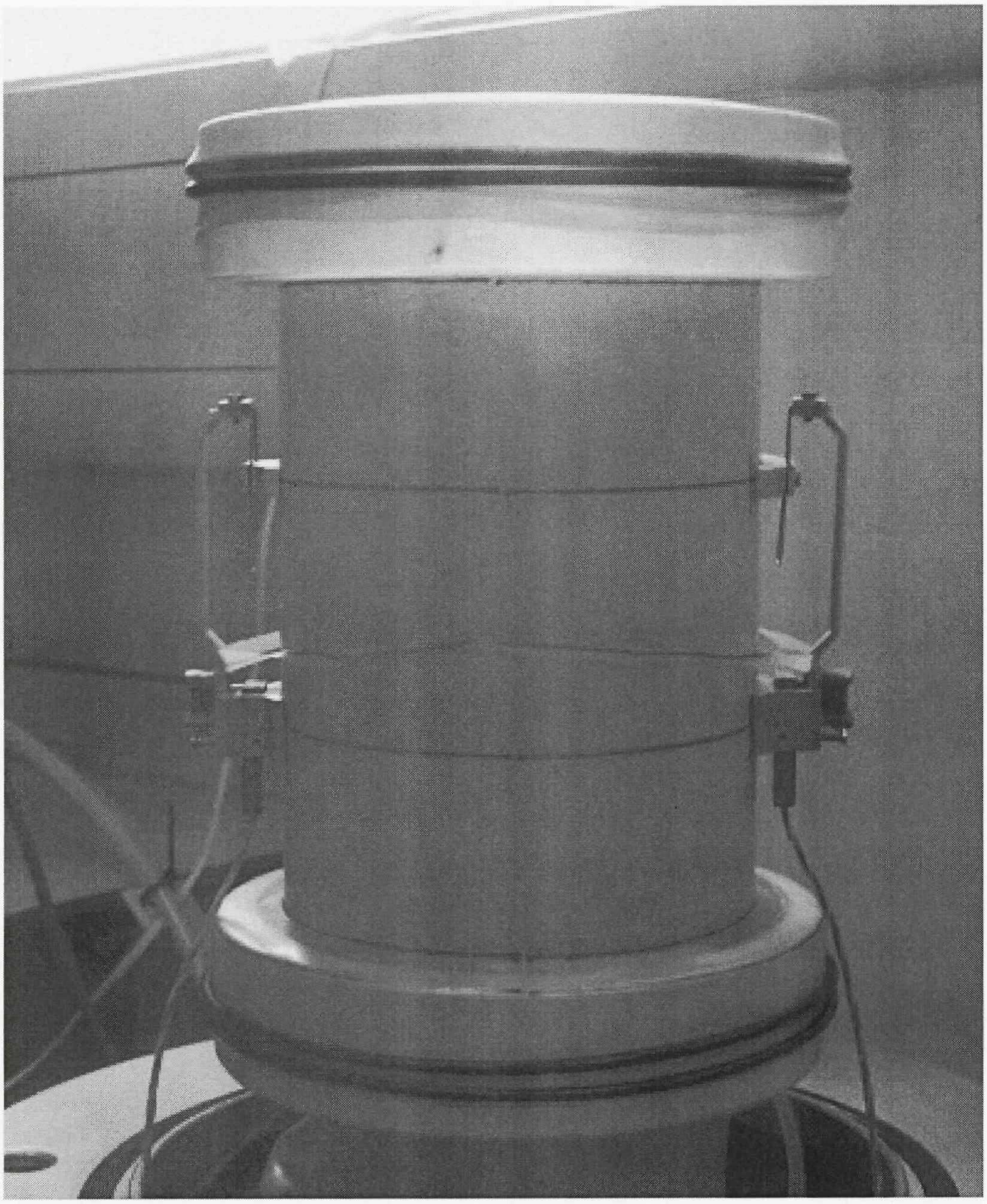

Figure 5.10: A photograph of the specimen (after preparation) with Hall-effect gauges in place for local strain measurements.

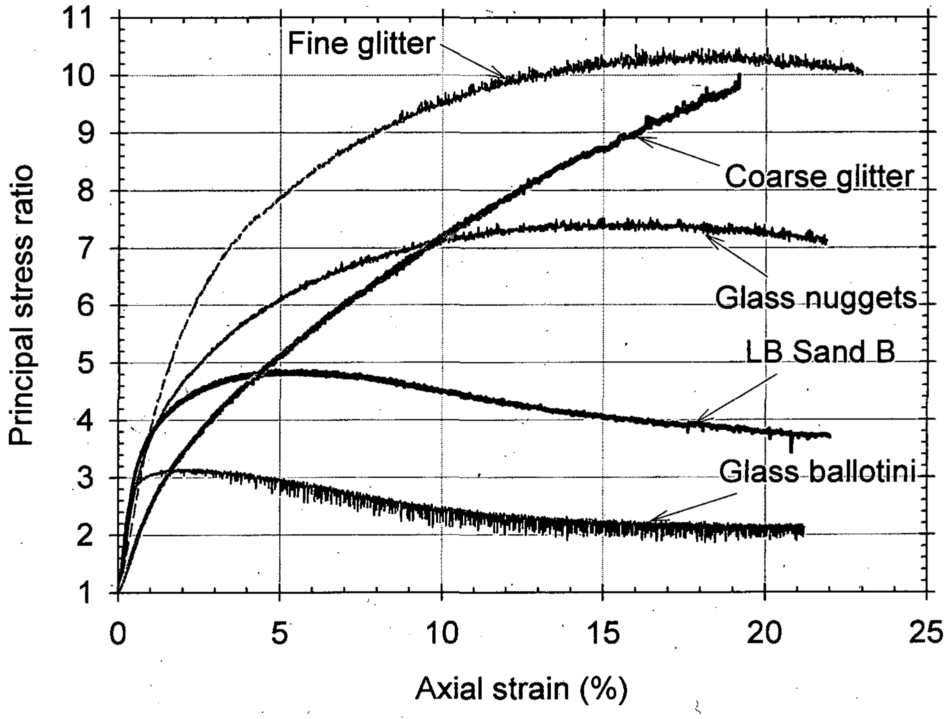

(a)

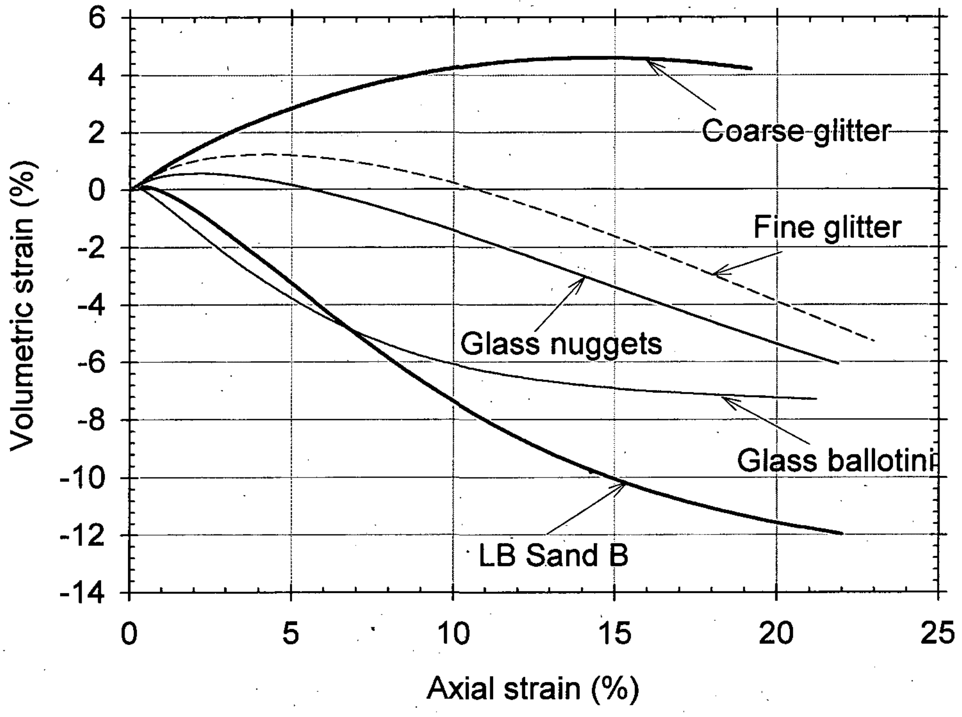

(b)

Figure 5.11: Variation of principal stress ratio (a) and volumetric strain (b) with axial strain, of all the materials.

(a) Glass ballotini
SEES = 1.000

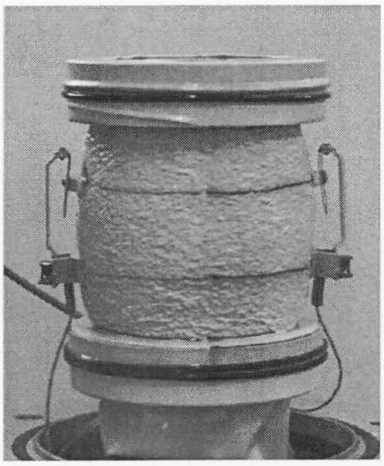

(b) Glass nuggets
SEES = 0.214

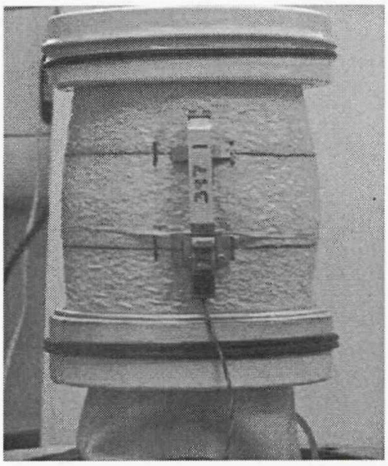

(c) Fine glitter
SEES = 0.134

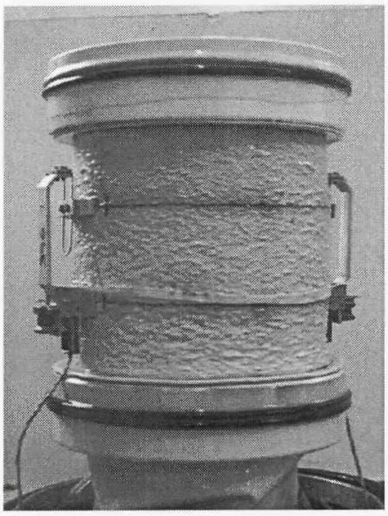

Figure 5.12: Deformed shape of specimens at the end of shearing
(i.e. 22% axial strain)

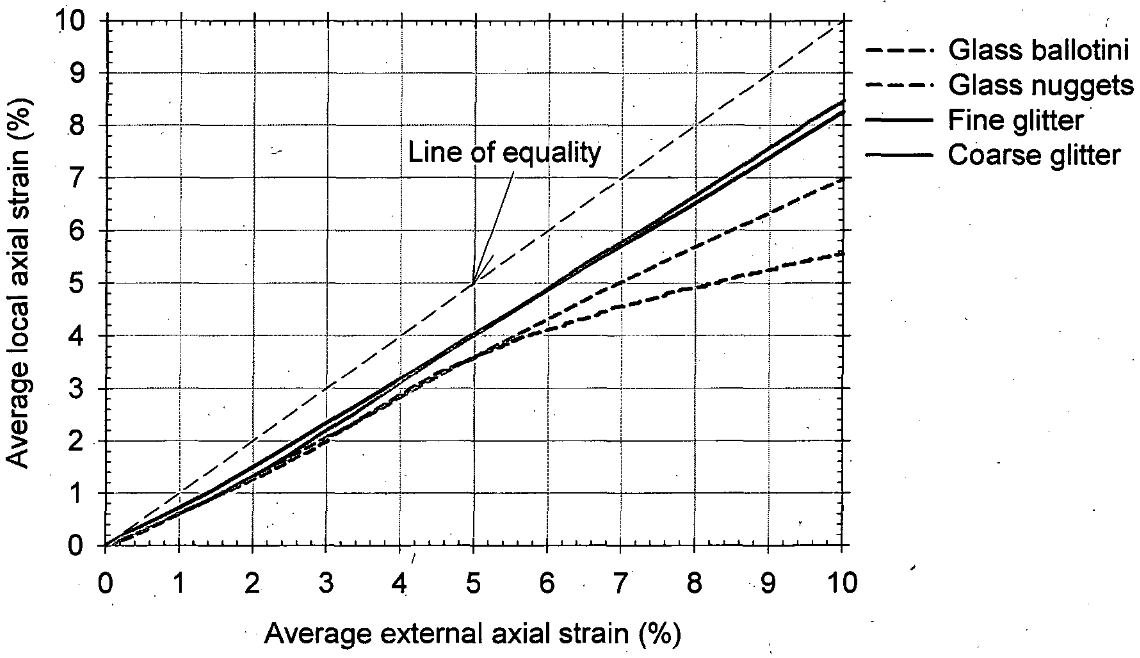

Figure 5.13: Comparison of external and local strain measurements

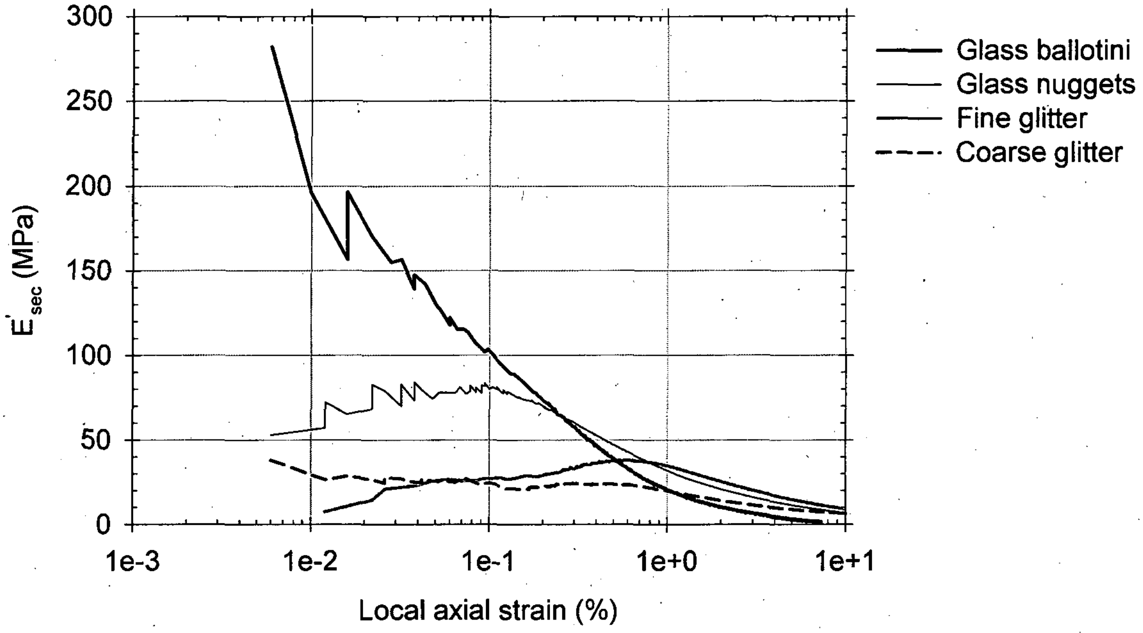

Figure 5.14: Variation of secant stiffness with local strain for different materials

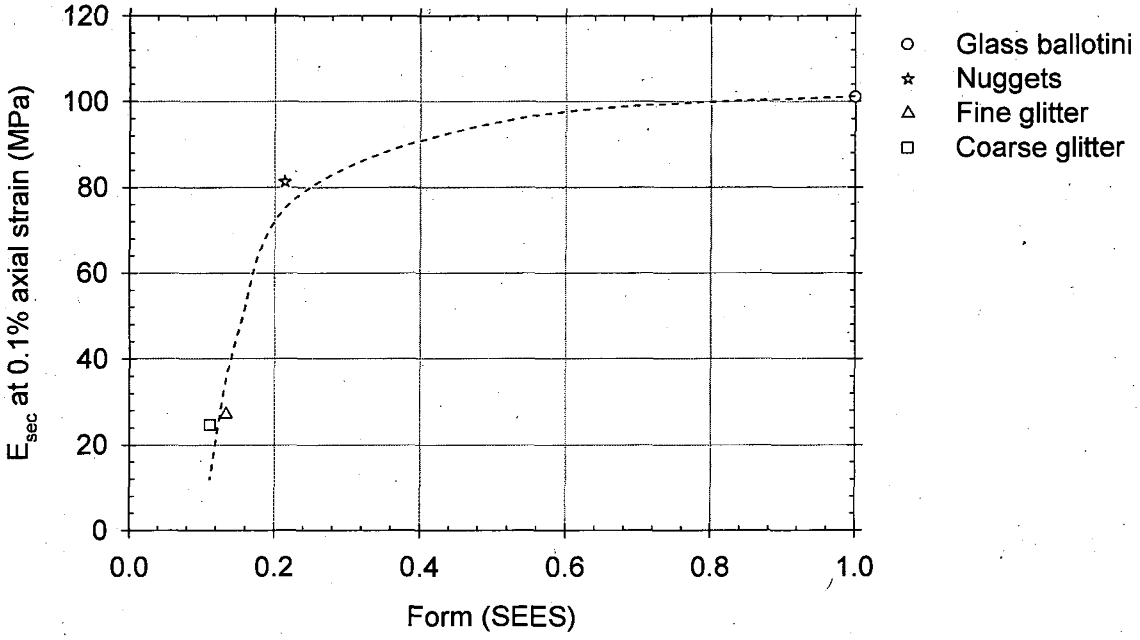

Figure 5.15: Variation of E'_{sec} at 0.1 % axial strain with SEES

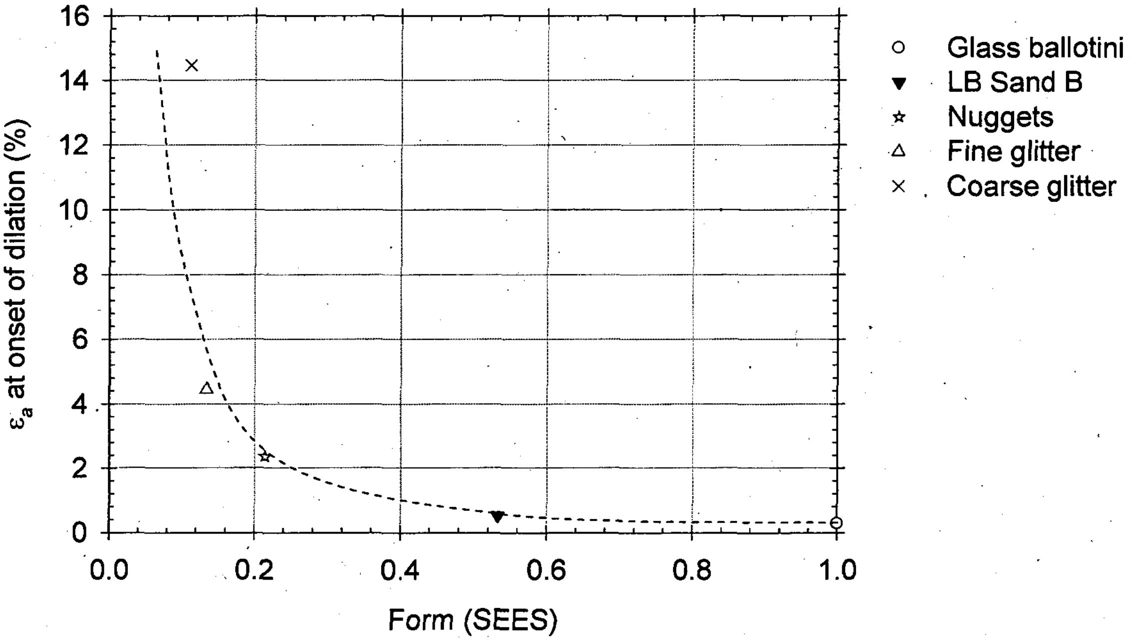

Figure 5.16: Variation of axial strain at onset of dilation with SEES

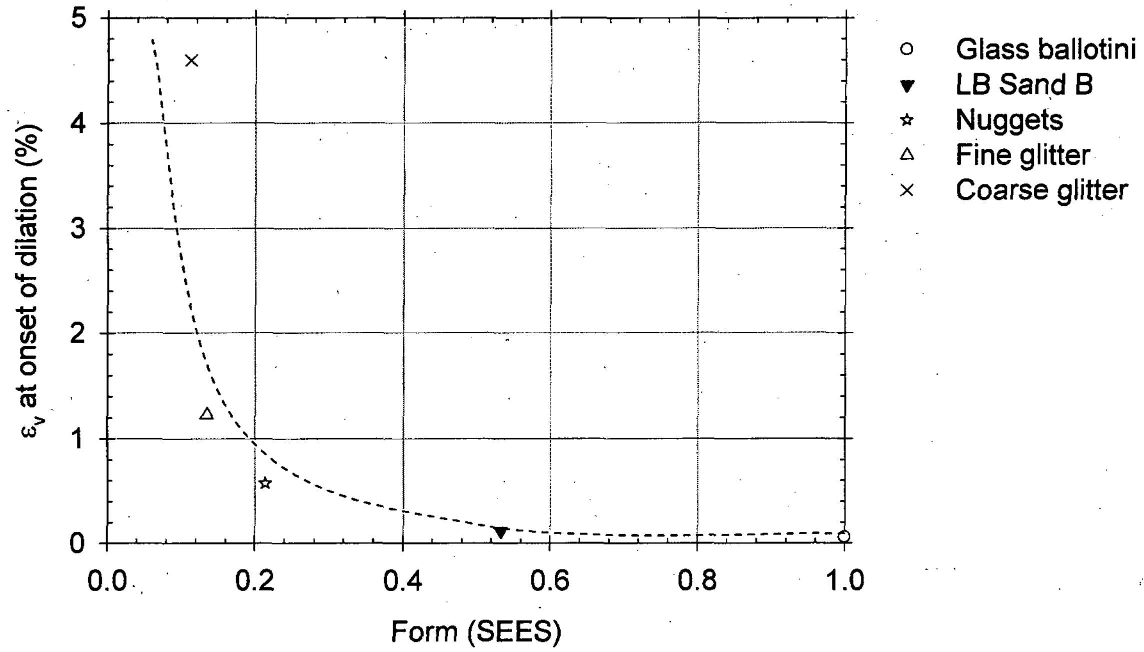

Figure 5.17: Variation of volumetric strain at onset of dilation with SEES

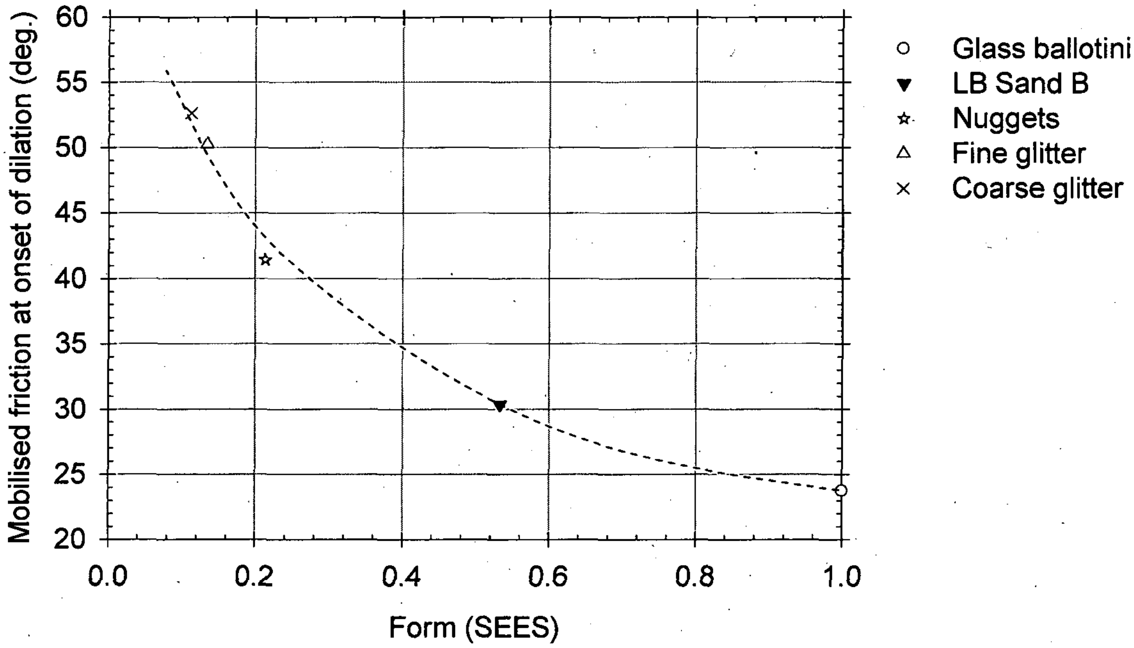

Figure 5.18: Variation of mobilised friction at onset of dilation with SEES

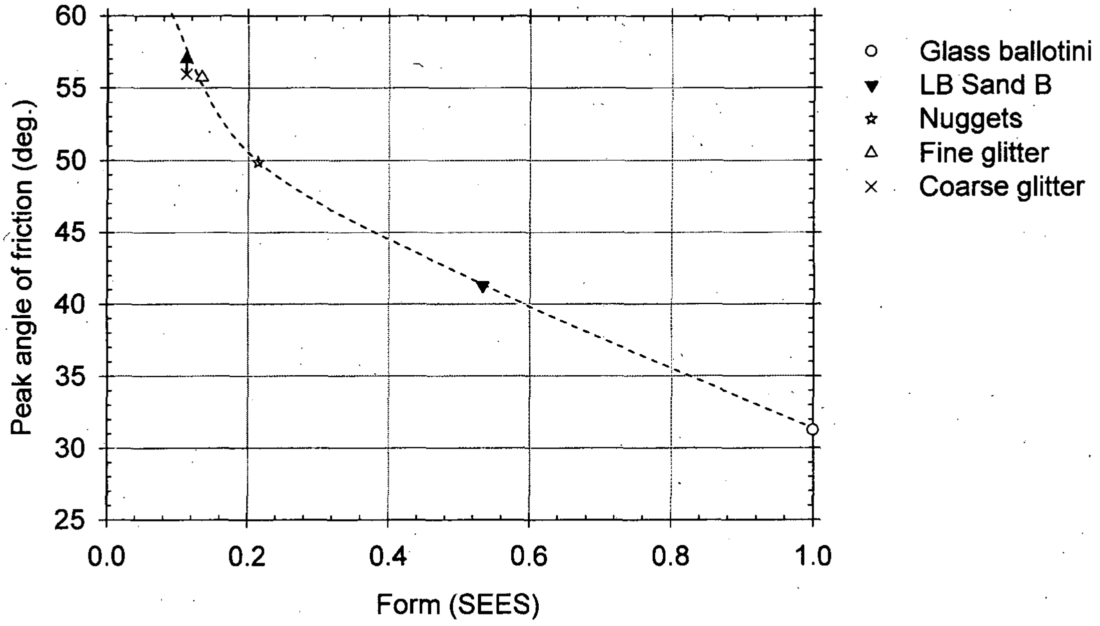

Figure 5.19: Variation of peak friction angle with SEES

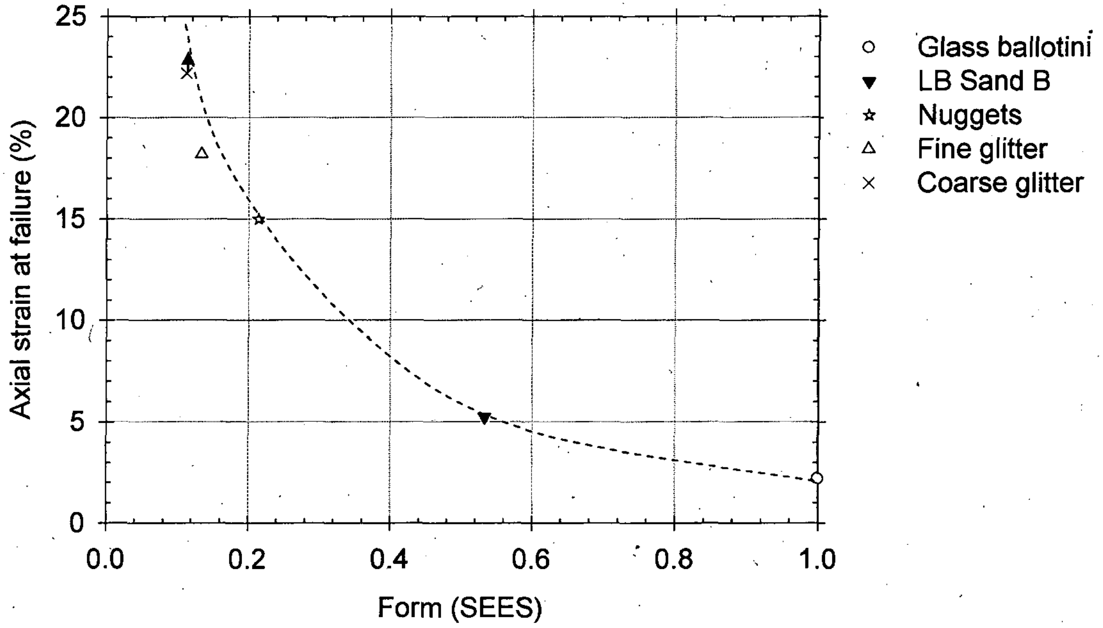

Figure 5.20: Axial strain to reach failure in relation to SEES

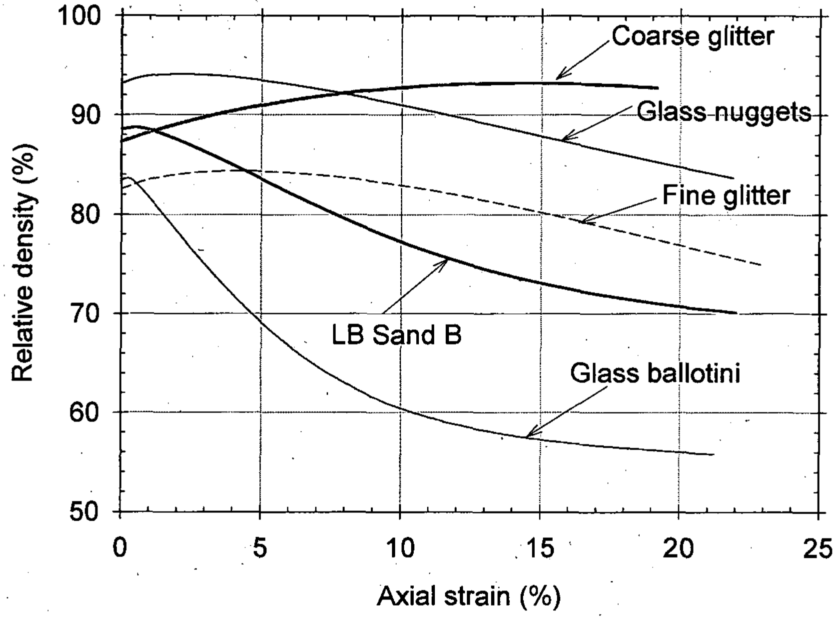

(a)

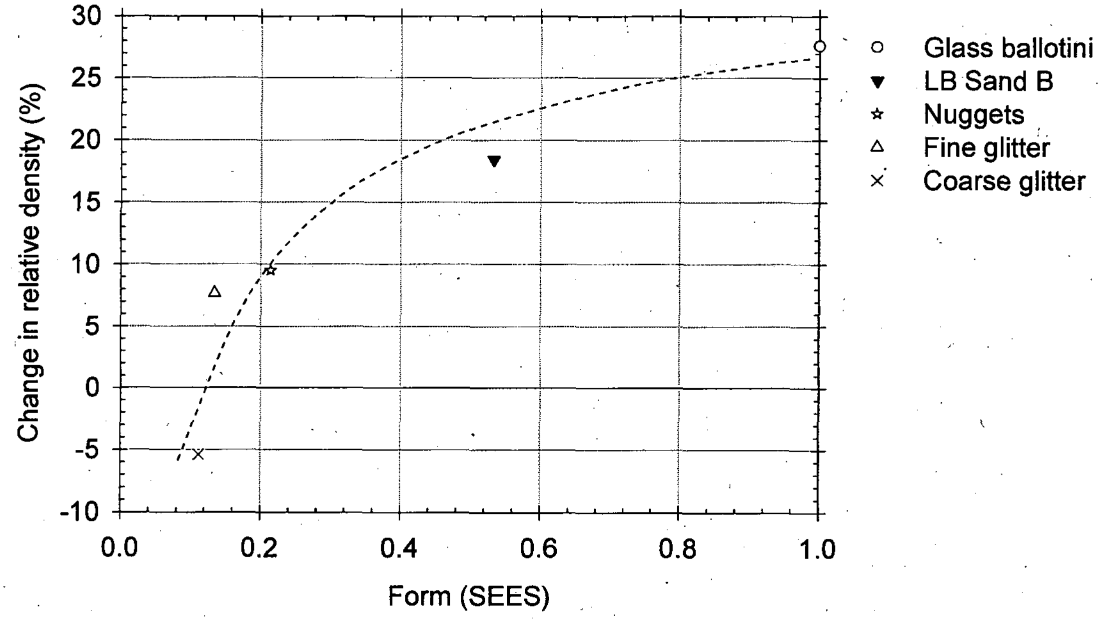

(b)

Figure 5.21: Variation of relative density with axial strain (a) and difference in D_r (between the start and end of shearing) in relation to SEES (b).

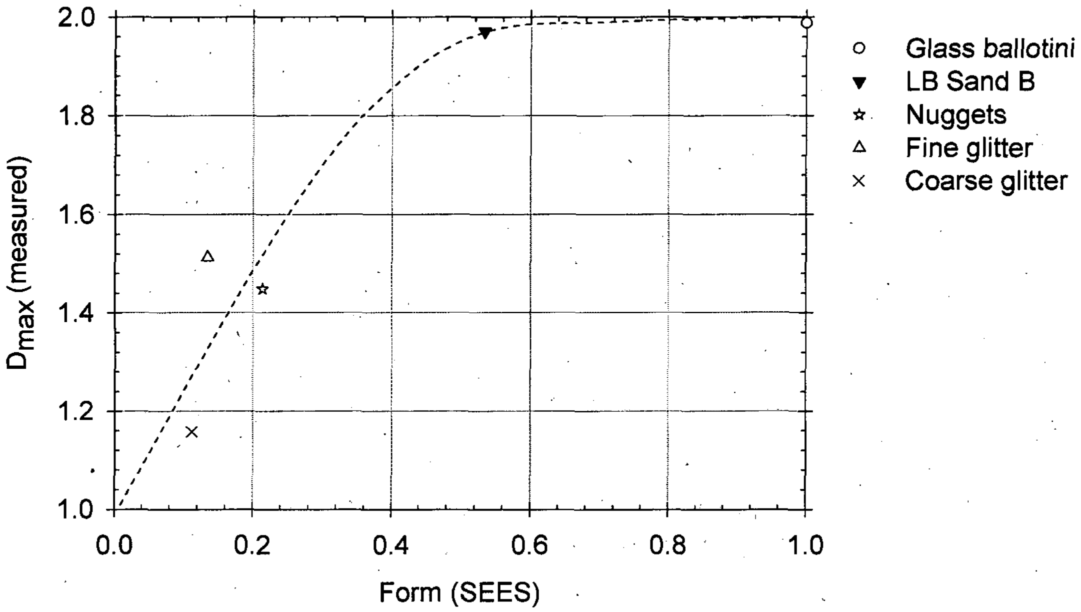

(a)

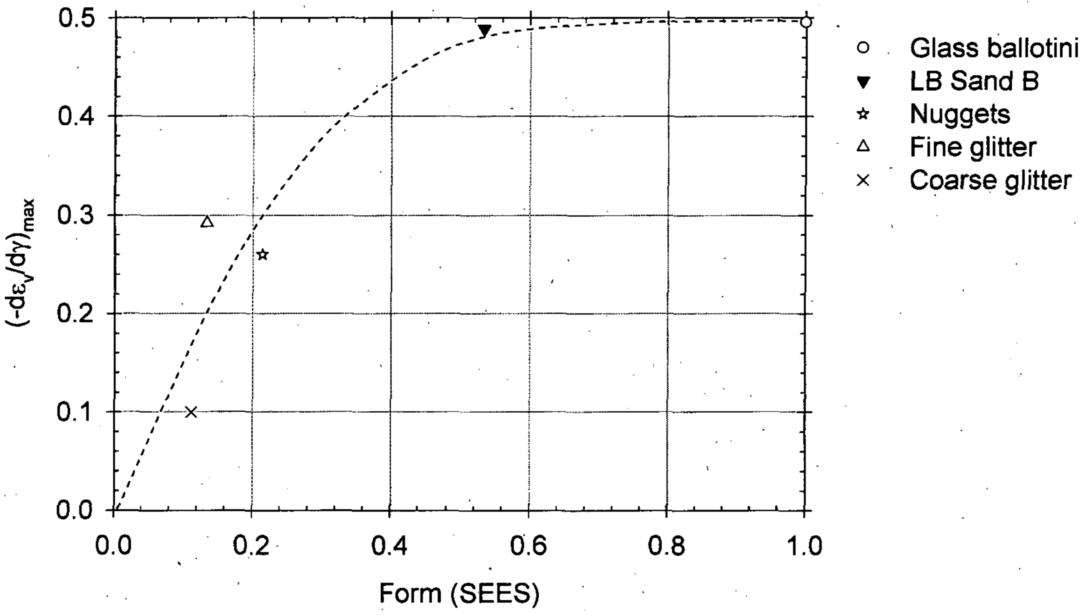

(b)

Figure 5.22: Maximum dilatancy factor (a) and maximum rate of volumetric strain / shear strain (b), in relation to SEES

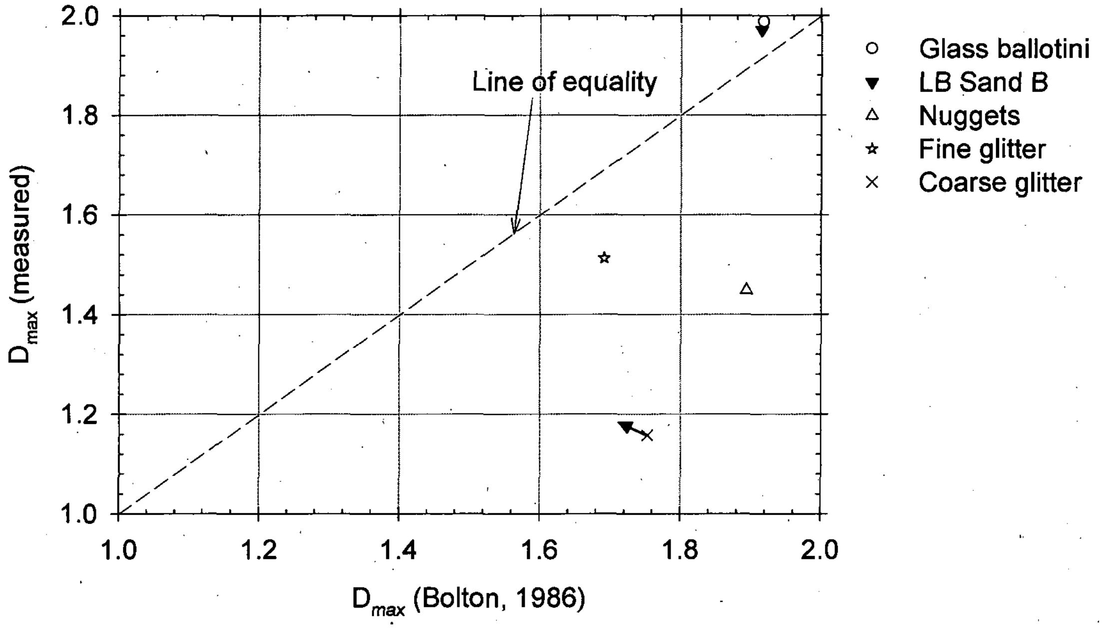

Figure 5.23: Comparison of measured D_{max} with Bolton's empirical equation.

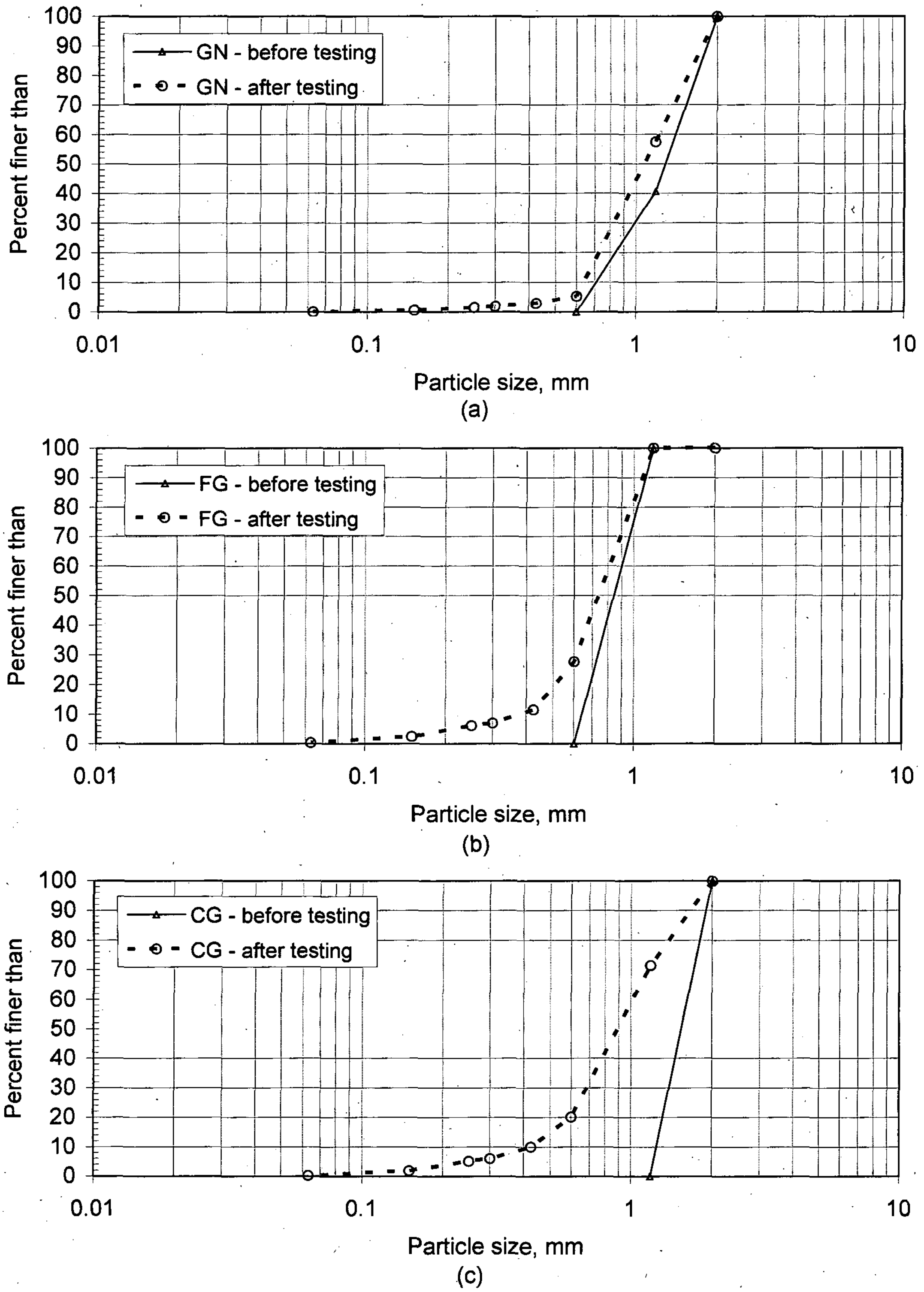

Figure 5.24: PSD of Glass nuggets (a), Fine glitter (b) and Coarse glitter (c), before and after shearing at an effective confining pressure of 100kPa

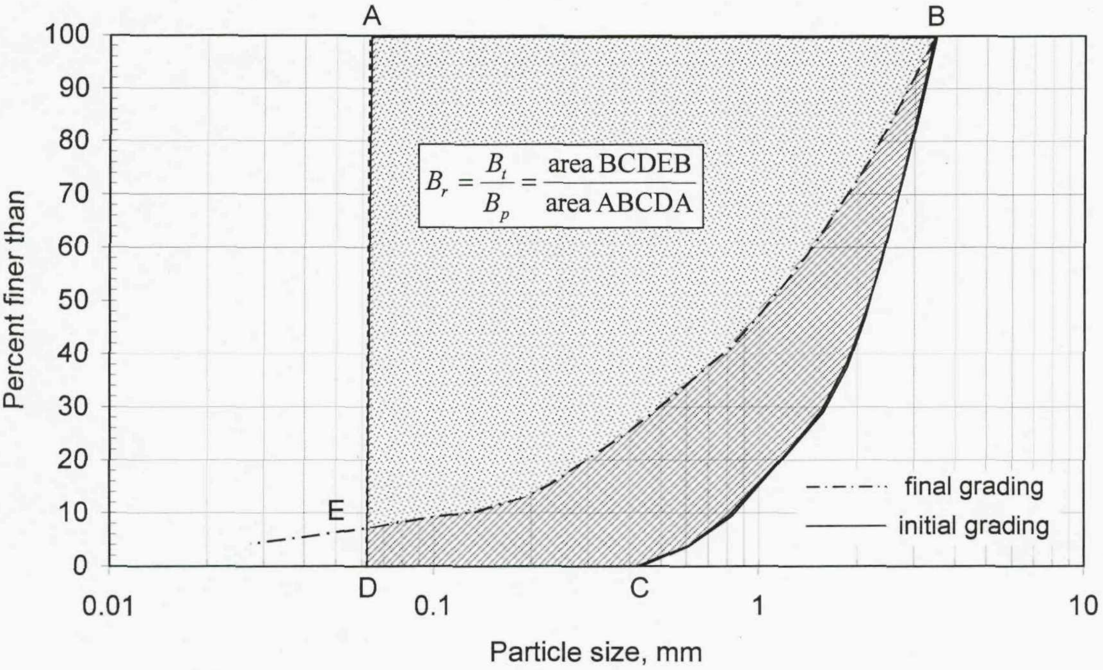

Figure 5.25: Definition of relative breakage, *Br* (Hardin, 1985)

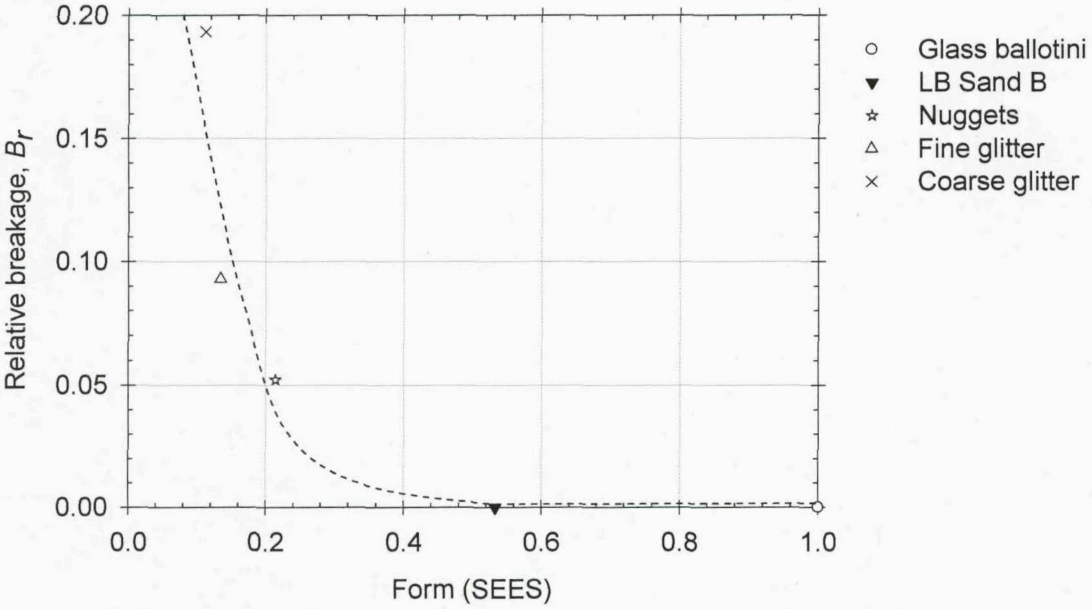

Figure 5.26: Particle breakage in relation to SEES

CHAPTER 6 NUMERICAL SIMULATIONS

This chapter presents the results of a numerical study carried out on rod-like particles of different shapes. It examines the effects of particle form, inter-particle friction and surface roughness on depositional packing, and the effect of form on drained shear behaviour in 2D. The main findings are summarised at the end of the chapter.

6.1 Numerical modelling

Numerical simulations have been carried out on uniformly-sized particles of different forms using PFC2D. PFC2D is a Particle Flow Code in 2 Dimensions, developed by Itasca Consulting Group Inc. (Itasca, 2004) based on the Distinct Element Method (DEM) proposed by Cundall (1978).

6.1.1 Distinct Element Method

The DEM is a numerical modelling technique that is capable of describing the mechanical behaviour of granular materials. The name "Distinct Element" signifies that each element of the granular media displaces independently and interacts only at the contact points. The DEM was originally developed by Cundall (1971) for the analysis of rock mechanics problems and then applied to soils by Cundall and Strack (1979). A brief description of the DEM is presented in the following paragraphs. However, for a more detailed description, the reader should refer to Cundall (1978) and Itasca (2004).

In the DEM, the interaction of particles is treated as a dynamic process with states of equilibrium developing whenever the internal forces balance. The contact forces and displacements of a stressed assembly of particles are found by tracing the movements of the individual particles. Movements result from the propagation through the particle system of disturbances caused by specified wall and particle motion and/or body forces. This is a dynamic process in which the speed of propagation depends on the physical properties of the discrete system.

The dynamic behaviour is represented numerically by an explicit time-stepping algorithm, using a central-difference scheme to integrate accelerations and velocities. The DEM is based upon the idea that the time-step chosen may be so small that, during a single time-step, disturbances cannot propagate from any particle further than its immediate neighbours. Then, at all times, the forces acting on any particle are determined exclusively by its interaction with the particles with which it is in contact. Since the speed at which a disturbance can propagate is a function of the physical properties of the discrete system, the time-step can be chosen appropriately to satisfy the above constraint. The use of an explicit, as opposed to an implicit, numerical scheme makes it possible to simulate the non-linear interaction of a large number of particles without excessive memory requirements or the need for an iterative procedure.

The calculations performed in the DEM alternate between the application of Newton's second law to the particles and a force-displacement law at the contacts. Newton's second law is used to determine the motion of each particle arising from the contact and body forces acting upon it, while the force-displacement law is used to update the contact forces arising from the relative motion at each contact. Newton's second law is not applied to walls, since the wall motion is specified by the user.

Calculation cycle in PFC2D

The calculation cycle in PFC2D is a time-stepping algorithm that consists of the repeated application of the law of motion to each particle, a force-displacement law to each contact, and a constant updating of wall positions. Contacts, which may exist between two balls or between a ball and a wall, are formed and broken automatically during the course of a simulation. The calculation cycle is illustrated in Figure 6.1.

At the start of each time-step, the set of contacts is updated from the known particle and wall positions. The force-displacement law is then applied to each contact to update the contact forces based on the relative motion between the two entities at the contact and the contact constitutive model. Next, the law of motion is applied to each particle to update its velocity and position based on the resultant force and moment arising from the contact forces and any body forces acting on the particle. At each time step, the accelerations (translational and rotational) are integrated twice, using a centred finite-difference procedure, for each particle to obtain the updated velocities and new positions. Also, the wall positions are updated based on the specified wall velocities.

Contact Constitutive model

The contact constitutive model used in this study consists of two parts: a stiffness model, and a slip model.

The stiffness model provides an elastic relation between the contact force and relative displacement. A linear contact model defined by the normal and shear stiffnesses, k_n and k_s (force/displacement), of the two contacting entities (ball-to-ball and ball-to-wall), has been used in this study. The contact stiffnesses for the linear contact model are computed assuming that the stiffnesses of two contacting entities act in series.

The slip model enforces a relation between shear and normal contact forces such that the two contacting entities may slip relative to one another. The slip model limits the shear force between two contacting entities. Both ball and wall are given a friction coefficient, and the friction coefficient at the contact, μ, is taken to be smaller of the two contacting entities. The maximum elastic shear force, $F_{s(max)}$, that the contact can sustain before sliding occurs is limited to $\mu \times F_n$, where F_n is the normal force at the contact. If the shear force at the contact exceeds $F_{s(max)}$ then it will be set equal to $F_{s(max)}$.

Clump Logic

In PFC2D 'world', all particles are cylindrical. However, clump logic supports the creation of super-particles of arbitrary shape by rigidly connecting a number of cylindrical particles together. A clump behaves as a rigid body (i.e. the particles comprising the clump remain at a fixed distance from each other). Contacts internal to the clump are skipped during the calculation cycle, resulting in a saving of computer time compared to a similar calculation in which all contacts are active. However, contacts with particles external to the clumps are not affected (i.e. such contacts will develop when the particles comprising the boundary of a clump come into contact with other particles). Particles within a clump may overlap to any extent; contact forces are not generated between any of these particles, but any contact forces that exist when the clump is created or when a particle is added to the clump will be preserved unchanged during cycling. Thus, a clump acts as a rigid body (with a deformable boundary) that will not break apart, regardless of the forces acting upon it. The reader should refer to Itasca (2004) for theoretical background of the clump logic.

6.1.2 Outline of numerical simulations

A wide range of particle forms were created by rigidly connecting a series of cylindrical particles together using clump logic as shown in Figure 6.1. In this study, the parameters "inscribed circle sphericity" (Riley, 1941) and Wadell's "roundness" (Wadell, 1932), respectively, have been used as measures of the form and roundness of idealised particles. Particle form (F) is the ratio of the largest diameter of inscribed circle to its smallest circumscribing circle. Roundness (R) is the ratio of the average of the radii of corners of a particle to its largest inscribed circle. It can be seen from Figure 6.1 that roundness is constant and form varies. Particle volume has been kept constant in all the cases. The effects of particle form, surface roughness and inter-particle friction on packing arrangement of particles have been examined by means of pluviation tests, and on shear behaviour by means of drained biaxial shear tests.

6.2 Effect of particle form on depositional packing

Physical basis for achieving the loosest and densest possible packing

In general, to achieve the densest packing, particles should be able to move freely and reach their minimum potential energy positions soon after their deposition; and for the loosest packing, particle mobility should be constrained after deposition.

In physical experiments, it has become widely accepted (refer to Sections 2.6 and 2.7) that the densest packing can be achieved by air-pluviation at low depositional intensities and high fall heights, and the loosest packing can be achieved by water-pluviation, which is independent of depositional intensity and fall height. Therefore, the air- and water-pluviation techniques, respectively, were simulated for determining the minimum (densest packing) and maximum (loosest packing) void ratios using PFC2D.

Simulation of air-pluviation process

The air-pluviation process was simulated by creating non-overlapping particles at incremental random x-positions and incremental y-positions, but at random orientations, in a rectangular depositional zone and then allowing them to fall under gravitational force with zero inter-particle friction. The purpose of creating particles at incremental random x-positions, incremental y-positions and random orientations was to ensure uniform rain and low depositional intensity. Zero inter-particle friction allows particles to slide over each other easily and attain minimum potential energy positions during deposition, which resembles the hammering effect produced by the falling grains in physical air-pluviation experiments.

Simulation of water-pluviation process

The water-pluviation process was simulated following a procedure similar to that of air-pluviation but with a higher inter-particle friction coefficient (i.e. 1.0). The higher inter-particle friction inhibits particle sliding as soon as the particles make contact with the rising surface of the deposited material, which was thought to be similar to the drag resistance offered by the water in physical water-pluviation experiments.

Outline of numerical simulations carried out

A series of numerical air- and water-pluviation tests were carried out on assemblies of particles of different forms (1.0, 0.67, 0.5, 0.33, 0.25, 0.2 and 0.1), all having the same roundness. If the balls comprising the clump are overlapped then PFC2D overestimates the mass of the clump since it overestimates the area. To overcome this problem, a correction factor was applied for the mass density of balls (with which the clumps were made), which was defined as the ratio of actual area of clump to that of the area calculated by PFC2D. The DEM parameters used in the simulations are presented in Table 6.1.

The initial positions and orientations of the particles were identical in all the simulations, regardless of form, since the procedure followed to create the particles was same. It should be noted that all other parameters, such as particle volume, number of particles and the width of the rectangular depositional zone (in relation to the particles' major dimension), were kept constant in all the simulations (see Table 6.1).

Problems of particle-overlaps after deposition

In simulations, as the deposition progressed, particles started either to overlap neighbouring particles or to move outside the depositional zone under the increasing weight of overlying particles i.e. overburden weight. However, these problems were corrected by setting the acceleration due to gravity to zero (after all particles were deposited and reached equilibrium) and cycling until the particle assembly reached equilibrium. During cycling, the kinetic energy of all the particles was reduced to zero several times in order to avoid the generation of large repulsive forces which otherwise might have disrupted the whole packing. This process was continued until the overlaps became negligible.

Effects of boundaries on depositional packing

Figures 6.2(a) and 6.2(b), respectively, show a sample of platy particles corresponding to a form of 0.20 in their densest (pluviated under zero inter-particle friction) and loosest (pluviated under an inter-particle friction of 1.0) states. During the depositional process, the packing arrangement of the particles was found to be affected by the boundaries (walls) of the depositional zone. However, these effects appeared to be significant only in the immediate vicinity of the boundaries, which can be clearly seen from the Figures 6.2(a) and 6.2(b). Post-depositional void ratios were therefore calculated in the central portion of the deposited particle assemblies, avoiding a zone with a width of 1.0 times the particles' major dimension around the periphery, in order to exclude the boundary effects.

Effect of form on limiting void ratios and void ratio range

Figure 6.3(a) shows that both the maximum and minimum void ratios increases with decreasing form of particles. e_{max} appears to be more sensitive than e_{min} especially at lower values of form. Therefore, void ratio range increased with decreasing form of particles; see Figure 6.3(b). Williams & Jia (2003) have also noted an increase in depositional void ratio in the case of short fibres when they were deposited by a raining technique.

Polar distribution of particle orientations in deposited assemblies

Figures 6.4(a) and 6.4(b), respectively, show the polar distribution of platy particle orientations corresponding to two extreme forms (i.e. 0.67 and 0.10) in their loosest and densest packing states. The radial ordinate on the polar histogram represents the fraction of particles oriented in the corresponding angular sector. The figures show that majority of particles tend to lie horizontal in their densest state, and their proportion increases with decreasing form regardless of their packing state. Comparison of polar histograms in densest and loosest states corresponding to identical form values suggest that the preferred horizontal alignment of particles is more pronounced in their densest states. Similar results have been reported by Nouguier-Lehon et al. (2003) in the case of elongated polygons with an aspect ratio of around 3.0, which is equivalent to a form of 0.33.

Polar distribution of contact orientations in deposited assemblies

Figures 6.5(a) and 6.5(b), respectively, show the polar distribution of contact orientations corresponding to two extreme forms (i.e. 1.00 and 0.10) in their loosest and densest packing states. The radial ordinate in these polar histograms represents the fraction of contacts oriented in the corresponding angular sector. Figure 6.5(a) indicates that the contacts were uniformly distributed over all orientations in loosest state, and in few major preferential directions in densest state mainly due to the cubic packing with some dislocations. On the other hand, the majority of contacts were oriented vertically in platy particles of form 0.10 (see Figure 6.5(b)) both in their loosest and densest states, since particles tend to lie flat (or horizontal) during the depositional process (see Figure 6.4(b)).

Anisotropy of particle orientations and contact orientations

The anisotropy of particle orientations and contact orientations was quantified by the following two parameters, similar to those proposed by Nouguier-Lehon et al. (2003 and 2005) and Azema et al. (2007):

(i) anisotropy of particle orientations

$$A_{PO} = \frac{2\left(PO_{yy} - PO_{xx}\right)}{\left(PO_{yy} + PO_{xx}\right)};\, where\, PO_{xy} = \frac{1}{N_p}\sum_{p=1}^{N_p} n_x^p n_y^p \qquad (6.1)$$

(ii) anisotropy of contact orientations

$$A_{CO} = \frac{2\left(CO_{yy} - CO_{xx}\right)}{\left(CO_{yy} + CO_{xx}\right)}; where\, CO_{xy} = \frac{1}{N_c}\sum_{p=1}^{N_c} n_x^c n_y^c \tag{6.2}$$

Where n_x^p, n_y^p and n_x^c, n_y^c, respectively, are the direction cosines of particle orientation (PO) and contact orientation (CO) vectors.

The anisotropy indices

- A_{PO} (or A_{CO}) < 0 indicates that the majority of particles (or contacts) are horizontal i.e. perpendicular to the direction of gravity.
- A_{PO} (or A_{CO}) $= 0$ indicates isotropy (i.e. particles or contacts uniformly distributed in all directions).
- A_{PO} (or A_{CO}) > 0 indicates majority of particles (or contacts) aligned vertical (i.e. in the direction of gravity).

The following observations can be made from Figures 6.6(a) and (b):

- In the case of loosest packing, the majority of (i) high form (i.e. 0.67 and 0.50) particles were oriented vertically, (ii) intermediate form (i.e. 0.33 and 0.25) particles were more or less uniformly distributed over all orientations, and (iii) low form particles were oriented horizontally, see upper trend line and data points in Figure 6.6(a).
- In the case of densest packing, the majority of particles were oriented horizontal irrespective of form, and their proportion was quite large in low form (0.10) particles assembly, see lower trend line and the corresponding data points in Figure 6.6(a).
- Contact orientations were uniformly distributed over all directions in the case of the loosest packing of cylindrical particles (see data points corresponding to form 1.0 in Figure 6.6(b)), and concentrated in a few major preferential directions (Figure 6.5(a)) in the case of densest packing due to ordered geometrical packing.
- In the case of other forms, the majority of contact orientations were vertical and their proportion was found to increase significantly with decreasing form and slightly with increasing density (Figure 6.6(b)).

In the case of e_{max} simulations, it is worth noting that the depositional intensity is low in the current simulations. If the depositional intensity was increased it could be expected, due to the increased opportunity for particles to interfere with each other, that inherent anisotropy (preferential horizontal alignment of particles after the deposition) would be decreased especially in low form particles. A decrease in inherent anisotropy would lead to an increase in depositional void ratio due to a more open structure.

In addition, in the case of small colloidally-active particles, the double layer repulsive and edge-to-face attractive forces helps in forming a very loose structure, leading to large initial void ratios in case of clay soils, as noted by Olson & Mesri (1970).

The e_{max} and e_{min} values determined from air- and water-pluviated tests (as described at the beginning of this section) were subsequently used to determine the relative densities of isotropically compressed assemblies in drained shear tests.

6.3 Effects of surface roughness and inter-particle friction on depositional packing

The effects of surface roughness and inter-particle friction on depositional void ratio and packing arrangement of particles (inherent anisotropy) were investigated by means of pluviation tests on particles with different surface roughnesses and inter-particle frictions as shown in Table 6.2.

Three different surface roughness configurations namely single-, double- and triple-layered clumps as shown in Figure 6.7 with zero inter-particle friction, and triple layered clumps with four different inter-particle friction coefficients ranging from 0.0 to 1.0 (in addition to the surface roughness), were considered in this study.

The surface roughness was characterised by a new parameter called asperity friction, which was defined as the tangent of implied angle of rise (δ) of the surface asperity of a particle over the surface of another similar particle (see Figure 6.7(d)) and is written as follows

$$\text{Asperity friction} = \tan\delta \qquad (6.3)$$

Numerical pluviation tests were carried out on platy particles (corresponding to a form of 0.20) with the above-mentioned friction configurations. The purpose of this investigation was to check whether or not surface roughness and inter-particle friction influence packing in a similar way.

Figure 6.8 shows that the depositional void ratio increases with increasing friction coefficient irrespective of whether it is inter-particle friction or asperity friction. Comparison of polar histograms in Figures 6.9(a) and 6.9(b) for the equivalent friction coefficients show that both the friction coefficients have a similar effect on inherent anisotropy. Figure 6.9(b) shows that the proportion of particles orienting in horizontal direction (i.e. inherent anisotropy) increases with decreasing inter-particle friction.

The results indicate that both the friction coefficients (asperity friction and inter-particle friction) have similar effects on depositional void ratio as well as on inherent anisotropy, which further suggests that surface roughness can be considered as an equivalent inter-particle friction.

6.4 Effect of form on drained shear behaviour

Drained biaxial shear test simulations were carried out on six assemblies of uniformly-graded, constant-volume particles of different forms (1.0, 0.67, 0.5, 0.33, 0.25 and 0.2) but with same roundness and roughness. Each of these six assemblies was prepared at three different density states with relative densities of approximately 30% (loose), 50% (medium dense) and 70% (dense). The DEM parameters used in the shear simulations are presented in Table 6.3 and the relative densities of the isotropically compressed samples (or samples at the start of shearing) are given in Table 6.4.

Sample preparation

Samples for shear tests were prepared from the loosely packed assemblies which were initially used for determining the maximum void ratios, as discussed in section 6.2. The positions and orientations of particles of the loosely-packed assemblies were captured and reproduced. The reproduced assemblies were then bounded by four platens and compressed isotropically to the desired stress level using the numerical servo-control mechanism on all four platens. Samples with desired relative densities were achieved by changing the inter-particle friction during isotropic compression. Large inter-particle friction produced loose samples and small inter-particle friction produced dense samples. It is to be noted that the friction on platens was set equal to that of the particles during isotropic compression stage, since this would otherwise have disrupted the packing.

Shearing procedure

The friction between the sample and the side platens, and the top and bottom platens, was set to zero at the start of shearing in order to provide friction-less boundaries. The normal stiffness of top and bottom end platens were set equal to that of the particles, and lateral platens were set equal to 1/10th of that of particles in order to provide a flexible boundary effect. Isotropically compressed assemblies of particles were then sheared by moving the top and bottom end platens towards each other at a constant velocity, whilst maintaining the lateral stress constant i.e. 50kPa in the current simulations. Therefore, the major principal stress direction was vertical and the minor principal stress was horizontal. Shearing was continued up to an axial strain of 40%.

6.4.1 Global shear behaviour

The drained shear tests results were analysed in terms of stress-ratio, void ratio and volumetric strain against axial strain. The results are presented in Figures 6.10 to 6.18. The following observations were made from the figures, in terms of their global shear behaviour:

- A transition from peak and subsequent softening to completely hardening type of behaviour was observed as the particle shape changed from spherical to platy (see Figures 6.10(a), 6.11(a), 6.12(a), 6.13(a), 6.14(a) and 6.15(a)).
- In the case of assemblies comprising particles of form 1.0, 0.67 and 0.5 (Figures 6.10 to 6.12)
  - All dense samples exhibited a peak strength which decreased with decreasing density.
  - The strain to reach peak increased with decreasing form.
  - All samples reached a unique ultimate strength irrespective of their initial densities.

  - The difference between peak and ultimate strengths decreased as form decreased.
  - Dense samples dilated and loose samples initially contracted and then dilated, and all samples reached a unique ultimate void ratio irrespective of their initial densities.
- In the case of assemblies comprising particles of form less than 0.50 (i.e. 0.33, 0.25 and 0.20 – Figures 6.13 to 6.15):
  - All samples exhibited hardening behaviour irrespective of their initial densities.
  - At small strains, the mobilised strength was lower for loose samples and it increased with increasing initial density.
  - At large strains, all samples reached same strength and void ratio but continued to increase with strain at the same rate irrespective of their initial densities.
  - Dense samples continued to dilate at a constant rate from the beginning to the end of shearing whereas loose and medium dense samples contracted initially and then dilated at a constant rate until the end of shearing.

In summary, the following conclusions can be drawn on global shear behaviour:

- In samples comprising particles with form greater than 0.5, the peak friction angle and the difference between peak and large strain friction angle decreased with decreasing form , see Figures 6.16(a) and (b).
- The void ratio and strength at large strains increased with decreasing form, see Figure 6.17(a) and (b).
- At strains less than 10%, the maximum dilatancy was found to decrease with decreasing form irrespective of initial density, and the trend was consistent for all forms (see Figures 6.18(a) to (c)). However, the trend was not clear at strains greater than 10%, especially in medium dense and dense samples.

6.4.2 Evolution of micro-structural parameters

Figures 6.19 and 6.20, respectively, show the dense assemblies of particles at the start and end of shearing, corresponding to two extreme forms (1.0 and 0.2). This section explores the evolution of the following "micro-structural" parameters as shear progresses:

a) Distribution of particle orientations
b) Distribution of contact orientations
c) Distribution of normal and tangential contact forces
d) Distribution of contact forces

a) Distribution of particle orientations

Figures 6.21 and 6.22, respectively, show the polar distribution of particle orientations corresponding to forms 0.67 and 0.20 of loose and dense samples at different stages of shearing (0%, 2%, 10% and 40% strains). 0% refers to the start of shearing, 2% refers to the peak stage (approx.), and 10% to 40% refer the later stages of shearing. It can be clearly seen from the figures that:

- As shear progressed, particles re-oriented themselves perpendicular to the major principal stress direction, both in loose and dense assemblies of all forms.
- The proportion of particles orienting perpendicular to major principal stress direction was high for low form particles, and low for high form particles, at all stages of shearing, both in loose and dense states.

The anisotropy of particle orientations was quantified by the parameter A_{PO} as defined previously in equation (6.1). Here again,

- $A_{PO} < 0$ indicates a majority of particles oriented perpendicular to the major principal stress direction i.e. horizontal.
- $A_{PO} = 0$ indicates isotropy i.e. particles uniformly distributed in all directions.
- $A_{PO} > 0$ indicates a majority of particles oriented in major principal stress direction i.e. vertical.

Figure 6.23(a) and (b) show the evolution of the parameter A_{PO} during shear in loose and dense samples. The following points can be drawn from this figure:

- The initial particle anisotropy of loose and dense samples of identical forms was almost the same despite their different densities.

- At the start of shearing, the majority of particles corresponding to form 0.67 and 0.5 were oriented vertically (since $A_{PO} > 0$), 0.33 and 0.25 were more or less uniformly distributed over all orientations (since $A_{PO} \approx 0$); and 0.2 were oriented horizontally (since $A_{PO} < 0$).
- Comparison of Figures 6.23(a) and (b) for identical forms reveals that the anisotropy evolution is quite similar in all the samples irrespective of their relative densities.
- Anisotropy increased with the strain for all forms and density states. However, the rate of increase of anisotropy diminished with the strain (i.e. after it reached a critical anisotropy) in high form particles and continued to increase in low form particles.

b) Distribution of contact orientations

Figures 6.24 and 6.25, respectively, shows the polar distribution of contact orientations corresponding to two extreme forms (i.e. 1.0 and 0.2) of loose and dense samples at different stages of shearing.

In assemblies comprising cylindrical particles (i.e. form = 1.0):

- Initially, contacts were oriented in few major preferential directions (Figures 6.24(a) and 6.25(a)) because of ordered geometrical packing with some discontinuities, which can be easily seen from Figure 6.19(a).
- In dense samples, the proportion of contacts oriented towards the major principal stress direction increased with the strain before reaching a peak and then decreased after the peak (see Figure 6.25(a)). Whereas in loose samples their proportion increased continuously with strain (see Figure 6.24(a)).

On the other hand, in assemblies comprising particles of other forms, the proportion of contacts oriented in the major principal stress direction increased (whereas the ones oriented in the minor principal stress direction decreased) with the strain continuously, regardless of their initial densities.

The anisotropy of contact orientations was quantified by the parameter A_{CO}, as defined previously in equation (6.2). Figure 6.26(a) and (b), respectively, show the evolution of contact anisotropy with axial strain in loose and dense samples. The following points arise from this figure:

- The contact anisotropy of cylindrical particles increased until the peak, then decreased and reached a unique critical value at an axial strain of around 10%. Particles corresponding to a form of 0.67 also reached a critical contact anisotropy but at a strain higher than that of cylindrical particles. These two observations together suggest that high form particles will continuously re-arrange during shear and reach a critical state at large strains.
- The contact anisotropy of particles with form less than 0.67 increased continuously without reaching any critical value even by the end of shearing (i.e. 40% strain) in both dense and loose samples.
- Close observation of Figures 6.26(a) and (b) reveals that at strains less than 10% (approx.) the anisotropy of dense samples was higher than that of loose samples. This was consistent for all forms.

c) Distribution of normal and tangential contact forces

Figures 6.27 to 6.30, respectively, show the polar distribution of normal and tangential contact forces in loose and dense samples corresponding to two extreme forms (1.0 and 0.2). The radial ordinate on these figures represents the mean normal (or tangential) contact forces oriented in the corresponding angular sectors, normalised with respect to the mean normal contact force over the whole sample.

The following points can be drawn from these figures:

- At the start of shearing, the normal force distribution was more or less isotropic both in loose and dense samples of all forms, see Figures 6.27 and 6.29. However, as shear progressed the normal force distribution became slightly anisotropic and it slightly increased with increasing form, see Figures 6.27 and 6.29.
- Comparison of Figures 6.28(a) and (b) indicates that low form particles can mobilise large tangential forces compared to high form (cylindrical) particles, mainly due to increased interlocking or sandwiching between particles. In general, cylindrical particles can easily slide and/or roll compared to platy particles. Furthermore, comparison of Figures 6.28 and 6.30 for identical

forms shows that the interlocking or sandwiching effect increases with increasing density.

d) Distribution of contact forces

Figures 6.31 and 6.32 show the contact force networks in dense assemblies of particles (corresponding to forms 1.0 and 0.2) at the end of shearing. The figures give an impression that the contact forces are more uniform in high form (cylindrical) particles than in low form (platy) particles. This could be due to effective lateral contact networks in cylindrical particles as opposed to dominated vertical contacts (i.e. parallel to major principal stress direction) in low form particles, see Figures 6.24 and 6.25 corresponding to 40% strain. Also, close observation of Figures 6.31 and 6.32 reveals the contact force localisation in few thin bands (in the direction of major principal stress) which could be due to preferred horizontal orientation of particles and popping out of particles edges. In fact, the contact forces are very high in Figure 6.32 compared to those in Figure 6.31. However, this feature is not obvious from the figures since the scale (of contact force magnitudes) is not same in both the figures. If they were plotted to the same scale, the contact forces in Figure 6.31 would completely disappear.

To gain more insights into the contact force distributions, they were analysed in the following ways:

- Probability density functions (PDF's) were plotted for contact forces (normalised by the mean contact force at the start of shearing) at different stages of shearing of loose and dense samples – see Figures 6.33 to 6.35. It should be noted that in order to improve the clarity, only strong contact forces (i.e. normalised contact force > 1.0) are shown in these figures.
- The variation of mean contact forces (normalised by the mean contact force at the start of shearing) was plotted as a function of axial strain, see Figures 6.36(a) and (b).

The following observations can be made from PDF plots of contact forces presented in Figures 6.33 to 6.35:

- Comparison of PDF plots of loose and dense samples corresponding to identical form values indicate that the magnitude of maximum contact force and the proportion of very strong force contacts (i.e. normalised contact force > 10) increases with increasing density.
- At 2% axial strain, there is no definite trend in either the maximum contact force or the proportion of strong force contacts, since the particles were still establishing strong contacts at that stage. However, at strains greater than 10%, there exists a definite increasing trend in both the maximum contact force as well as the proportion of very strong force contacts with decreasing form.
- Moreover, the rate of increase of maximum contact force and the proportion of strong force contacts with respect to form was much higher than that with the density.

The normalised contact force plots presented in Figures 6.36(a) and (b) show that:

- The mean contact force increased with increasing density for all forms, and at all stages of shearing.
- After establishment of relatively stable contacts (roughly at strains >10%), the mean contact force increased quite significantly with decreasing form.
- The rate of increase of mean contact force with respect to form was much higher than that with the density.
- Cylindrical particles and particle with form 0.67 showed a unique critical mean contact force at large strains, irrespective of their initial densities. Others did not reach a unique critical value, but instead continued to increase with the strain.

6.5 Summary

- Two novel techniques have been used for determining the maximum and minimum void ratios of numerical 'samples'.

- The effect of particle form on packing has been investigated by simulating the air- and water- pluviation processes. The following observations were made:

  - Both, e_{max} and e_{min}, increased with decreasing form, but e_{max} was more sensitive than e_{min} especially at lower values of form. Void ratio range (difference between e_{max} and e_{min}) increased with decreasing form.
  - In their loosest packing, the majority of high form particles were oriented vertically, intermediate form particles were uniformly distributed in all orientations, and low form particles were oriented horizontally. On the other hand, in their densest packing, the majority of particles aligned horizontal irrespective of their form and their proportion increased with decreasing form.
  - The majority of contacts were oriented vertically, and their proportion increased significantly with decreasing form and slightly with increasing density.

- A new parameter termed the 'asperity friction', defined as the tangent of implied angle of rise of the surface irregularity, has been introduced for characterising the surface roughness of clumps in PFC2D.

- The effects of inter-particle friction and surface roughness on depositional packing of platy particles were examined and the following points were noted:
  - Depositional void ratio increased with increasing inter-particle friction as well as with increasing asperity friction.
  - The inherent anisotropy of particle orientations decreased with increasing inter-particle friction.
  - Both types of friction (i.e. asperity friction and inter-particle friction) had similar effect on depositional void ratio as well as on inherent anisotropy, suggesting that surface roughness can be considered as an equivalent inter-particle friction.

- A novel technique was developed to prepare numerical 'samples' of the desired relative density with more or less the same fabric.

- The effects of particle form and density on shear behaviour were investigated by means of drained biaxial shear tests. The following points were noted with regards to the global shear behaviour and the evolution of micro-structural parameters.

Global shear behaviour

- In particles with form greater than 0.5, the peak friction angle and the difference between the peak and large strain friction angle decreased with decreasing form.
- The strength and void ratio at large strain increased with decreasing form.
- At strains less than 10%, the maximum rate of dilation decreased with decreasing form irrespective of their initial densities and forms. However, the trend was not clear at strains greater than 10%, especially in medium dense and dense samples.

Evolution of micro-structural parameters

- Anisotropy of particle orientation increased with strain for all forms and density states. However, the rate of increase of anisotropy diminished with the strain in high form particles (i.e. reached a critical anisotropy) and continued to increase in low form particles.
- The contact anisotropy of cylindrical particles exhibited a peak and a unique critical value at large strain; particles with form = 0.67 did not exhibit peak but reached a critical contact anisotropy which was higher than that of cylindrical particles. Anisotropy of particles with form less than 0.67 increased continuously without reaching any critical value. However, at strains less than 10% (approx.), the contact anisotropy of dense samples was higher than that of loose samples and it was consistent for all forms.
- The normal force distribution was more or less isotropic at the start of shearing, and became slightly anisotropic as the shear progressed. The anisotropy slightly increased with decreasing form.
- Low form particles mobilised higher tangential forces than high form particles. Tangential force mobilisation increased with increasing density. This could be due to increased interlocking or sandwiching between particles.
- At strains greater than 10% (approx.), the magnitude of maximum contact force and the proportion of very strong force contacts increased with decreasing form as well as with increasing density. However, the rate of increase with respect to form was much higher than that with respect to density.

- Only cylindrical particles reached a unique critical mean contact force, whereas in non-cylindrical particles it continued to increase with the strain. The mean contact force increased with decreasing form and with increasing density. However, the rate of increase of mean contact force with respect to form was much higher than with respect to density.

Table 6.1: DEM parameters used in gravity tests

Parameter	**Numerical values adopted**
Particle shapes modelled	Particles with different form i.e. 1.0 (cylindrical), 0.67, 0.5, 0.33, 0.25, 0.2, and 0.1; all having Wadell's roundness of unity - see Figures 6.2(a) to (g)
Number of particles	4005
Radius of cylindrical particle, m (particle volume has been kept constant for other shapes)	$\cong 0.001$
Density of particles, kg/m^3	$2640\times(A_{actual}/A_{PFC})$
Acceleration due to gravity in y-direction (g_y), m/s^2	-9.81
Width of deposition zone	30 times the particles' major dimension
Normal and shear stiffness of particles, N/m	1×10^5
Damping coefficient	0.70
Normal and shear stiffness of walls, N/m	1×10^5
Asperity friction coefficient	0.258 (double layer)
Inter-particle friction coefficient	0.0 for e_{min} tests 1.0 for e_{max} tests
Friction on sides of depositional zone	0.0 for e_{min} tests 1.0 for e_{max} tests

Table 6.2: Parameters varied in frictional equivalence gravity tests

Parameter	**Numerical values adopted**
Particle shapes modelled	Platy particles with form 0.2
Asperity friction coefficient (Surface roughness)	0.577 (single layered clumps), 0.258 (double layered clumps) and 0.126 (triple layered clumps) – see Figures 6.8 (a) to (c); All with zero inter-particle friction.
Inter-particle friction coefficient	0.0, 0.128, 0.5 and 1.0; All with triple layered clumps (Figure 6.8 (c)).

Table 6.3: DEM parameters used in shear tests

Parameter	**Numerical values adopted**
Particle shapes modelled	Particles with different form i.e. 1.0, 0.67, 0.5, 0.33, 0.25, and 0.2; all with a roundness of unity – see Figures 6.2(a) to (f)
Number of particles	4005
Radius of each circular particle, m	$\cong 0.001$
Density of particles, kg/m^3	$2640\times(A_{actual}/A_{PFC})$
Normal and shear stiffness of particles, N/m	5×10^8
Damping coefficient	0.70
Asperity friction coefficient	0.258 (double layer)
Inter-particle friction coefficient	0.50
Coefficient of friction on platens	0.00
Normal stiffness of loading platens, N/m	5×10^8 - top & bottom 5×10^7 - lateral
Confining stress, N/m^2	5×10^4
Relative densities (%)	~30 % (loose), ~50% (medium dense), and ~70% (dense) – see Table 6.4

Table 6.4: Initial relative densities of samples

Form	**Initial Dr (%) (Loose ~ 30%)**	**Initial Dr (%) (Medium ~ 50%)**	**Initial Dr (%) (Dense ~ 70%)**
1.00	33.95	55.14	70.70
0.67	28.84	55.80	69.90
0.50	36.66	53.79	69.25
0.33	30.38	48.58	66.89
0.25	28.54	50.49	67.60
0.20	26.65	50.99	68.29

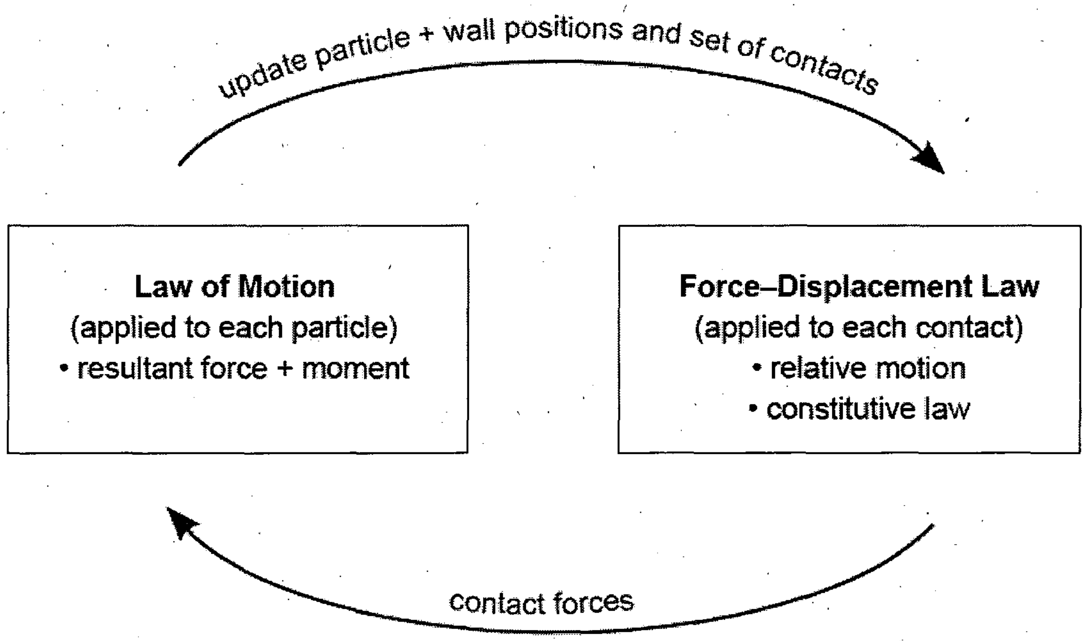

Figure 6.1: Calculation cycle in PFC2D (Itasca, 2004)

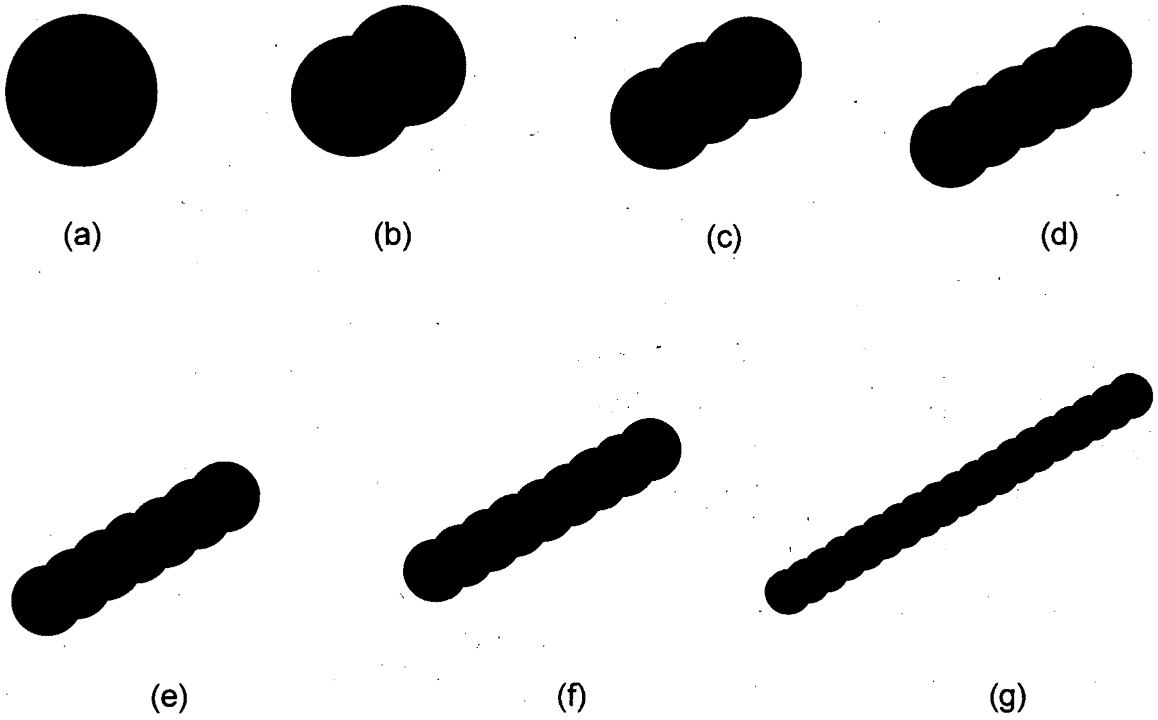

Note:- Particle area is constant in all the cases.

Figure 6.2: Particle shapes modelled: with forms 1.00 (a), 0.67 (b), 0.50 (c), 0.33 (d), 0.25 (e), 0.20 (f) and 0.10 (g); and roundness 1.0.

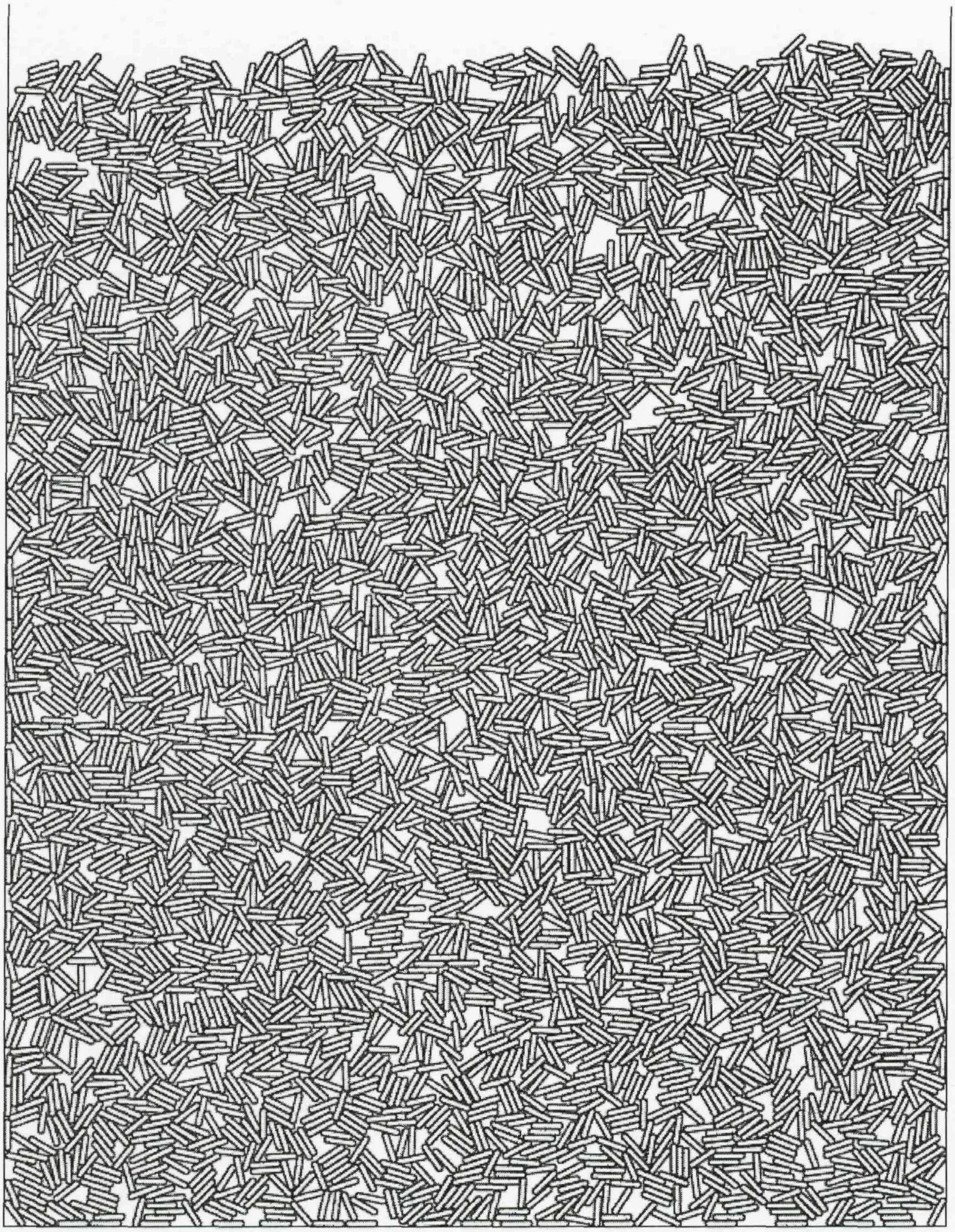

(a)

Figure 6.3: DEM model showing the packing arrangement of particles in their loosest (a) and densest (b) states (F = 0.20)

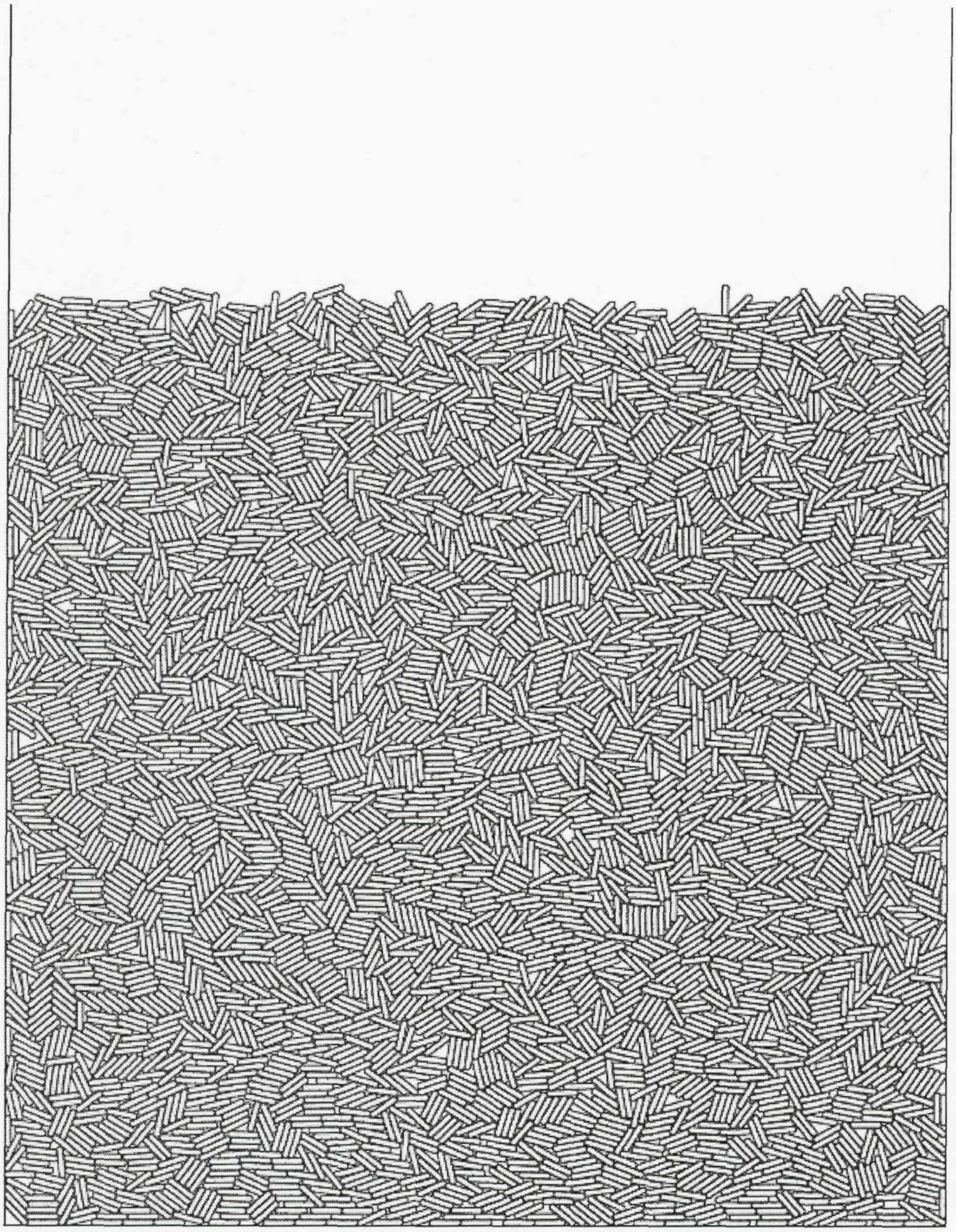

(b)

Figure 6.3: DEM model showing the packing arrangement of particles in their loosest (a) and densest (b) states (F = 0.20)

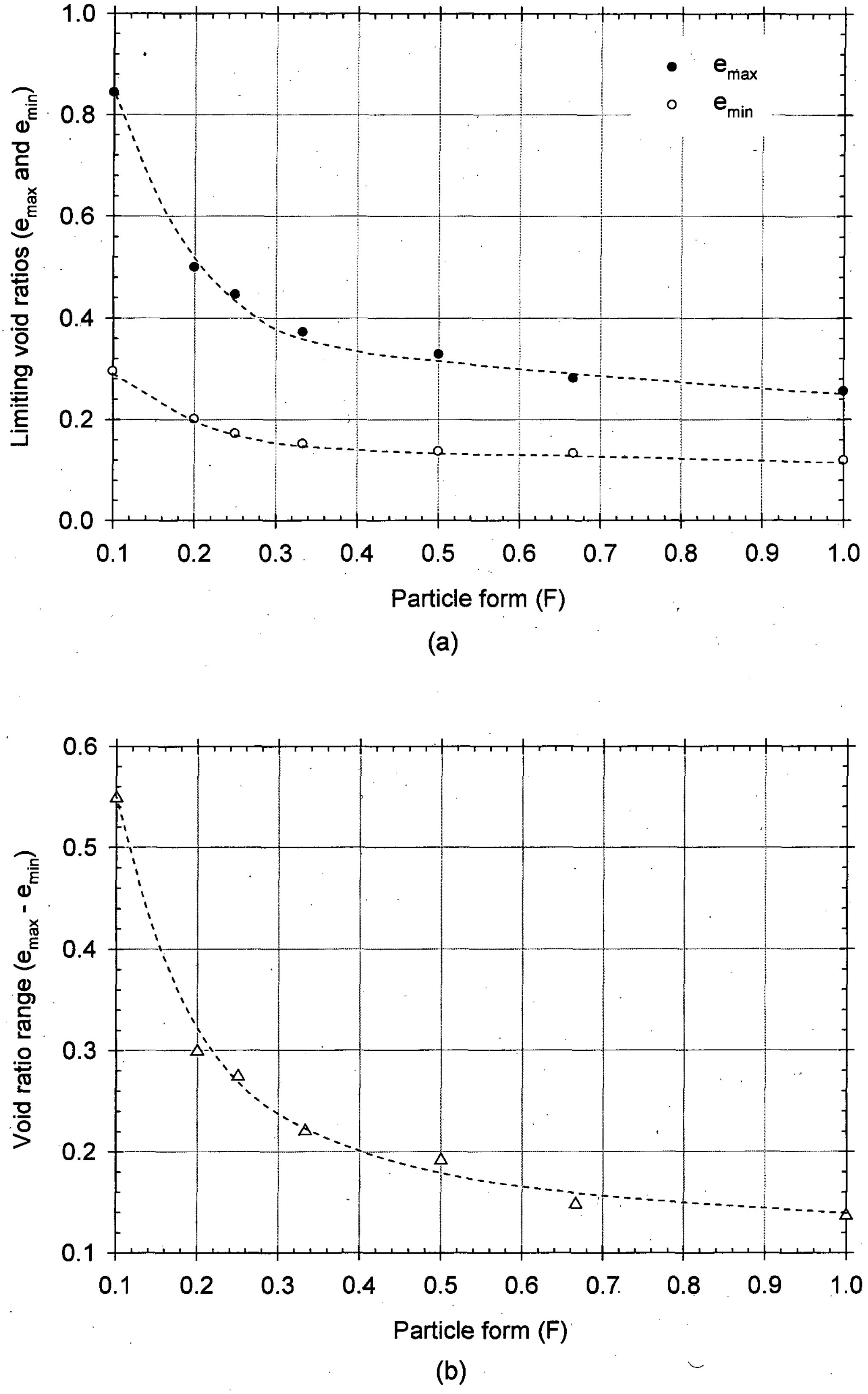

(a)

(b)

Figure 6.4: Variation of DEM (a) limiting void ratios and (b) void ratio range, with respect to form.

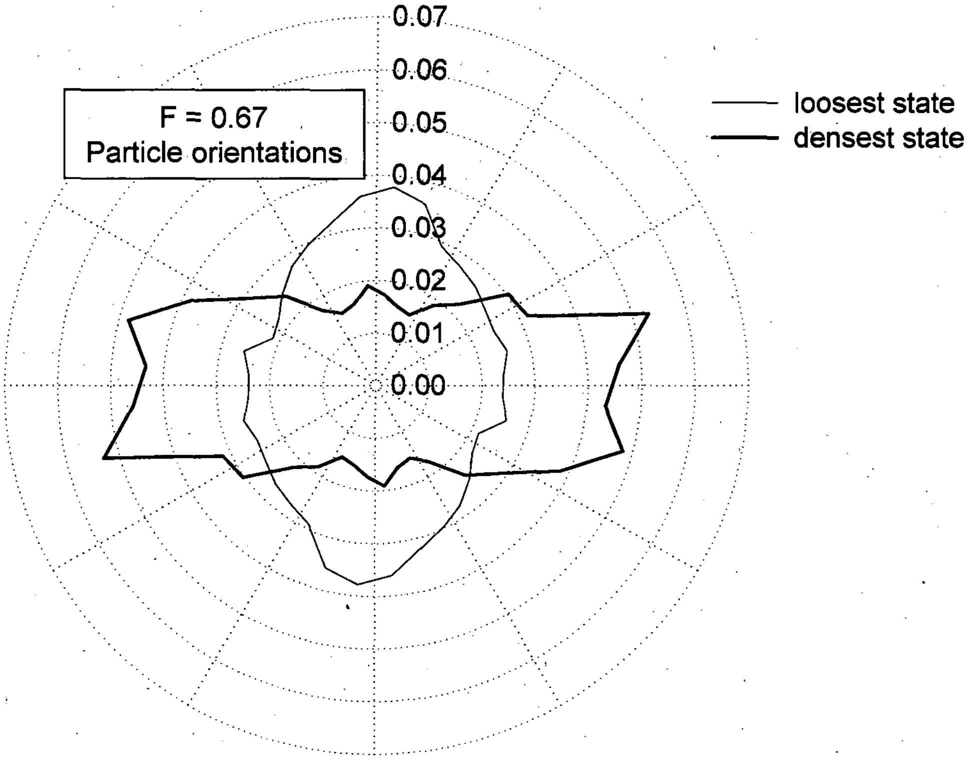

(a)

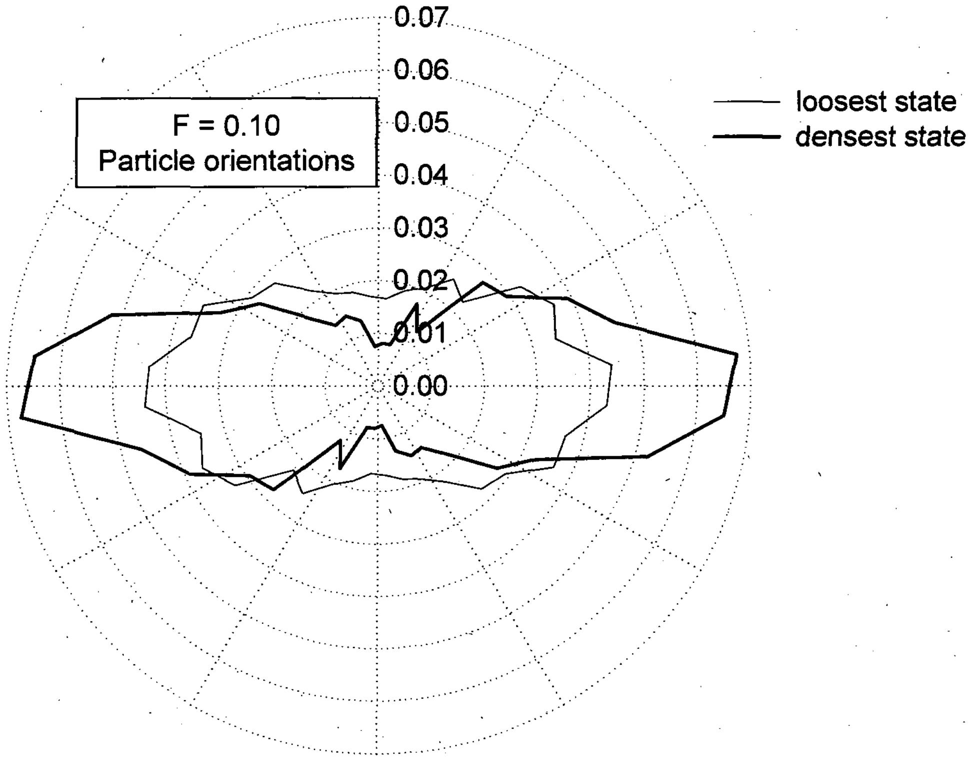

(b)

Figure 6.5: Polar distribution of particle orientations corresponding to forms 0.67 (a) and 0.10 (b) in loosest and densest states

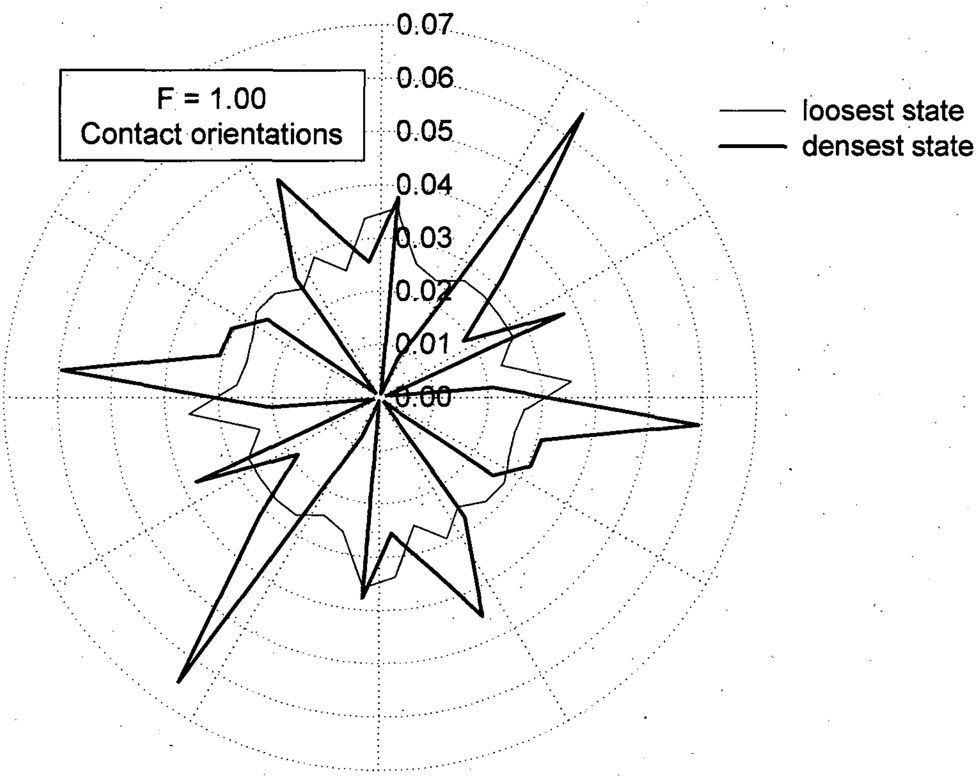

(a)

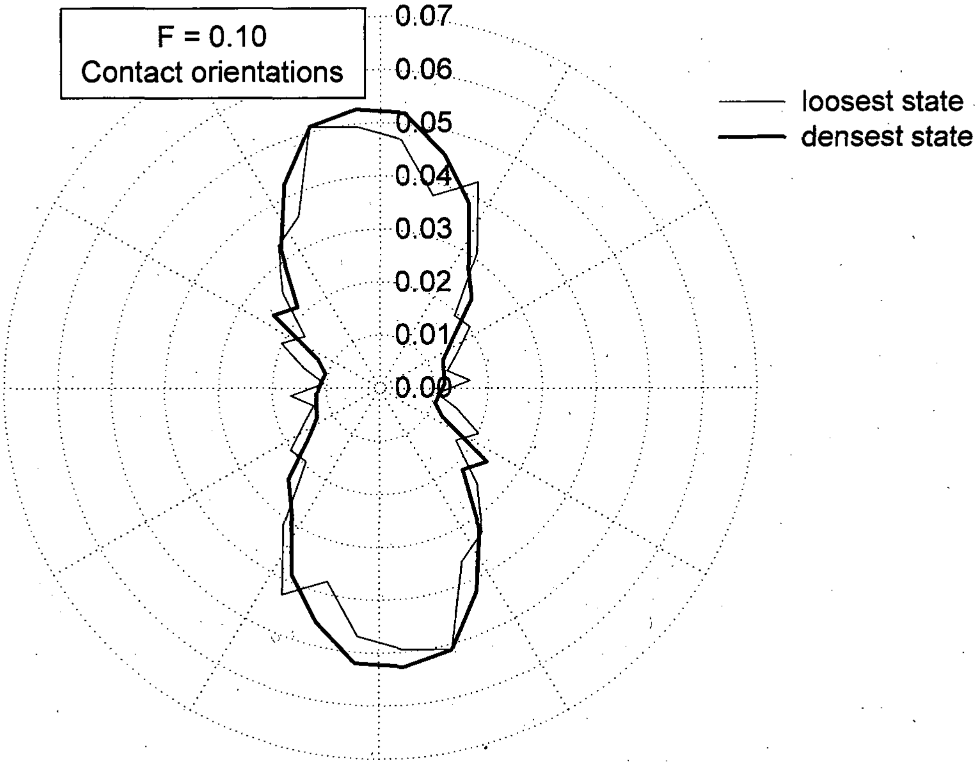

(b)

Figure 6.6: Polar distribution of contact orientations corresponding to forms 1.00 (a) and 0.10 (b) in loosest and densest states

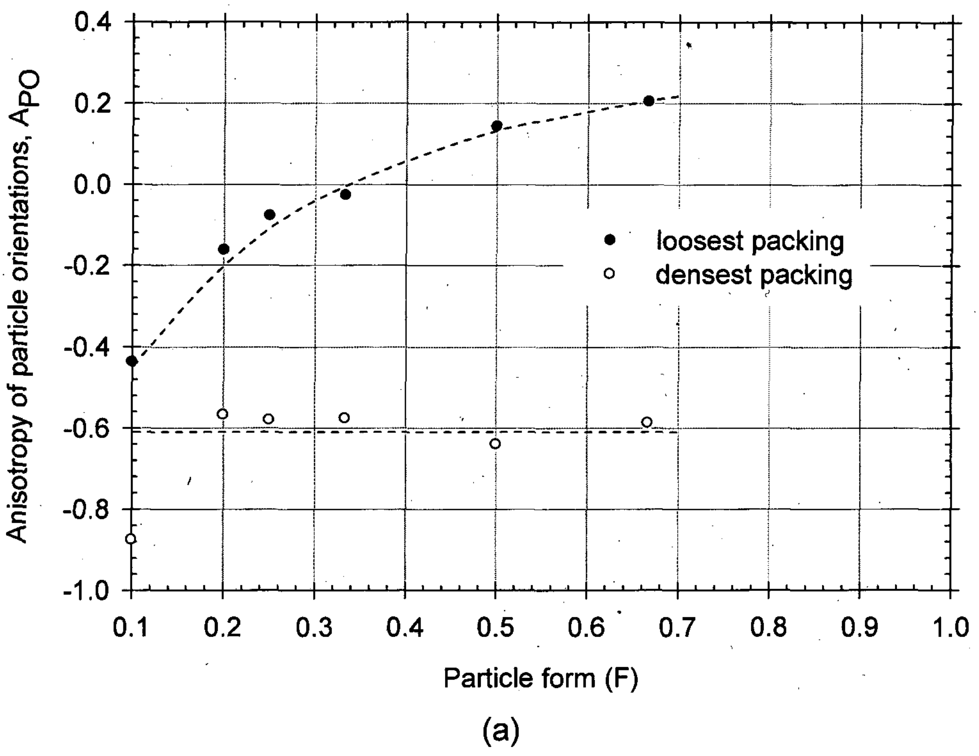

(a)

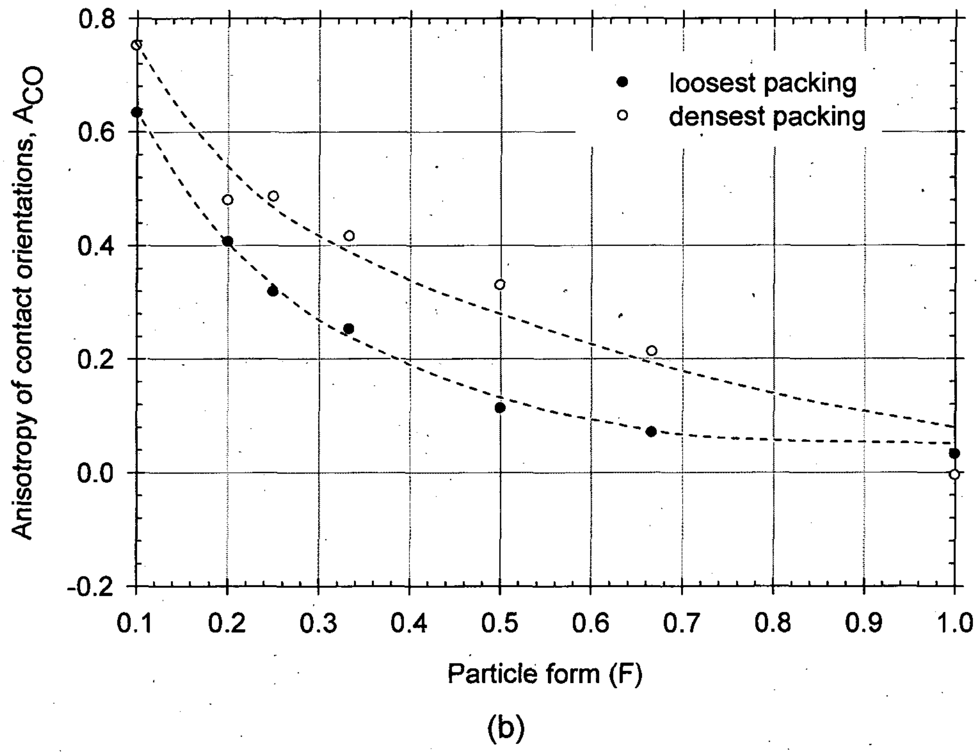

(b)

Figure 6.7: Variation of anisotropy of particle orientations (a) and contact orientations (b) with form in their loosest and densest states

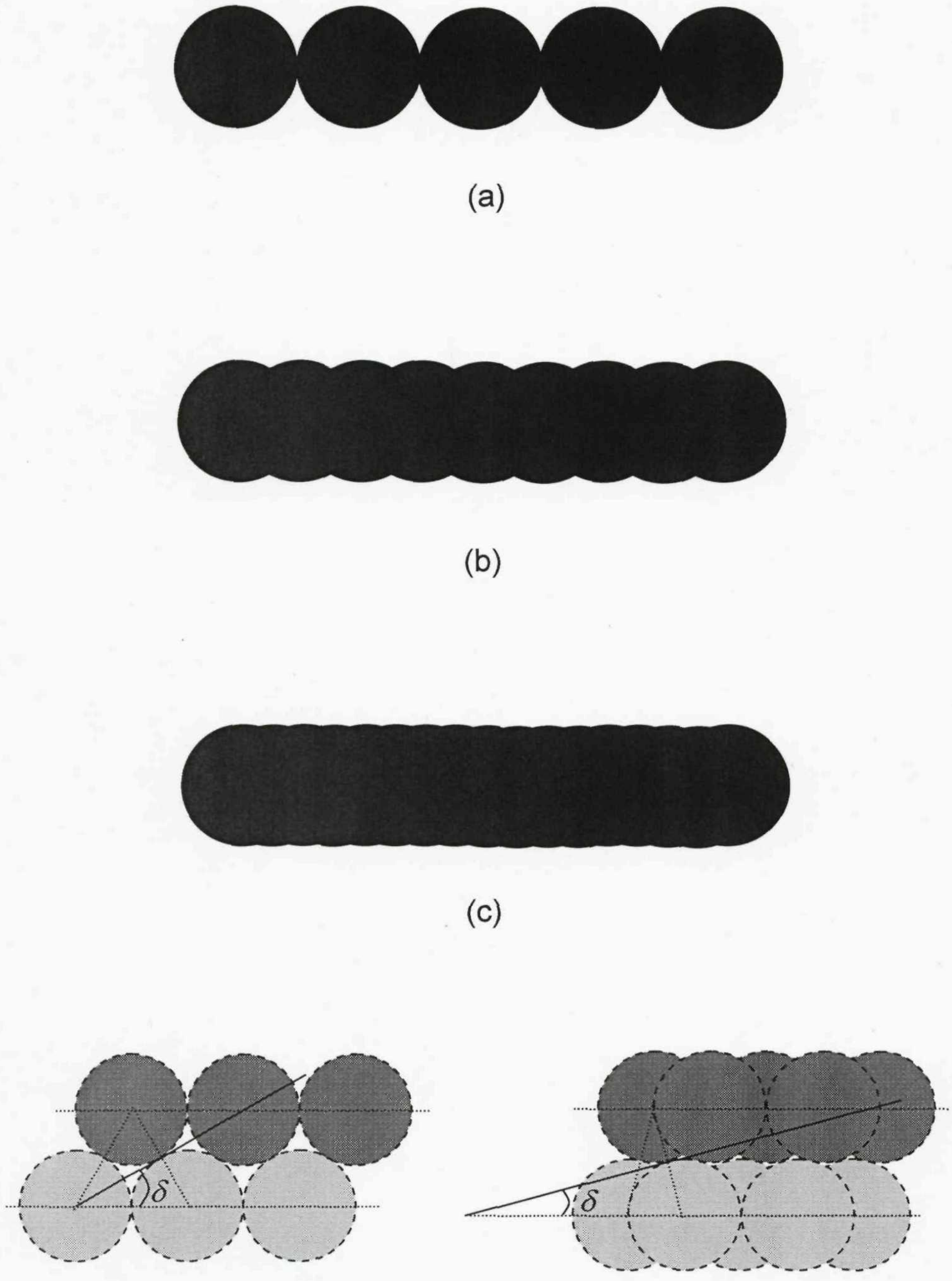

Note: See Table 6.2 for the corresponding asperity friction co-efficients.

Figure 6.8: Particle surface roughnesses (asperities) modelled: (a) single layer, (b) double layer, (c) triple layer, and (d) illustration of implied angle of rise (δ).

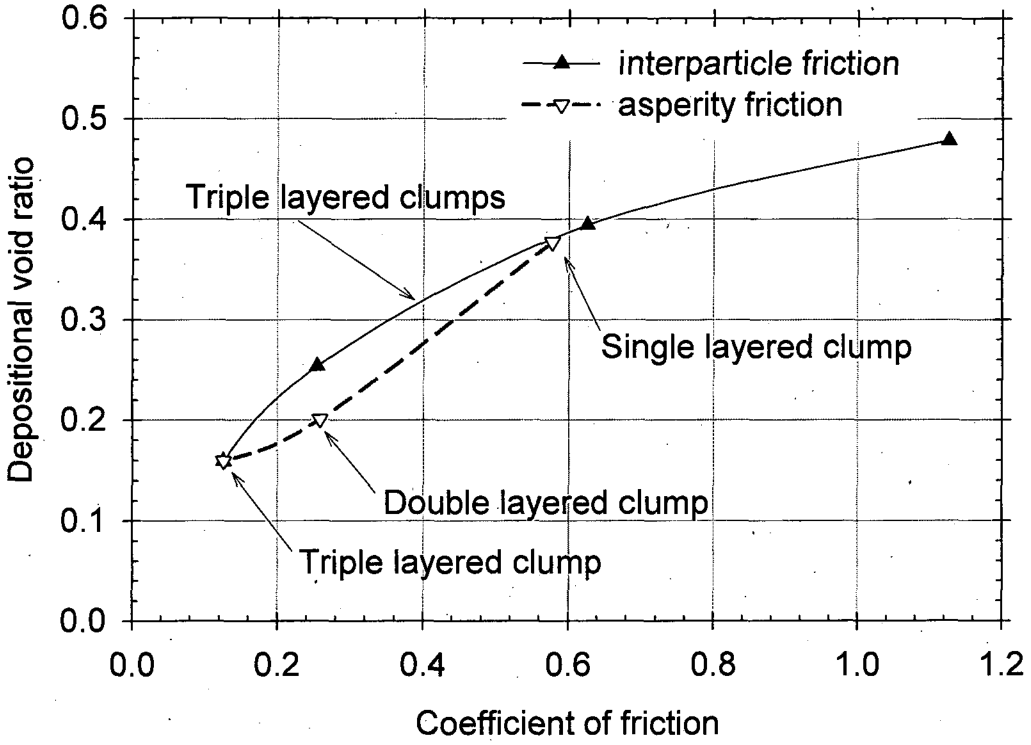

Figure 6.9: Variation of depositional void ratio with asperity friction and interparticle friction.

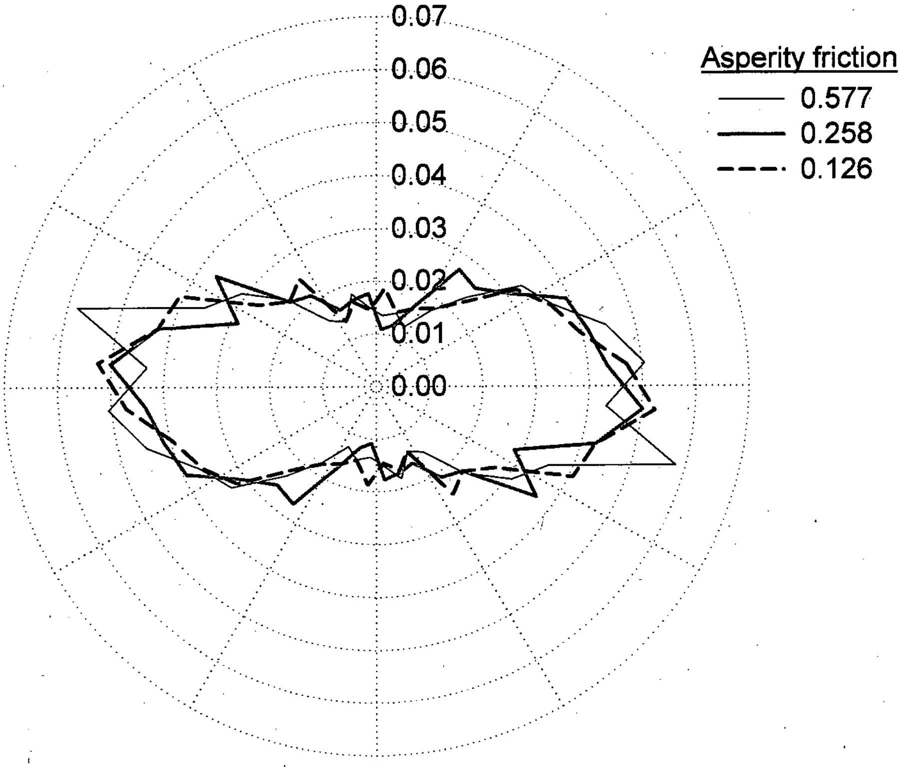

(a)

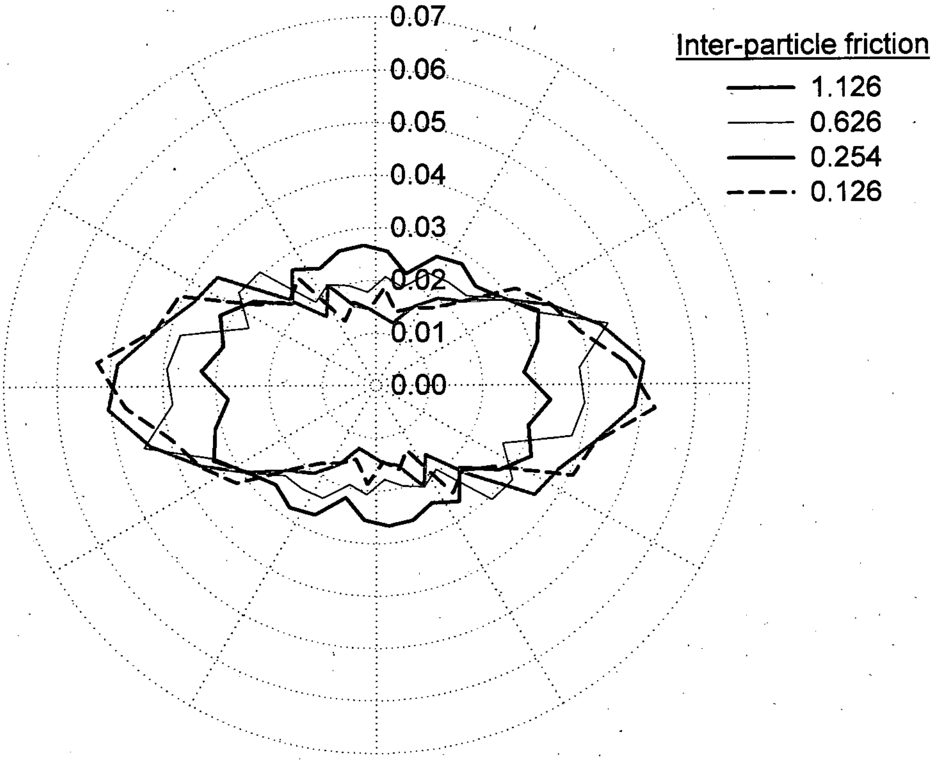

(b)

Figure 6.10: Polar distribution of particle orientations corresponding to various values of asperity friction (a) and inter-particle friction (b).

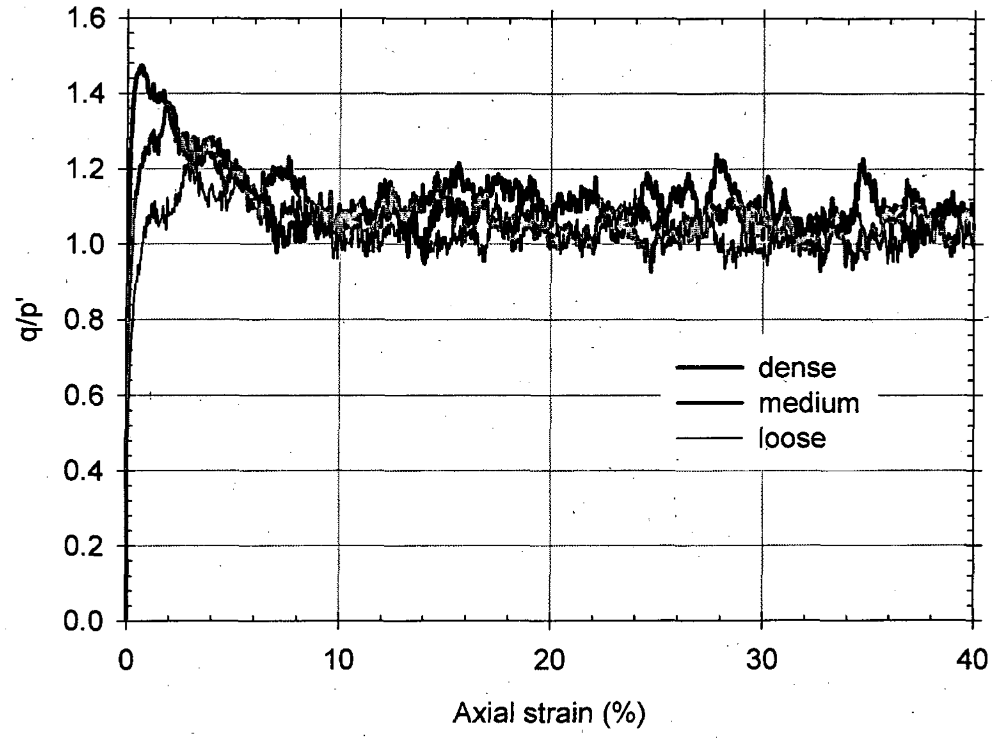

(a)

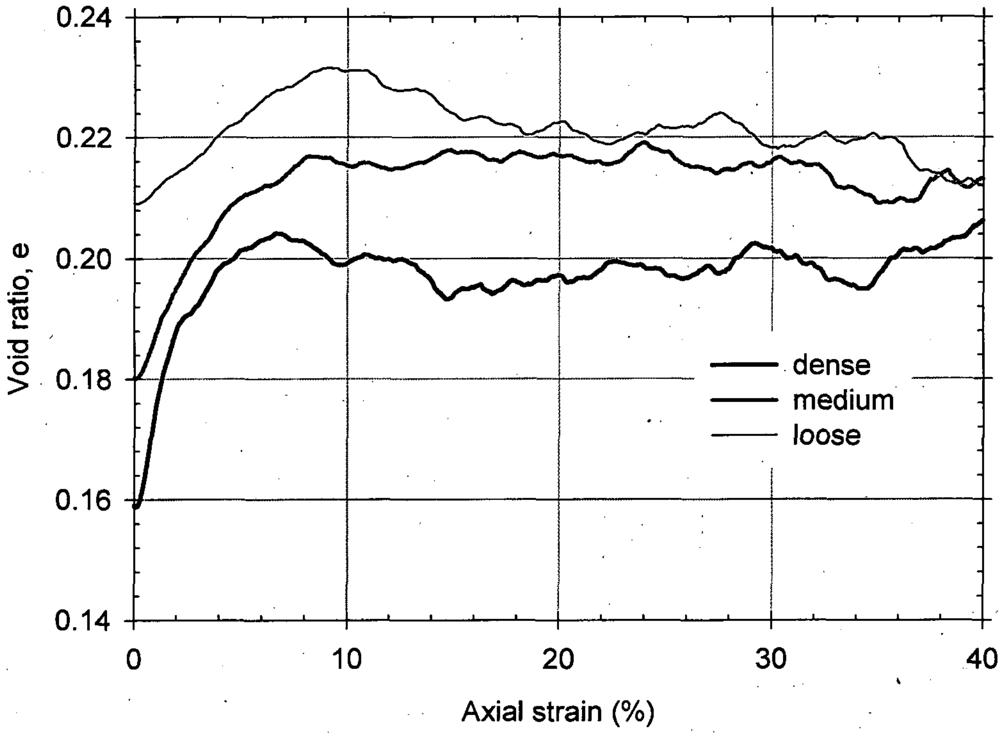

(b)

Figure 6.11: Stress ratio (a) and void ratio (b) vs. axial strain for form 1.0

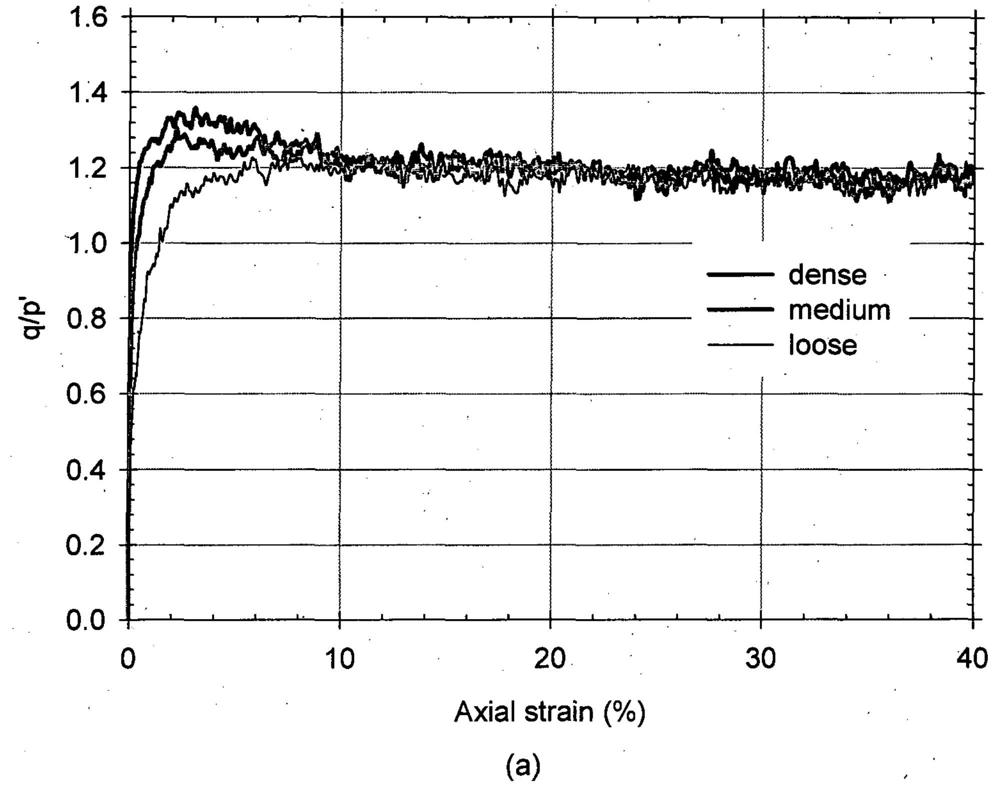

(a)

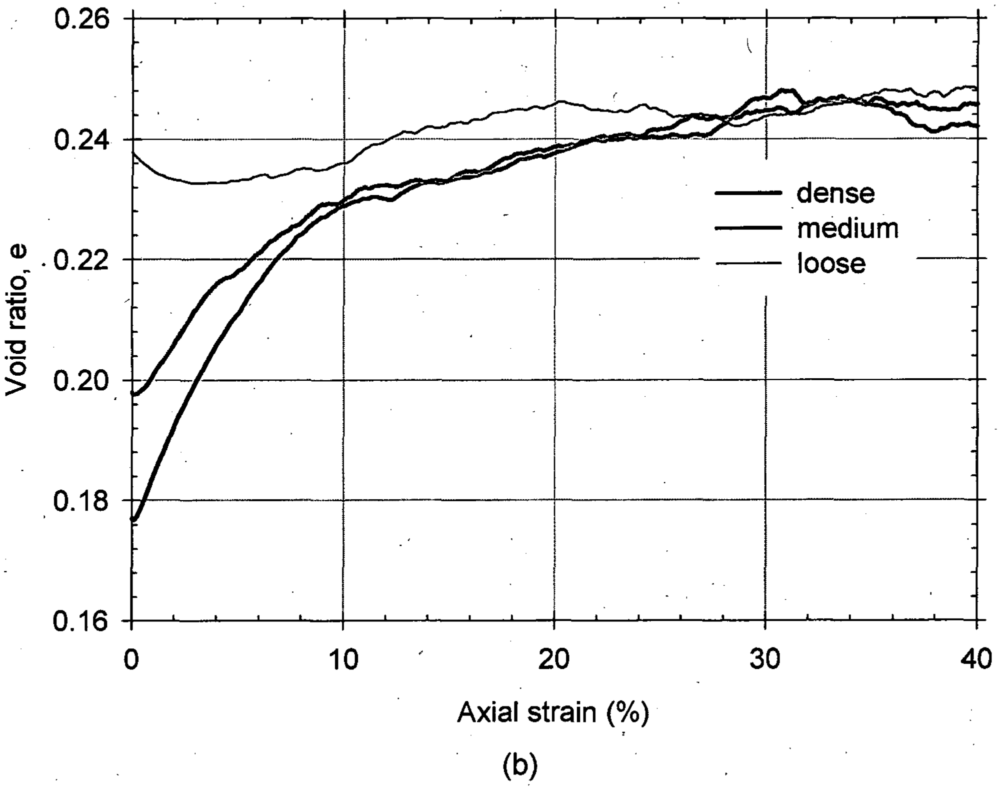

(b)

Figure 6.12: Stress ratio (a) and void ratio (b) vs. axial strain for form 0.67

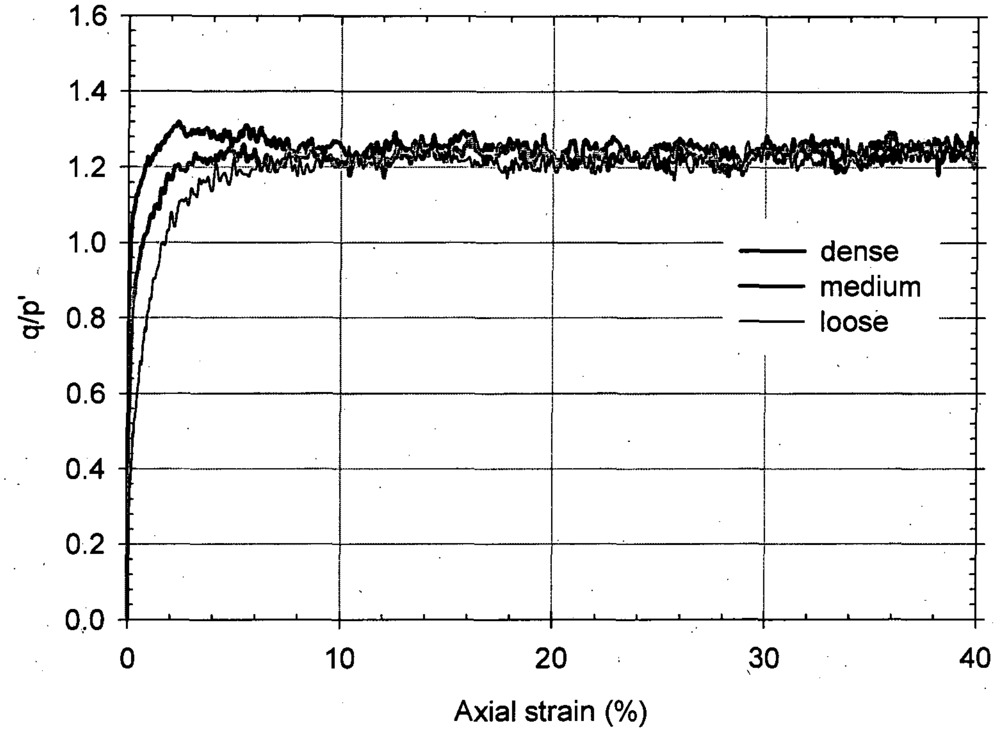

(a)

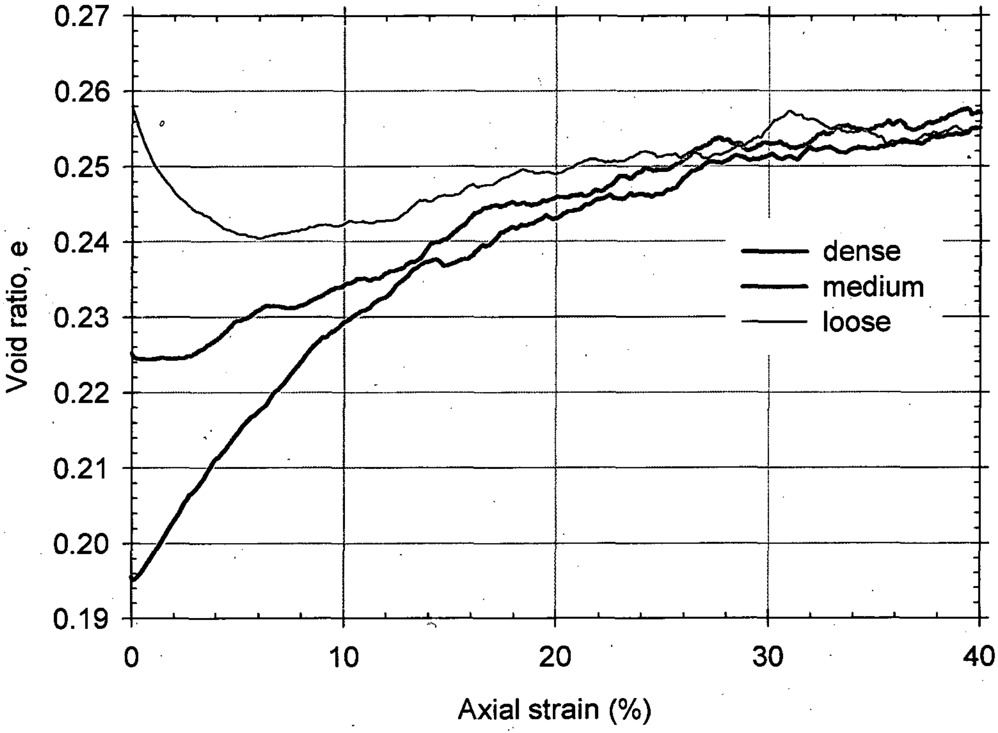

(b)

Figure 6.13: Stress ratio (a) and void ratio (b) vs. axial strain for form 0.50

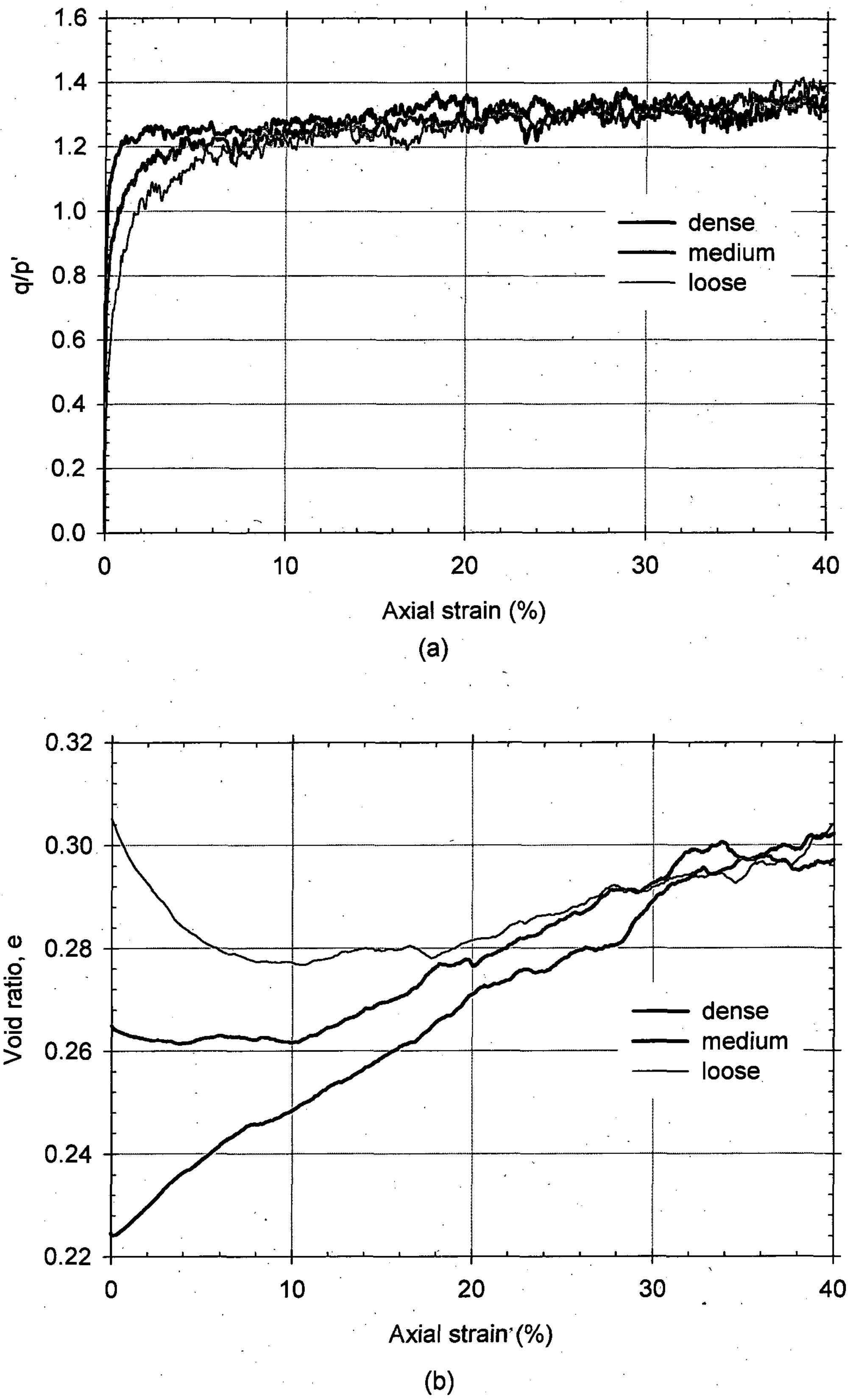

Figure 6.14: Stress ratio (a) and void ratio (b) vs. axial strain for form 0.33

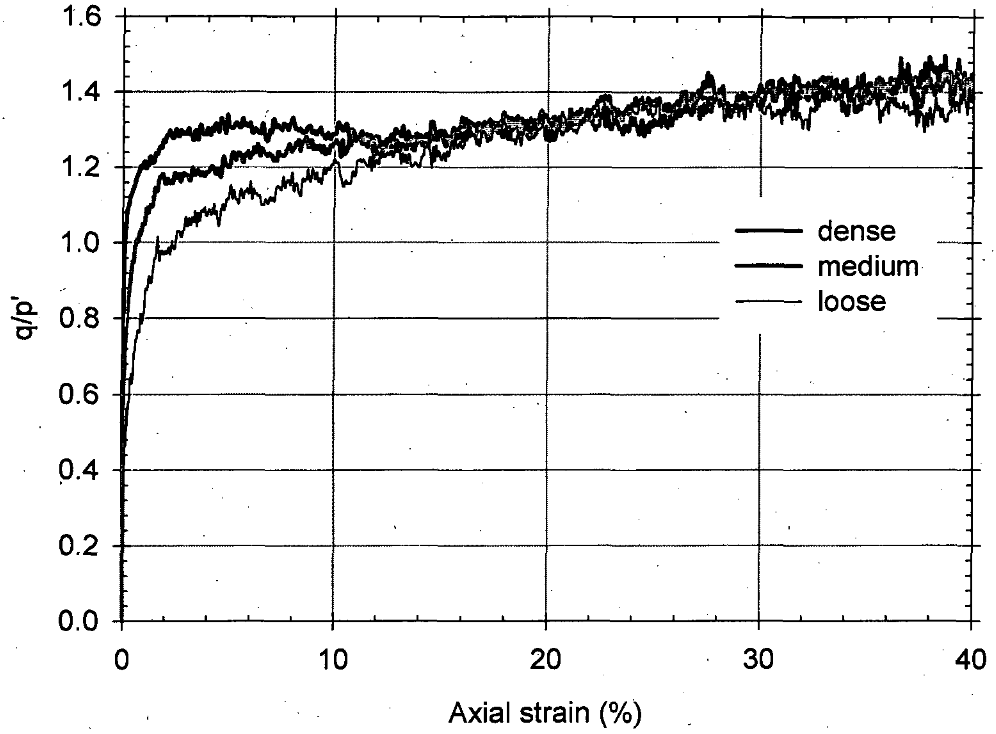

(a)

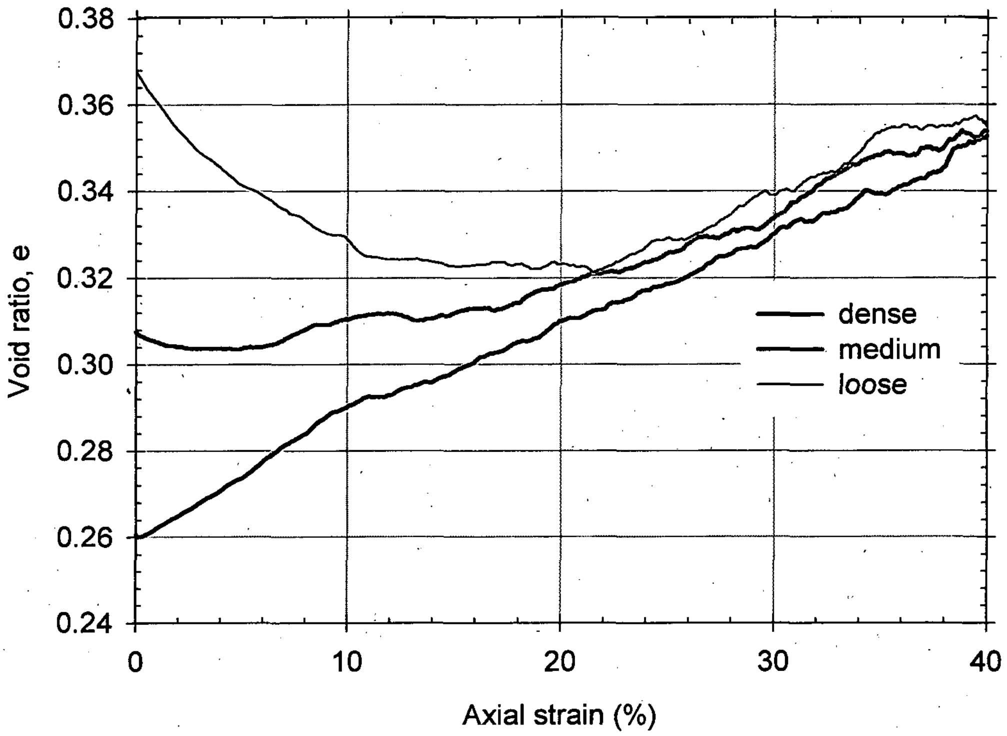

(b)

Figure 6.15: Stress ratio (a) and void ratio (b) vs. axial strain for form 0.25

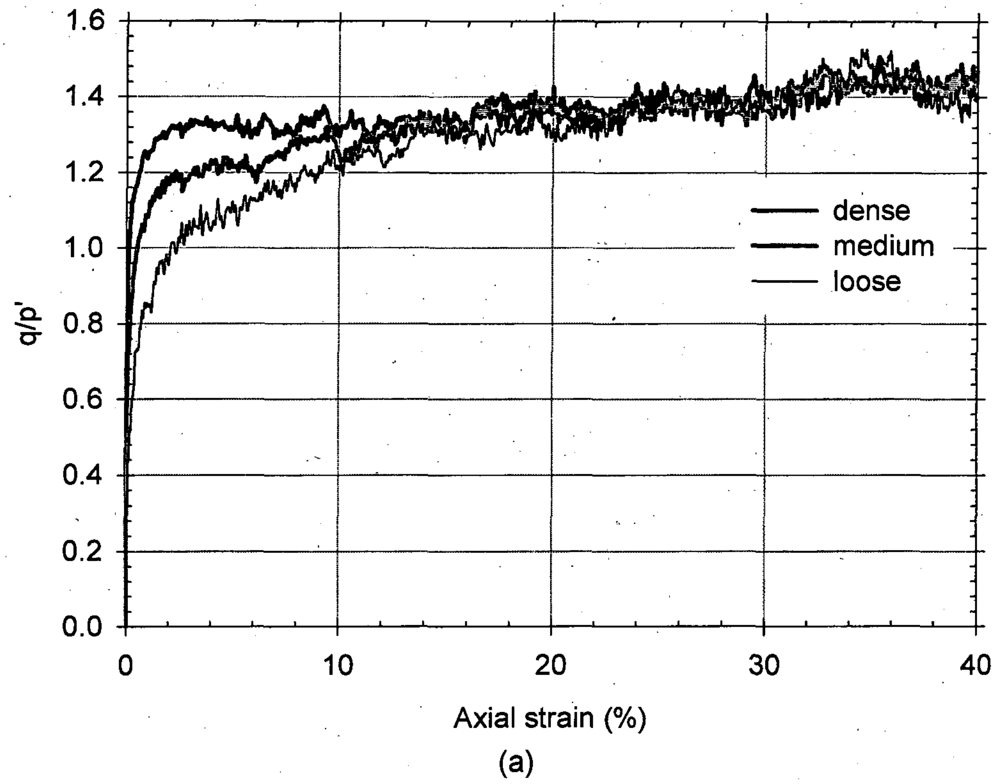

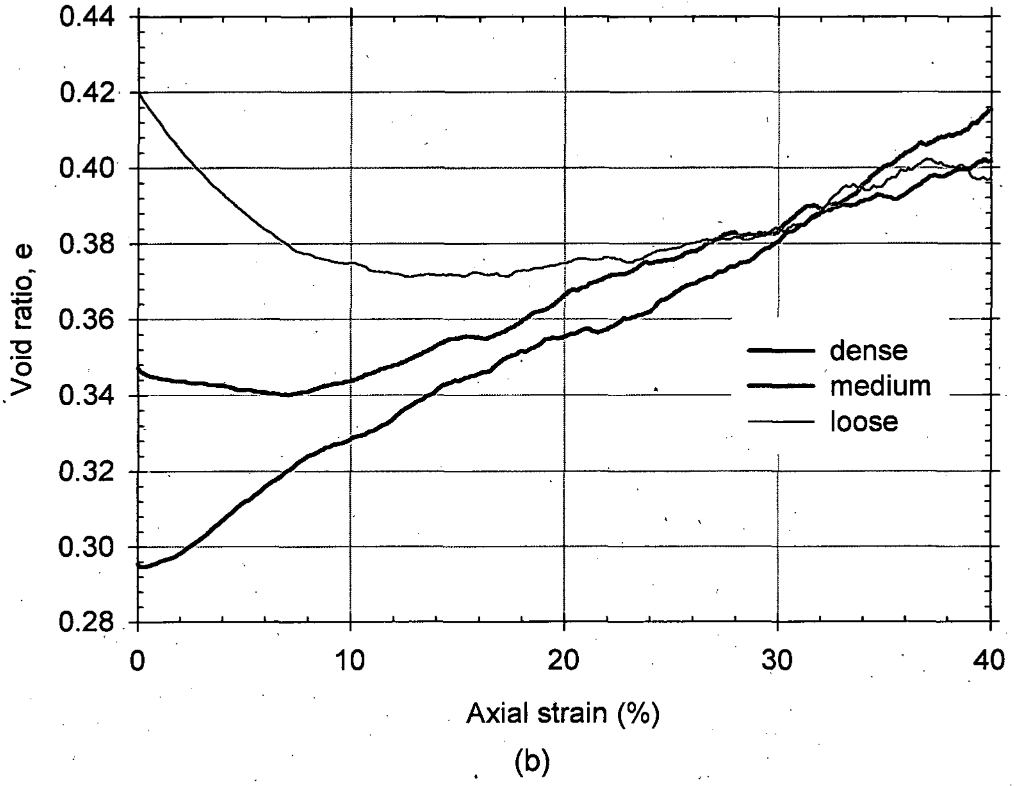

Figure 6.16: Stress ratio (a) and void ratio (b) vs. axial strain for form 0.20

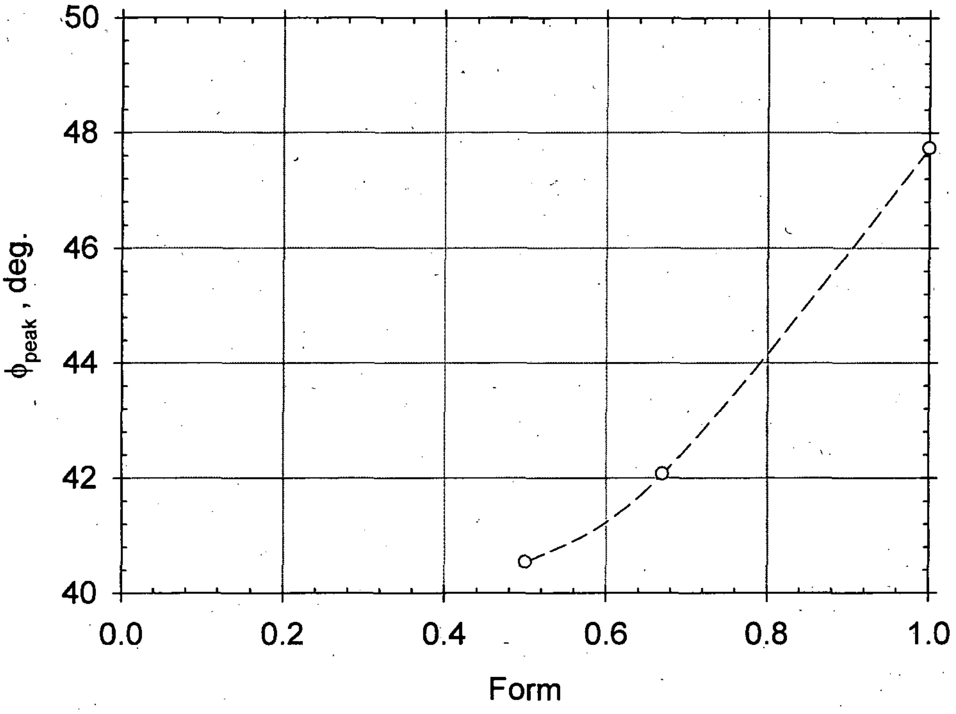

(a)

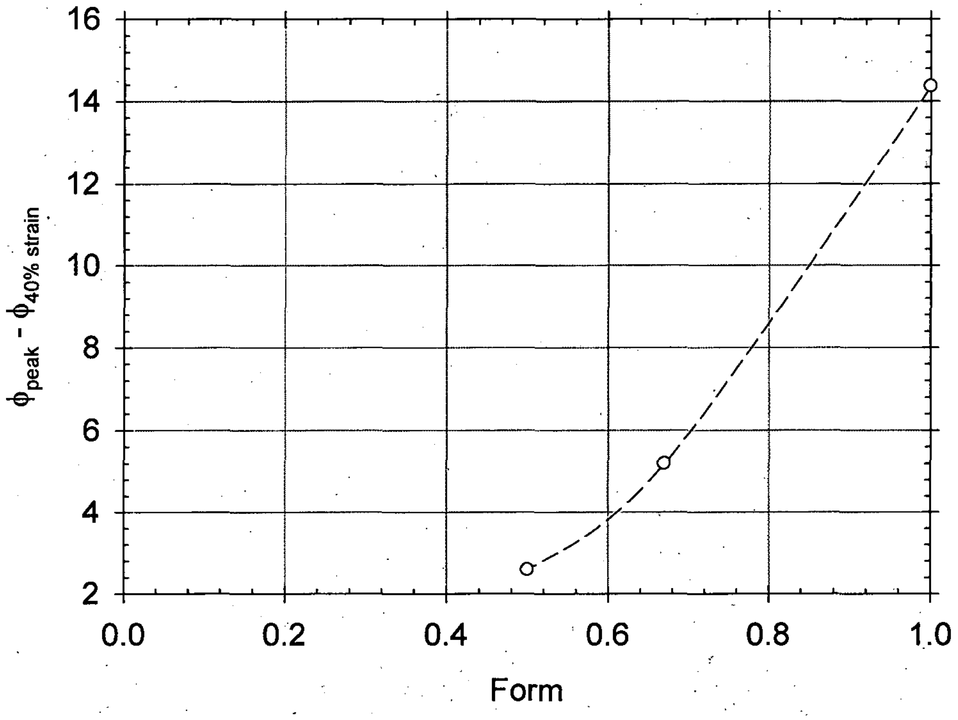

(b)

Figure 6.17: Variation of peak friction angle (a) and difference between peak and large strain friction angle (b) with respect to form

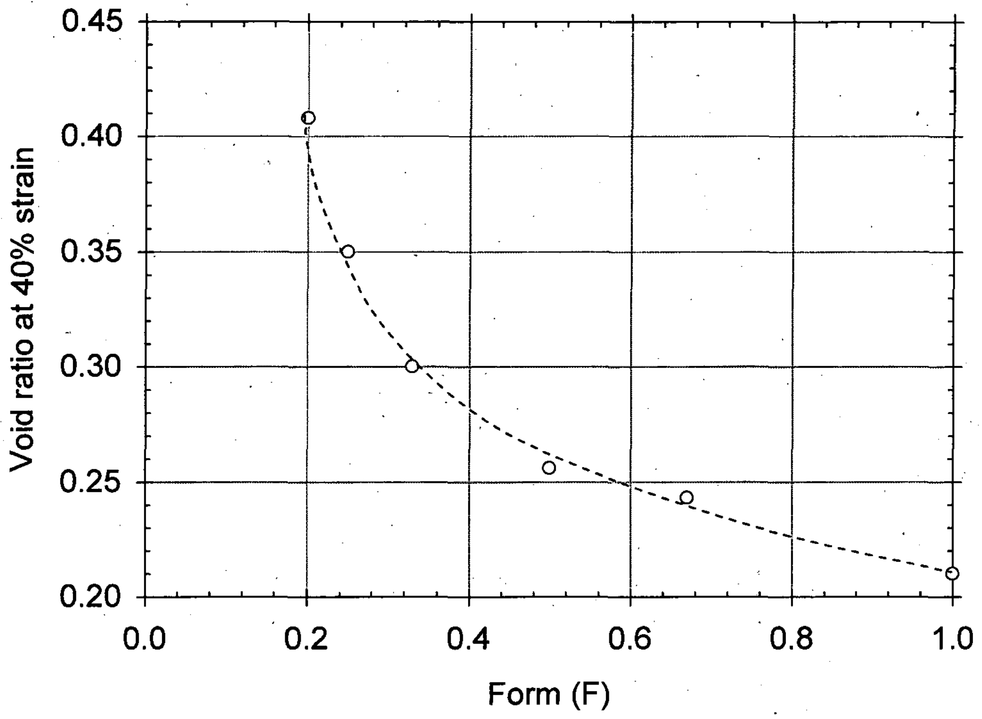

(a)

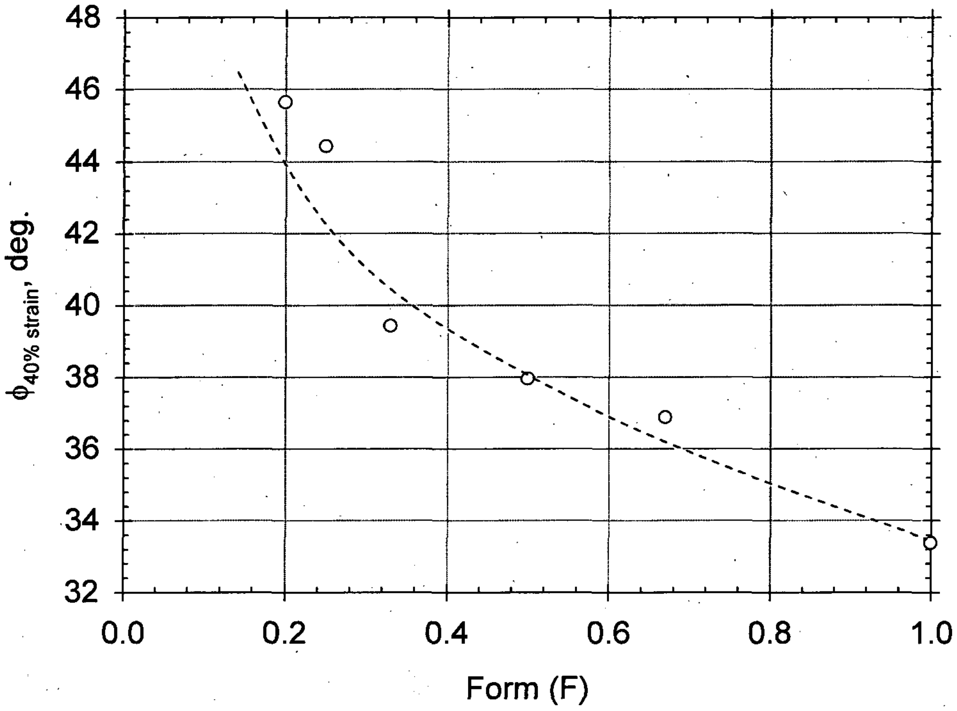

(b)

Figure 6.18: Variation of void ratio (a) and mobilised friction angle (b) at 40% strain with respect to form

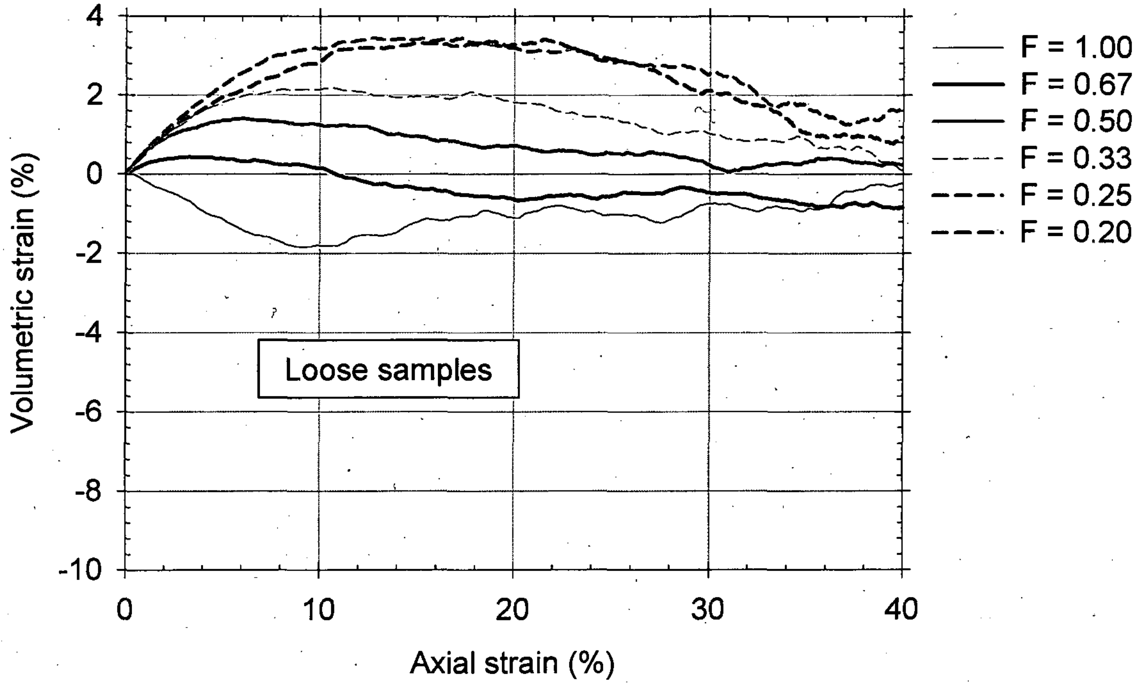

(a)

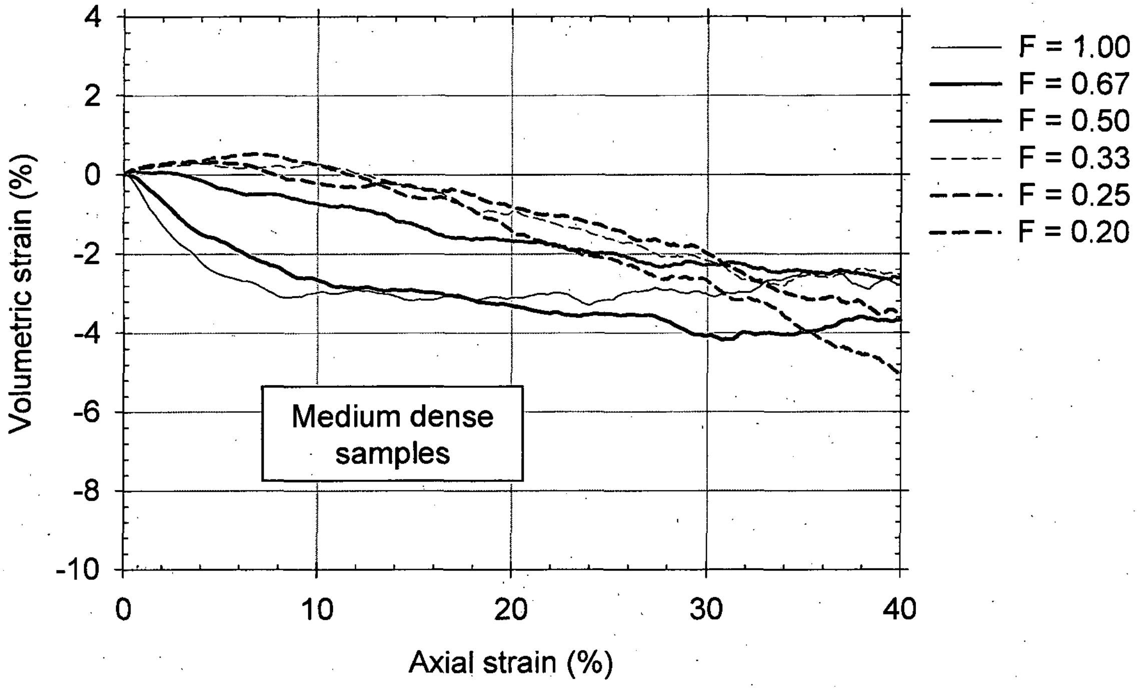

(b)

Figure 6.19: Volume change behaviour of (a) loose, (b) medium dense and (c) samples corresponding to various forms (contd..)

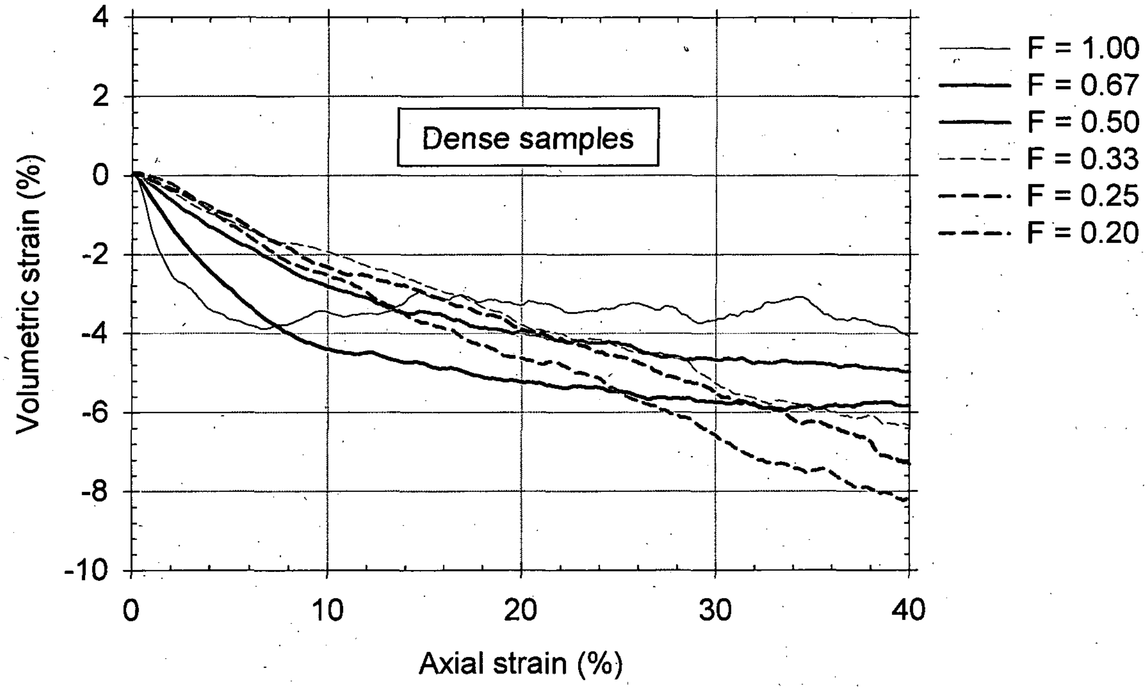

(c)

Figure 6.19: Volume change behaviour of dense samples corresponding to various forms

(a)

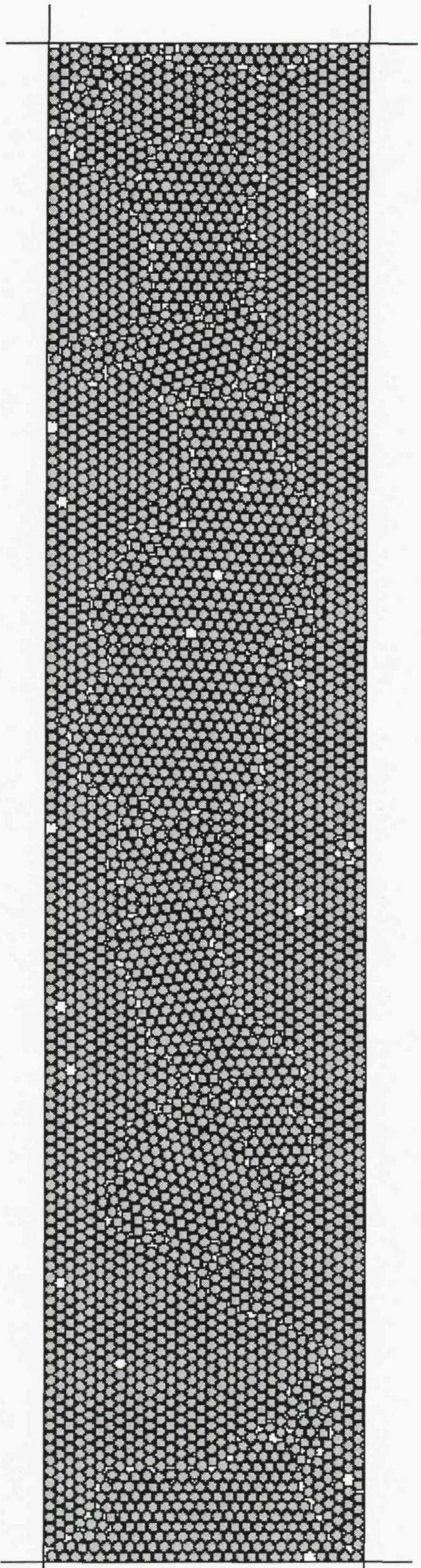

Figure 6.20: Packing arrangement of cylindrical particles (F = 1.0) in dense sample at the (a) start of shearing and (b) end of shearing i.e. 40% axial strain (contd..)

(b)

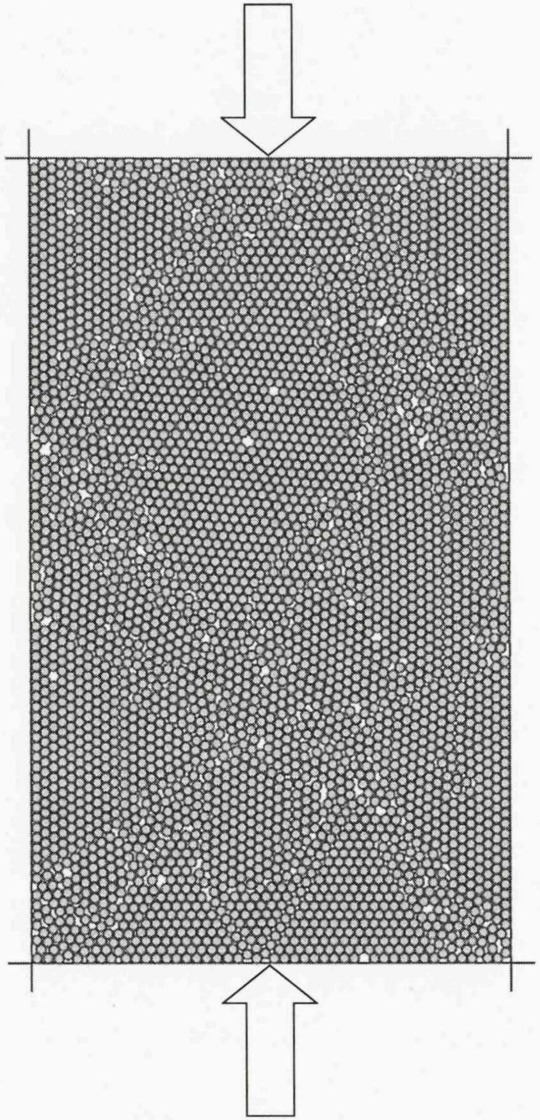

Figure 6.20: Packing arrangement of cylindrical particles (F = 1.0) in dense sample at the (a) start of shearing and (b) end of shearing i.e. 40% axial strain

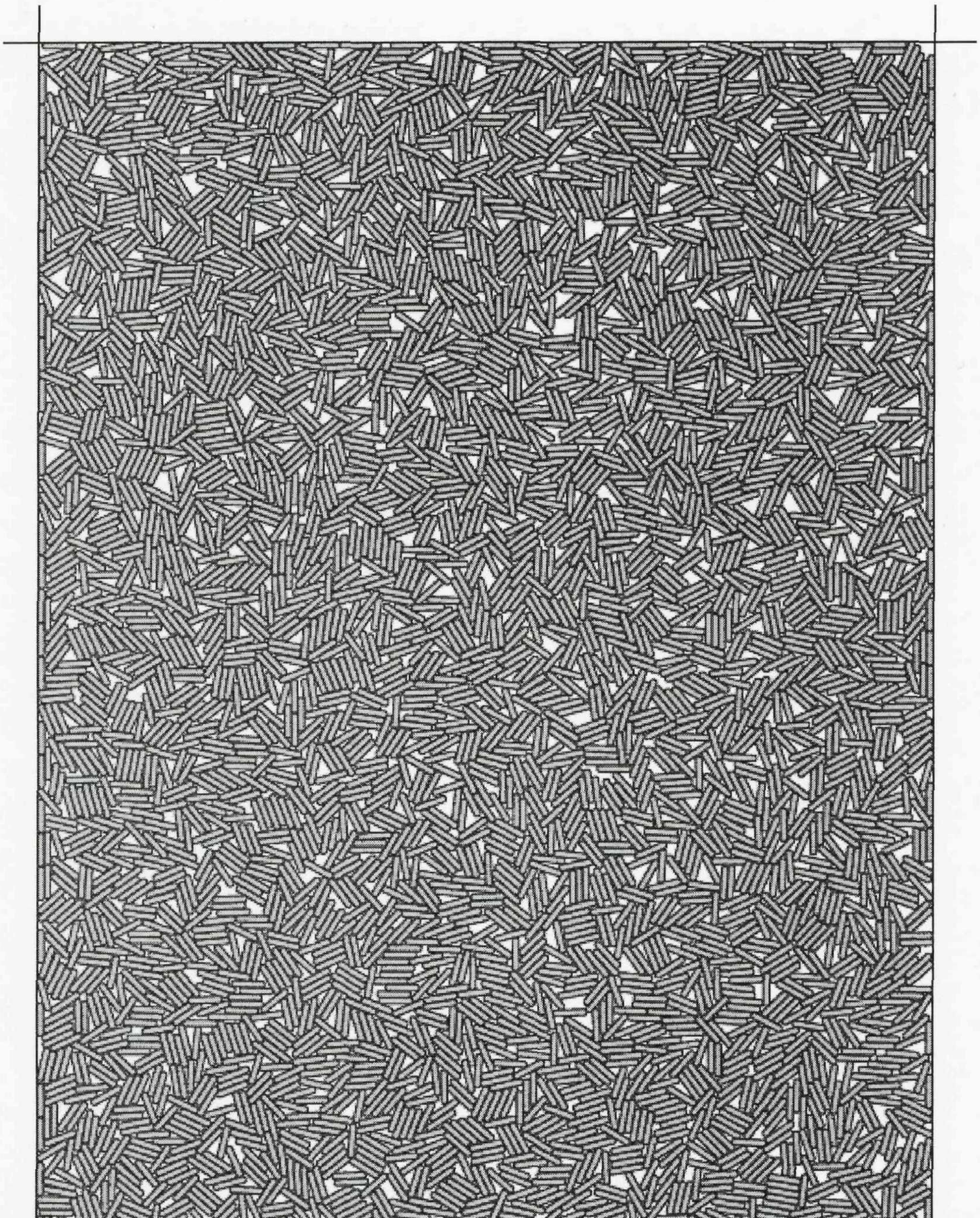

(a)

Figure 6.21: Packing arrangement of platy particles (F = 0.20) in dense sample at the (a) start of shearing and (b) end of shearing (contd..)

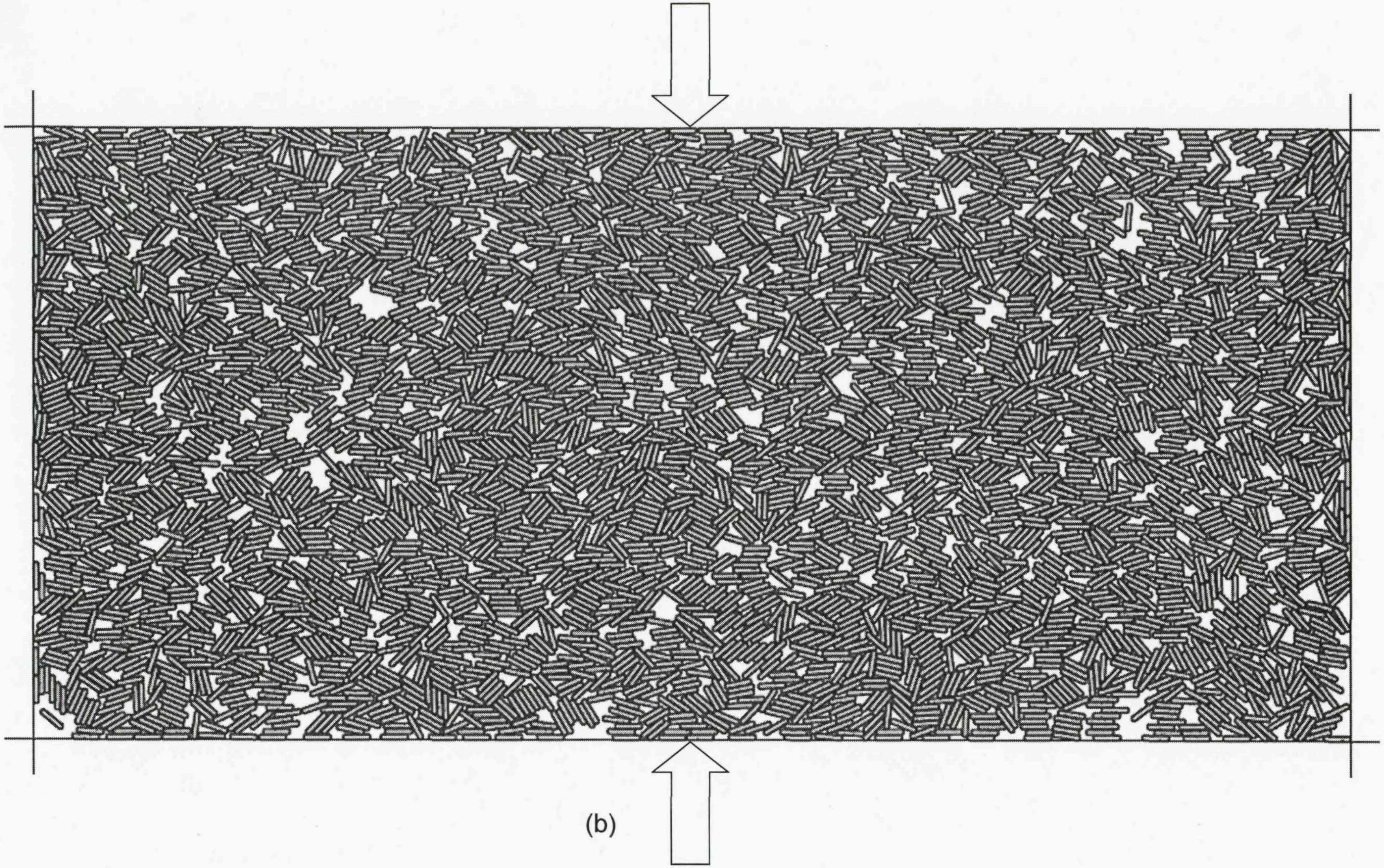

(b)

Figure 6.21: Packing arrangement of platy particles (F = 0.20) in dense sample at the (a) start of shearing and (b) end of shearing

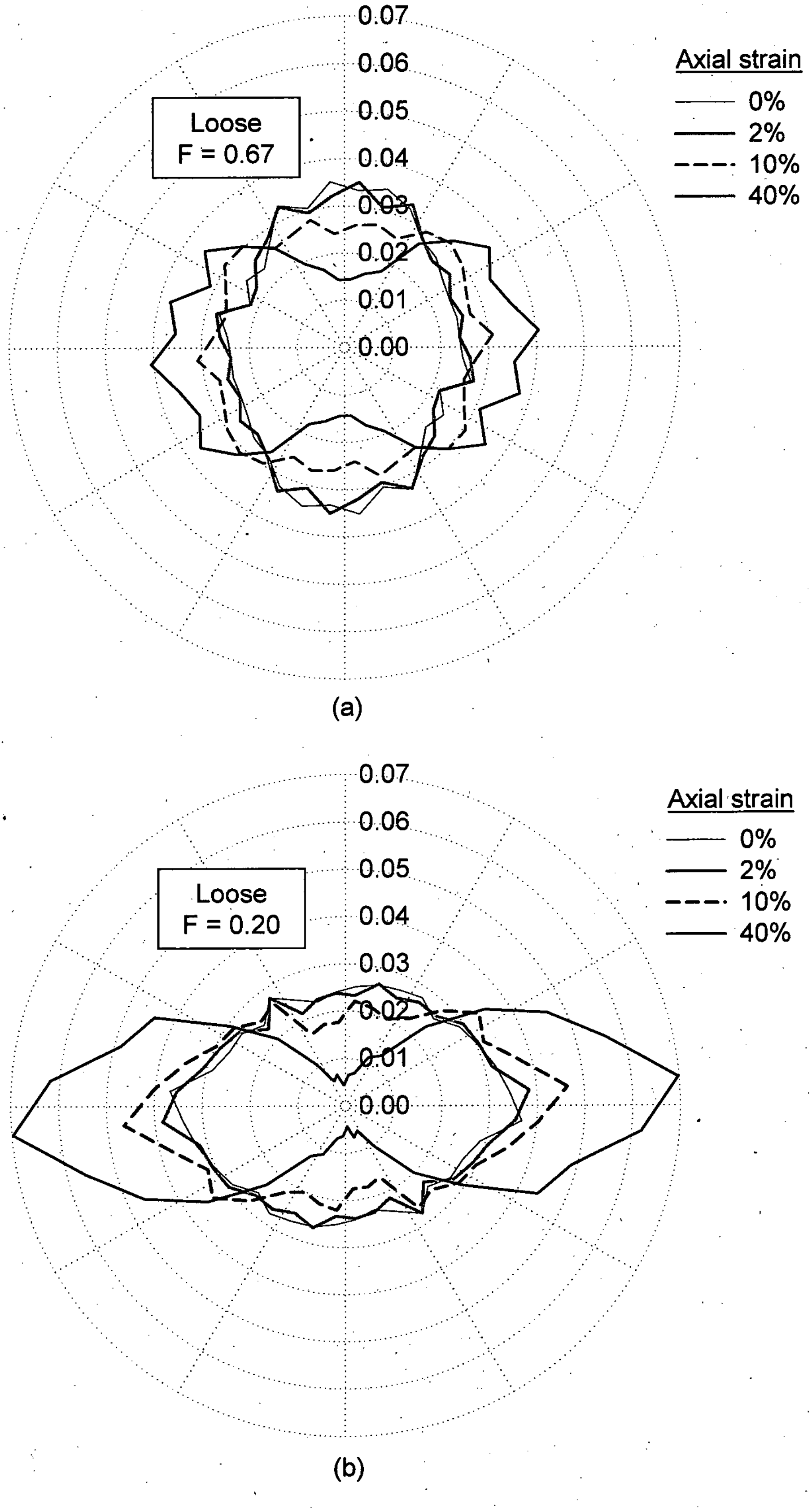

Figure 6.22: Polar distribution of particle orientations corresponding to forms (a) 0.67 and (b) 0.20 – loose samples

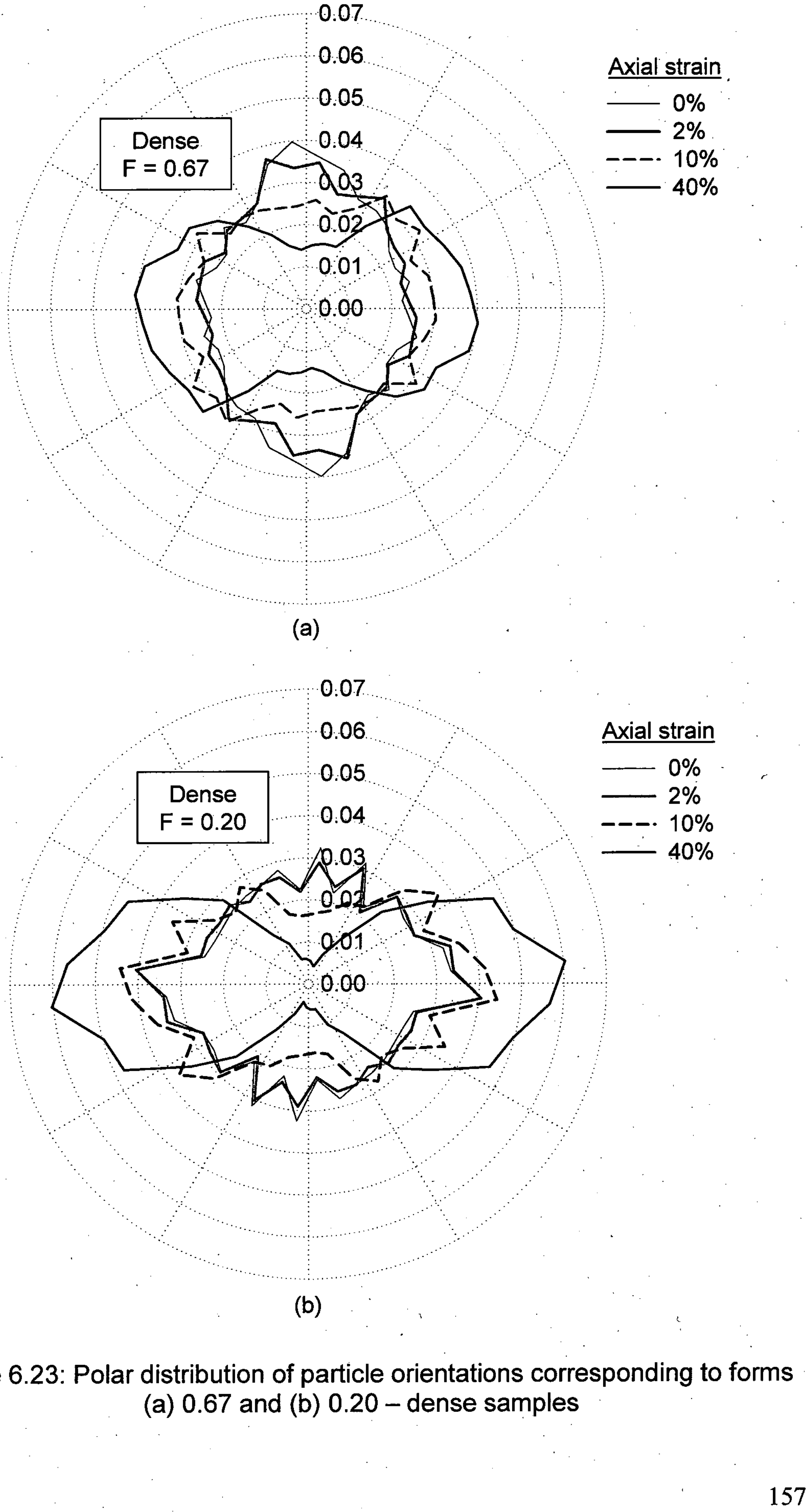

(a)

(b)

Figure 6.23: Polar distribution of particle orientations corresponding to forms (a) 0.67 and (b) 0.20 – dense samples

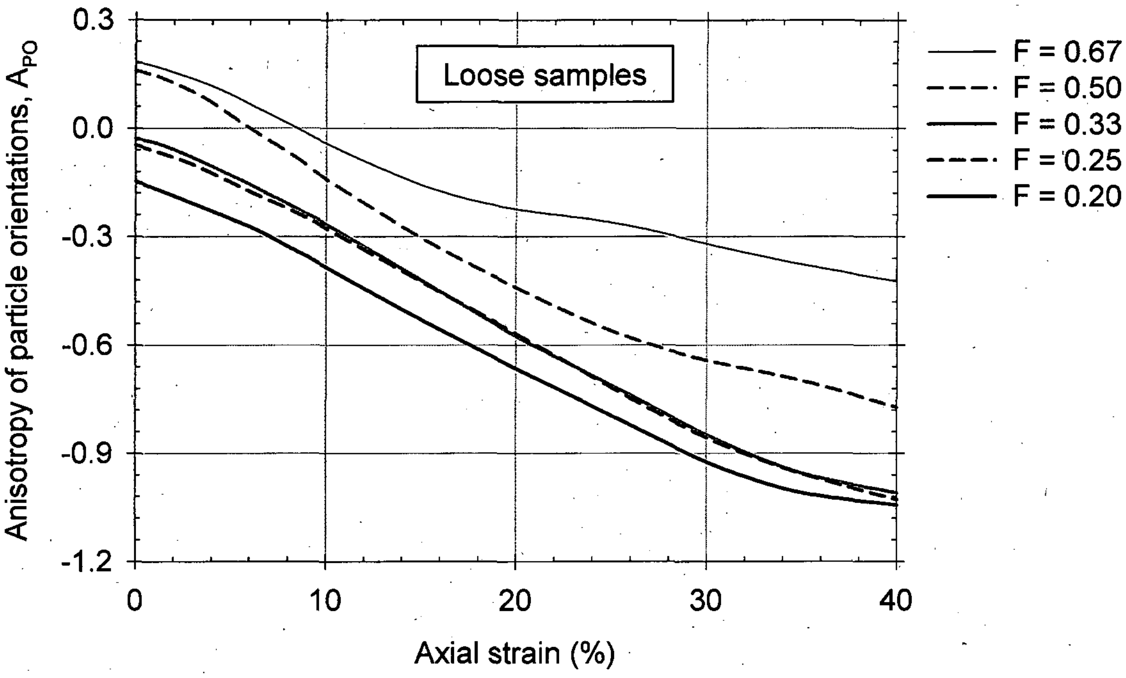

(a)

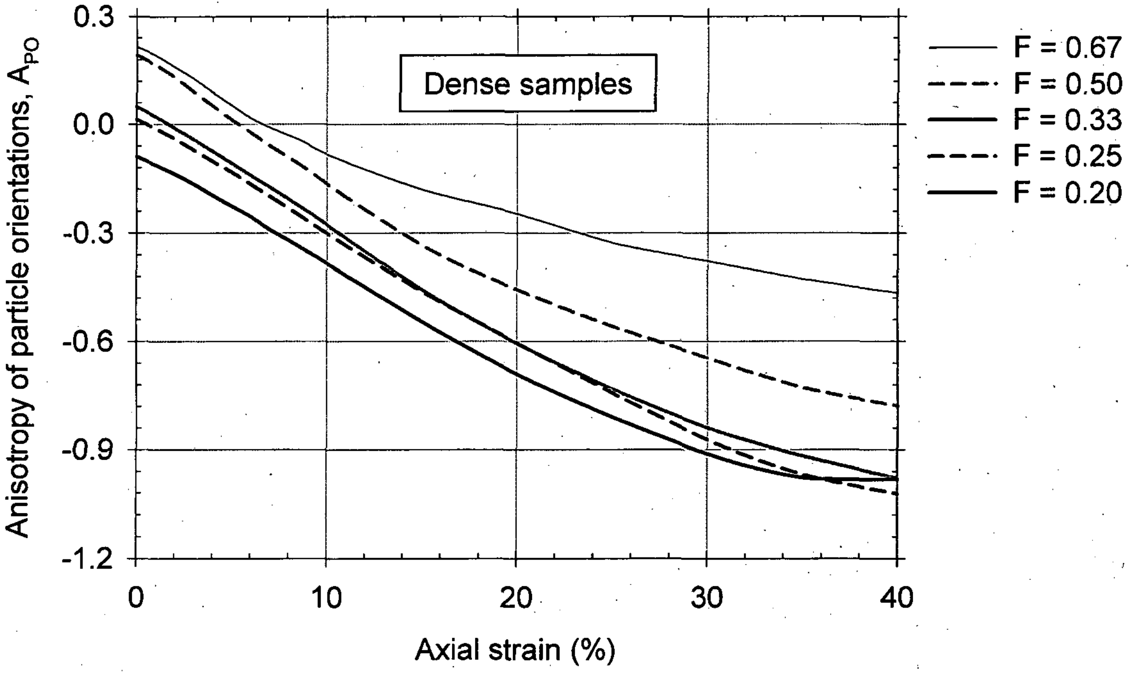

(b)

Figure 6.24: Evolution of anisotropy of particle orientations in (a) loose and (b) dense samples of various forms

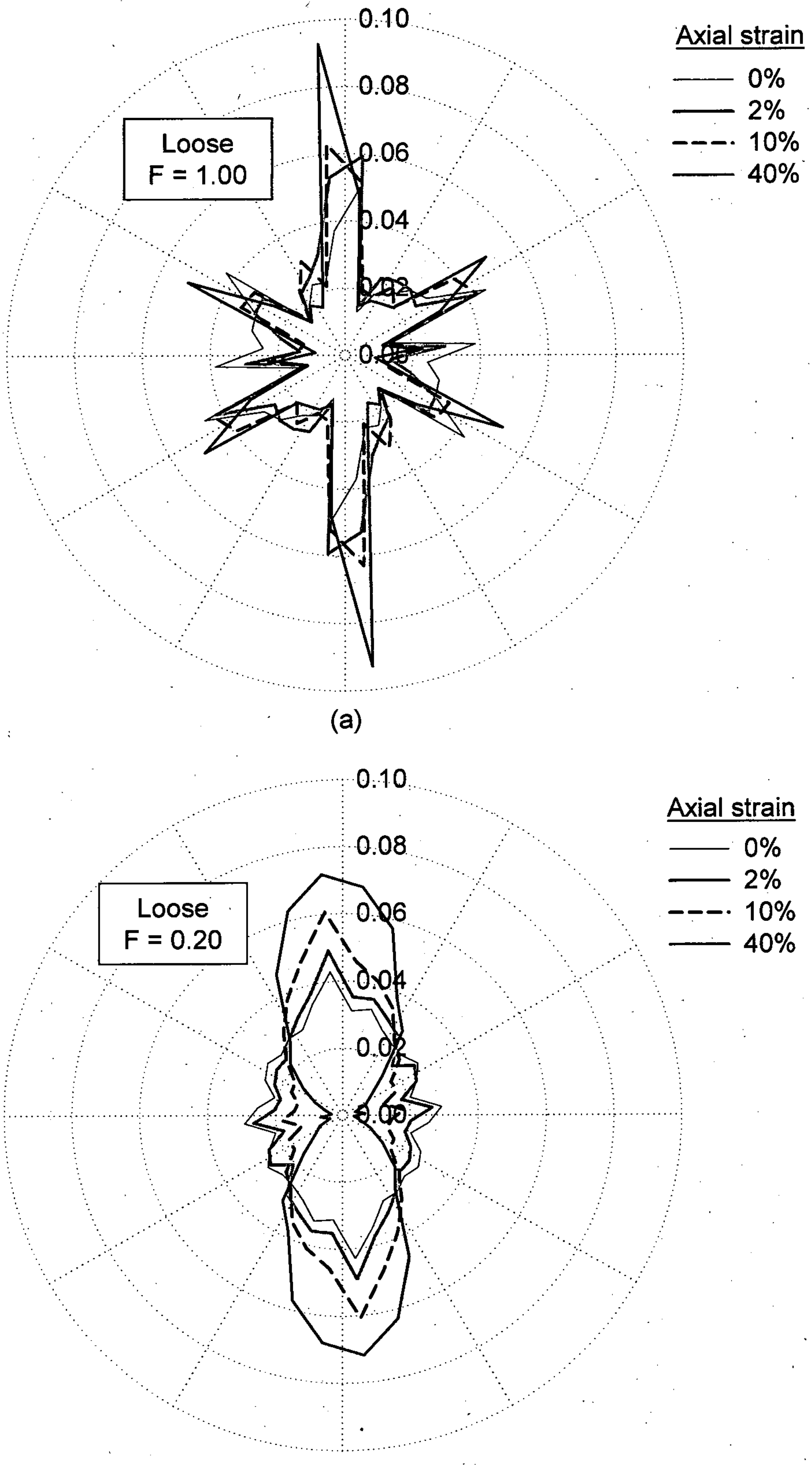

(a)

(b)

Figure 6.25: Polar distribution of contact normals corresponding to forms (a) 1.00 and (b) 0.20 – loose samples

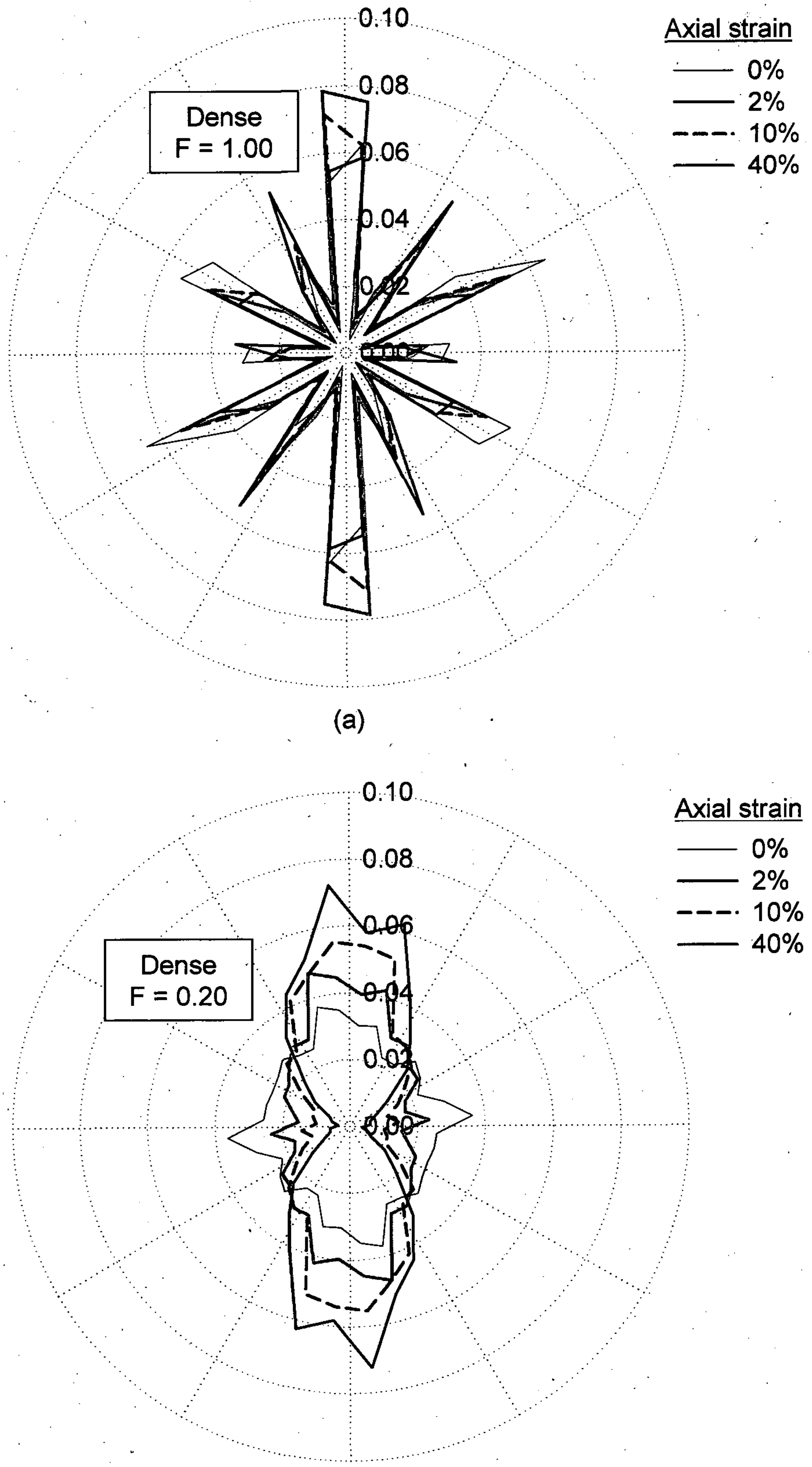

(a)

(b)

Figure 6.26: Polar distribution of contact normals corresponding to forms (a) 1.00 and (b) 0.20 – dense samples

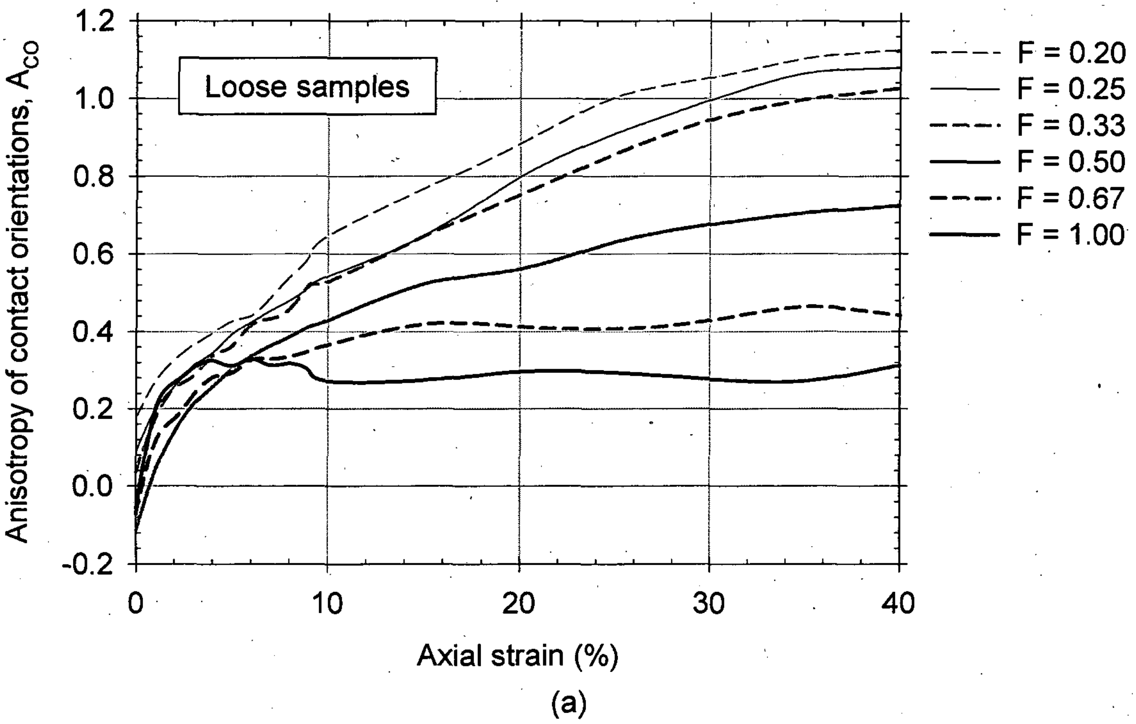

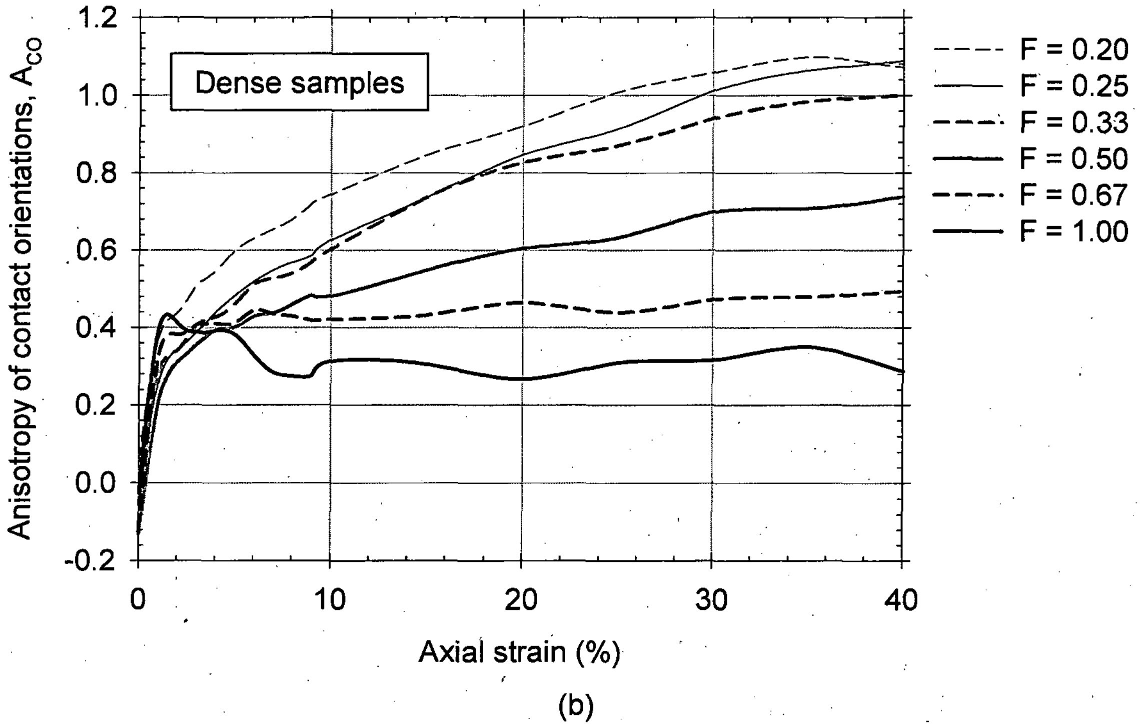

Figure 6.27: Evolution of anisotropy of contact orientations in (a) loose and (b) dense samples for various forms

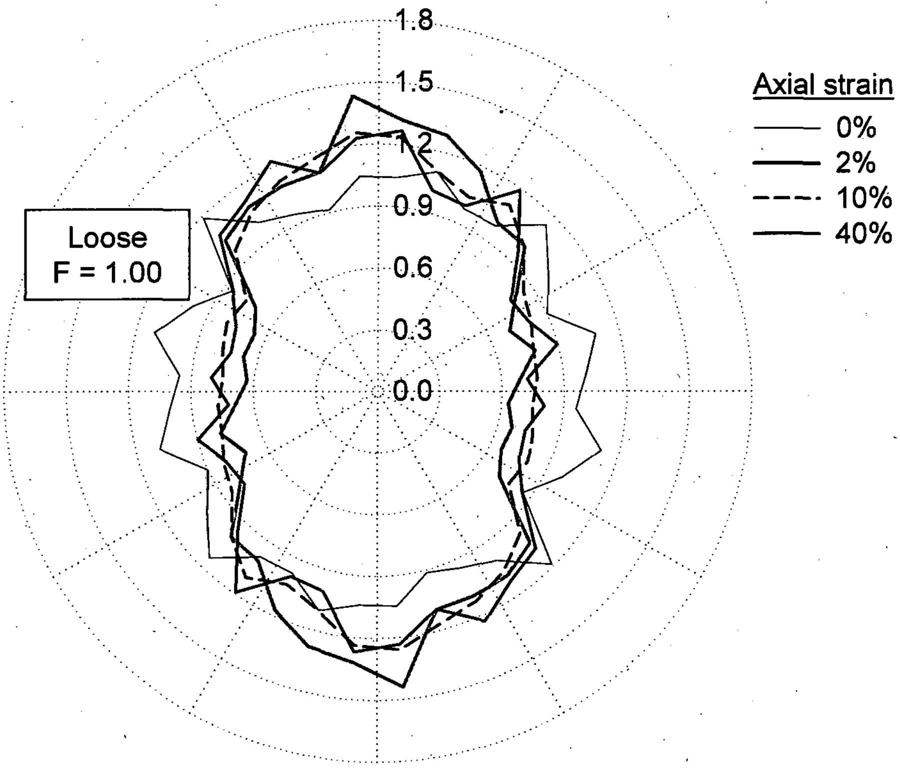

(a)

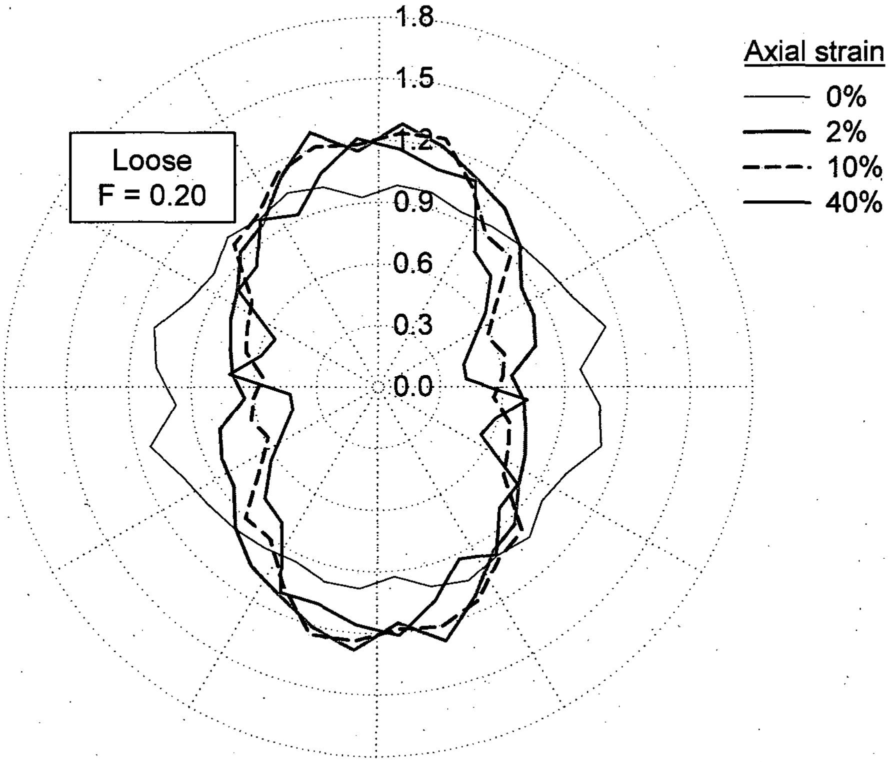

(b)

Figure 6.28: Polar distribution of normal forces corresponding to forms (a) 1.00 and (b) 0.20 – loose samples

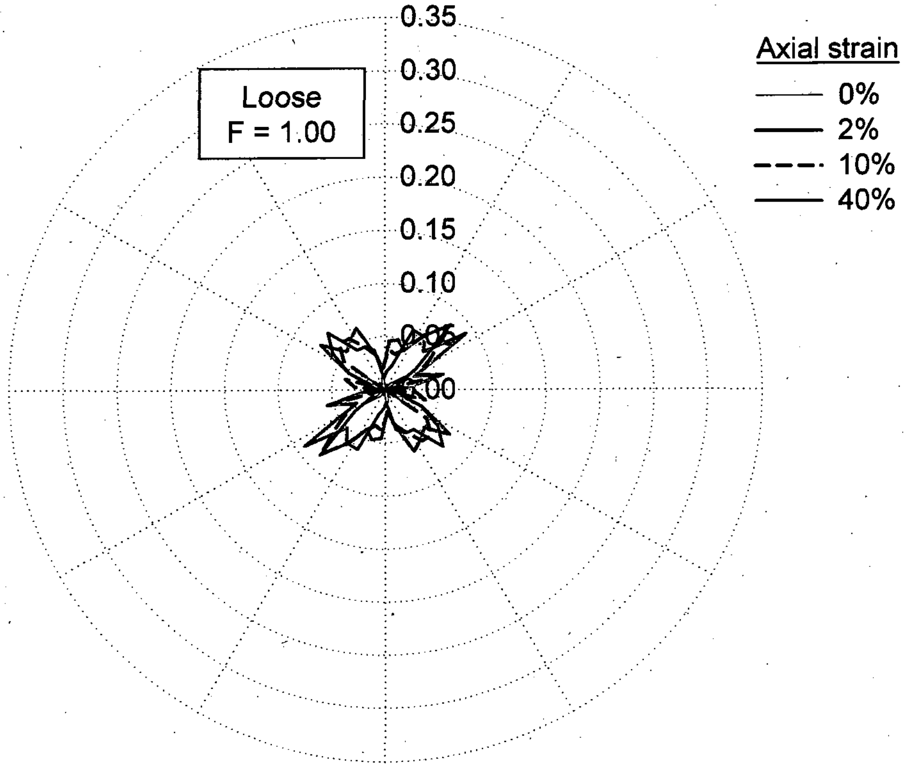

(a)

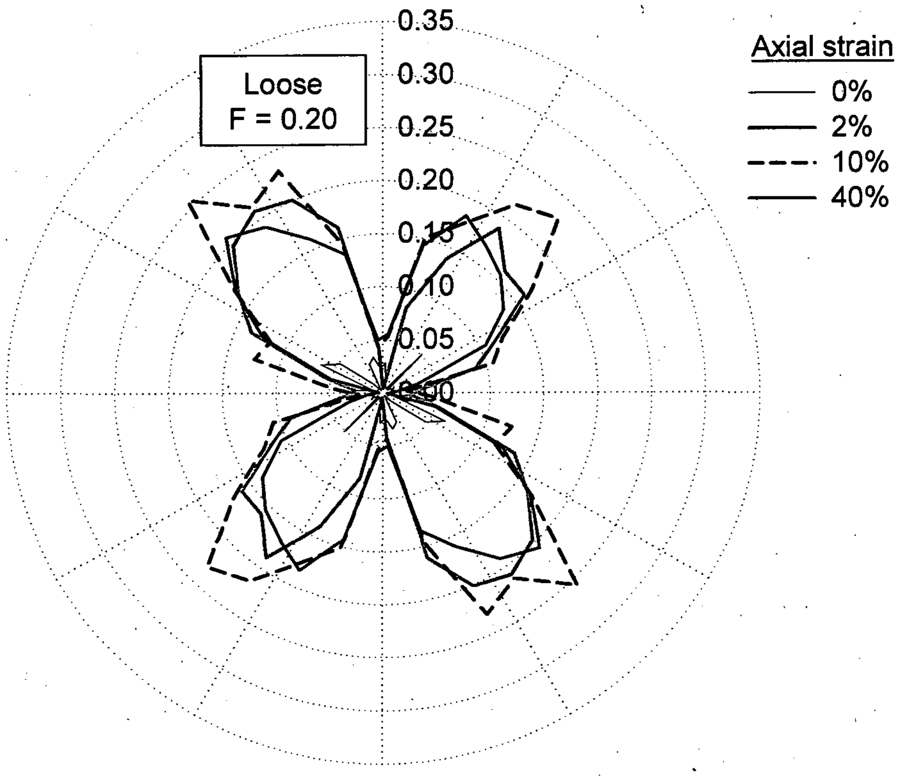

(b)

Figure 6.29: Polar distribution of tangential forces corresponding to forms (a) 1.00 and (b) 0.20 – loose samples

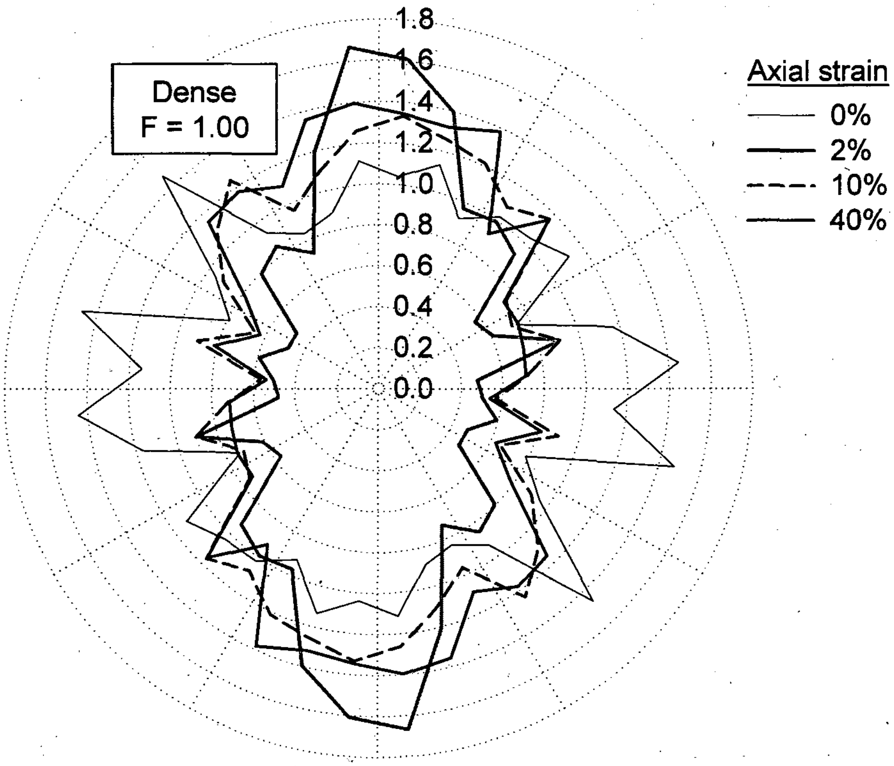

(a)

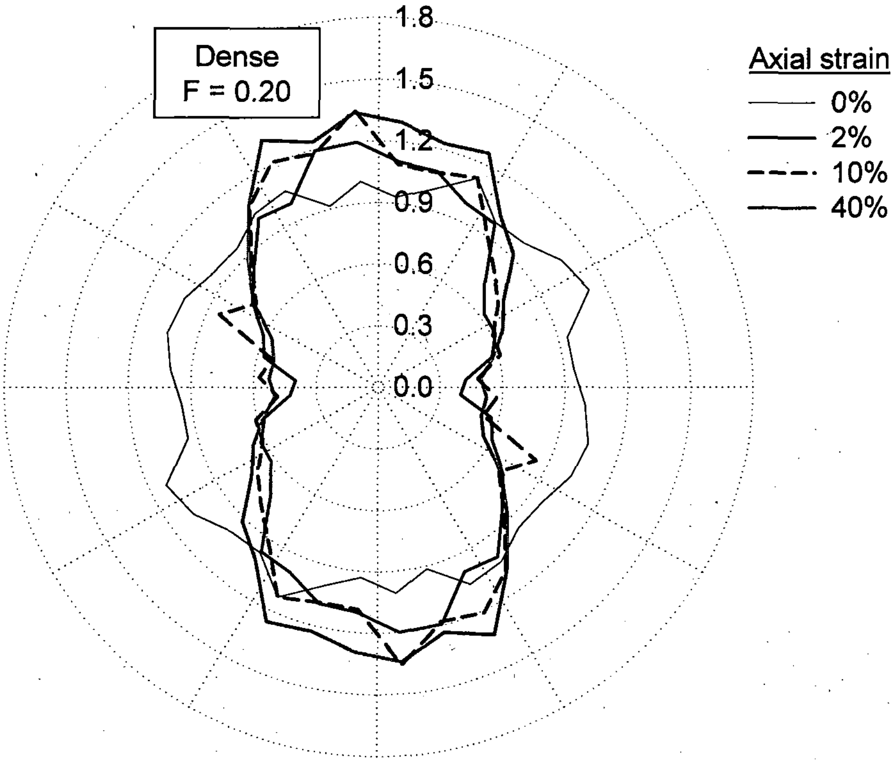

(b)

Figure 6.30: Polar distribution of normal forces corresponding to forms (a) 1.00 and (b) 0.20 – dense samples

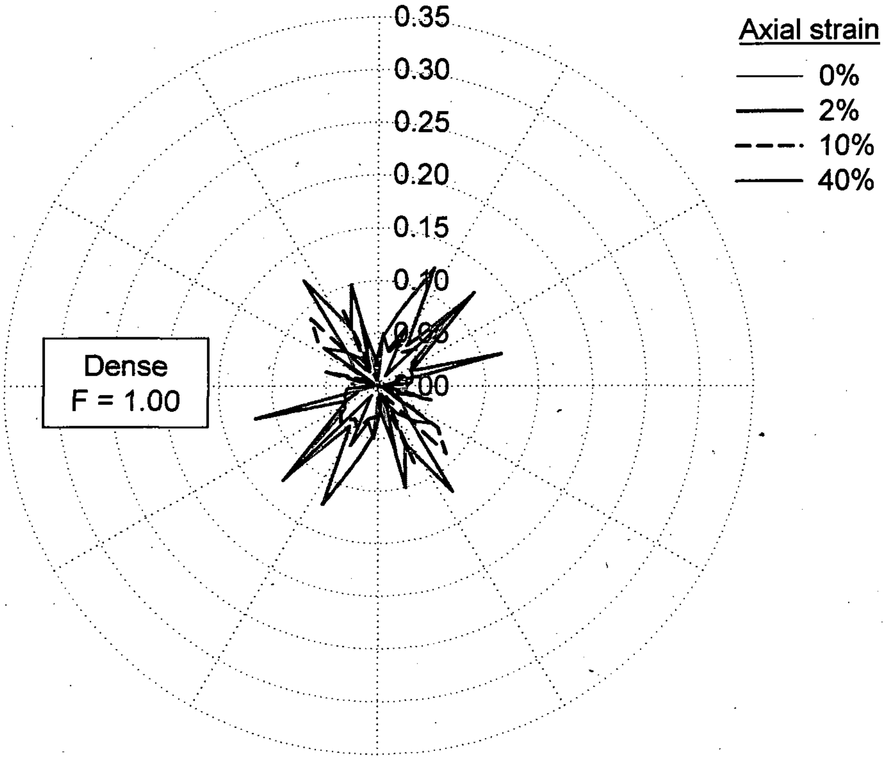

(a)

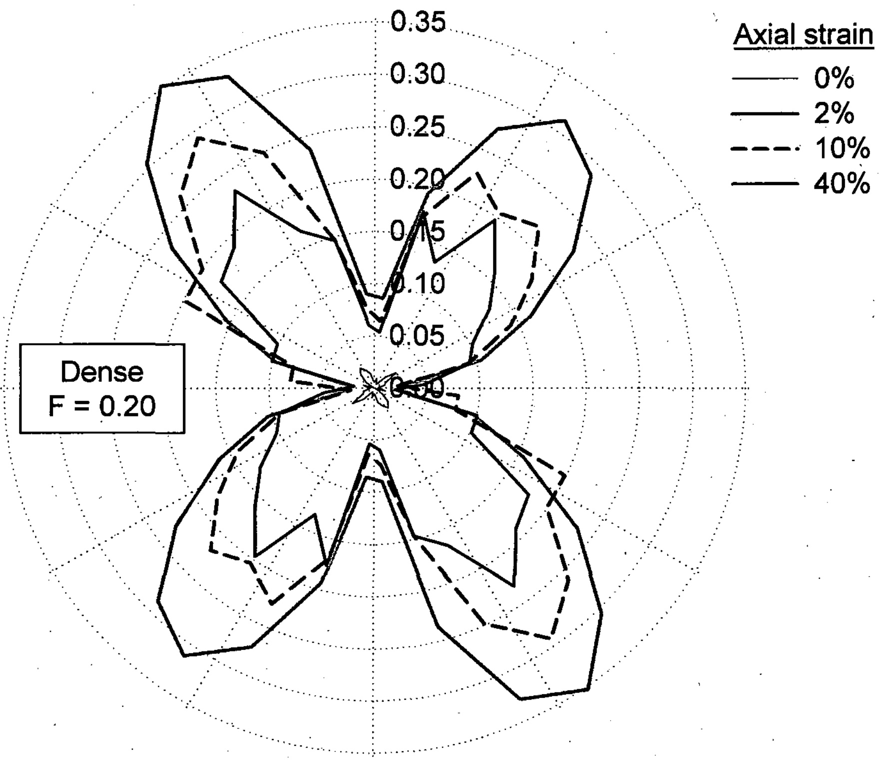

(b)

Figure 6.31: Polar distribution of tangential forces corresponding to forms (a) 1.00 and (b) 0.20 – dense samples

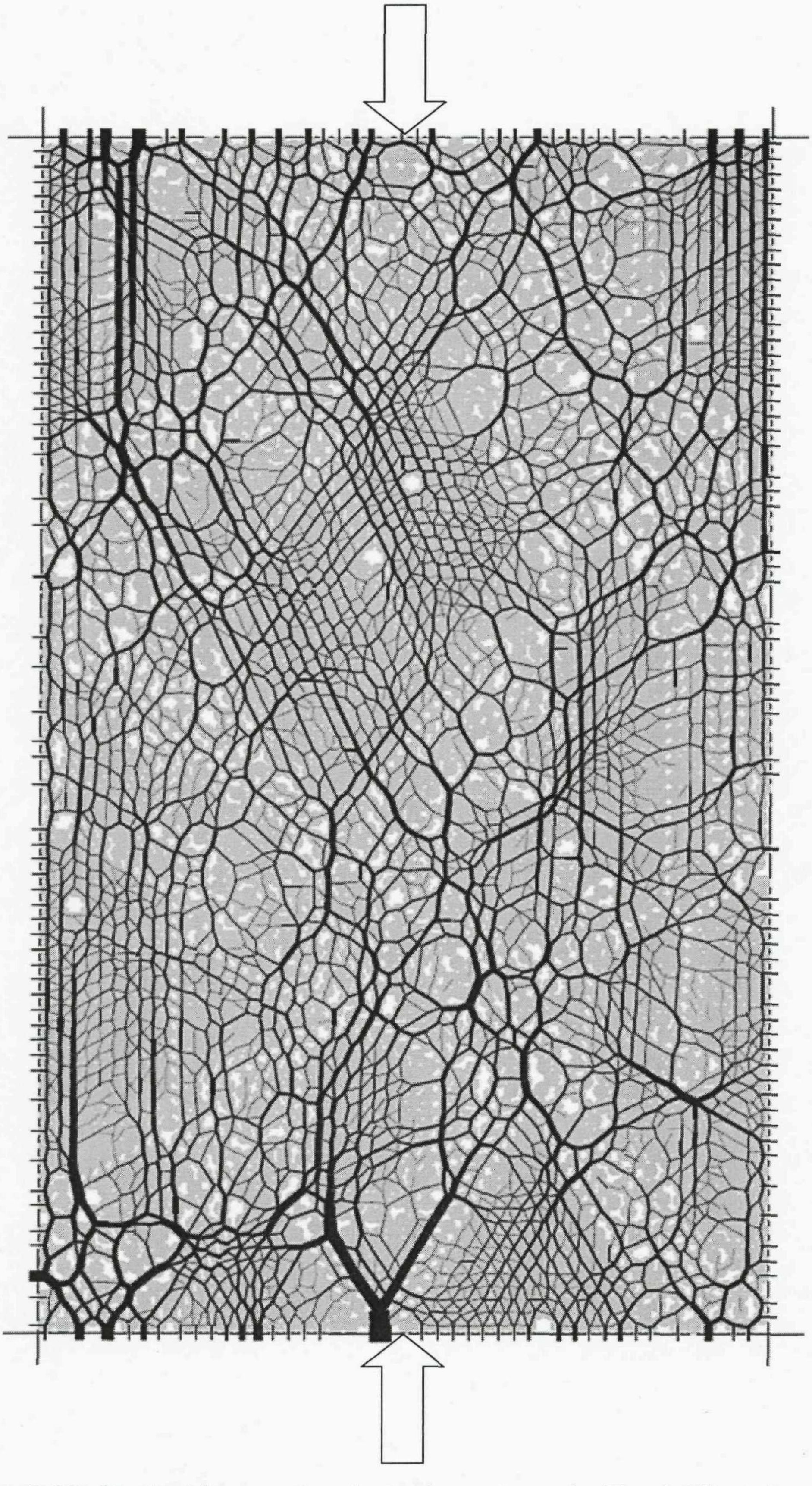

Figure 6.32: Contact force networks in dense sample (F = 1.00) at the end of shearing (40% axial strain)

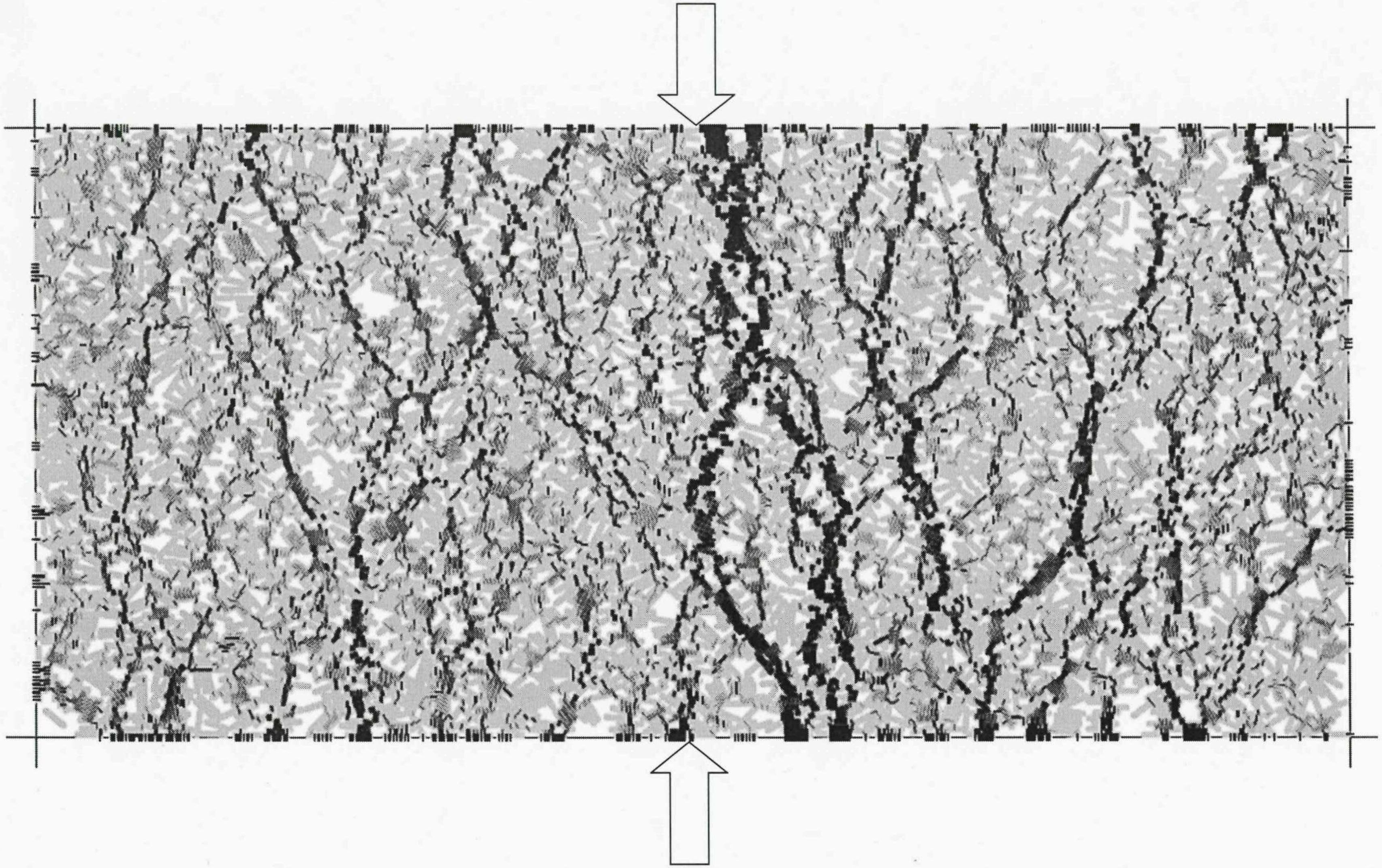

Figure 6.33: Contact force networks in dense sample (F = 0.20) at the end of shearing (40% axial strain)

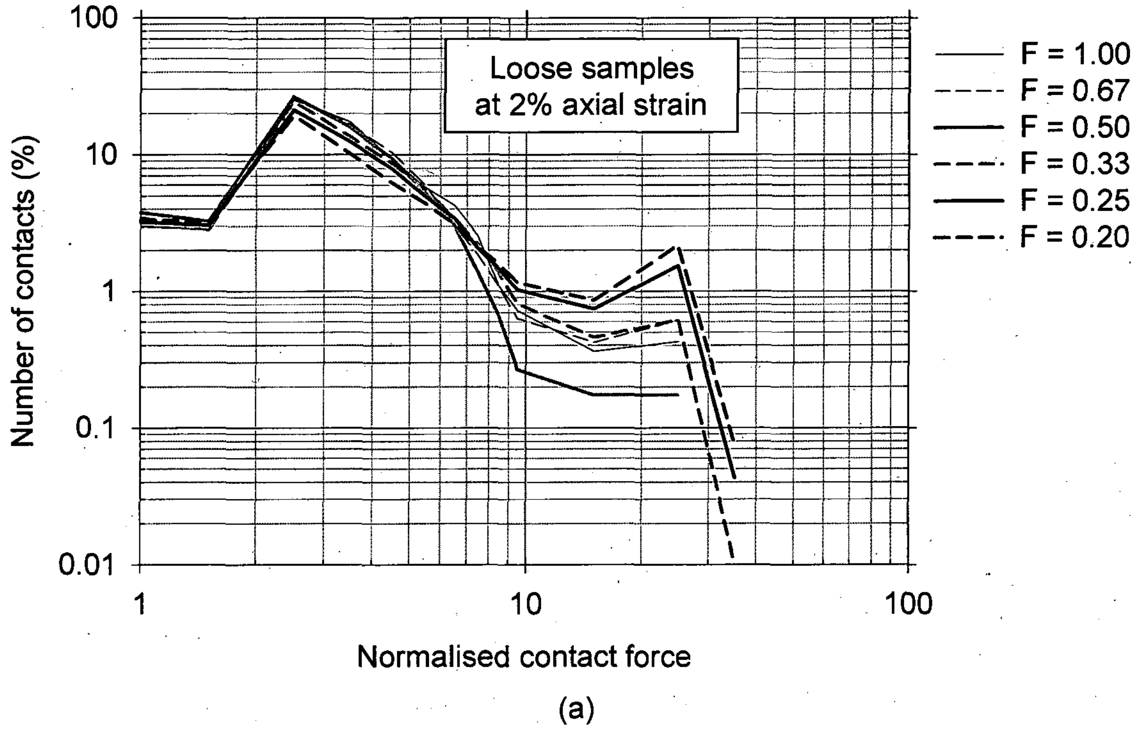

(a)

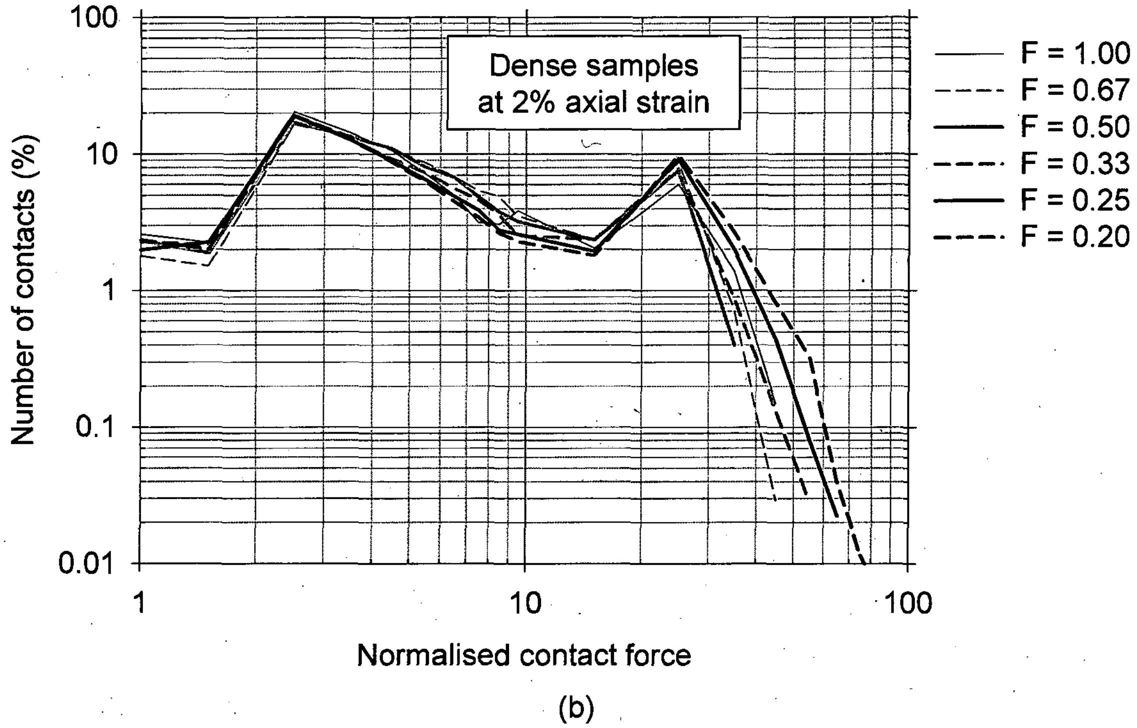

(b)

Figure 6.34: Probability density functions of strong contact forces in (a) loose and (b) dense samples, at 2% axial strain for various forms

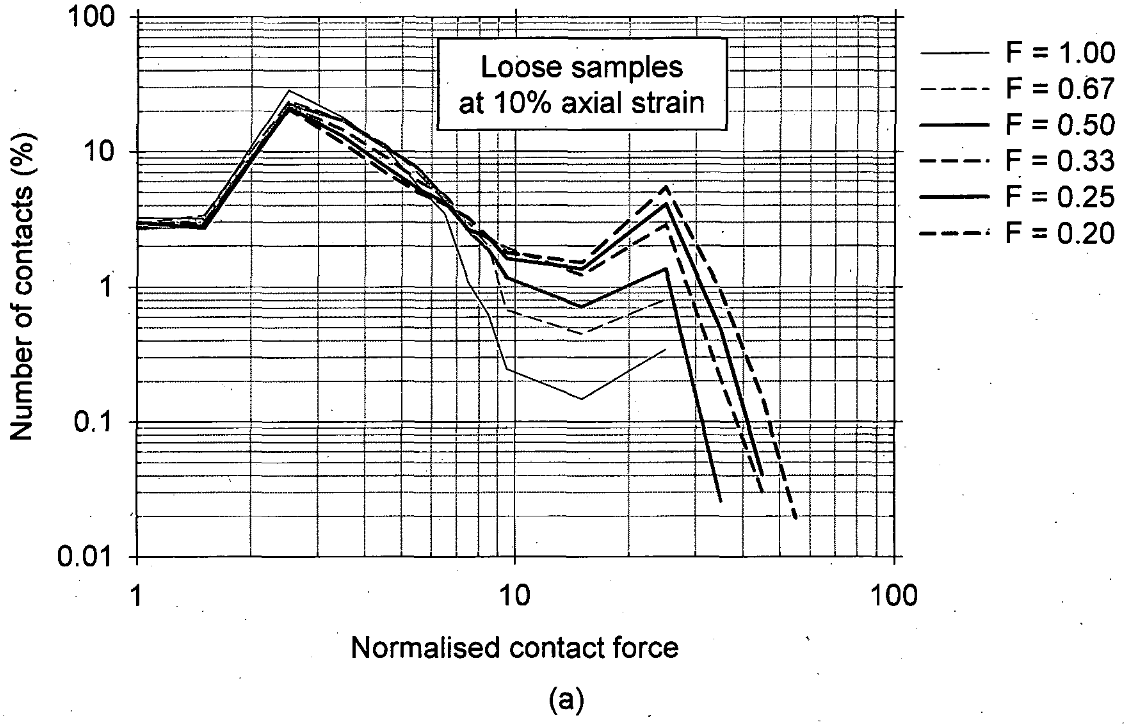

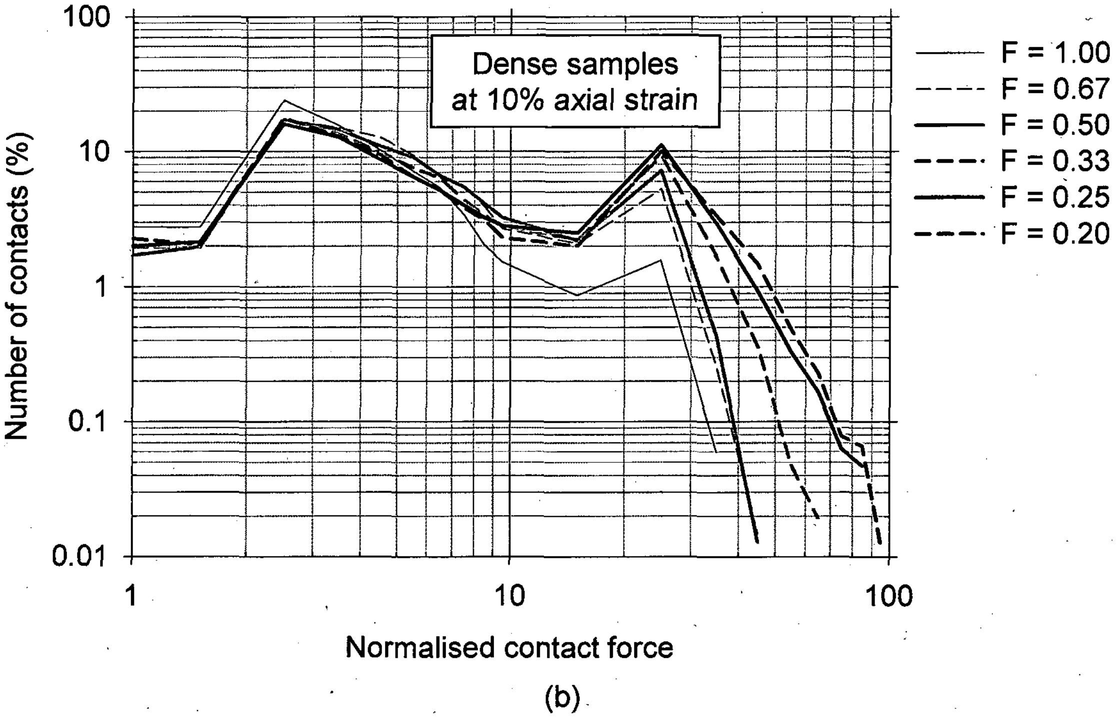

Figure 6.35: Probability density functions of strong contact forces in (a) loose and (b) dense samples, at 10% axial strain for various forms

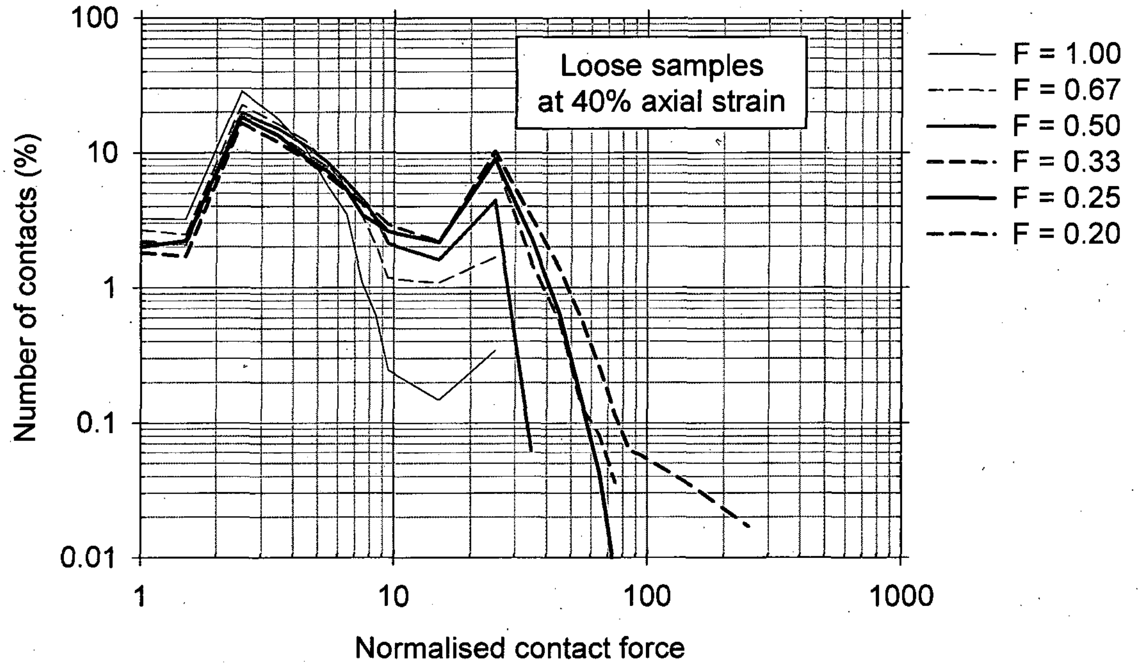

(a)

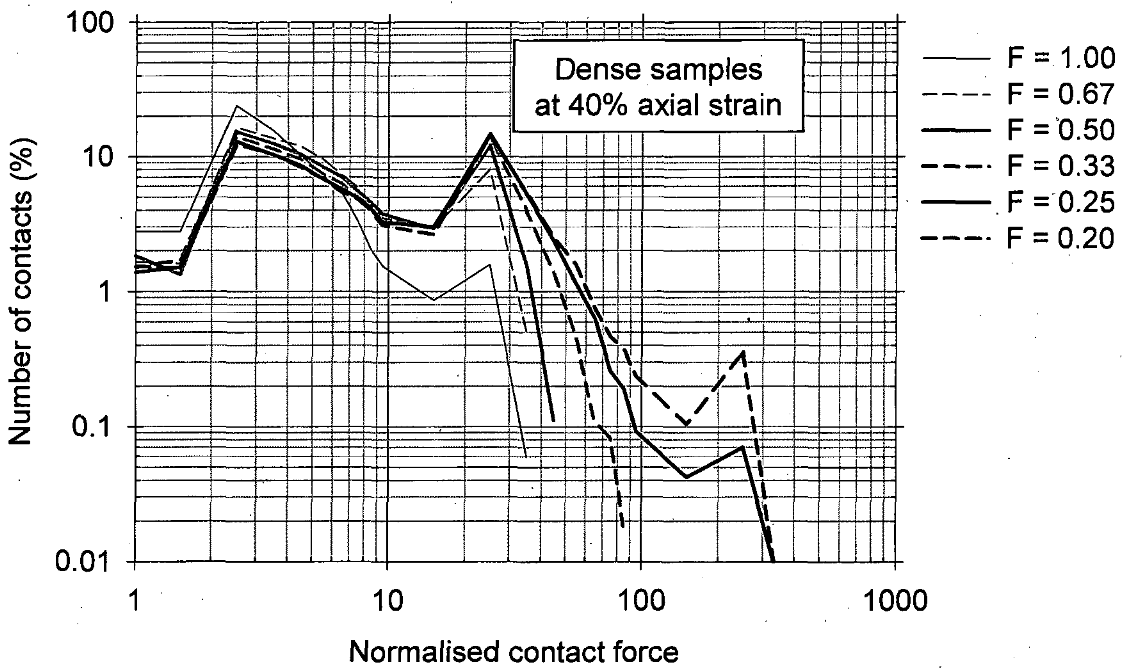

(b)

Figure 6.36: Probability density functions of strong contact forces in (a) loose and (b) dense samples, at 40% axial strain for various forms

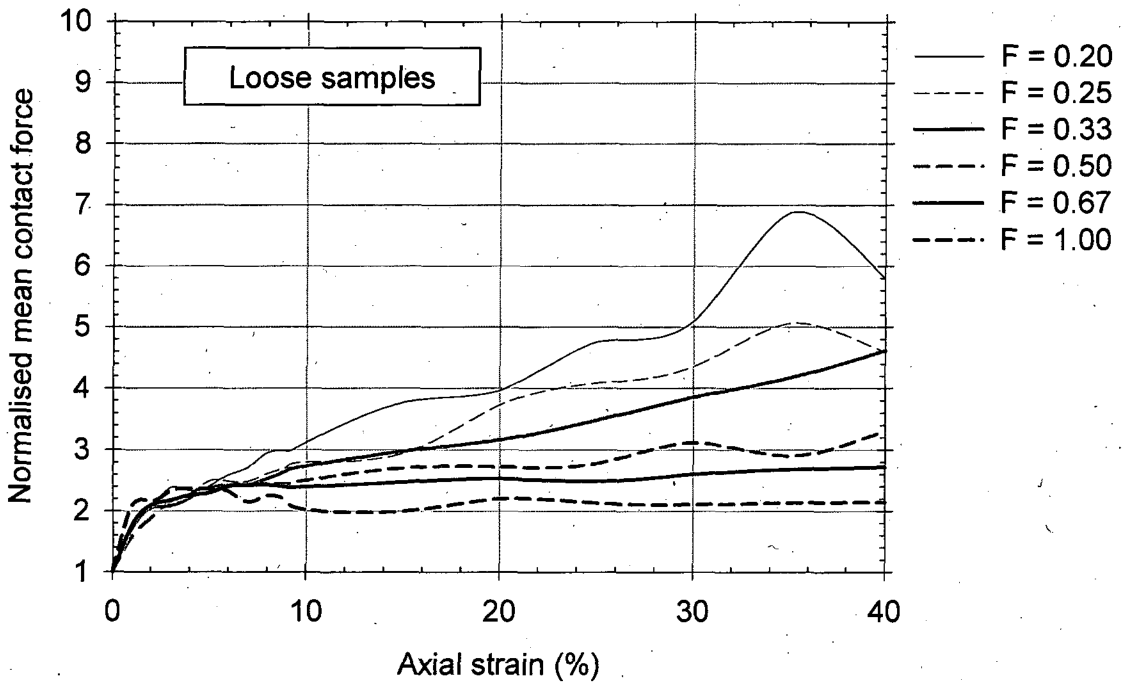

(a)

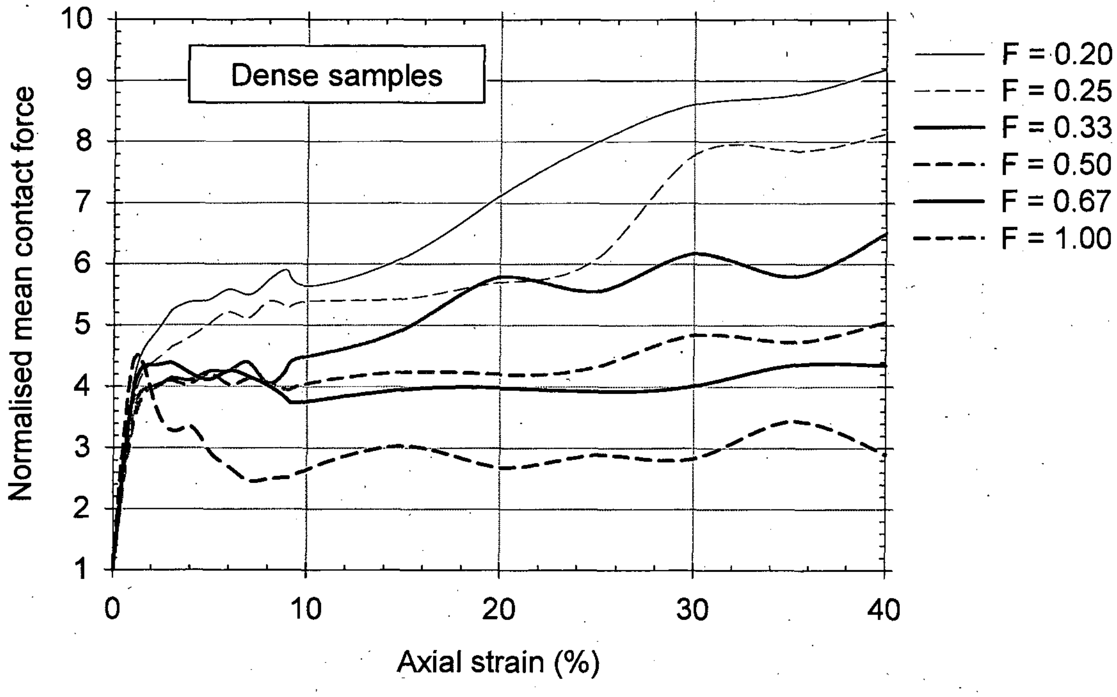

(b)

Figure 6.37: Evolution of normalised mean contact forces in (a) loose and (b) dense samples, for various forms

CHAPTER 7 SYNTHESIS

There has already been much discussion of the individual topics in Chapters 3 to 6. This chapter brings together the information presented in the previous chapters, and draws further conclusions. Firstly, it discusses the methods developed in this research for estimating the form of coarse and fine particles. Secondly, it compares the experimental and numerical modelling results (on depositional packing and drained shear behaviour) and gathers the possible mechanisms responsible for the observed differences. Thirdly, it compares the drained shear behaviour observed in both experiments and simulations with the Critical State framework, and discusses the possible reasons for the observed divergences. In addition, the results from this study are compared with the literature wherever appropriate.

7.1 Development of practical methods of estimating the form

The literature reviewed in Section 2.1 indicated that materials made of bulky particles would behave quite differently from those comprising platy particles. A means to quantify this aspect of particle shape was required in order to distinguish them. At the beginning of this research, it was thought that this particular aspect of particle shape, namely 'form', could be reasonably quantified by the ratio of the minimum to the maximum particle dimensions. Several methods (direct or indirect) were available for estimating the form as discussed in Sections 2.4 and 2.5, respectively, for coarse and fine particles. However, most of them were two-dimensional, so they could not differentiate bulky and platy materials. The three-dimensional methods were either impractical, tedious and time consuming, or could not sufficiently differentiate. Therefore, two different new methods (one for the coarse and the other for the fine particulates) were developed in this research for estimating form, and presented in Chapters 3 and 4.

The method developed for coarse particulates consider the particles as scalene ellipsoids. Based on this assumption, a new definition of form termed 'Scalene Ellipsoid Equivalent Sphericity (SEES)' was developed (refer to Section 3.1 and in particular equation 3.3). SEES was evaluated rigorously by applying it to a range of geometrical shapes and irregular particles (see Section 3.2). It was found that SEES could effectively distinguish between bulky and platy particles having the same major and intermediate dimensions whereas the existing practical measures could not (Table 3.1). Having seen the effectiveness of SEES parameter, an automated method was proposed to determine the SEES (refer to Section 3.2). The success of the automated method depends on the following:

- successful dispersion of particles on a flat stage without overlaps
- acquisition of good quality projected images of particles by static imaging (refer to second last paragraph in Section 2.3), and
- precision in weighing of particles (as a whole)

Successful dispersion and accurate measurement of mass would be extremely difficult (or tedious) in the case of fine (or small) particles. The writer's experience suggests that this method can be applied easily to particles coarser than 600μm (approx.), see Section 3.2. Other methods had to be sought for particles of size below 600μm. Another limitation of SEES is that it cannot differentiate between rod-like and plate-like particles having the same major and minor dimensions. However, the literature reviewed in Section 2.2 indicated that the population of rod-like particles is insignificant in almost all clastic sediments.

A few methods were described in the literature to determine the aspect ratio of fine particles (refer to Section 2.5). Only limited materials (mainly Kaolin) appear to have been tested in the past. The aspect ratio values determined using them were very different from the image based measurements. It was not clear that these methods could sufficiently differentiate the bulky and platy materials. So, as a first step towards developing a new method, the existing methods were evaluated by applying them to a range of particle shapes. It was found that none of the existing methods were reliable and could sufficiently differentiate the particles of different shapes (refer to Section 4.1). Therefore, a new method based on laser diffraction and turbidity measurement (using Malvern Mastersizer 2000) was developed (refer to Section 4.2). This method considers particles as oblate spheroids rather than scalene ellipsoids, since laser diffraction method produces only the equivalent diameter of a sphere based on the measured diffraction pattern as opposed to both major and intermediate dimensions produced by static imaging. The new method was evaluated by applying it to a range of particle shapes and platy material of various size fractions (refer to Section 4.3). It was found that the new method could differentiate well between particles of different shapes and form, as well as particles of same shape but with different form (see Table 4.2). In addition, the form estimates determined by this method were in line with the values obtained from qualitative interpretations of SEM images. The reader should refer Chapter 4 for more detailed description and discussion of this method. The success of this method depends on the following:

- effective dispersion of particles in the liquid medium during measurements
- appropriateness of optical properties chosen for the materials
- precision of weight of the material used for measurements

This method cannot be applied to coarse particles (>600μm approx.) because of the limitations posed by the instrument.

It should be noted that both these methods do not measure the same quantity. The SEES method measures the ratio of the minimum to the maximum particle dimensions (approx.). On the other hand, the turbidity-based method measures the ratio of the minimum dimension of particle to that of its projected area equivalent diameter (approx.).

7.2 Comparison of experiments and simulations

This section compares the experiments and the simulations that were carried out with an objective of investigating the (i) effects of particle form on depositional packing by means of physical pluviation experiments and simulations, and (ii) effects of particle form on drained shear behaviour using triaxial (or biaxial) compression tests. It also compares the results obtained from this study with published studies wherever appropriate.

7.2.1 Depositional packing

The effect of particle form on depositional packing (in loosest and densest states) was investigated by carrying out physical experiments as well as numerical simulations. In addition, the effects of inter-particle friction and surface roughness (or asperity friction) were investigated via simulations. The results were presented in Sections 5.3, 6.2 and 6.3.

It was observed in experiments as well as in simulations (Sections 5.3 and 6.2) that both e_{max} and e_{min} increases with decreasing form. e_{max} was more sensitive to form than e_{min} (refer to Figures 5.6 and 6.3). In experiments not only form but also angularity was varied (see Table 5.2), and it was difficult to separate the effect of form and angularity, especially in the case irregular particles. Same was the problem with all the published experimental studies (those examined the effect of particle shape on limiting void ratios) e.g. Koerner, 1968; Maeda, 1994; Sukumaran and Ashmawy, 2001; and Cho et al., 2006. Moreover, in all these studies form (termed sphericity or shape factor) was determined based on 2D images of particles, which could not differentiate bulky and platy particles. As a result, their correlations between limiting void ratios and form were poor compared to the present study.

However, in the current numerical study, all the parameters (except form) was kept constant; therefore, the observed differences in e_{max} and e_{min} were solely due to changes in form. Williams and Jia (2003) have noted an increase in depositional void ratio in the case of short fibres when they were deposited by a raining technique. Nouguier-Lehon et al. (2005) have noted an increase in pluviated void ratio (corresponding to e_{min}) with increasing aspect ratio (1 / form) in the case of polygonal particles. They varied the aspect ratio between 1 and 3 (form between 1.0 and 0.33). Again in their study, both form and angularity were varied simultaneously. It can be clearly concluded from the above discussion that both e_{max} and e_{min} increases with decreasing form and the mechanisms responsible for this observation will be discussed in the next paragraph.

As form decreases, particles can either pack in random orientations forming an open (card-house-like) structure with large local voids between individual and/or groups of particles, see Figure 6.2(a); or pack anisotropically forming a face-to-face arrangement of particles (see Figure 7.1(a) and (b)). In the dense state, an increase in e_{min} with decreasing form is mainly due to small bridge-like openings in face-to-face arrangements of particles (see Figure 7.1(a) and (b)). The large e_{max} and e_{min} values observed by the researchers (e.g. Gilboy, 1928, Koerner, 1968, Olson and Mesri, 1970) in mica supports this hypothesis. Increased inherent anisotropy with decreasing form was also noted by Nouguier-Lehon et al (2003) and (2005) in the case of elongated polygonal particles (see Figure 7.1(c)) but again in their study both form and angularity were varied simultaneously.

In reality, for a given particle form, packing appears to be affected by many factors during deposition (such as inter-particle friction, surface roughness, depositional intensity and the nature of fluid medium through which the deposition is taking place) which ultimately lead to different initial void ratios. Some of these factors were addressed in this thesis via numerical simulations (refer to Section 6.3). The results suggest that the depositional void ratio increases either with increasing inter-particle friction or with increasing surface roughness (see Figure 6.8). Higher inter-particle friction (or surface roughness) inhibits the sliding of particles after their deposition. In this study, the depositional intensity was quite low in both the physical as well as numerical pluviation tests. However, if depositional intensity is increased it can be expected, due to increased opportunity for particles to interfere with each other, that the post-depositional anisotropy will be decreased. A decrease in anisotropy leads to an increase in depositional void ratio due to a more open structure, especially in low form (platy) particles. Lagioia et al. (2006) have noted decreasing density with increasing depositional intensity in vacuum pluviation tests on Tricino river sand. In addition, for small colloidally-active particles, the double layer repulsive and edge-to-face attractive forces help in forming a very loose structure, leading to large initial void ratios in case of clay soils, as noted by Olson and Mesri (1970).

7.2.2 Drained shear behaviour in triaxial (or biaxial) compression

The effect of particle form on drained shear behaviour of dense specimens was investigated by carrying out laboratory triaxial compression tests on a wide variety of particle shapes (where both form and angularity were varied) and biaxial numerical simulations on a range of particle shapes (where only form was varied). In addition, the effect of density was investigated via numerical simulations, corresponding to all forms. The results were presented in Sections 5.4.3 and 6.4.1.

Specimen preparation techniques

The specimens were prepared by pluviation technique in both the cases. However, in order to explicitly explore the effect of density on shear behaviour (i.e. without changing the fabric), the numerical specimens were prepared from the loosely packed assemblies (i.e. pluviated under high friction see Figure 6.2(a)) by changing the inter-particle friction during the isotropic compression stage. The main advantage of this sample preparation method is that a range of densities can be produced with more or less the same fabric (see Figures 7.2 and 7.3). Consequently, the fabric of dense specimens in simulations was quite different from that in experiments, even though both were prepared by the same technique. Comparison of Figures 5.7(d) and 6.2(b) qualitatively suggests that the fabric of experimental samples would resemble the densely packed assemblies (i.e. pluviated under zero friction). Conversely, the fabric of dense numerical samples does not resemble the densely packed assemblies but resemble the loosely packed assemblies (compare Figures 6.6(a) and 7.3) since they were originally derived from the loosely packed assemblies as discussed above. Therefore, it can be inferred from the above discussion that the initial or inherent anisotropy (i.e. preferential horizontal orientation of particles) of experimental samples is higher than that of numerical samples.

Differences between the conditions in modelling and the reality

There appeared to be four major differences between the conditions in modelling (in simulations) and the reality (in physical experiments) as stated below:

i) *Dimensionality*

The simulations were carried out using 2D particles under conditions of plane strain, whereas the experiments were carried out under 3D (axi-symmetric) conditions.

ii) *Particle shape*

In experiments both form and angularity were varied (Table 5.2) whereas in simulations only form was varied (Table 6.3).

iii) *Fabric anisotropy*

The inherent anisotropy of experimental samples was higher than the numerical samples, since the latter were prepared from the loosely packed assemblies in order to achieve a range of densities with more or less the same fabric.

iv) *Particle breakage*

The particles were crushable in experiments and non-crushable in simulations. Although particles were crushable in experiments, under an effective confining stress of 100kPa (at which the samples were tested), high form particles (bulky i.e. SEES ≥ 0.50) did not crush whilst low form particles (platy i.e. SEES < 0.50) crushed significantly, see Figures 5.24 and 5.26.

Global shear behaviour

I. *High form (bulky) materials (form or SEES ≥ 0.50)*

A well-defined peak-and-softening behaviour was clearly evident in high form (bulky) materials both in simulations as well as in experiments (see Figures 5.11 and 6.10 to 6.12). However, experiments showed a clear increasing trend in peak strength with decreasing form, in contrast to a decreasing trend in peak strength in simulations (compare Figures 5.19 and 6.16(a)). This difference may result from the combination of differences in stress conditions (plane strain and axi-symmetric), particle shape (mainly angularity) and fabric anisotropy. The numerical study carried out by Mirghasemi et al. (2002) on polygon-shaped particles indicates that shear strength increases with increasing angularity. Nouguier-Lehon et al. (2005) have noted higher shear strength in samples when sheared in the direction of deposition than when sheared perpendicular to the direction of deposition, due to higher initial anisotropy. These two studies together support the above-mentioned explanation.

The strain to reach peak strength increased with decreasing form and it was consistent in both simulations and experiments.

II. *Low form (platy) materials (form or SEES < 0.50)*

Samples comprising low form (platy) particles continued to gain strength with increasing strain (without exhibiting any clear peak) in simulations as well as the experiments, but at a diminishing rate in experiments (compare Figure 5.11(a) with Figures 6.13 to 6.16 corresponding to identical forms) which could be due to significant particle crushing (see Figures 5.24 and 5.26).

The strength at large strains increased significantly with decreasing form in experiments and simulations, which could be due to the immobile nature of particles i.e. low form particles cannot easily slide (since they are sandwiched or interlocked between their neighbours) or roll (since they are rotationally frustrated) and move laterally. This effect would be more in dense samples than in loose samples.

The tangential force mobilisation was higher in low form (platy) particles than in high form (bulky) particles; compare Figures 6.28(b) with 6.28(a) or 6.30(b) with 6.30(a). It was consistent for all density states, see Figures 6.28 and 6.30. This supports the above mentioned argument that low form particles are less mobile compared to high form particles for a given density state. The immobility of particles may increase with increasing inherent anisotropy due to kinematic inadmissibility. Due to the immobile nature of particles (e.g. like a stack of bricks in a masonry wall), as the deviatoric stress increases, the contact stresses increase enormously (see Figure 6.36(b)) which causes significant crushing in experiments leading to a significant rise in shear strength at large strains. However, shear behaviour depends on the direction and mode of shearing. For example, De Josselin De Jong (1988) has noted a significant difference in shearing behaviour between the toppling of vertical columns of particles and sliding of horizontal rows of particles, in association with simple shear test.

In contrast, high form particles can easily slide or roll and move laterally without building up of huge contact forces, therefore they exhibit low shear strength at large strains.

The maximum rate of dilation decreased and the strain at which it occurred increased significantly with decreasing form. This was consistent for all forms, in experiments as well as the simulations (compare Figures 5.22 and 6.18). Although the initial relative densities were quite high (>80%) in all experiments for all the materials, the volume change behaviour changed from dilative to contractive as the particle shape changed from spherical (glass ballotini) to platy (coarse glitter), see Figure 5.11. In the past, a few researchers have also noted suppressed dilatancy (although they have not measured form) in materials other than rotund (or natural) sands, as mentioned below:

- Fine fraction of quartz particles (platy), Chlorite (platy), and Mica (platy) by Koerner (1968)

- Fine fraction of Mizpah tailings (platy) by Vermeulen (2001)
- Classified mine tailings (angular, elongated and flattened) by Wesseloo (2004)

Significant crushing was observed in the case of glass nuggets, fine glitter and coarse glitter (low form materials), see Figures 5.24 and 5.26. As low form materials crush (or break), their form increases significantly since particles normally tend to break transverse to their major dimension either because of high bending stresses (due to rotational frustration) or because of high contact stresses (due to sandwiching or interlocking) between the neighbouring particles. After crushing or breaking, the material is not the same i.e. both size and shape changes. As a result, the void ratio range (i.e. $e_{max} - e_{min}$) would expect to decrease since the form of the new material is higher than the original material. The relative density of the crushed or broken material is lower than in the initial state even though the void ratio is reduced. So, in essence, the new material behaves either as a medium dense or loose material depending on the extent of crushing. This could be one of the reasons for decreased dilation and transition from peak-and-softening to hardening type behaviour with decreasing form.

In summary, a clear transition from peak-and-softening to hardening (and from dilative to contractive) type behaviour was observed as the particle shape changed from spherical to platy, in dense samples. In general, a higher mobilised stress ratio was observed in experiments (especially in materials comprising anisometric particles) than in simulations, which could be attributed to higher inherent anisotropy and/or significant particle crushing and subsequent reduction in void ratio.

The observations made in this study are purely based on shearing in triaxial (or biaxial) compression mode. Therefore these observations may not hold true for other shearing modes e.g. direct (or ring) shear, simple shear and triaxial extension.

7.3 Comparison of shear behaviour with the critical state framework

This section is divided into three subsections. The first subsection describes the critical state framework as relevant to drained shear behaviour of cohesionless soils. The second and third subsections, respectively, compares the triaxial compression tests results and biaxial shear simulations results with the critical state framework.

7.3.1 Critical state framework

The critical state concept was originally introduced by Casagrande (1936) and was further developed by Taylor (1948) and Roscoe et al. (1958). Figures 7.4(a) to (c) shows idealised plots of stress ratio (*q/p'*), volumetric strain, and voids ratio as a function of axial strain for two drained triaxial compression tests corresponding to the wet side of critical (i.e. normally consolidated clays or loose sands) and the dry side of critical (i.e. overconsolidated clays or dense sands). The initial state of soil (i.e. wet or dry side of critical) is a function of both void ratio as well as mean effective stress. Therefore, at a given mean effective stress, the state of a soil can be represented by void ratio alone (see Figure 7.5).

As shear progresses, soils initially on wet side of critical contract while those on dry side dilate after a small initial contraction (Figure 7.4(b)). Both the soils ultimately reach critical states (where the soil continues to deform at constant stress ratio and constant voids ratio) but soils initially on dry side exhibit a peak before reaching the critical state (Figures 7.4(a) and (c)). It should be noted that the initial mean effective stress is the same in both the samples but the initial void ratio of the sample on the wet side is higher than that on the dry side. However, both the samples reach their critical states at the same void ratio, which is termed the critical void ratio.

The volume changes that take place in soils are primarily due to re-arrangement of particles. At a given effective stress, the grains of the loose (or normally consolidated) soils are spaced well apart and, upon shearing, they move into the neighbouring void spaces and become denser, while the grains of the dense (or overconsolidated) soil are closely packed so they must move apart (or break) during shearing (Figure 7.5). The strain at which the peak stress ratio occur is thought (from energy considerations) to coincide with that at which the maximum rate of dilation occurs, see Taylor (1948). The critical state framework was developed mainly based on experimental data from bulky particles e.g. steel balls, glass ballotini, Ottawa sand, Leighton Buzzard sand (see Casagrande, 1936; Taylor, 1948; Wroth, 1958; Roscoe et al., 1958). It will be noted that these materials do not represent the whole range of geo-materials, or even of clastic sediments. The importance of this will be discussed in the following subsections.

7.3.2 Comparison of experimental results with the critical state framework

The effect of particle form on drained shear behaviour was investigated by carrying out triaxial compression tests on a wide variety of particle shapes as discussed in Section 5.4. Figures 5.11(a) to (b) and 5.21(a) show the triaxial compression tests results of all these materials.

It should be noted that the limiting maximum and minimum void ratios of these materials were not constant but depended on the shape of the constituent particles. Therefore, void ratio alone could not represent state at a constant mean effective stress. It was necessary to use relative density rather than the void ratio to compare the results. To plot all the data together in one graph, the void ratio variation during shear was plotted in terms of relative density versus axial strain (instead of void ratio vs. axial strain). It can be clearly seen from Figure 5.21(a) that the initial relative densities of all the samples were quite high (i.e. >80%). The initial mean effective stress was 100kPa in all the samples, which is not high. Therefore, it could reasonably be expected, based on previous experimental data (e.g. Bolton, 1986) that the initial state of all the samples would lie on the dry side of critical. Consequently, they were expected to behave like dense samples, exhibiting a clear peak and subsequent softening to reach the critical state, and dilating heavily after a small initial contraction.

Figures 5.11(a) and (b), and 5.21(a) indicate that only the glass ballotini and LB sand B showed a clear peak and softening (resembling the critical state framework) whereas others did not. The following points can be drawn from these figures:

- Only the glass ballotini reached a critical state (i.e. sample continuously deforming under constant stress ratio and void ratio) at the end of shearing, and showed a clear peak before reaching the critical state.
- LB sand B did not reach a critical state even by the end of shearing but showed a potential for reaching a critical state. It had a clear peak before reaching the critical state, but at a higher strain than the glass ballotini.
- Glass nuggets and fine glitter showed hardly any peak in stress ratio. This occurred at unusually high strains. Coarse glitter continued to gain the strength

with strain (i.e. strain-hardening) without exhibiting any peak even by the end of shearing i.e. at 20% axial strain.

- Glass nuggets and fine glitter had reached an almost constant stress ratio towards the end of shearing, but continued to dilate at a constant rate without showing any potential for reaching a critical state.
- The strain at which the sample changed from its initial contractive to dilative behaviour (i.e. onset of dilation) was least in glass ballotini and highest in coarse glitter (and the difference in strain was quite high). Other results fell in between these two in accordance with their form (SEES).
- A clear peak and the associated maximum dilation rate was present only in the case of glass ballotini and LB sand B whereas in others (glass nuggets and fine glitter) peak stress ratio and the maximum dilation rate was spread over a large strain range.

7.3.3 Comparison of simulations results with the critical state framework

Drained biaxial shear simulations were carried out on a range of particle forms (from spherical to platy) each at three different density states (loose, medium and dense), see Table 6.4. The global shear behaviour was presented in Figures 6.10 to 6.15 and discussed in Section 6.4.1. The figures indicate that high form (bulky) particles (corresponding to form ≥ 0.50 i.e. 1.0, 0.67 and 0.50) followed the critical state framework closely whereas others (low form (platy) particles, corresponding to form < 0.50 i.e. 0.33, 0.25 and 0.20) did not follow. Two different patterns of behaviour were evident from these figures, as discussed below:

- In the case of high form (bulky) particles (i.e. form ≥ 0.50)
  - Dense samples exhibited peak stress ratio that decreased with decreasing initial density, and all samples reached a unique constant critical stress ratio irrespective of their initial densities.
  - Dense samples dilated and loose samples initially contracted and then dilated, and all samples reached a unique constant critical void ratio regardless of their initial densities.
- In the case of low form (platy) particles (i.e. form < 0.50)
  - All samples exhibited hardening behaviour irrespective of their initial relative densities. At low strains the stress ratio was higher in dense samples. This

decreased with decreasing initial relative density. However, at large strains all samples reached similar stress ratios but these continued to increase with the strain (instead of reaching a constant value as per the critical state framework) at a constant rate irrespective of their initial densities.

- Dense samples dilated continuously from the beginning to the end of shearing, whereas loose and medium dense samples contracted initially and then dilated until the end of shearing, all at the same rate without reaching a unique constant void ratio.
- The peak stress ratio was associated with maximum dilation rate only in the case of bulky particles. This was observed both in simulations as well as in experiments. Nouguier-Lehon et al. (2003) have also observed the non-coincidence of peak and maximum dilatancy rate in the case of elongated polygons. Similar observations were also reported by Cresswell and Powrie (2004) but in the case of locked sand, where the grains were bulky and interlocked. These observations together disprove the widely believed hypothesis that any mobilised stress ratio in excess of critical state is due to dilation (Taylor, 1948; and Roscoe et al., 1958).

7.3.4 Possible reasons for divergence of results from critical state framework

The divergence of behaviour (as discussed in Sections 7.3.2 and 7.3.3) from critical state behaviour in the case of glass nuggets, fine glitter, coarse glitter (and in the case of low form particulates in simulations i.e. form < 0.50) can be primarily attributed to differences in particle shape and in particular form.

As discussed earlier in Section 7.3.1, the critical state framework was developed mainly based on the experimental data from unstructured rotund sands. Published studies of cohesionless materials that agree well with critical state framework have also been based on rotund sands (see Bolton, 1986). There is no particular reason why critical state framework should be applicable for whole range of particle shapes. The current experimental and numerical studies both suggest that critical state framework is not applicable for single-sized low form materials. In addition, the work by Been and Jefferies (1985) suggest that the other major attribute of Critical State Soil Mechanics, a unique NCL does not exist for sands.

In general, the implied assumption of dense state is that grains are so closely packed, any distortion (or shearing movement) would cause particles to override against their neighbours (dilate) especially at low confining pressures. However, as form decreases, particles neither pack that closely (as discussed in Section 7.2.1) nor override (dilate) to the same extent as illustrated in Figure 7.6. In addition, shear behaviour seems to be highly dependent on the direction of loading/shearing (with respect to inherent anisotropy) and the mode of shearing (e.g. direct or ring shear, triaxial compression or extension, simple shear), see Figures 7.6 to 7.9.

In biaxial (or triaxial) compression mode, as the shear progresses, high form particles can easily slide or rotate and move laterally without building-up of high contact stresses whereas low form particles cannot easily slide or rotate, or move laterally (since they are either sandwiched or interlocked between their neighbours, or rotationally frustrated). As a result, in the case of low form materials, the contact stresses in sandwiched particles and the bending stresses in bridged particles increase significantly and cause considerable crushing. At large strains, high form particles can continuously reorient whereas low form particles re-orient in a preferential direction and reach a terminal orientation (i.e. perpendicular to the major principal stress direction). Moreover, the mechanism of dilation in low form particles seems to be entirely different from the widely believed interlocking in rotund sands. Therefore, the shear behaviour of low form particles does not follow the critical state framework.

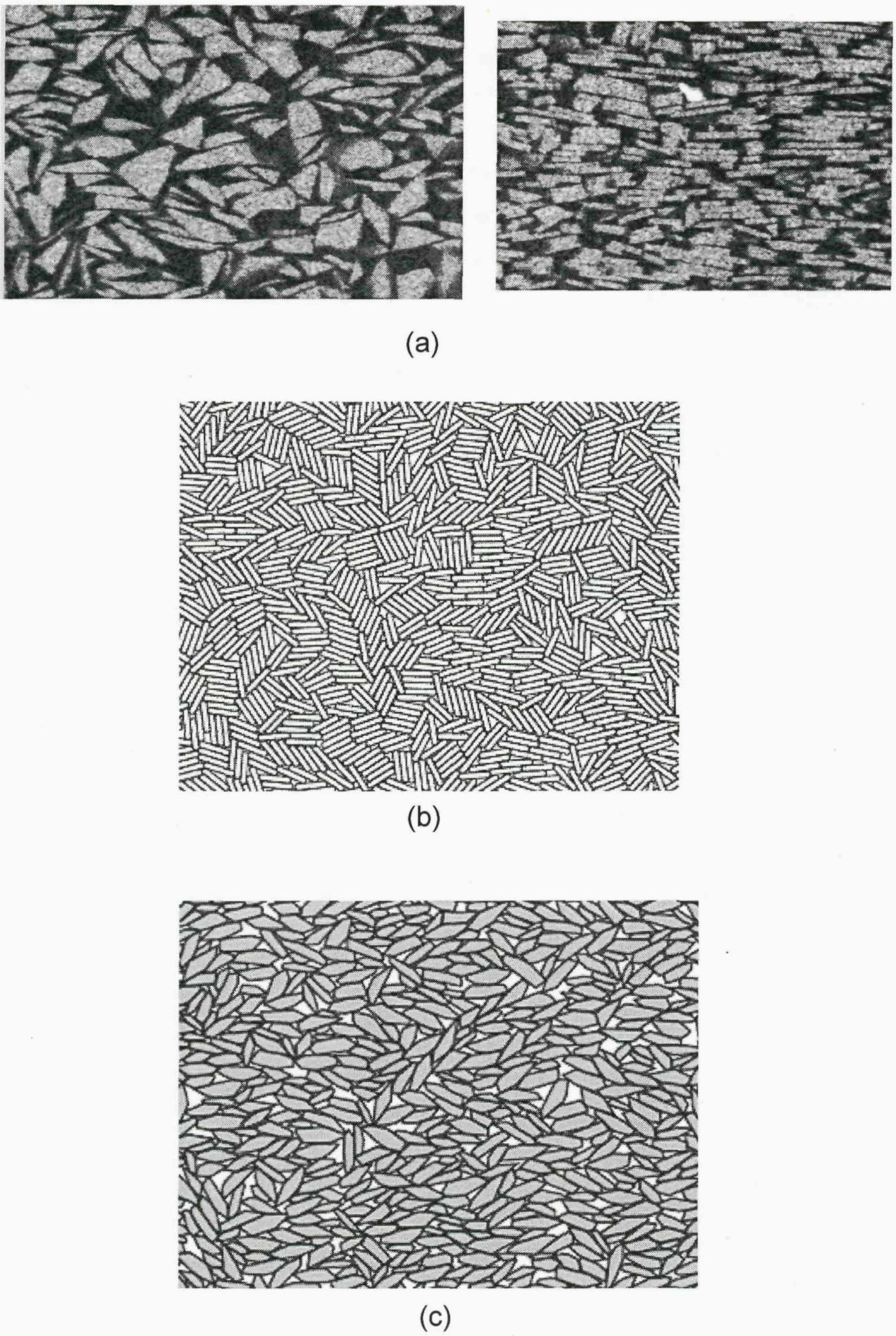

(a)

(b)

(c)

Figure 7.1: Inherent anisotropy observed in pluviated samples – (a) physical experiments on glass nuggets and glitter and (b) platy particles using PFC2D in the current study, and (c) elongated polygons by Nouguier-Lehon et al. (2005).

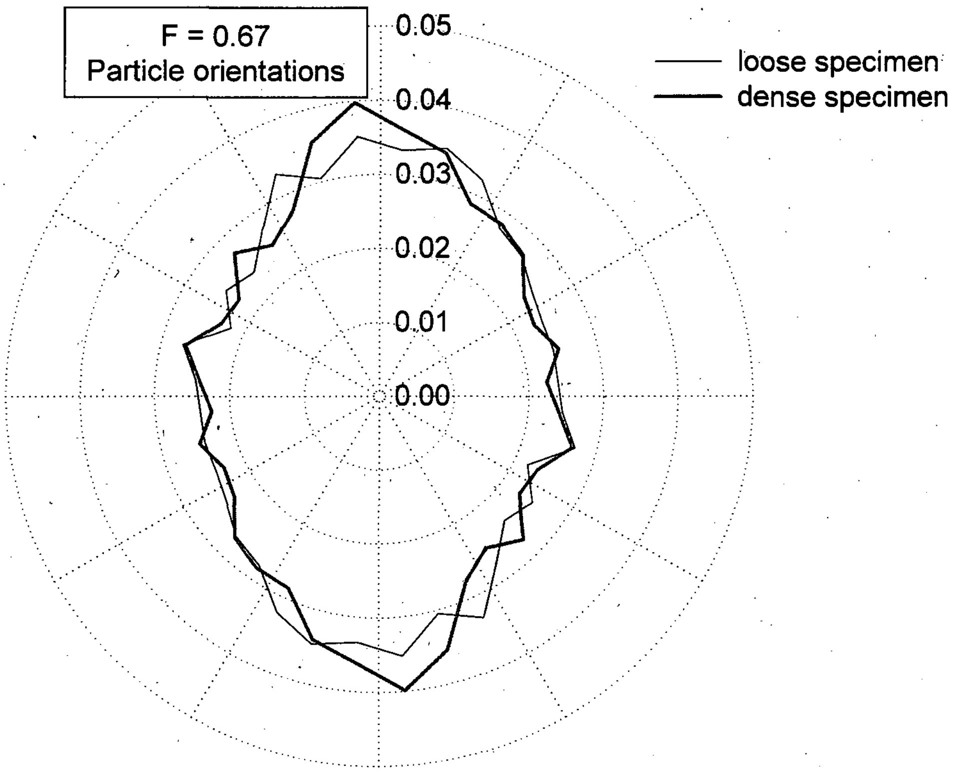

(a)

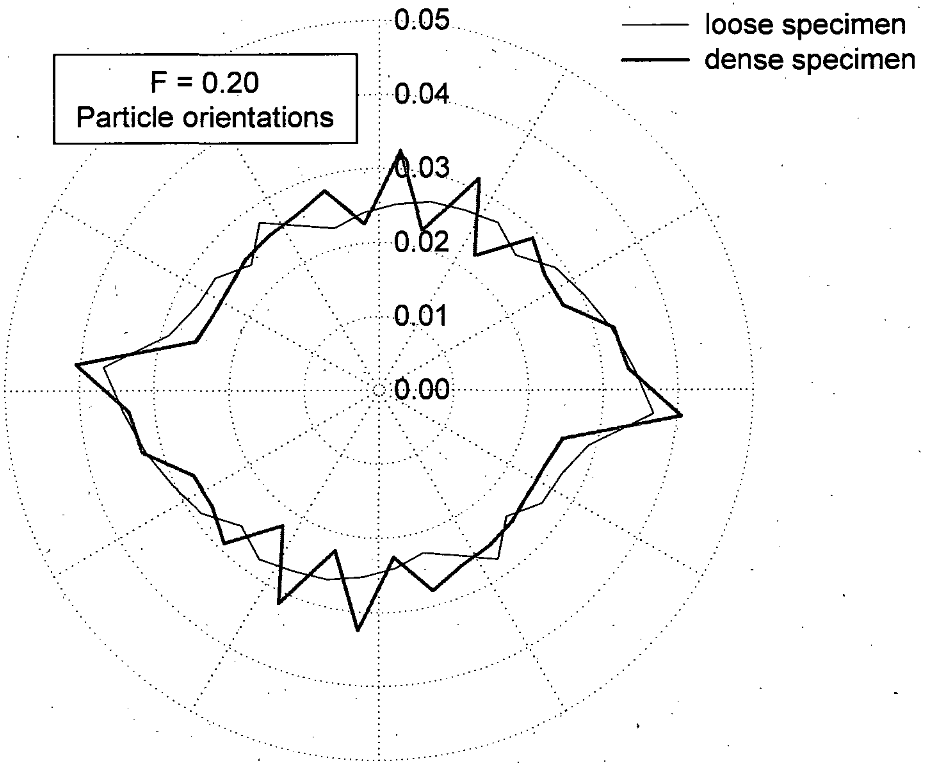

(b)

Figure 7.2: Polar distribution of particle orientations corresponding to forms 0.67 (a) and 0.20 (b) of loose and dense specimens

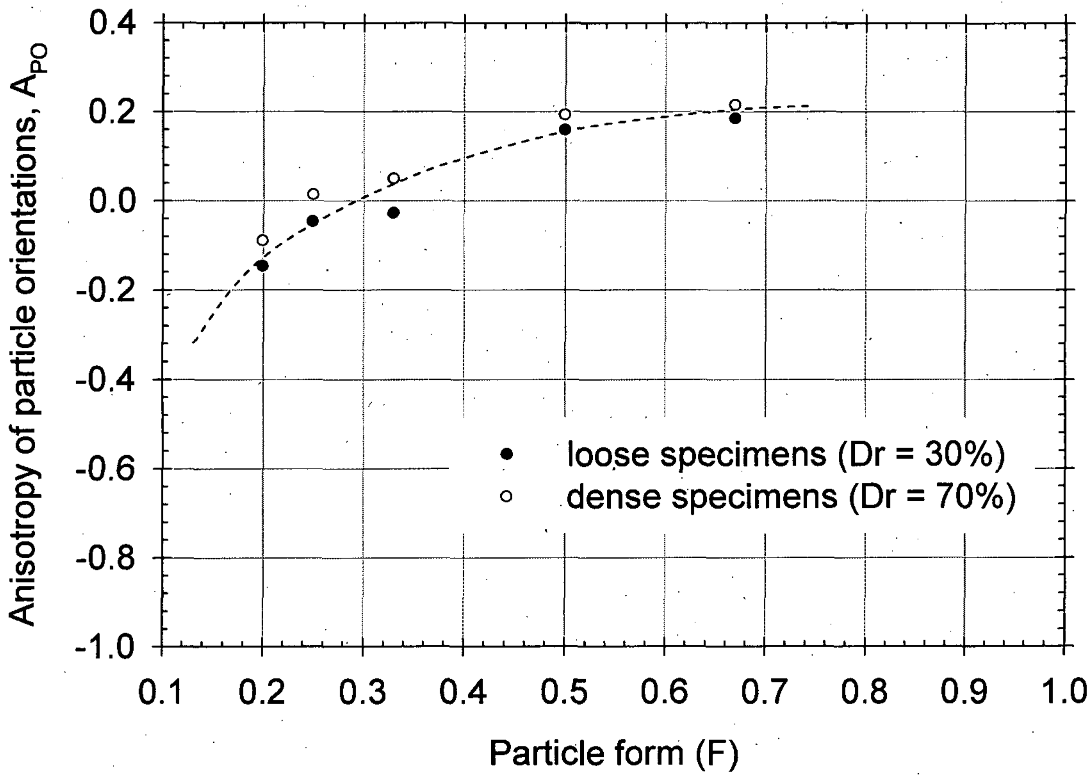

Figure 7.3: Anisotropy of particle orientations in loose and dense specimens corresponding to all forms

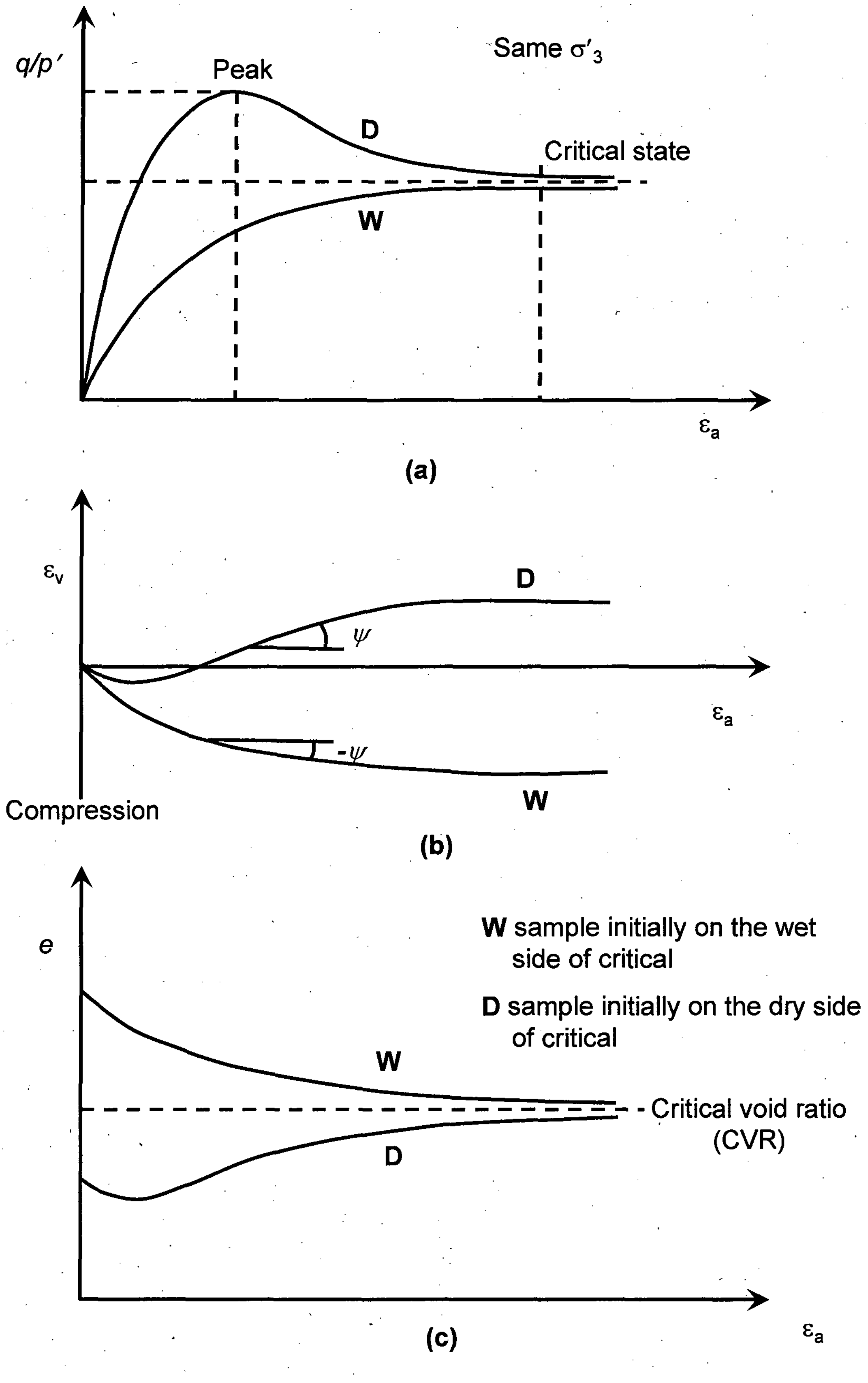

Figure 7.4: Typical drained shear behaviour of soils in triaxial compression

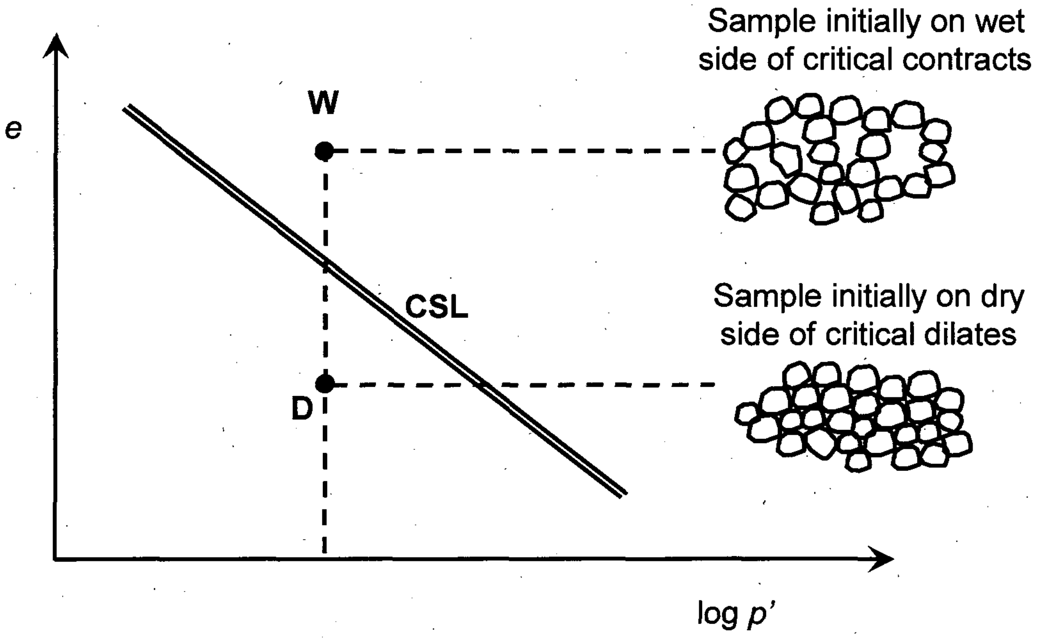

Figure 7.5: Illustration of Initial state of soil in relation to CSL

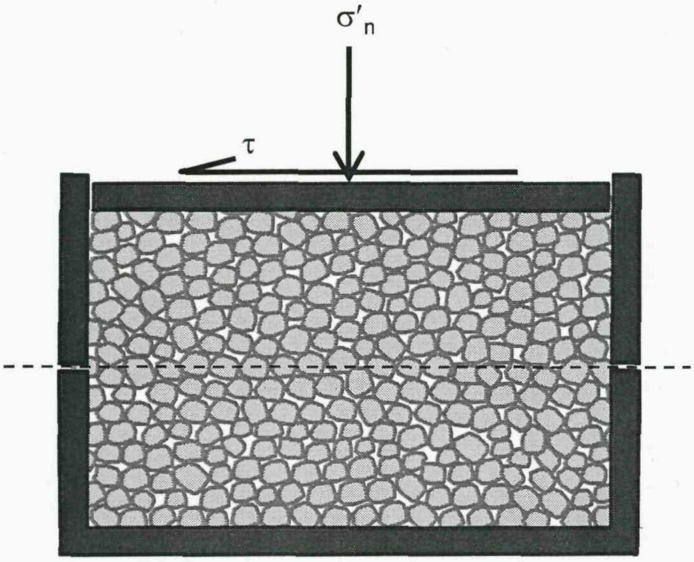

Irregular bulky particles
(form ≈ 0.8)

(a)

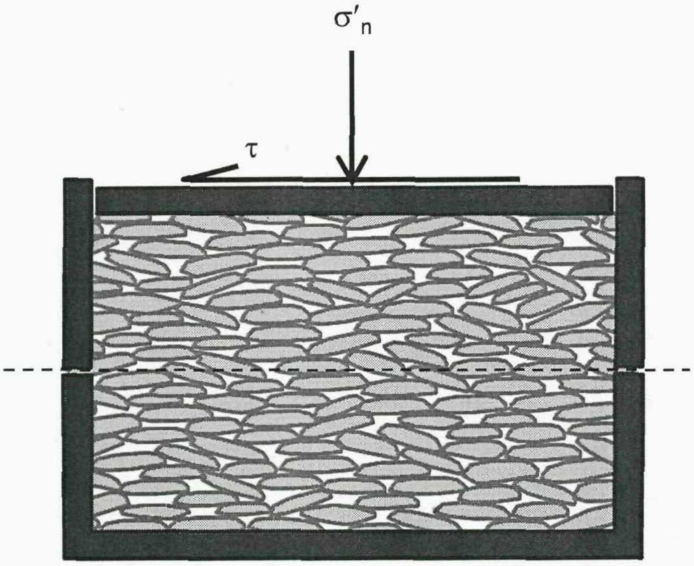

Irregular platy particles
(form ≈ 0.25)

(b)

Figure 7.6: Bulky (a) and platy (b) particles sheared along the direction of inherent anisotropy in direct shear.

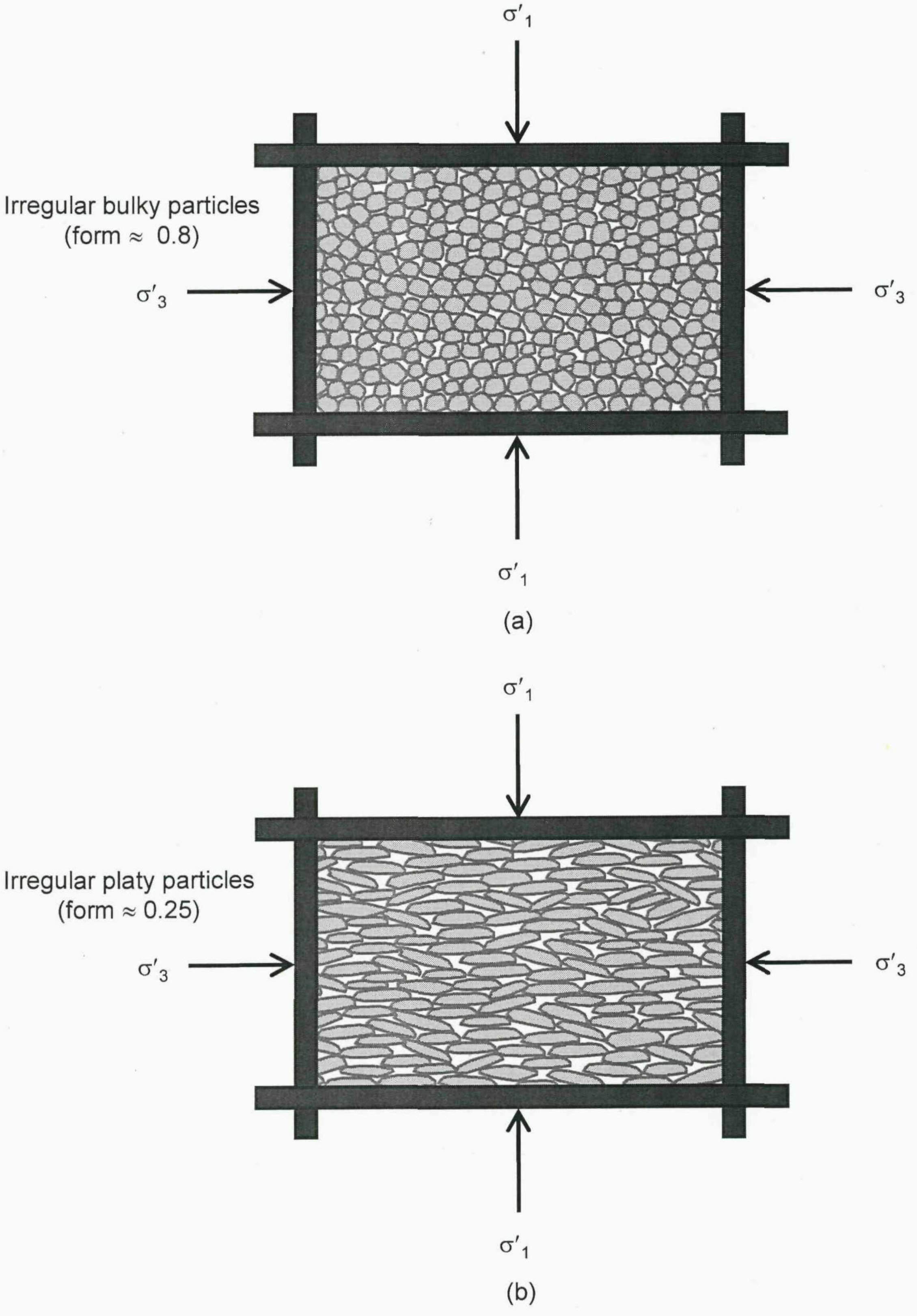

Figure 7.7: Bulky (a) and platy (b) particles loaded perpendicular to the direction of inherent anisotropy in biaxial shear.

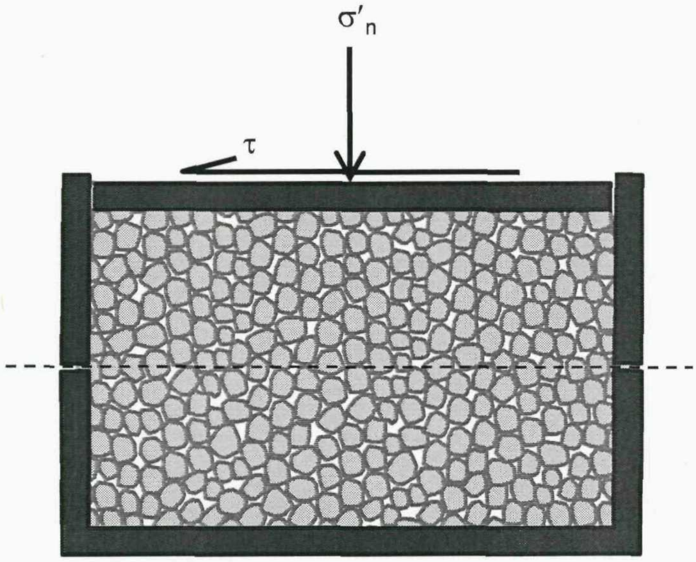

Irregular bulky particles
(form ≈ 0.8)

(a)

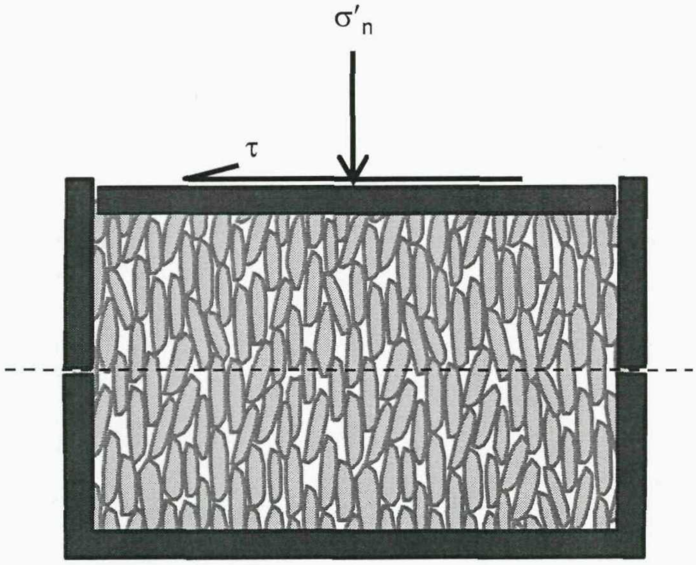

Irregular platy particles
(form ≈ 0.25)

(b)

Figure 7.8: Bulky (a) and platy (b) particles sheared perpendicular to the direction of inherent anisotropy in direct shear.

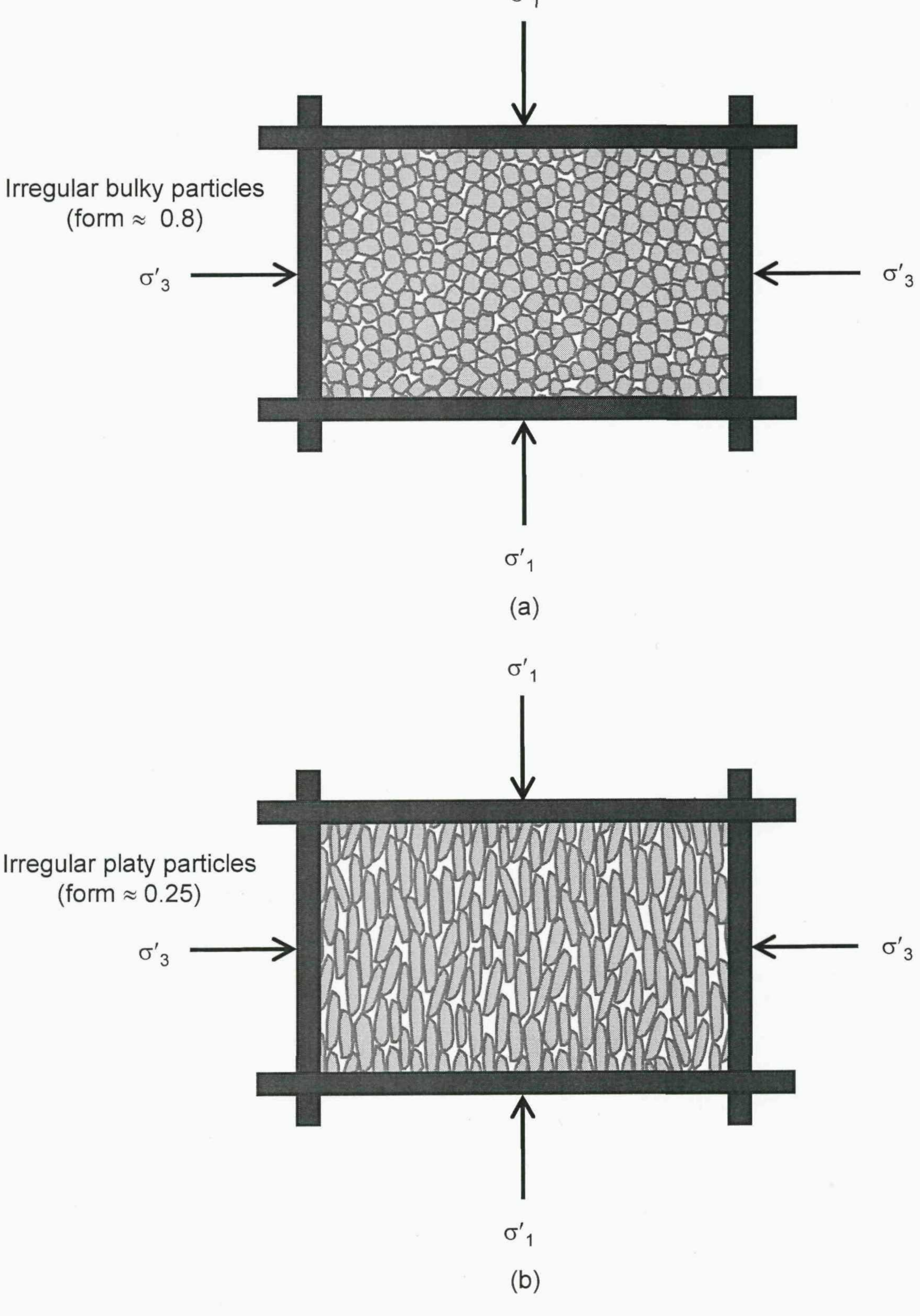

Figure 7.9: Bulky (a) and platy (b) particles loaded in the direction of inherent anisotropy in biaxial shear.

CHAPTER 8 CONCLUSIONS AND RECOMMENDATIONS FOR FUTURE WORK

8.1 Interpretation of the literature

- The sizes and shapes of clastic and crushed rock particles routinely encountered by geotechnical engineers may vary very widely. Size varies from a few tens of millimetres to a fraction of a micron. The overall shape of particles ranges from bulky to platy. Surface features of coarse particles vary from smooth and well-rounded to rough and angular depending on the nature of their formation and the depositional environment. The fine fraction does not seem to have the same range of surface irregularities since fine particles tend to fracture along their cleavage planes. See Section 2.2.

- Traditionally, particle size distribution of coarse fraction is carried out by sieving and fine fraction by sedimentation. Many automated particle sizing techniques are now commercially available, among all, only the image based techniques provide physically meaningful PSD in the case of well-dispersed anisotropic particles whereas in others PSD is biased by the random orientation of particles during the measurements. See Section 2.3.

- This thesis deals with form, sometimes also termed 'sphericity'. Most existing measures of form of coarse particles are two-dimensional. They cannot differentiate bulky and platy particles having similar outline. Of the remaining, three-dimensional parameters, most require the measures of the largest, intermediate and smallest particle dimensions (L, I and S) but it is very difficult and time consuming to obtain reliable measurement of these dimensions for irregular particles such as those normally encountered by geotechnical engineers. In future high-resolution computerised tomographic (CT) scanning (nanotomography) may help to overcome this difficulty, but for the present, simple and reliable measurement techniques are required. See Section 2.4.

- In the case of fine particles, many researchers (in other scientific fields) have proposed methods for determining the aspect ratios based on comparison of particle sizes obtained by pairs of particle sizing techniques. However, in most cases these methods have been applied to a limited range of particle shapes. Also, the aspect ratios determined using these methods were very different from those measured by microscopy techniques. See Section 2.5.

- In order to assess the impact of form on shear behaviour, the relative density should be known which depends on density of the sample and its limiting densities. The maximum density is normally determined by compaction based (BS or ASTM) methods. However, these methods are applicable only for non-crushable materials but most geo-materials are crushable. In essence the limiting maximum densities being determined do not correspond to the original material but the modified (crushed) material. Air-pluviation technique seems to be a good alternative for compaction based methods. The minimum density can be determined reasonably well either by inverted cylinder method or by water-pluviation method. See Sections 2.6 and 2.7.

- The literature reveals that the particle form may have an enormous influence on the mechanical behaviour of soils, however the systematic study is lacking. The immediate obstacle to carry out a systematic study is the lack of a proper form characterisation method. See Section 2.1.

- Experimental evidence available on mixtures of bulky and platy particles reveals that the presence of even small quantities of platy particles in rotund sands converts 'sand-like' behaviour (high stiffness, low compressibility, and dilation during shear) into 'clay-like' behaviour (low stiffness, high compressibility and contractive behaviour during shear). See Section 2.1.

- Even in clays, physico-chemical effects appear to affect only the initial structure, and the subsequent behaviour is largely controlled by the mechanical interaction between particles. See Section 1.1.

- Limited DEM studies also suggest that particle form is a key parameter that controls the mechanical behaviour. See Section 2.1.

8.2 Development of methods of estimating form

- Two new methods were developed for estimating the form of coarse and fine grained materials based considering particles as uniform-sized scalene ellipsoids and oblate spheroids respectively. See Chapters 3 and 4.

8.2.1 Coarse particulates

- A practical definition of form (namely the Scalene Ellipsoid Equivalent Sphericity (SEES)) has been proposed and evaluated its effectiveness by applying it to standard geometrical shapes and regular and irregular particles, and by comparing it with existing measures of form. See Section 3.1.

- The proposed measure of form (SEES) can differentiate bulky particles with the same major, intermediate and minor dimensions but different volumes, and can effectively distinguish between bulky and platy particles having same major and intermediate dimensions. The limitation of this parameter is that it cannot differentiate between rod-like and plate-like particles having the same major and minor dimensions, since it does not consider the intermediate dimension. However, the population of rod-like particles is insignificant in almost all clastic sediments. See Section 3.2.

- An automated method of determining the SEES of particles has been proposed, described, applied to various groups of regular and irregular particles of wide range of shapes. Its effectiveness has been demonstrated over other methods. See Section 3.2.

8.2.2 Fine particulates

- Existing methods of determining the form of fine particles, based on comparisons of particle sizes obtained from two different instruments, were evaluated for their applicability to three different particle shapes. The results show that only the methods of Clift (1988) and Barreiros et al. (1996) gave plausible results, and that (based upon visual estimates from SEM images) these appeared unreliable. See Section 4.1.

- A method of measuring the form of fine-grained materials, based on turbidity and laser diffraction measurement using a single instrument (the Malvern Mastersizer 2000), has been developed, used, and described. It has been applied to a range of synthetic, natural and crushed rock particles with widely varying shapes. The method appears practical, and for the materials tested yields in qualitative agreement with those that could be estimated from SEM images. See Sections 4.2 and 4.3.

8.3 Developments of apparatus and experimental techniques

- A special sliding type 6-part split mould to ease the sample preparation with enlarged end platens, and a simple air-pluviation device for preparing the samples directly on the triaxial apparatus, were developed in this research. See Sections 5.1.3 and 5.1.4.

- The CT scanning technique has been successfully used, for the first time, to examine the orientations of particles in the pluviated specimens. See Section 5.3.

8.4 Developments in DEM simulations

- Two different techniques simulating water-pluviation and air-pluviation were modelled in PFC2D to determine the limiting void ratios (i.e. e_{max} and e_{min}) of numerical 'samples'. The air-pluviation process was simulated by randomly placing the particles in a depositional zone, and then applying gravitational force with zero inter-particle friction. The water-pluviation process was simulated by following the same procedure but with a higher inter-particle friction coefficient. These techniques were applied to a range of particle shapes and produced plausible limiting void ratios. See Section 6.2.

- A new parameter termed the 'asperity friction', defined as the tangent of implied angle of rise of the surface asperity, has been introduced to characterise the surface roughness of clumps in PFC2D. See Section 6.3.

- A novel technique has been developed to prepare numerical 'samples' of the desired relative density with more or less the same fabric. Desired density can be achieved by progressively changing the inter-particle friction during isotropic compression stage. This technique has been successfully applied to a range of particle shapes, and prepared samples with a wide range of relative densities (i.e. 30%, 50% and 70%) all with almost the same fabric. See Section 6.4.

8.5 Observations on the impact of form on depositional packing

- In both numerical and physical experiments, both e_{max} and e_{min} increased with decreasing form. e_{max} was more sensitive than e_{min} especially at lower values of form. The void ratio range (the difference between e_{max} and e_{min}) increased with decreasing form. See Sections 5.3 and 6.2.

- As form decreases, particles can either pack in random orientations forming an open (card-house-like) structure with large local voids between individual and/or groups of particles or pack anisotropically forming a face-to-face arrangement of particles. The inherent anisotropy increases with decreasing form. See Section 7.2.1.

- In numerical simulations, the void ratio increased and the inherent anisotropy decreased either with increasing inter-particle friction or with increasing surface roughness. Surface roughness can be considered as an equivalent inter-particle friction in DEM simulations, since both had an identical effect on depositional packing. See Section 6.3.

8.6 Observations on the impact of form on drained shear behaviour

- The conclusions drawn in this section are based on shearing in triaxial (or biaxial) compression of specimens loaded in the direction of deposition. These may not be valid in other shearing modes and loading directions because of inherent anisotropy.

8.6.1 Global shear behaviour

- The global shear behaviour of dense specimens consisting of uniform sand-sized particles has been found to be highly dependent on their form (SEES), as follows (see Sections 5.4.3 and 6.4.1):
  - The secant stiffness at small strains and its degradation is highly dependent on particle shape. Both small strain stiffness and the rate of degradation decrease with decreasing form.
  - The axial strain, volumetric strain and the mobilised friction at the onset of dilation increases significantly with decreasing form.
  - The peak strength and strain to reach the peak state increases significantly with decreasing form.
  - The ultimate strength and strain to reach the ultimate state increases with decreasing form.
  - The maximum dilatancy factor decreases with decreasing form and may approach unity (i.e. no dilation) in case of extremely platy material.
  - The maximum rate of volumetric strain with respect to shear strain decreases with decreasing form and may approach zero in the case of extremely platy material.
  - The maximum rate of decrease of relative density with respect to axial strain (i.e. maximum rate of dilation) decreases with decreasing form.
  - The difference in relative density between the start and end of shearing (i.e. the amount of dilation) decreases with decreasing form, and becomes negative (i.e. contractive) in extremely platy material.
  - Bolton's empirical equation overestimates the rate of dilatancy in case of low form (platy) materials, presumably because it was derived from experimental data on rotund sands.
  - Particle breakage increases with decreasing form.

- Even in dense samples, a clear transition in behaviour from peak-and-softening to hardening (and from dilative to contractive) was observed as the particle shape changed from spherical to platy. This observation was consistent in numerical as well as in physical experiments. See Section 7.2.2.

- The critical state exists only in high form (bulky) materials but not in low form (platy) materials. This observation was consistent in simulations as well as the experiments. See Section 7.3.

8.6.2 Evolution of micro-structural parameters

I. Anisotropy of particle orientations and contact orientations

- The preferential alignment of particles (anisotropy of particle orientations) increased with strain for all forms and density states. However, the rate of increase of anisotropy diminished with strain in high form (bulky) materials because of the continuous re-orientation of particles (i.e. reached a critical anisotropy). It continued to increase in low form (platy) materials because of the preferred re-orientation of the particles i.e. perpendicular to the major principal stress. See Section 6.4.2.

- The preferential orientations of contacts (contact anisotropy) of cylindrical particles exhibited a peak and a unique critical value at large strain; particles with form equal to 0.67 did not exhibit peak but reached a critical contact anisotropy which was higher than that of cylindrical particles. Anisotropy of particles with form less than 0.67 increased continuously without reaching any critical value. However, at strains less than 10% (approx.), the contact anisotropy of dense samples was higher than that of loose samples and it was consistent for all forms. See Section 6.4.2.

II. Contact forces

- The normal force distribution was more or less isotropic at the start of shearing, and became slightly anisotropic as shear progressed. Anisotropy increased slightly with decreasing form. See Section 6.4.2.

- Tangential force mobilisation at contacts increased with decreasing form as well as with increasing density. The rate of increase with respect to form was much higher than that with respect to density. This could be due to increased interlocking or sandwiching between particles. See Section 6.4.2.

- At large strains, the magnitude of maximum contact force and the proportion of very strong force contacts increased with decreasing form as well as with increasing density. However, the rate of increase with respect to form was much higher than with respect to density. See Section 6.4.2.

- Only cylindrical particles reached a unique critical mean contact force. In non-cylindrical particles mean contact force continued to increase with the strain. Mean contact force increased with decreasing form and with increasing density. However, the rate of increase of mean contact force with respect to form was much higher than with respect to density. See Section 6.4.2.

8.6.3 Mechanisms responsible for differences in observed behaviour between rotund and platy particles

- Evolution of anisotropy during deposition and shearing, crushing in experiments, and mobile and immobile natures of high and low form (bulky and platy) particles during shearing, are thought to be the main mechanisms that are responsible for differences in the observed behaviour between rotund and platy particles. See Section 7.2.

8.7 Practical implications of this research

- Particle form has a significant impact on maximum and minimum densities. The difference between maximum and minimum densities is low in bulky materials and high in platy materials. This means there is a large potential for volume changes when platy materials are subjected to shear or compression.

- Particle form has a significant influence on the initial structure of soils. Its effect is higher in platy materials than in bulky materials.

- Behaviour during shear depends on the initial structure setup prior to shear, and mode of shear in addition to the "state" (void ratio and mean effective stress). The dependency of shear behaviour on initial structure and mode of shear increases with decreasing form. Dilatancy decreases with decreasing form. Dilatancy can be suppressed by the inclusion of platy particles. Therefore, the strength and compressibility may not be uniquely defined either by state parameters proposed by Been and Jefferies or by CSL and NCL. Hence, Critical State may not exist for platy materials.

- Particle form has a significant effect on crushing. For a given initial effective stress, particle crushing is more in platy materials and less in bulky materials. Permeability decreases with decreasing form due to the generation of fines. Stiffness decreases with decreasing form because of sliding and crushing. Bulky materials are less compressible and platy materials are highly compressible.

- Particle form has an effect on undrained shear strength via dilation. For a given initial effective stress, undrained shear strength decreases with decreasing form because of increased excess pore pressure generation. This leads to increased liquefaction potential in the event of earthquakes or any other rapid loading.

8.8 Recommendations for future work

- The methods developed in this research for estimating form have assumed the shape of particles to be uniform, but in reality they are not. Future form characterisation methods should be developed to assess samples with mixed particle shapes.

- This study has mainly concentrated on the drained shear behaviour of particulate materials sheared in triaxial compression. However, it is anticipated that behaviour would be quite different if sheared in other modes e.g. simple shear, triaxial extension, direct shear, ring shear, which need further study.

- This research indicates that fabric anisotropy may have a significant effect on shear behaviour in the case of anisometric particles. This was not explored in this study and needs further research.

- Significant particle breakage and/or crushing were observed in experiments especially in low form materials. This and particle bending should be incorporated in DEM for realistic simulations of the effects of particle form.

REFERENCES

Allen, T. (1990)

Particle size measurement. Chapman & Hall, London

Al-Rousan, T., Masad, E., Tutumluer, E. and Pan, T. (2007)

Evaluation of image analysis techniques for quantifying aggregate shape characteristics, *Construction and Building Materials* 21: 978–990.

Alshibli, K. A. and Alsaleh, M. I. (2004)

Characterizing surface roughness and shape of sands using digital microscopy, *Journal of Computing in Civil Engineering,* ASCE, 18(1), 36-45.

Application note

Obtaining particle shape information using low angle laser light scattering. Malvern Instruments Ltd

Aschenbrenner, B. C. (1956)

A new method of expressing particle sphericity, *Journal of Sedimentary Petrology*, 26(1): 15-31.

Assallay, A. M., Rogers, C. D. F., Smalley, I. J. and Jefferson, I. F. (1998)

Silt: 2-62μm, 9-4ϕ, *Earth-Science Reviews* 45, 61-88.

ASTM D 4253-00

Standard test methods for maximum index density and unit weight of soils using a vibratory table.

ASTM D 4254-00

Standard test methods for minimum index density and unit weight of soils and calculation of relative density.

ASTM D422-63 (2002)

Standard Test Method for Particle-Size Analysis of Soils. ASTM International, Pennsylvania, USA.

Azema, E., Radjai, F., Peyroux, R., and Saussine, G. (2007)

Force transmission in a packing of pentagonal particles, *Physical Review E* 76, 011301

Barreiros, F. M., Ferreira, P. J., and Figueiredo, M. M. (1996)

Calculating shape factors from particle sizing data, *Particle and Particle Systems Characterisation* 13: 368-373.

Barrett, P. J. (1980)

The shape of rock particles, a critical review, *Sedimentology* 27: 291-303.

Baudet, G., Bizi, M. and Rona, J. P. (1993)

Estimation of the average aspect ratio of lamellae-shaped particles by laser diffractometry, *Particulate Science and Technology* 11(1): 73-96.

Been, K., and Jefferies, M. G. (1985)

A state parameter for sands, *Geotechnique*, 35(2), 99-112.

Bishop, A. W. , and Green, G. E. (1965)

The influence of end restraint on the compression strength of a cohesionless soil, *Geotechnique*, 15(3), 243-266.

Bishop, A. W., and Wesley, L. D. (1975)

A hydraulic triaxial apparatus for controlled stress path testing, *Geotechnique*, 25(4), 657-670.

Blatt, H. (1987)

Perspectives; Oxygen isotopes and the origin of quartz, *Journal of Sedimentary Petrology* 57(2): 373-377.

Blott, S. J. and Pye, K. (2007)

Particle shape: a review and new methods of characterisation and classification, *Sedimentology* (OnlineEarly Articles). doi:10.1111/j.1365-3091.2007.00892.x

Blott, S. J., Al-Dousari, A.M., Pye, K., and Saye, S. E. (2004)

Three-dimensional characterisation of sand grain shape and surface texture using a nitrogen gas adsorption technique, *Journal of sedimentary research*, 74(1): 156-159.

Bokman, J. W. (1952)

Clastic quartz particles and their indices of provenance, *Journal of Sedimentary Petrology* 22(1): 17-24.

Bollmann, J., Quinn, P.S., Vela, M.,Brabec, B.,Brechner, S., Cortés, M.Y., Hilbrecht, H., Schmidt, D.N., Schiebel, R., and Thierstein, H.R. (2004)

Automated particle analysis: Calcareous microfossils. In: Francus, P. (Editor): Image Analysis, Sediments and Paleoenvironments. Kluwer Academic Publishers, Dordrecht, The Netherlands, p. 229-252.

Bolton, M. D. (1986)

Strength and dilatancy of sands, *Geotechnique*, 36(1), 65-78.

Bowman, E. T., Soga, K., and Drummond, W. (2001)

Particle shape characterisation using Fourier descriptor analysis, *Geotechnique*, 51(6): 545-554.

BS 1377-2 (1990)

Methods of test for soils for civil engineering purposes - classification tests. British Standards Instiution, London.

BS 1377-4 (1990)

Methods of test for soils for civil engineering purposes - classification tests. British Standards Institution, London.

BS ISO 13319 (2000)

Determination of particle size distributions-Electrical sensing zone method. British Standards Institution, London.

BS ISO 13320-1 (1999)

Particle size analysis-Laser diffraction methods-Part 1: General principles. British Standards Institution, London.

Casagrande, A. (1936)

Characteristics of cohesionless soils affecting the stability of slopes and earth fills. *Journal of Boston Society of Civil Engineers*, 23(1), 13-32.

Cheng, Y. P., Nataka, Y., and Bolton, M. D. (2003)

Discrete element simulation of crushable soil, *Geotechnique*, 53(7): 633–641.

Cheng, Y. P., Bolton, M. D. and Nataka, Y. (2004)

Crushing and plastic deformation simulation of soils using DEM, *Geotechnique*, 54(2): 131–141.

Cho, G. C., Dodds, J., and Santamarina, J. C. (2006)

Particle shape effects on packing density, stiffness and strength: natural and crushed sands, *Journal of Geotechnical and Geoenvironmental Engineering*, 132(5): 591-602.

Clark, M. W. (1981)

Quantitative Shape analysis: A review, *Mathematical Geology*, 13(4), 303-320.

Clayton, C. R. I., and Khatrush, S. A. (1986)

A new device for measuring local axial strains on triaxial specimens, *Geotechnique*, 36(4), 593-597.

Clayton, C. R. I and Obula Reddy, A.C. (2006)

Influence of particle form on initial packing and dilation of particulate materials-a numerical study, *Int. Symp. on Geomechanics and Geotechnics of Particulate Media, IS Yamaguchi-2006*, Japan, 12-14 September: Paper No. 041.

Clayton, C.R.I., Xu, M. and Bloodworth, A. (2006)

A laboratory study of the development of earth pressure behind integral bridge abutments, *Geotechnique*, 55, 8, 561–571.

Clayton, C.R.I., Theron, M. and Vermeulen, N.J. (2004)

The effect of particle shape on the behaviour of gold tailings, *Proc. 'Advances in Geotechnical Engineering-The Skempton Memorial Conference'* (ed. Jardine, R.J., Potts, D.M. and Higgins, K.G.), 1, 393-404.

Clayton, C.R.I., Khatrush, S.A., Bica, A.V.D. & Siddique, A. 1989.

The Use of Hall Effect Semiconductors in Geotechnical Instrumentation, *Geotechnical Testing Journal*, ASTM, 12(1), 69-76.

Clift, R. (1988)

Inertial, sedimentation, image analysis and electrozone measurements of particle size, *In Particle size analysis* 1988 ed. By P. J. Lloyd, pp. 3-17, John Wiley

Coop, M. R., Sorensen, K. K., Freitas, T. B. and Georgoutsos, G. (2004)

Particle breakage during shearing of a carbonate sand, *Geotechnique*, 54(3): 157–163.

Corey, A. T. (1949)

Influence of shape on fall velocity of sand grains. MSc thesis, Colorado A&M College, 102pp.

Cresswell, A., and Powrie, W. (2004)

Triaxial tests on an unbonded locked sand, *Geotechnique*, 54(2), 107-115.

Cresswell, A., Barton, M. E. & Brown, R. (1999)

Determining the maximum density of sands by pluviation, *Geotechnical Testing Journal* GTJODJ, 22(4), 324-328.

Cundall, P. A. (1971)

A computer model for simulating progressive, large-scale movements in blocky rock systems. Proceedings of International Society of Rock Mechanics, Nancy 2, No. 8.

Cundall, P. A. (1978)

BALL – A program to model granular media using the distinct element method. Technical note, Advanced Technology Group, Dames and Moore, London.

Cundall, P. A. and Strack, O. D. L. (1979)

A discrete numerical model for granular assemblies. Geotechnique 29(1): 47-65.

De Josselin De Jong, G. (1988)

Elasto-plastic version of the double sliding model in undrained simple shear tests, *Geotechnique*, 38(4), 533-555.

Ehrlich, R. and Weinberg, B. (1970)

An exact method for characterisation of grain shape, *Journal of Sedimentary petrology* 40, 205-212.

Ehrlich, R., Brown, P. J., Yarus, J. M. and Przygocki, R. S. (1980)

The origin of shape frequency distributions and the relation ship between size and shape, *Journal of Sedimentary Petrology* 60, 476-484.

Endoh, S., Kuga, Y., Ohya, H., Ikeda, C. and Iwata, H. (1998)

Shape estimation of anisotropic particles using size measurement techniques, *Part. Part. Syst. Charact.* 15: 145–149.

Ferreira, P. J., Rasteiro, M. G., and Figueiredo, M. M. (1993)

Influence of shape on particle size analysis, *Particulate Science and Technology* 11(3):199-206.

Frost, D. J. (2003)

Effect of boundary conditions on volumetric microstructure evolution, *FHWA-NSF Workshop on Imaging and Simulation of Concrete Structure*, Evanston.

Frost, D. J. & Park, J. Y. (2003)

A critical assessment of the moist tamping technique, *Geotechnical Testing Journal* GTJODJ, 26(1), 57-70.

Gilboy, G. (1928)

The compressibility of sand-mica mixtures, *Proc. ASCE transactions*, 54, 555-568.

Grengg, R. and Kammel, K. (1924)

Charakteristik einiger Wiener Bausande nach ausseren Kennzeichen. *Zeitschrift des Oesterreichischen Ingenieur- und Architekten-vereines.* Heft 43-44.

Guimaraes, M. S., Valdes, J. R., Palomino, A. M., and Santamarina, J. C. (2007)

Aggregate production: Fines generation during rock crushing, *International Journal of Mineral Processing* 81: 237-247.

Hardin, B. O. (1985)

Crushing of soil particles, *Journal of Geotechnical Engineering*, ASCE, 111(10): 1177–1192.

Hawkins, A.E., (1993)

The shape of powder-particle outlines. Research Studies Press, Taunton and Wiley, New York, 150pp.

Hayton, S., Nelson, N. S., Ricketts, B. D., Cooke, S. and Wedd, M. W. (2001)

Effect of mica on particle-size analysis using the laser diffraction technique, *Journal of Sediementary Research*, 71(3), 507-509.

Hentschel, M. L. and Page, N. W. (2003)

Selection of descriptors for particle shape characterization, *Particle and Particle Systems Characterisation*, 20, 25-38.

Heymann, G. (1998)

The stiffness of soils and weak rocks at very small strains. PhD thesis, University of Surrey, Guildford.

Hight, D.W. and Leroueil, S. (2003)

Characterisation of soils for engineering purposes, *Proc. Symp. on Characterisation and Engineering Properties of Natural Soils*, Tan et al. (eds.), Swets & Zeitlinger, Lisse, 255-360.

Hofmann, F. (1959)

Experimental determination of specific surface and grain shape of foundry sands, *Modern Castings* 35, 125-128.

Holubec, I. and D'Appolonia, E. (1973)

Effect of particle shape on the engineering properties of granular soils, *Evaluation of relative density and its role in geotechnical projects involving cohesionless soils*, ASTM STP 523: 304-318.

Inoue (1995)

Determination of aspect ratios of clay sized particles, *Clay Science* 9: 259–274.

Ishihara, K. (1993)

Liquefaction and flow failure during earthquakes, *Geotechnique* 43(3): 351–415.

Itasca., (2004)

PFC2D 3.1 Manual: Theory and Background. Itasca Consulting Group, Inc., Minneapolis.

BS ISO 13322:1 (2004)

Particle size analysis — Image analysis methods — Part 1: Static image analysis methods. British Standards Institution, London.

BS ISO 13322:2 (2006)

Particle size analysis — Image analysis methods — Part 2: Dynamic image analysis methods. British Standards Institution, London.

Jang, D. J. 1997.

Quantification of sand structure and its evolution during shearing using image analysis. School of Civil and Environmental Engineering, Georgia Institute of Technology, Atlanta, Ph.D Dissertation: 259pp.

Jardine, R. J., Symes, M. J., and Burland, J. B. (1984)

The measurement of soil stiffness in the triaxial apparatus, *Geotechnique*, 34(3), 323-340.

Jefferson, I., and Smalley, I.J. (1995).

Six definable particle types in engineering soils and their participation in collapse events: proposals and discussion, *In: Genesis and Properties of Collapsible Soils*, NATO ASI Series C: Math. and Physical Sciences, Vol. 468, 16-31.

Jefferson, I. F., and Smalley, I. J. (2002)

Distinctive particle types and their intrinsic behaviour, *Proceedings of 9th Congress of the International Association of Engineering Geology and the Environment*, Durban, Sept. 16-20, pp. 244-252.

Jefferson, I. F., Jefferson, B. Q., Assallay, A. M., Rogers, C. D. F. and Smalley, I. J. (1997)

Crushing of quartz sand to produce silt particles, *Naturwissenschaften* 84: 148-149.

Jennings, B. R. (1993)

Size and thickness measurement of polydisperse clay samples, *Clay Minerals* 28: 485-494.

Jennings, B. R. and Parslow, K. (1988)

Particle size measurement: The equivalent spherical diameter, *Proc. R. Soc. A, Mathematical and Physical Sciences* 149 (1856): 137–149.

Kirkapatrick, W. M. & Belshaw, D. J. (1968)

On the interpretation of the triaxial test, *Geotechnique* 18(3), 336-350.

Kock and Huhn (2007)

Influence of particle shape on the frictional strength of sediments-A numerical case study, *Sedimentary Geology* 196: 217–233.

Koerner, R. M. (1968)

The behaviour of cohesionless soils formed from various minerals. PhD thesis, Department of Civil Engineering, Duke University, 304 pages.

Koerner, R. M. (1970a)

Behaviour of single mineral soils in triaxial shear, *Journal of the Soil Mechanics and Foundations Division*, Proc. of ASCE, 96(4), 1221-1234.

Koerner, R. M. (1970b)

Energy and surface characteristics of quartz soils, *Proceedings of 9th Annual Engineering Geology Engineering Symposium*, Pocatello, Idaho, 187- 195.

Konert, M. and Vandenberghe, J. (1997)

Comparison of laser grain size analysis with pipette and sieve analysis: a solution for the underestimation of clay fraction, *Sedimentology* 44: 523–535.

Krinsley, D. H., and Smalley, I. J. (1973)

The shape and the nature of small sedimentary quartz particles, *Science* 180(4092): 1277-1299.

Krumbein, W. C. (1941)

Measurement and geological significance of shape and roundness of sedimentary particles, *Journal of Sedimentary Petrology*, 11(2), 64-72.

Krumbein, W. C. and Sloss, L. L. (1963).

Stratigraphy and sedimentation, second edition, W.H. Freeman and Company, San Francisco, p. 660.

Lade, P. V., Yamamuro, J. A. and Bopp, P. A. (1996)

Significance of particle crushing in granular materials, *Journal of Geotechnical Engineering*, ASCE, 122(4): 309–316.

Lagioia, R., Sanzeni, A. & Colleselli, F. (2006)

Air, water and vacuum pluviation of sand specimens for the triaxial apparatus, *Soils and foundations*, 46(1), 61-67.

Lambe, T. W. (1951)

Soil testing for Engineers. New York, Wiley. 165 pages.

Leroueil, S. and Hight, D.W. (2003)

Behaviour and properties of natural soils and soft rocks, *Proc. Symp. on Characterisation and Engineering Properties of Natural Soils*, Tan et al. (eds.), Swets & Zeitlinger, Lisse, 29-254.

Lips, A., Hart, P. M., and Evans, I. D. (1992)

Use of low angle laser light scattering in characterisation of non-spherical particles and swelling of microgel particles, *Proceedings of 5th European Symposium in Particle Characterisation*, Nurnberg Messe, Nurnberg 443-451.

Lu, N., Ristow, G. H., and Likos, W. J. (2000)

The accuracy of hydrometer analysis for fine-grained clay particles, *ASTM Geotechnical Testing Journal*, 23(4), 487-195.

Maeda, K. (1994)

A study on the deformation-failure behaviour of sands with different primary properties. Thesis (doctoral)-Hokkaido University.

Margolis, S. V. and Krinsley, D. H. (1974)

Processes of formation and environmental occurrence of microfeatures on detrital quartz grains, *American journal of Science* 274: 449-464.

Mirghasemi, A. A. Rothenberg, L. & Matyas, L. (2002)

Influence of particle shape on engineering properties of assemblies of two-dimensional polygon-shaped particles, *Geotechnique* 52(3): 209-217.

Moss, A. J. and Green, P. (1975)

Sand and silt grains: predetermination of their formation and properties by microfractures in quartz, *Australian Journal of Earth Sciences* 22: 485-495.

Moss, A.J. (1966)

Origin, shaping and significance of quartz sand grains, *Journal of the Geological Society of Australia*, 13, 97–136.

Mundegar, A.K. (1997)

An investigation into the effect of platy mica particles on the behaviour of sand. MSc. Dissertation, Imperial College of Science and Technology, University of London.

Nouguier-Lehon, C., Cambou, B. and Vincens, E. (2003)

Influence of particle shape and angularity on the behaviour of granular materials: a numerical analysis, *Int. Journal of Numerical Analytical Methods in Geomechanics*, 27,1207–1226.

Nouguier-Lehon, C., Vincens, E., and Cambou, B. (2005)

Structural changes in granular materials: The case of irregular polygonal particles, *International Journal of Solids and Structures*, 42, 6356-6375.

Novak, J. W. and Thompson, J. R. (1986)

Extending the use of particle sizing instrumentation to calculate particle shape factors, *Powder Technology* 45: 159-167.

Oakely, D. M., Jennings, B. R., Waterman, D. R. and Fairey, R. C. (1982)

An electro-optic birefringence fine-particle sizer, *Journal of Physics E: Scientific Instruments* 15: 1077-1082.

Olson, R. E. and Mesri, G. (1970)

Mechanisms controlling compressibility of clays, *Journal of the Soil Mechanics and Foundations Division*, Proc. ASCE 96(6): 1863-1878.

Olson, S.M. and Stark, T.D. (2002)

Liquefied strength ratio from liquefaction flow failure case histories, *Canadian Geotechnical Journal*, 39: 629–647.

Pabst, W., Kunes, K., Havrda, J. and Gregorova, E. (2000)

A note on particle size analyses of kaolins and clays, *Journal of European Ceramic Society* 20: 1429-1437.

Parslow, K. and Jennings, B. R. (1986)

Simultaneous size and thickness measurements for heterogeneous micrometer-sized particles, *Journal of Physics D: Applied Physics* 19: 1233-1243.

Podczeck, F. (1997)

A shape factor to assess the shape of particles using image analysis, *Powder Technology*, 93: 47-53.

Powers, M. C. (1982)

Comparison charts for estimating roundness and sphericity

AGI data sheets, American Geological Institute, Alexadria, Va.

Pye, W. D. and Pye, M. H. (1943)

Sphericity determinations of pebbles and sand grains, *Journal of Sedimentary Petrology*, 13(1), 28-34.

Riley, A. (1941)

Projection Sphericity, *Journal of Sedimentary Petrology* 11(2): 94–97.

Rogers, C. D. F. and Smalley, I. J. (1993)

The shape of loess particles, *Naturwissenschaften* 80: 461-462.

Roscoe, K. H., Schofield, A. N., and Wroth, C. P. (1958)

On the yielding of soils, *Geotechnique*, 8(1), 22-53.

Rowe, P. W. & Barden, L. (1964)

Importance of free ends in triaxial testing, *Journal of the Soil Mechanics and Foundations Division*, ASCE, 90(SM1), 1-27.

Santamarina, J. C. Klein, K. and Fam, M. (2001)

Soils and waves: Particulate materials behaviour, characterization and process monitoring. John Wiley and Sons, Ltd., Chichester, UK, 488 pages.

Santamarina, J.C., Klein, K.A., Wang, Y.H. and Prencke, E. (2002)

Specific Surface: Determination and Relevance, *Canadian Geotechnical Journal*, vol. 39, no. 1, pp. 233-241.

Sarsby, R. W., Kalteziotis, N. & Haddad, E. H. 1982.

Compression of "free-ends" during triaxial testing, *Journal of Geotechnical Engineering Division*, Proceedings of ASCE, 108(GT1), 83-107.

Shibuya, S. and Hight, D.W. (1991)

Liquefaction Line-a new concept for initiation of liquefaction of soil, *Proc. Int. Conf. on Geotechnical Engineering for Coastal Development*. Geo-Coast '91, Yokohama, Japan, Discussion to Session 5.

Slepetys, R. A., and Cleland, A. J. (1993)

Determination of shape of kaolin pigment particles, *Clay Minerals* 28: 495-508.

Smalley, I. J., Jefferson, I. F., O'Hara Dhand, K. and Evans, R. D. (2006)

An approach to the problem of loess deposit formation: Some comments on the 'in situ' or 'soil-eluvial' hypothesis, *Quaternary International* 152-153: 109-117.

Smalley, I. J., Kumar, R., O'Hara Dhand, K., Jefferson, I. F. and Evans, R. D. (2005)

The formation of silt material for terrestrial sediments: Particularly loess and dust, *Sedimentary Geology* 179: 321-328.

Smalley, I. J., Krinsley, D. H., Moon, C. F. and Bentley, S. P. (1978)

Processes of quartz fracture in nature and the formation of clastic sediments. In: Easterling, K. E. (ed.) *Mechanisms of deformation and fracture*, Pergamon Press, Oxford, 119-127.

Smalley, I. J., Kumar, R., O'Hara Dhand, K., Jefferson, I.F. and Evans, R. D. (2004)

The formation of quartz silt for terrestrial sediments: particularly loess deposits, *International Workshop Particle Size Sediment Dynamics*. Hanse-Wissenschaftskol Delmenhorst 15-18 April, pp. 129-130.

Smalley, I. J. (1966)

Formation of quartz sand, *Nature* 211: 476-479.

Smalley, I. J., and Glendinning, S. (1991)

Two distinct particle types in the Lanzhou loess, *Naturwissenschaften* 78(4): 167.

Smalley, I. J. (1995)

Making the mineral: The formation of silt sized primary mineral particles for loess deposits, *Quaternary Science Reviews* 14: 645-651.

Sneed, E. D. and Folk, R. L. (1958)

Pebbles in the lower Colorado river, Texas-a study in particle morphogenesis, *Journal of Geology* 66(2): 114–150.

Sukumaran, B. and Ashmawy, A. K. (2001)

Quantitative characterisation of the geometry of discrete particles, *Geotechnique*, 51(7), 619-627.

Taylor, D. W. 1941.

Seventh progress report on shear research to U. S. Engineers. Massachusetts Institute of Technology Publication.

Taylor, D. W. (1948)

Fundamentals of soil mechanics. New York: John Wiley.

Terzaghi, K. (1925)

Principles of soil mechanics: V-Physical differences between sand and clay, *Engineering News Record*, 95(26), 912-915.

Theron, M., Vermeulen, N. and Clayton, C.R.I. (2005)

Fabric: A governing mechanism in the behaviour of gold tailings, *Proc. Int. Conf. on Problematic Soils*, May 2005, Famagusta, (Ed. Huriye Bilsel and Zalihe Nabantoglu) vol. 1, pp. 361-369. Eastern Mediterranean University Press, Famagusta, Northern Cyprus. ISBN: 975-8401-22-X.

Thomas, M. C., Wiltshire, R. J., and Williams, A. T. (1995)

The use of Fourier descriptors in the classification of particle shape, *Sedimentology*, 42, 635-645.

Thomsen, K. (2004)

http://home.att.net/~numericana/answer/ellipsoid.htm#thomsen

Accessed 20 January 2008.

Vaid, Y. P., Sivathayalan, S. & Stedman, D. 1999

Influence of specimen-reconstituting method on the undrained response of sand, *Geotechnical Testing Journal* GTJODJ, 22(3), 187-195.

Vermeulen, N.J. (2001)

The composition and state of gold tailings. Ph.D. thesis, University of Pretoria, South Africa.

Wadell, H. (1932)

Volume, shape and roundness of rock particles, *Journal of Geology*, 40, 443-451.

Wadell, H. (1933)

Sphericity and roundness of rock particles, *Journal of Geology*, 41, 310-331.

Wadell, H. (1935)

Volume, shape and roundness of quartz particles, *Journal of Geology*, 43, 250-280.

Wesseloo, J. (2004)

The strength of Geocell support packs. Ph.D. Thesis, University of Pretoria, South Africa.

Wettimuny, R. and Penumadu, D. (2004)

Application of Fourier analysis to digital imaging for particle shape analysis, *Journal of Computing in Civil Engineering*, ASCE, 18(1), 2-9.

White, D. J. (2003)

PSD measurement using the single particle optical sizing (SPOS) method. *Geotechnique*, 53(3), 317-326.

Wiegner, G. (1920)

Ueber eine neue methode der schlammanalyse, *Zentralblatt fur die gesamte landwirtschaft*, Bd. I, No. 1.

Wright, J. S., Smith, B., Whalley, B. (1998)

Mechanisms of loess-sized quartz silt production and their relative effectiveness: laboratory simulations, *Geomorphology* 23: 15-34.

Wright, J. S. (1995)

Glacial comminution of quartz sand grains and the production of loessic silt: a simulation study, *Quaternary Science Reviews* 14: 669-680.

Wright, J. S. (2001)

"Desert" loess versus "glacial" loess: quartz silt formation, source areas and sediment pathways in the formation of loess deposits, *Geomorphology* 36: 231-256.

Wright, J. S. (2004)

The role of weathering in the production of quartz silt, *International Workshop Particle Size Sediment Dynamics*. Hanse-Wissenschaftskol Delmenhorst 15-18 April, pp. 154-158.

Williams, R. A. & Jia, X. 2003.

A new method for prediction of bulk particle packing behaviour for arbitrary-shaped particles in containers of any shape, *Particulate Science and Technology*, 21: 195-205.

Wroth, C. P. (1958)

The behaviour of soils and other granular media when subjected to shear. Ph.D. Thesis, University of Cambridge.

Xu, M. (2005)

The behaviour of soil behind full-height integral abutments. Ph.D. thesis, University of Southampton.

Yoshimine, M., Robertson, P.K., and Wride (Fear), C.E. (1999)

Undrained shear strength of clean sands to trigger flow liquefaction. *Canadian Geotechnical Journal*, 36(5): 891–906.

Zingg, T. (1935)

Beitrage zur Schootteranalyse. Schweizminer. *Petrog. Mitt.* 15, 38-140.

Zuriguel, I. and Mullin, T. (2007)

The role of particle shape on the stress distribution in a sandpile, *Proc. R. Soc. A, Mathematical and Physical Sciences*, published online, doi:10.1098/rspa.2007.1899, 18 pp.

APPENDIX A

FORM CORRECTION FACTOR FOR RANDOM ORIENTATION OF PARTICLES

Mastersizer 2000 uses the following relation to determine the *Obscuration* during a laser diffraction particle size measurement

$$Obscuration = \frac{I_0 - I_t}{I_0} \qquad \text{(A1a)}$$

This can be re-written as

$$\frac{I_t}{I_0} = (1 - Obscuration) \qquad \text{(A1b)}$$

As per Beer-Lambert law,

$$\frac{I_t}{I_0} = e^{-Tb}; \qquad \text{where } T = \sum \frac{M_i \pi d_i^2 Q_i}{4} \qquad \text{(A2)}$$

Equation (A2) can be re-written as follows by substituting equation (A1b)

$$\sum \frac{M_i \pi d_i^2}{4} = \frac{\log_e (1 - Obscuration)}{-b \sum Q_i} \qquad \text{(A3)}$$

L.H.S part of equation (A3) represents the projected area of particles per unit volume if the particles under consideration are circular and isotropic in cross-section with diameter d_i. If particles are anisotropic, the projected area (of a given number of particles) determined using equation (A3) is approximately equal to their mean value rather than the maximum possible, due to their random orientation during measurement. Therefore, equation (A3) must be corrected in order to capture the maximum projected area, and can be written as

$$\sum \frac{M_i \pi d_i^2}{4} = \frac{\log_e (1 - Obscuration)}{-b \sum Q_i} \times C_f \qquad \text{(A4)}$$

where C_f is the correction factor to account for random orientation of particles.

Projected area of particles can also be determined from the known volume-weighted particle size distribution predicted by Mie theory of light scattering.

As per Cauchy's theorem, the mean projected area of any randomly oriented convex solid particle is expected to be approximately equal to one-quarter of its total surface area (Cauchy, 1908), although (as notedby Vickers, 1996) this is not true for shapes such as cuboids. Using this principle, the projected area of particles per unit mass (cm^2/gm) can be expressed in terms of PSD by volume as follows

$$\Pr ojected\ area\ per\ unit\ mass = \frac{Surface\ area\ per\ unit\ mass}{4} = \frac{\frac{6}{\rho}\sum\frac{V_i}{d_i}}{4} \qquad \text{(A5)}$$

The above equation can be re-written for projected area of particles per unit volume as follows

$$\Pr ojected\ area\ per\ unit\ volume = \left(\frac{C_s}{\rho}\right)\frac{3}{2}\sum\frac{V_i}{d_i} \qquad \text{(A6)}$$

Where C_S is the solids concentration in gm/cm^3. The dimensionless ratio $\left({C_s}/{\rho}\right)$ is the theoretical volume concentration (C_{th}) of solids.

Upon equating equations (A4) and (A6), an equation of the following form can be obtained for determining the corrected C_{th} (%),

$$Corrected\ C_{th} = \frac{100\log_e(1-Obscuration)}{-\frac{3}{2}b\sum\frac{V_iQ_i}{d_i}}\times C_f \qquad \text{(A7)}$$

Since particle orientation is random during measurement, the projected area of a given number of particles seen by the Mastersizer (during obscuration measurements) will not be equal to the maximum possible, but will equal the mean, which leads to an underestimation of C_{th} and subsequently an overestimation of form. C_{th} must be corrected by multiplying a factor (C_f), defined as a ratio of the maximum possible and the mean of randomly projected areas of a particle.

Considering the particles as scalene ellipsoids ($L > I > S$):

- the mean projected area of a group of randomly oriented particles can be determined by using the Cauchy's theorem (Cauchy, 1908) in conjunction with Thomsen's formula (Thomsen, 2004) for estimating the true surface area, using the following equation

$$A_{mean} = \frac{Surface\,area}{4} = \frac{\pi}{8}\left[(LI)^p + (IS)^p + (SL)^p\right]^{1/p} \tag{A8}$$

  where $p \approx \ln(3)/\ln(2)$

- the maximum possible projected area of a scalene ellipsoid is

$$A_{max} = \frac{\pi LI}{4} \tag{A9}$$

Thus, the correction factor (defined as a ratio of the maximum possible and the mean of randomly projected areas) can be expressed in terms of two dimensionless ratios, *S/L* (i.e. initial estimate of form determined using equation (4.3)) and *I/L*, as follows:

$$C_f = \frac{A_{\max}}{A_{mean}} = \frac{2}{\left[1 + \left(\frac{S}{L}\right)^p + \left(\frac{S/L}{I/L}\right)^p\right]^{1/p}} \tag{A10}$$

The variation of C_f with respect to *S/L* and *I/L* are shown in Figure 4.4.

APPENDIX B

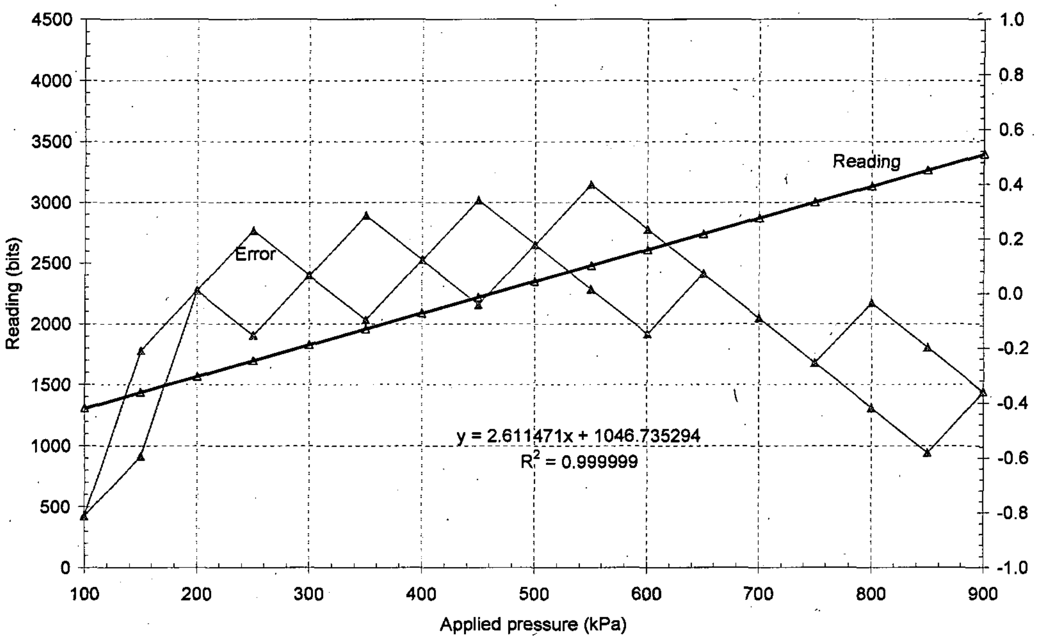

Figure B.1: Typical calibration result of the pressure transducer

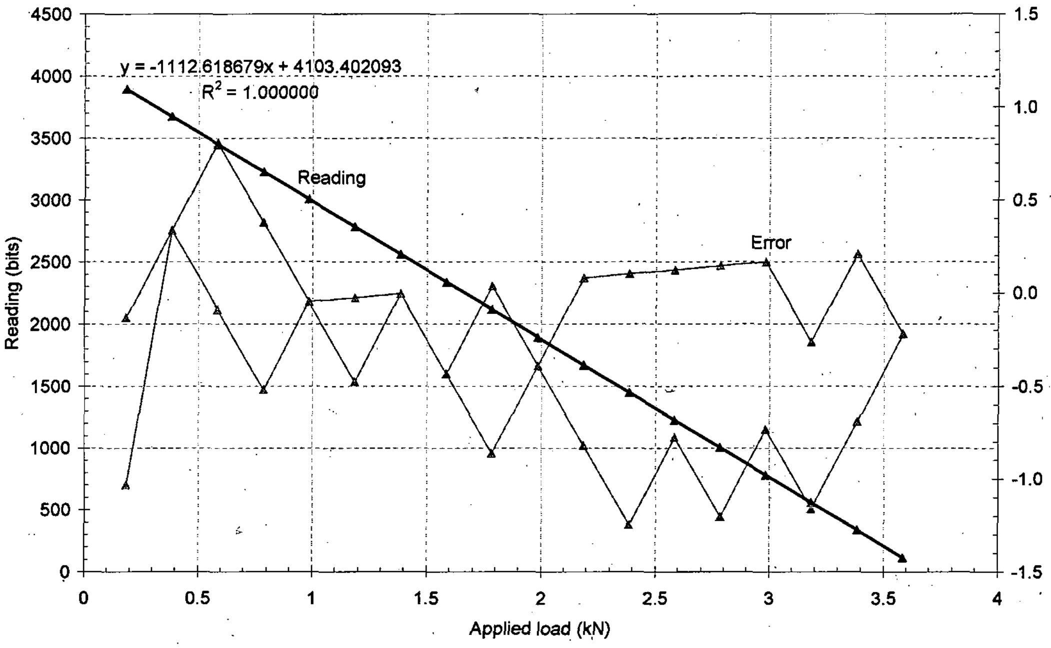

Figure B.2: Typical calibration result of the axial load cell

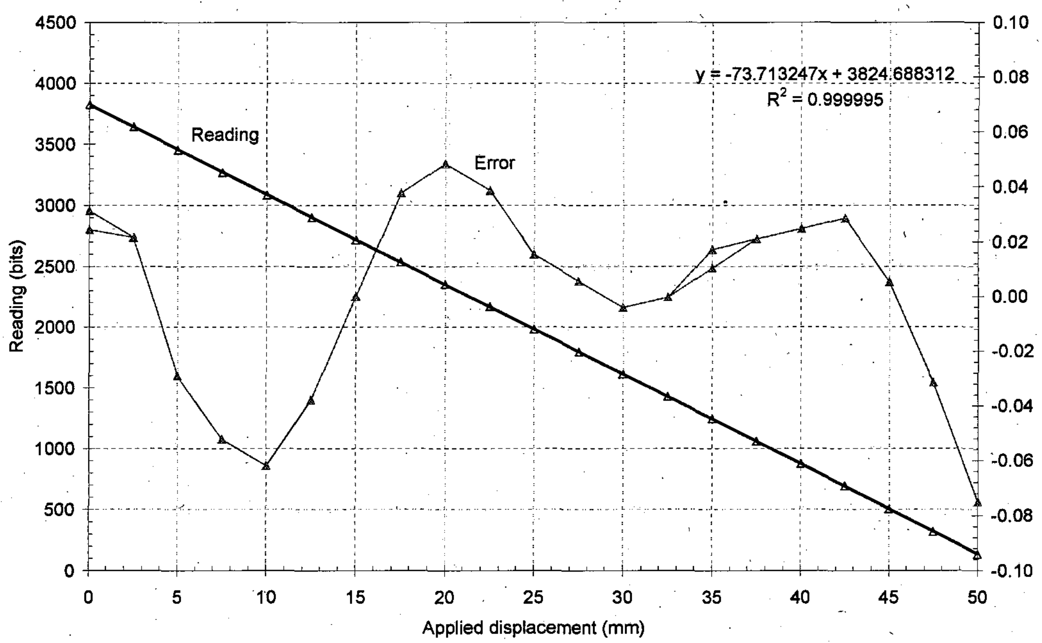

Figure B.3: Typical calibration result of the DC-to-DC LVDT transducer

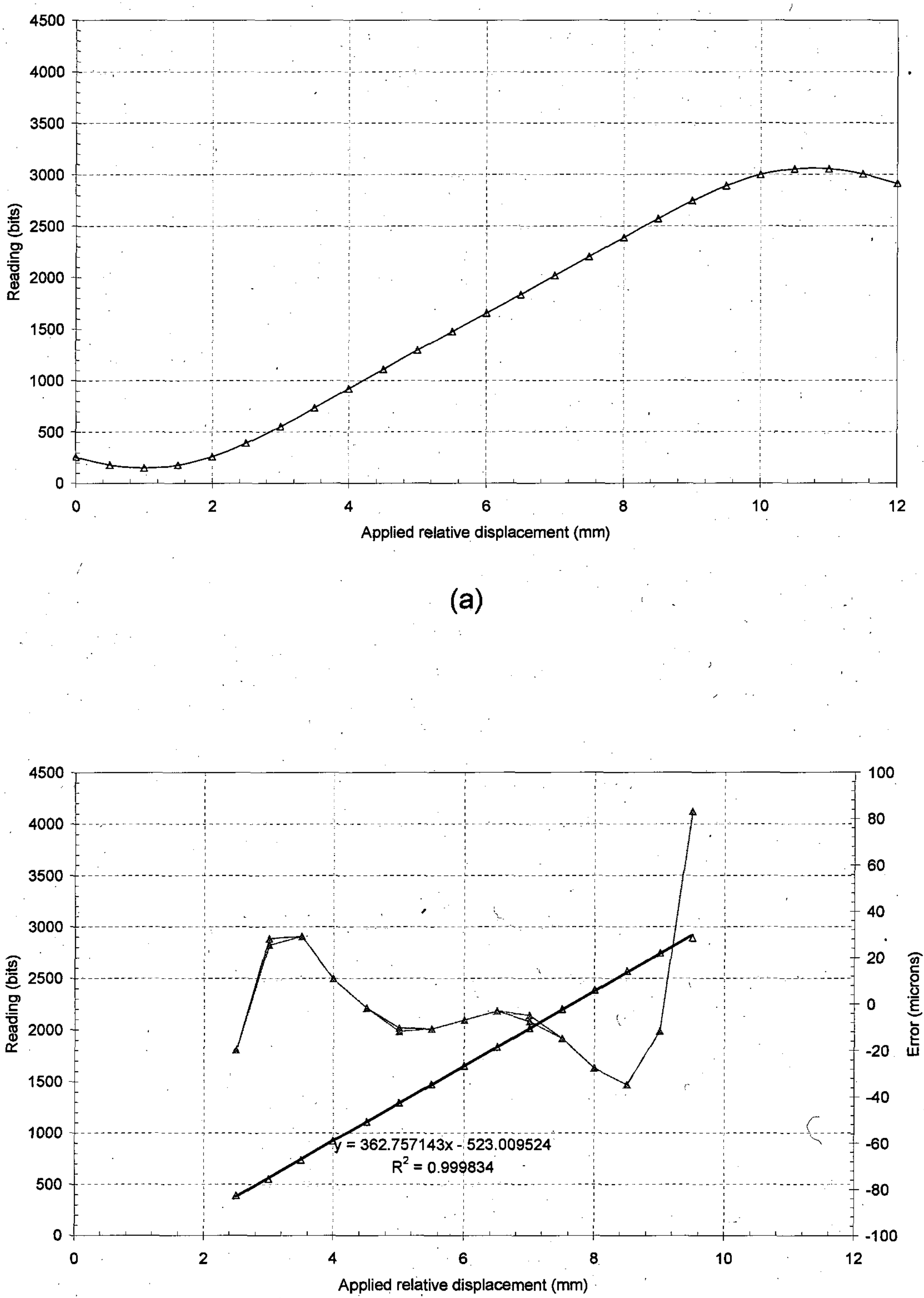

(a)

(b)

Figure B.4: Typical calibration result of the Hall-effect strain gauge